
A Surface Science Approach to Catalysis

Ronnie T. Vang

Interdisciplinary Nanoscience Center (iNANO) and
Department of Physics and Astronomy
University of Aarhus, Denmark

PhD thesis
July 2005

The thesis has been submitted to the Faculty of Science at the University of Aarhus, Denmark, in order to fulfil the requirements for obtaining the PhD degree in physics. The studies have been carried out under the supervision of Prof. Flemming Besenbacher in the scanning probe microscopy group at the Interdisciplinary Nanoscience Center (iNANO) and the Department of Physics and Astronomy from August 2001 to July 2005.

Contents

List of Publications	v
List of abbreviations	vii
1 Introduction	1
1.1 Introduction	2
1.2 Heterogeneous catalysis	2
1.2.1 The surface science approach	4
1.3 Challenges of the hydrogen society	5
1.3.1 Production of hydrogen	6
1.3.2 Storage of hydrogen	6
1.3.3 Fuel cells	6
1.3.4 Outline	7
2 Methods	9
2.1 Surface science and scanning tunneling microscopy	10
2.1.1 Basic principles of the STM	10
2.1.2 The Aarhus STM	11
2.1.3 Theory of tunneling	12
2.2 Complimentary experimental techniques	13
2.2.1 Temperature-programmed desorption	14
2.2.2 X-ray photoelectron spectroscopy	14
2.3 Theory in catalysis	15
2.3.1 Density functional theory	16
2.3.2 Modelling catalysis	18
3 Reactivity of catalytic surfaces	21
3.1 Introduction	22
3.2 Active sites	22
3.2.1 Thiophene on MoS ₂	24
3.2.2 C on Ni(111)	27

3.2.2.1	CO dissociation on Ni(111)	29
3.2.2.2	C ₂ H ₄ dissociation on Ni(111)	29
3.3	Changing the reactivity	31
3.3.1	Ni(111)	33
3.3.2	Cu/Pt(111)	36
3.3.2.1	Background	36
3.3.2.2	STM	38
3.3.2.3	TPD	42
3.3.2.4	XPS	45
3.3.2.5	Conclusion	47
4	Surface structures at reaction conditions	49
4.1	Introduction	50
4.2	The pressure gap	50
4.2.1	CO/Pt(111)	52
4.2.2	NO/Pd(111)	55
4.2.3	CO on Au/Ni(111)	58
4.3	Oxide formation	61
4.3.1	O/Pt(110)	63
4.3.2	O/Ag(111)	64
5	Summary and outlook	71
	Bibliography	75
	Acknowledgements	85

List of Publications

- [I] *Chemistry of one-dimensional metallic edge states in MoS₂ nanoclusters*, J. V. Lauritsen, M. Nyberg, R. T. Vang, M. V. Bollinger, B. S. Clausen, H. Topsøe, K. W. Jacobsen, E. Lægsgaard, J. K. Nørskov, and F. Besenbacher, *Nanotechnology* **14**, 385 (2003).
- [II] *CO desorption rate dependence on CO partial pressure over platinum fuel cell catalysts*, J. C. Davies, R. M. Nielsen, L. B. Thomsen, I. Chorkendorff, Á. Logadóttir, Z. Lodziana, J. K. Nørskov, W. X. Li, B. Hammer, S. R. Longwitz, J. Schnadt, E. K. Vestergaard, R. T. Vang, and F. Besenbacher, *Fuel Cells*, **4** 309 (2003).
- [III] *High-coverage structures of carbon monoxide adsorbed on Pt(111) studied by high-pressure scanning tunneling microscopy*, S. R. Longwitz, J. Schnadt, E. K. Vestergaard, R. T. Vang, E. Lægsgaard, I. Stensgaard, H. Brune, and F. Besenbacher, *J. Phys. Chem. B*, **108**, 14497 (2004).
- [IV] *Oxidation of Pt(110)*, W. X. Li, L. Österlund, E. K. Vestergaard, R. T. Vang, J. Matthiesen, T. M. Pedersen, E. Lægsgaard, B. Hammer, and F. Besenbacher, *Phys. Rev. Lett.*, **93**, 146104 (2004).
- [V] *Controlling the catalytic bond-breaking selectivity of Ni surfaces by step blocking*, R. T. Vang, K. Honkala, S. Dahl, E. K. Vestergaard, J. Schnadt, E. Lægsgaard, B. S. Clausen, J. K. Nørskov, and F. Besenbacher, *Nat. Mater.*, **4**, 160 (2005).
- [VI] *Adsorbate induced alloy phase-separation: A direct view by high-pressure scanning tunneling microscopy*, E. K. Vestergaard, R. T. Vang, J. Knudsen, T. M. Pedersen, T. An, E. Lægsgaard, I. Stensgaard, B. Hammer, and F. Besenbacher, *Phys. Rev. Lett.*, accepted
- [VII] *The adsorption structure of NO on Pd(111) at high pressures studied by STM and DFT*, R. T. Vang, J.-G. Wang, J. Knudsen, J. Schnadt, E. Lægsgaard, I. Stensgaard, and F. Besenbacher, *J. Phys. Chem. B*, **109**, 14262 (2005).

- [VIII] *CO dissociation on Ni(111): Step blocking by Ag, Au, and S*,
R. T. Vang, E. K. Vestergaard, E. Lægsgaard, I. Stensgaard, and F. Besenbacher,
In manuscript.
- [IX] *Ethylene dissociation on flat and stepped Ni(111): A combined STM and DFT study*,
R. T. Vang, K. Honkala, S. Dahl, E. K. Vestergaard, J. Schnadt, E. Lægsgaard,
B. S. Clausen, J. K. Nørskov, and F. Besenbacher, Surf. Sci., submitted.
- [X] *From Atom-resolved Scanning Tunneling Microscopy (STM) Studies To the Design of New Catalysts*,
J. V. Lauritsen, R. T. Vang, and F. Besenbacher, Catal. Today, submitted.
- [XI] *Cu/Pt subsurface alloy; an improved catalyst for the water-gas shift reaction*,
R. T. Vang, A. U. Nilekar, J. Knudsen, J. Schnadt, E. Lægsgaard, M. Mavrikakis,
and F. Besenbacher, In preparation.
- [XII] *A combined STM and XPS study of the different surface oxide structures of Ag(111)*,
J. Schnadt, J. Knudsen, R. T. Vang, E. Lægsgaard, and F. Besenbacher, In preparation.

Patents

Fuel cell and anode,
J. H. Hyltoft, B. S. Clausen, F. Besenbacher, R. T. Vang, J. K. Nørskov,
C. G. L. Olsen, and E. K. Vestergaard, patent number 04012278.0

List of abbreviations

AES	Auger electron spectroscopy
DFT	Density functional theory
fcc	Face-centered cubic
GGA	Generalized gradient approximation
hcp	Hexagonally close-packed
HDS	Hydrodesulphurization
HP	High pressure
LDA	Local density approximation
LEED	Low energy electron diffraction
ML	Monolayer
PEMFC	Polymer electrolyte membrane fuel cell
PM-IRAS	Polarization modulation infrared reflection absorption spectroscopy
SFG	Sum frequency generation
STM	Scanning tunneling microscopy/microscope
SPARG	Sulphur passivated reforming
SPM	Scanning probe microscopy
TEM	Transmission electron microscope
TPD	Temperature-programmed desorption
UHV	Ultra high vacuum
WGS	Water-gas shift
XDS	X-ray diffraction
XPS	X-ray photoelectron spectroscopy

CHAPTER 1

Introduction

In this chapter a general introduction to heterogeneous catalysis is given as a motivation for the work presented in the rest of the thesis. Special emphasis is given to the surface science approach and its relevance to applied catalysis. The importance of the development of new and improved catalysts is illustrated by the example of the emerging hydrogen technology, which poses many great challenges within the field of catalyst design.

1.1 Introduction

Catalysis is a not often used expression in everyday life, but nonetheless it plays a major role for our very existence. Were it not for the catalytic properties of the enzymes in our bodies we would not be able to function as human beings. Also the catalytic production of ammonia fertilizer is essential to sustain the current world population. It is estimated that without the chemical production of ammonia from the Haber-Bosch process we would not be able to feed more than 3 billion people [1]. For this reason the Haber-Bosch process is by many considered as the most important invention of the 20th century in front of such landmark achievements as the computer, the television, or the aeroplane, and both Fritz Haber and Carl Bosch were awarded the Nobel price in chemistry for their development of the process [2, 3].

Without knowing it we surround ourselves with products whose manufacturing and utilization rely on catalytic processes every single day. The products range from the gasoline with which we fuel our cars, to the batteries of our mobile phones and even to the plastic bag we use to carry home some of these products from the super market. The chemical industry is the largest in the world and the annual value of the products produced from catalytic processes well exceeds of one trillion US\$ [4, 5].

The most well known application of catalysis in everyday life is without doubt the automotive three-way catalyst, which is used for cleaning exhaust gases from gasoline driven combustion engines in, e.g., automobiles. This is just one example of the utilization of catalysts for environmental protection. Another example is the removal of sulfur impurities from fuels and exhaust gasses from, e.g., coal-based powerplants. If released into the atmosphere sulfur leads to the formation of sulfuric acid, which again leads to forest death due to acid rain. With the increasing awareness of the environmental problems caused by the industrialized society, increasing efforts will be put into the development of catalysts which can prevent or diminish these potentially devastating issues. Traditionally, catalysts have been developed by simple *trial and error* methods, but in order to continue the development of new and improved catalysts for the future it is essential that we understand the fundamental properties of catalysts and catalytic processes. This thesis is dedicated to the study of some of the fundamental issues concerning a number of different catalytic systems.

1.2 Heterogeneous catalysis

For many chemical reactions the rate of reaction is practically zero even at conditions under which the reaction is thermodynamically favorable, which is due to the large activation energy associated with the formation of the intermediate or final products. The use of a catalyst can increase the reaction rate by several orders of magnitude without being consumed in the reaction. By definition a catalyst is [6]

a substance that increases the rate of a reaction without modifying the overall standard Gibbs energy change in the reaction; the process is called catalysis.

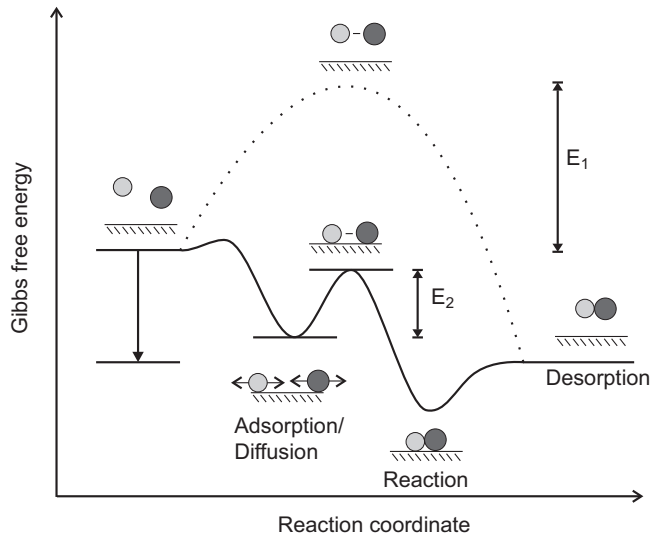


Figure 1.1: Energy diagram illustrating the role of a heterogeneous catalyst. E_1 and E_2 are the activation barriers for the gas phase reaction and the reaction on the catalyst surface, respectively.

A distinction is made between homogeneous catalysis, in which the reactants and the catalyst are in the same phase, and heterogeneous catalysis, in which the reaction takes place at or near the interface between different phases. Homogeneous catalysis is mainly relevant in enzymatic processes, and will not be dealt with in this thesis. Heterogeneous catalysis, on the other hand, applies to most industrial catalytic processes. The most typical heterogeneous catalytic reaction is that of two or more gas phase molecules reacting on the surface of a solid metal or oxide. The energy diagram of figure 1.1 shows the role of the catalyst for the simplest possible gas phase reaction, the reaction between molecules A and B to form a new molecule AB :



The dotted line in the energy diagram shows the gas phase reaction to directly form molecule AB , whereas the full line shows the same reaction taking place on a metal surface. This reaction pathway consists of three elementary steps: adsorption (and diffusion) of molecules A and B , reaction to form molecule AB , and finally the desorption of molecule AB . It is seen that the overall change in the Gibbs free energy (ΔG) is the same for both reaction pathways, while the activation barriers (E_1 and E_2) are different. The rate constant, k_r , can be described by an Arrhenius expression [7]:

$$k_r = \nu \cdot \exp\left(-\frac{E_A}{k_B T}\right), \quad (1.2)$$

where E_A is the activation energy, k_B the Boltzmann constant, and T the absolute temperature. Because of the exponential dependence, only a relatively small decrease in the activation barrier is needed in order to strongly increase the rate of a given reaction. For more complex reactions there may be numerous elementary steps to consider and the overall rate is given by the interplay between all of these reactions. In some cases a single elementary step has such a high barrier compared to the other elementary steps that this essentially determines the rate of the overall reaction. This is referred to as the *rate-limiting step* of the reaction. In other cases it might not be possible to identify a single rate-limiting step and one has to employ micro-kinetic modelling to find the overall reaction rate.

There are several properties that describe a catalyst, and among the most important are the *activity*, the *active sites*, and the *selectivity* of a catalyst. The activity describes the rate at which a catalytic reaction takes place and is usually given as the *turnover frequency* (events per second per active site), where an active site refers to the particular site on a catalyst surface, at which a given reaction takes place. The selectivity describes the ratio between the final products of a reaction with multiple reaction pathways leading to different end products. Often the desired catalytic reaction is associated with several unwanted side-reactions, which may simply be a waste of the reactants or in many cases even *poison* the catalyst surface; meaning that the activity of the catalyst drops.

1.2.1 The surface science approach

Most heterogeneous catalysis takes place on surfaces and often the catalyst consists of precious metals. As a consequence the active material is dispersed into small particles on a highly porous support material - typically an oxide. Such a high surface area, oxide-supported catalyst is very difficult to characterize with standard surface science tools. The typical approach has therefore been to use single crystal surfaces of the active material as simple catalyst models, and in this way a vast amount of knowledge about the interaction of gas molecules with single-crystal surfaces relevant for catalysis has been gathered over the past four decades [4, 7, 8].

Although many catalytic systems have been examined in great detail, doubt can be raised as to whether or not information about a given system under the ultra-high vacuum (UHV) conditions of typical surface science experiments can be extrapolated to real-life catalysis, which typically takes place at pressures well in excess of one atmosphere and often at elevated temperatures. It is also questionable to what extent a single-crystal surface shows the same characteristics as that of the dispersed nanoparticles of an oxide-supported catalyst. These apparent gaps between surface science and real-life catalysis have been termed the *pressure gap* and the *materials gap*, and much effort has been put into bridging them [8–10].

Several techniques exist for *in situ* characterization at high pressures. This will be the topic of chapter 4, where the use of the scanning tunneling microscope (STM) to bridge the pressure gap is demonstrated. The materials gap can be partly bridged by refining the model systems and, e.g., grow the active catalyst material as nanoclusters on an oxide support [11]. One example of such a model system for a hydrodesulfurization catalyst is given in section 3.2.1. In chapter 3 examples will be given of how the

unique imaging capabilities of the STM can be used to gain very detailed information on the active sites on metal surfaces. It will also be demonstrated that the knowledge gained from the surface science studies can be used for the design of new and improved catalyst materials. This work along with many other efforts in the same direction will hopefully mark the beginning of a new era in which fundamental science will replace the traditional trial and error method as the main pillar in the future development of new and improved catalysts.

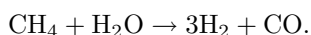
1.3 Challenges of the hydrogen society

One of the greatest challenges facing mankind in the 21st century is the increasing demand for energy following the almost explosive economic development in especially the Asian countries. Due to the depletion of the energy resources [12] and to environmental issues we cannot rely on fossil fuels as the primary energy source in the future; we must find alternatives. Despite being a nearly perfect source of energy, fusion is still very far from being a technically viable solution, and fission energy still has unresolved aspects concerning the handling of nuclear waste as well as the lack of general support from the public due to the fear of catastrophic accidents as the Chernobyl meltdown. It seems that at present the only true alternative to a continued and increased use of fossil fuels is to use solar energy in either its direct form by harvesting the light from the sun or in its indirect form as wind or water energy or biomass production. The solar irradiance onto the planet Earth is more than sufficient to provide for even a highly increased energy consumption, even when it is taken into account that the present technology can only utilize a fraction of the solar energy [13]. However, the distribution of renewable energy is very non-uniform and often out of phase with the energy consumption. Or put in another way: the Sun shines most intensively in the Sahara desert during the summer, whereas the energy consumption is largest in the cold northern regions in the winter time. Finding ways in which the energy from renewable sources can be stored and transported in an effective way is thus a tremendous challenge. The challenge is particularly overwhelming for mobile uses such as for transport, where mass and volume of the energy carrier are important issues.

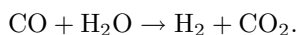
An elegant solution to the problem of storage and transportation of renewable energy would be to use hydrogen as an energy carrier. In an ideal *hydrogen society*, solar energy will be used to split water into hydrogen and oxygen. The hydrogen can then be stored and transported to its place of use, where fuel cells are used to convert the chemical energy of the hydrogen molecule into electric energy. This ideal hydrogen society is in principle fully renewable, non-polluting, and CO₂ neutral. But although the technology already exists, both scientific and technical landmark achievements still have to be made within hydrogen production, hydrogen storage, and fuel cells before a full transition from the present use of fossil fuels can be achieved. However, hydrogen technology has already started to move out from the laboratories and onto the global markets, and hydrogen will certainly play a major role in the future energy system.

1.3.1 Production of hydrogen

Ideally hydrogen would be produced from sunlight and water, either using electricity from photovoltaics to electrolyze water [14] or in a direct water splitting process [15]. Another sustainable pathway would be to derive hydrogen from biomass, a method which has been demonstrated using both metal catalysts [16] and bacteria [17]. All these methods, however, suffer from low conversion efficiencies, and the vast majority of the present hydrogen production comes from *steam reforming* of fossil fuels, a reaction which for the reformation of methane is described by



The product gasses are usually reacted further to remove CO and produce additional hydrogen in the *water-gas shift reaction*:



Although the production of hydrogen from fossil fuels is not a sustainable method, it may play a very important role in the early stages of the transition to a hydrogen-based society. With natural gas being practically a waste product in the oil industry, steam reforming can offer a cheap way of producing hydrogen, and this could help in motivating the development of other hydrogen technologies. Furthermore, emission gasses from cars could be eliminated, thus preventing the severe air pollution encountered in many of the world's large cities.

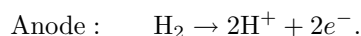
1.3.2 Storage of hydrogen

The storage of hydrogen for transport applications is perhaps the most severe obstacle for the large scale implementation of hydrogen technology [18]. Storage in pressurized tanks is inefficient due to the low volumetric energy density in hydrogen gas [19], and the liquefaction of hydrogen is associated with a relatively high energy loss [20]. The most promising solution seems to be the storage of hydrogen in a solid or liquid compound such as a metal hydride or alcohol [21]. A good storage material should not only have a high hydrogen storage capacity, it should also absorb and desorb hydrogen at near-ambient conditions, allow for fast refuelling, show cyclic stability, and consist of cheap and abundant materials. Hundreds of different metal hydrides have been studied [22] but none fulfill all of these demands, and at present the hydrogen storage problem is still a major obstacle for the hydrogen economy. Within the last few years much of the ongoing research has focused on a new class of complex hydrides such as NaAlH_4 [23, 24] and LiAlH_4 [25]. Also the storage of hydrogen in clathrates (solid water matrices) is considered [26], but so far these new materials are far from being technologically viable solutions, and a breakthrough discovery is still much awaited within this field of research.

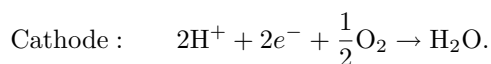
1.3.3 Fuel cells

One of the main advantages in using hydrogen as an energy carrier is that hydrogen can be converted to electricity and heat with high efficiency in a fuel cell. In the *polymer*

electrolyte membrane fuel cell (PEMFC) hydrogen is dissociated at the anode:



At the cathode the protons react with oxygen and electrons:



The protons are conducted through a polymer electrolyte membrane, whereas the electrons are forced into an external circuit, thus creating an electromotive force. Several types of fuel cells exist, differing in electrolyte material and operating temperature, but they are all based on the same basic principle [27–29]. Both the anode and the cathode reactions are catalytic processes, and the typical choice of catalyst in the PEMFC is for both platinum. Platinum is a very expensive metal, and this is partly the reason for the high price of state-of-the-art fuel cells. Furthermore, the platinum based anode catalysts are very sensitive to even small amounts of CO (10–100 ppm) in the hydrogen feed gas. CO binds very strongly to the Pt surface, which leads to a *CO poisoning* of the catalyst. This is a serious problem since most hydrogen is produced from the steam reforming of natural gas, and there is therefore a great interest in finding new and preferably cheaper catalyst materials that can overcome this problem. One strategy to improve the performance of the presently used anode catalysts is to design new surface alloy systems with a higher CO tolerance [30].

1.3.4 Outline

The work presented in this thesis comprises several studies, which are all related to gas surface interactions relevant to catalytic systems. The individual studies are presented in detail in separate articles appended to this thesis, whereas the opening 5 chapters are meant to put these studies into context and discuss their relevance to the overall theme of the thesis - the surface science approach to catalysis.

Following the general introduction to heterogeneous catalysis in this chapter, a presentation of the experimental and theoretical methods used in the present studies is given in chapter 2. Chapter 3 deals with the reactivity of catalytic surfaces, and in particular it is demonstrated how the STM can be used to gain very detailed knowledge on the nature of the active sites. Furthermore, it is demonstrated how new catalytic materials can be designed based on fundamental surface science studies. In chapter 4 several high-pressure studies are presented and examples are given of both systems which display no apparent pressure gap as well as systems where completely new physics is observed at elevated pressures. Finally the results are summarized and an outlook for future work is given in chapter 5 prior to the individual articles.

CHAPTER 2

Methods

The principal experimental methods used for the work of the present thesis are introduced. Especially scanning tunneling microscopy (STM) is dealt with in some detail since it has been the main tool for all of the studies presented in the following chapters. Two other techniques, which I have made use of during my PhD study, are also briefly introduced. These are temperature-programmed desorption (TPD) and x-ray photoelectron spectroscopy (XPS). Density functional theory (DFT) has been widely used to complement or confirm the experimental findings in the present thesis for which reason a short introduction to the basics of DFT is given at the end of this chapter.

2.1 Surface science and scanning tunneling microscopy

The development of efficient pumping systems in the 1960's paved the way for an almost explosive growth of the field of surface science. Ultra-high vacuum (UHV) conditions allow for both maintaining clean surfaces over periods of hours as well as enabling the use of a wide range of electron or photon-based techniques which are not applicable at higher pressures due to the low mean free path of the electrons. A second revolution within surface science was seen with the advent of the scanning probe microscopy (SPM) techniques, pioneered in 1982 by the work of G. Binnig and H. Rohrer, both of whom received the Nobel prize for their development of the scanning tunneling microscope (STM) [31].

The STM is a local probe with the unique capability of imaging single atoms on conducting surfaces. This gives a great advantage over the majority of standard surface science tools which are averaging techniques, and the STM and SPM in general have provided a tremendous amount of new insight into the chemistry of solid surfaces [32]. With the STM it is possible to study single defects, an ability that is especially desirable for studying the active sites of catalytic surfaces. Despite the extraordinary possibilities offered by the STM, there are also some drawbacks which must be kept in mind when analyzing STM data. The STM possesses no chemical specificity, which often complicates the assignment of features in the STM images to specific atoms or molecules. The local nature of the STM can also be deceitful and tempt one to draw too wide conclusions based on detailed observations that may not be representative for the system as such. This is often referred to as *tunnel vision*. To make a comprehensive study it is thus always a good idea to use several complimentary techniques for the characterization of a given system. For this purpose our UHV chamber is equipped for low energy electron diffraction (LEED), Auger electron spectroscopy (AES), and temperature-programmed desorption (TPD), besides the STM. For the performance of STM studies at high gas pressures a dedicated high pressure (HP) cell with a dedicated HP-STM has been developed within the group [33].

2.1.1 Basic principles of the STM

In light of the enormous impact of the STM on experimental surface science, its principle of operation is astonishingly simple (see figure 2.1 (left)). The STM exploits quantum mechanical tunneling which allows electrons to “tunnel” through an otherwise classically forbidden region. This effect implies that if a metal tip is brought into close proximity of a conducting surface so that the electron wavefunctions overlap, a small (tunneling) current will flow between the tip and the sample when a voltage difference is applied. Due to the exponential decay of the wavefunctions into the vacuum gap between tip and sample, the tunneling current is strongly dependent on the gap width and varies markedly even over the distance of a single atom. The current measured when raster-scanning the tip across the surface then gives an image of the (electronic) structure of the surface.

In practical applications, sub-Ångström, lateral resolution is achieved by mounting the tip on a scanner tube made of piezo-electrical ceramics. These piezo ceramics change

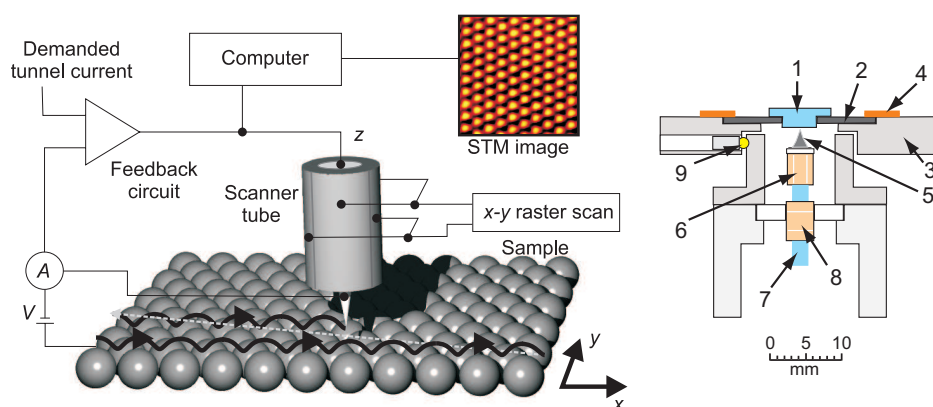


Figure 2.1: **Left:** The operating principle of a scanning tunneling microscope. **Right:** Schematic drawing of the Aarhus STM. See the text for details

their physical dimensions in response to an applied voltage. Usually STM images are recorded in *constant current mode*, in which the tip is moved vertically during the xy-scanning in such a way that the tunneling current is kept at a constant, predefined level. This mode of scanning has several advantages. First, it allows the tip to scan across areas with relatively large height differences and second, it maintains a constant set of tunneling parameters (tunneling voltage and current). The latter is often preferable since the imaging of surfaces, and in particular adsorbates on surfaces, may very often vary with the tunneling parameters.

2.1.2 The Aarhus STM

Utilizing the STM principle in real experiments is a huge task that demands positioning and vibrational stability with sub-Ångström precision. These technical difficulties have been overcome in several ingenious ways [34]. In the present studies the home-built Aarhus STM developed by Erik Lægsgaard *et al.* [35] was used.

A schematic drawing of the Aarhus STM is given in fig.2.1 (right). The crystals (1) are mounted on tantalum holders (2) and placed face-down into the STM. Electric and thermal contact to the top plate (3) is ensured by two copper springs (4). A polycrystalline tungsten tip (5) is attached to a cylindrical scanner tube (6) consisting of a piezoelectric ceramic with four separated electrodes of gold coating. By applying voltages to these electrodes individually the tube can be bend, thus facilitating the lateral scanning. By applying equal voltages to the four electrodes with respect to the inner electrode on the scanner tube, the tube can contract or expand lengthwise, thereby enabling the tip to follow the contour of the surface while scanning. The scanner tube is glued onto a ZrO rod (7), which can be moved by the “inchworm” (8), used for the coarse approach of the tip. The inchworm consists of a center electrode and two clamp electrodes made of

piezoelectric ceramics. By successively opening and closing the clamps and contracting and expanding the center electrode, the ZrO rod can be moved in a worm-like manner. The inchworm is used for coarse approach, and it is possible to move the tip from a distance of ca. 1 mm to within a few Ångströms of the sample in less than a minute without damaging the tip upon impact with the surface.

The STM is thermally and electrically isolated from the top plate by three quartz balls (9). The top plate, on the other hand, is in contact with a large aluminum block, which can either be cooled by liquid nitrogen or heated by Zener diodes. This allows us to scan at temperatures ranging from ~ 120 K to ~ 400 K.

The aluminum block containing the STM is suspended from three springs with a resonance frequency of a few Hertz, and in combination with the high resonance frequency of the rigid STM itself, external vibrations are effectively damped and no further vibrational isolation is needed.

The HP-STM has a design that is very similar to the one of the UHV-STM [33]. The main differences being a more compact design, which allows the STM to be incorporated into a small volume in the HP cell, and a gold coating of all metallic surfaces to avoid unwanted reactions occurring on the stainless steel parts of the STM. The scanning capabilities of the HP-STM are similar to those of the UHV-STM, but the HP-STM does not facilitate sample cooling or heating above ~ 370 K.

2.1.3 Theory of tunneling

Calculating the tunneling current between the tip of an STM and a metal surface is a complicated task, which requires the knowledge of the quantum mechanical states of both the tip and the surface. The formalism that is normally applied in theoretical treatments of STM is that of Tersoff and Hamann [36, 37]. In their approach the tip and sample are described as two non-interacting systems, in which case time dependent perturbation theory gives the tunneling current (from tip to sample) to first order and at low tunneling voltage as

$$I = \frac{2\pi e}{\hbar} \cdot \sum_{\mu,\nu} |M_{\mu\nu}|^2 \cdot f(E_\mu) \cdot (1 - f(E_\nu + eV)) \cdot \delta(E_\mu - E_\nu).$$

Here $f(E)$ is the Fermi function, $M_{\mu\nu}$ the tunneling matrix element between states ϕ_μ of the tip and states ϕ_ν of the sample, E_μ and E_ν the energies of the unperturbed states, and the delta function expresses energy conservation.

The crucial point is the evaluation of the tunneling matrix element, $M_{\mu\nu}$, which was shown by Bardeen [38] to be given by

$$M_{\mu\nu} = \frac{\hbar^2}{2m} \cdot \int d\vec{S} \cdot \vec{j}_{\mu\nu}$$

where $\vec{j}_{\mu\nu}$ is the current density operator, and the integration is over any surface lying entirely within the barrier region between the tip and the sample. Since the tip state

is in general unknown in STM, Tersoff and Hamann chose to approximate it with a spherically symmetric s-wave. This approximation holds very little information on the unknown state of the tip, but it does take into account the finite size of the tip compared to the size of the tunneling barrier. For small tip-sample bias, V , they arrive at a simple expression for the tunneling current:

$$I \propto V \cdot \sum_{\nu} |\phi_{\nu}(\vec{r}_0)|^2 \delta(E_{\nu} - E_f)$$

where \vec{r}_0 is the position of the tip center of curvature. The summation gives the *local density of states* ($\rho(\vec{r}_0, E_f)$) at the Fermi level evaluated at the position of the tip. In constant-current mode, the tip thus follows contours of constant local density of states, and it is important to bear in mind that an STM image is a convolution of the geometric and electronic surface structure.

The steep dependence on distance of the tunneling current originates from the exponential decay of ϕ_{ν} into the vacuum barrier, which leads to the following relation between the tunneling current and the sample-to-tip distance, s :

$$I \propto \exp\left(-\frac{\sqrt{8m\phi}}{\hbar}s\right)$$

with m being the electron mass and ϕ the work function. The exponential dependence of the tunneling current on tip-to-sample separation is indeed what enables the atomic resolution in STM. For typical values of the work function, the tunneling current changes an order of magnitude over a distance of ~ 1 Å. This also explains why the tip need not be sharp on a mesoscopic scale in order to achieve atomic resolution with the STM: If one atom reaches out further than the rest, this atom will carry almost all of the current.

The crucial factor when imaging with the STM is the local density of states at the Fermi level evaluated at the position of the tip. For simple metal surfaces this will give a “true” topographic picture in which protrusions can be associated with single atoms [37]. For adsorbates on a metal surface, however, the situation is in general not as simple. Such adsorbates can be imaged as depressions or protrusions depending on whether they add or subtract states at the Fermi level [39,40].

2.2 Complimentary experimental techniques

As already mentioned it is important to combine the STM studies with the information from other surface sensitive techniques. The complimentary techniques mostly employed in the work of the present thesis are TPD and XPS. TPD gives information on the coverage and binding of adsorbates, and XPS can provide information on both the electronic and structural properties of surface and subsurface atoms. When combined with STM this information provides a very strong toolbox for surface characterization.

2.2.1 Temperature-programmed desorption

Temperature-programmed desorption (TPD) is a very simple technique, but nonetheless it can provide valuable insight into the energetics of adsorbed molecules on surfaces. In a TPD experiment a surface is exposed to a given dose of a gas at low temperature. Subsequently the surface is heated with a linear temperature rate while the rate of desorption is measured, typically by means of a mass spectrometer. The technique can be used to characterize technical catalysts, but the most detailed information is found from experiments with single-crystal surfaces. If the molecules desorb into vacuum and the pumping speed is sufficiently high that readsorption can be neglected, then the rate of desorption, r , is given by:

$$r = -\frac{d\theta}{dt} = \nu \cdot \theta^n \cdot \exp\left(-\frac{E_{des}}{RT}\right), \quad T = T_0 + \beta t,$$

where θ is the coverage in monolayers, t the time, n the order of desorption, ν the preexponential factor, E_{des} the desorption energy, R the gas constant, T the temperature, T_0 the temperature of exposure, and β the heating rate. Although this expression looks intriguingly simple, the interpretation of TPD spectra is complicated by the fact that both ν and E_{des} , and in some cases even n vary with the coverage. A thorough study based on TPD requires a rigorous analysis of several spectra obtained after varying gas exposures and thus varying initial coverages. The so-called ‘‘complete analysis’’ as first suggested by King [41], is rather time consuming, and usually assumptions are made which greatly simplifies the analysis of the TPD data. The most popular approach is the one of Redhead [42], which assumes coverage independent desorption parameters and first order desorption:

$$E_{des} = RT_{max} \left\{ \ln\left(\frac{\nu T_{max}}{\beta}\right) - 3.46 \right\},$$

in which T_{max} is the temperature of the peak maximum. The critical point in using the Redhead formula for evaluating is that the preexponential factor must be known or at least estimated. The strength, on the other hand, is that the desorption energy can be found from a very simple analysis of a single spectrum. For values of $\frac{\nu}{\beta}$ between 10^8 K^{-1} and 10^{13} K^{-1} , the method of Redhead gives an error of a few percent [43], and this is the method used for analyzing the TPD data in the present thesis.

2.2.2 X-ray photoelectron spectroscopy

X-ray photoelectron spectroscopy (XPS) is a technique for probing the core electrons of the atoms at surfaces by means of high-energy photons. The governing principle of XPS is the photoelectric effect. In a simple picture, which will suffice for the present work, the photons with the energy $h\nu$ will excite electrons into the vacuum, and the kinetic energy, E_{kin} , of the emitted electrons will be given by

$$E_{kin} = h\nu - E_b - \Phi,$$

where Φ is the work function of the surface and E_b is the binding energy of the electron. The kinetic energy of the detected electrons thus provides information on the binding energies of the core electrons. These binding energies are element-specific and changes in the chemical surroundings are furthermore reflected in small shifts in these binding energies. The surface sensitivity of XPS derives from the low mean free path, μ , of electrons in solids, which implies that only electrons emitted from atoms close to the surface will avoid inelastic scattering and escape the solid. The intensity I_n measured from the n 'th layer of a single-crystal surface is given by

$$I_n = I_0 \cdot e^{-\frac{n \cdot d}{\mu}},$$

where I_0 is the intensity originating from the topmost (0'th) layer, and d is the interlayer spacing of the crystal. μ is typically of the order 5-10 Å for kinetic energies in the range between 50 eV and 100 eV which means that XPS is typically only sensitive to the topmost 5-10 layers.

The XPS measurements presented in my thesis have been carried out at the synchrotron radiation source at the Aarhus Storage Ring in Denmark (Astrid) which is conveniently located next-door to the STM laboratory. The closeness of the XPS facilities has enabled us to perform a vacuum transfer between the preparation chamber and the beamline chamber by means of a transferable loadlock pumped by an ion pump with a battery power supply. In this way we can prepare the sample and characterize it by STM before transferring the sample to the beamline for XPS measurements.

2.3 Theory in catalysis

Traditionally, theories for catalysis have mainly been descriptive, and the determination of important parameters such as the binding energies of atoms and molecules or the activation barriers for elementary processes on metal surfaces have come from experiments. The power of modern day computers along with the development of efficient computational algorithms have, however, made it possible to perform first-principles calculations on large and complex systems, and theory has reached a point where it can account for the energetics of catalytic model systems in good qualitative or even quantitative agreement with experiments [44,45]. This implies that theory is developing from a descriptive to a predictive discipline within heterogeneous catalysis [30,46].

Theory has become a very valuable complement to experimental surface science and it can often provide insight into atomistic details which are difficult, or even impossible, to probe with experimental techniques. For an accurate and computationally affordable theoretical treatment of adsorption properties, reaction pathways, and activation energies for surface chemical reactions, density functional theory (DFT) is the method of choice [44,45]. Throughout my four years as a PhD student I have had extensive collaborations with several of the world-leading groups working on the implementation of DFT studies in catalysis, including Bjørk Hammer's group at the University of Aarhus, Jens K. Nørskov's group at the Technical University of Denmark, and Manos Mavrikakis' group at the University of Wisconsin-Madison. The interplay with theory has significantly enhanced the scientific outcome of the work presented in this thesis, and for this

reason the basic theoretical concepts of DFT will be introduced, although I should point out that my own contribution to the theoretical studies has been limited to the level of discussions and suggestions.

2.3.1 Density functional theory

The foundation of any theory of electronic structure is the time-independent Schrödinger equation:

$$H\Psi = E\Psi,$$

where H is the Hamiltonian energy operator, E the total energy of the system, and Ψ is the wavefunction which contains all physical information about the system. The task is thus to provide a solution of the time-independent Schrödinger equation for a many-body system. The complexity in obtaining an exact solution, however, increases rapidly with increasing numbers of particles involved, and for the application to surface science some simplifications are needed. The first approximation used for most solid state physics applications is the Born-Oppenheimer approximation which states that the motion of the nuclei is slow enough, compared to the motion of the electrons, to treat the electrons as being influenced by an external potential set up by the static nuclei. In this way a potential energy surface can be treated as a function of the atomic arrangement of the system which, e.g., can form the basis of the determination of a minimum-energy reaction pathway.

DFT focuses on the electron density, $n(\mathbf{r})$, rather than the wavefunction of the system, and the foundation of DFT is due to a theorem by Hohenberg and Kohn which, for the ground state of a bound inhomogeneous electron gas in an external potential, $v(\mathbf{r})$, states that "... $v(\mathbf{r})$ is a unique functional of $n(\mathbf{r})$, apart from a trivial additive constant." [47]. This means that the potential, and thereby also the total Hamiltonian, is a unique functional of the electron density, and this in turn implies that the total energy can be viewed as a functional of the electron density. In particular the ground state energy, E , is given by

$$E = \int v(\mathbf{r})n(\mathbf{r})d\mathbf{r} + \frac{1}{2} \int \int \frac{n(\mathbf{r})n(\mathbf{r}')}{|\mathbf{r} - \mathbf{r}'|} d\mathbf{r}d\mathbf{r}' + G[n],$$

where G is a universal functional of the density independent of $v(\mathbf{r})$.

Kohn and Sham used an approach in which they split $G[n]$ into two parts [48]:

$$G[n] \equiv T_s[n] + E_{xc}[n],$$

where $T_s[n]$ is the kinetic energy for a non-interacting electron gas with the density $n(\mathbf{r})$, and $E_{xc}[n]$ is the *exchange and correlation energy* for an interacting electron gas with the density $n(\mathbf{r})$. By applying the variational principle of quantum mechanics, Kohn and Sham arrived at a set of one-particle Schrödinger equations also known as the Kohn-Sham equations [48]:

$$\left\{ -\frac{1}{2}\nabla^2 + [\phi(\mathbf{r}) + v_{xc}(\mathbf{r})] \right\} \psi_i(\mathbf{r}) = \epsilon_i \psi_i(\mathbf{r}),$$

where the set of ψ_i s must correspond to the electron density, $n(\mathbf{r})$, as given by the equation

$$\sum_{i=1}^N |\psi_i(\mathbf{r})|^2 = n(\mathbf{r}).$$

Where N is the total number of electrons. In these Kohn-Sham equations $\phi(\mathbf{r})$ is the total electrostatic potential

$$\phi(\mathbf{r}) = v(\mathbf{r}) + \int \frac{n(\mathbf{r}')}{|\mathbf{r} - \mathbf{r}'|} d\mathbf{r}',$$

and the functional derivative of E_{xc}

$$v_{xc}(\mathbf{r}) \equiv \frac{\delta E_{xc}[n]}{\delta n(\mathbf{r})}$$

describes an effective one-particle potential.

The Kohn-Sham equations must be solved self-consistently by first choosing a trial $n(\mathbf{r})$ from which $\phi(\mathbf{r})$ and $v_{xc}(\mathbf{r})$ are evaluated, and a new $n(\mathbf{r})$ can be found. This is repeated in an iterative way until convergence is reached, and the energy of the system, is then given by

$$E = \sum_{i=1}^N \epsilon_i - \frac{1}{2} \int \int \frac{n(\mathbf{r})n(\mathbf{r}')}{|\mathbf{r} - \mathbf{r}'|} d\mathbf{r}d\mathbf{r}' + E_{xc}[n] - \int v_{xc}(\mathbf{r})n(\mathbf{r})d\mathbf{r}.$$

When DFT is applied to surface science studies such as the binding of an adsorbate to a single-crystal metal surface, basically two different approaches can be used. In cluster calculations the metal surface is modelled as a finite cluster which will, however, only give reliable results for systems where the electronic structure of small clusters resembles that of a semi-infinite solid. In slab calculations the system is modelled by a super cell with periodic boundary conditions to account for a semi-infinite surface. The super cell consist of a finite number of layers which are periodically repeated perpendicular to the surface and separated by a vacuum. Slab calculations are the natural choice for periodic structures such as high-symmetry adsorbate structures on metal surfaces, whereas the treatment of individual adsorbates requires the super cell to be large enough for adsorbate-adsorbate interactions artificially imposed by the periodic boundary conditions to be neglected.

The errors resulting from the size of the cluster or the super cell, along with other errors introduced by the practical implementation of DFT, can in principle be reduced to any desired level given enough computational power. The only intrinsic error in DFT lies in the parametrization of the exchange and correlation functional. Kohn and Sham used the local density approximation (LDA) in which the electron density varies slowly, and the exchange and correlation functional is given by

$$E_{xc}[n] = \int n(\mathbf{r})\epsilon(n(\mathbf{r}))d\mathbf{r},$$

i.e., it is a function of $n(\mathbf{r})$ only. The approximation of a slowly varying electron density does not apply for surfaces where the density decreases exponentially due to the decay of the wavefunction into the vacuum region, and for this reason Kohn and Sham noted in their original paper that “We do not expect an accurate description of chemical binding [within the LDA approach].” This statement has, however, proved way too pessimistic since LDA-based DFT calculations turn out to give good quantitative agreement with experimental values for a number of physical surface properties [49]. The binding energy of adsorbates are, however, overestimated on the order of 1-2 eV within LDA-based DFT calculations [44], for which reason other approximations for the exchange and correlation functional have been introduced. A popular class of exchange and correlation functionals use the generalized gradient approximation (GGA) in which E_{xc} is a function of both the density and the gradient of the density and in most cases assume the form [50]:

$$E_{xc}[n] = \int f(n(\mathbf{r}), \nabla n(\mathbf{r})) d(\mathbf{r}).$$

The form of f varies in different approximations, some of the most popular ones being those of Perdew and Wang (PW91) [51] and of Perdew, Burke, and Ernzerhof (PBE) [52] along with a revised model of PBE introduced by Zhang and Yang (revPBE) [53] and further refined by Hammer, Hansen, and Nørskov (RPBE) [54]. The choice of exchange and correlation functional depends on several factors, but the use of GGA in general offers a significant improvement compared to the use of LDA [44].

The chemical properties of surfaces is almost exclusively determined by the valence electrons for which reason the core electrons need not be treated within the full self-consistent solution to the Kohn-Sham equations. Instead the core electrons can be “frozen out”, i.e. kept constant during the iterative solution, or they can be incorporated into a pseudopotential which adds to the external potential of the nuclei [55]. The latter approach has the advantage of not imposing the demand for the orthogonalization of valence electron wavefunctions and core electron wavefunctions. This causes the wavefunctions of the core electrons to have fewer radial nodes which reduces the number of plane waves necessary for an accurate description, and thus the use of ultrasoft potentials is widely used in slab calculations, where plane waves are the natural choice for the wavefunction basis set since they fulfil the requirement of the periodic boundary conditions.

2.3.2 Modelling catalysis

The results obtained in DFT calculations represent the total energies at zero temperature and zero pressure and thus do not directly relate to catalytically relevant conditions at high pressure and high temperature. Reuter *et al.* have shown how DFT in combination with statistical mechanics can be used to construct phase diagrams of surface structures as functions of partial gas pressures and temperatures [56]. In this approach the surface free energy, γ , is expressed in terms of the chemical potentials, μ_i , of the different species which are in turn functionals of the temperature, T , and the pressure, p . For a system consisting of a single-crystal metal surface and one type of adsorbates, the

surface free energy can be expressed as

$$\gamma(T, p) = (G_{total}(T, p) - G_{metal}(T, p) - N_{ads}\mu_{ads})/A,$$

where G is the Gibbs free energy, N_{ads} the number of adsorbates, and A the surface area. In many cases the effects of entropy and vibrations to G_{total} and G_{metal} can be neglected, and the Gibbs free energies can then be replaced by the total energies, E , calculated by DFT:

$$\gamma(T, p) \approx (E_{total} - E_{metal} - N_{ads}\mu_{ads})/A.$$

The chemical potential of the adsorbate depends on the temperature and pressure of the gas phase:

$$\mu_{ads}(T, p) = \mu_{ads}(T, p^\circ) + k_B T \ln\left(\frac{p}{p^\circ}\right),$$

where p° is a reference pressure (usually atmospheric pressure). The chemical potentials at standard pressure are tabulated for most of the common gas species [57], and a phase diagram showing the relative stability of different adsorbate phases as a function of pressure and temperature can thus easily be obtained once the total energies are found from DFT calculations. The described procedure can be extended to include multiple gasses and multi-component surfaces in a straightforward way [58, 59].

One of the main goals of surface science studies of catalyst model systems is to be able to use the obtained experimental and/or theoretical data on elementary processes and surface structures to predict the catalytic activity of a real working catalyst. One approach that has been very successful in doing this is the method of *micro-kinetic modelling* [60]. The most common way of performing micro-kinetic modelling is by assuming a reaction mechanism and treating the single steps in this mechanism as either being in thermodynamical equilibrium or as kinetically hindered one-way reactions. In the simplest case only one of the steps is not in thermodynamical equilibrium in which case the rate of this rate-limiting step is also the rate of the overall reaction. This relatively simple approach requires a high degree of knowledge about the reaction mechanism as well as a number of physical properties that determine the equilibrium constants and rate constants of the individual reaction steps. Stoltze and Nørskov performed micro-kinetic modelling of the ammonia synthesis based on surface science experiments on Fe single-crystal surfaces, and their model indeed showed a convincing agreement with reactivity measurements on supported Fe catalysts [61].

Although successful in some cases, the method used by Stoltze and Nørskov neglects the adsorbate interactions and dynamic effects such as surface restructuring, which may be important parameters in certain cases. Dynamic effects can be taken into account by performing kinetic Monte Carlo simulations, which was recently demonstrated by Reuter *et al.* for the CO oxidation on RuO₂, where it was indeed found that the dynamic surface reconstruction is an important factor since the high rate of CO oxidation is found along the boundary between different surface structures in the (T, p) phase diagram [62]. Honkala *et al.* included adsorbate interactions in a model ammonia synthesis over Ru catalysts by calculating the energetics of the rate limiting activation of N₂ for all possible

ensembles of adsorbates at the nearest neighbor positions [63]. In both of these studies all parameters entering the kinetic Monte Carlo simulations were found from first principles and they were both in good agreement with experimentally measured reaction rates. This shows that theory has by now reached a level of accuracy where it, in some cases, can describe the macroscopic kinetics of a working catalyst. This underlines the important role of theory in the understanding of heterogeneous catalysis.

CHAPTER 3

Reactivity of catalytic surfaces

The unique imaging capabilities of the STM are demonstrated through the determination of the precise location of the active sites in three different processes: Hydrodesulphurization on MoS_2 , CO dissociation on Ni(111), and ethylene dissociation on Ni(111). It is furthermore shown how fundamental insight into the atomic details of catalytic processes can be utilized in the rational design of new and improved catalysts. Examples of catalyst design are provided through surface alloying as well as selective site blocking.

3.1 Introduction

The reactivity of catalytic surfaces is controlled by many parameters such as binding energies of reactants, intermediates, and products, surface morphology, co-adsorbates, impurities etc. These different effects combine to give a huge parameter space for varying the reactivity of a surface. In surface science one usually tries to single out these parameters and use simplified models to describe their influence on the reactivity. For example the linear Brønsted-Evans-Polanyi relation between the activation energy and the reaction energy displayed by a number of elementary reactions can be combined with simple kinetic models to give the reactivity as a function of the reaction energy, which results in so-called volcano plots [64, 65]. The influence of the surface morphology can be examined by studying the properties of different single-crystal facets, or as shown in the following section, even very local effects related to, e.g., single defects on a surface can be probed. The combination of various detailed experiments can lead to a deeper understanding of the mechanisms governing the reactivity of a catalytic surface. However, the ultimate goal of surface science is not only to be able to describe how a catalyst works but also to design new and improved catalytic systems from first principles. Despite the many success stories of modern surface science, this goal is far from fully achieved, although a few examples do exist which could lead the way towards a rational design of catalysts. The last section of this chapter deals with examples of how this ultimate task within heterogeneous catalysis may be approached.

3.2 Active sites

The concept of active sites can be traced all the way back to the studies of Taylor and coworkers, who first published their ideas in 1925 [66]. In this work Taylor argues that highly unsaturated sites may be the active sites for the formation of nickel carbonyl in the presence of CO. It will be shown in section 4.2.3 that this foresighted interpretation has indeed proven to be correct, and today much effort is given to the study of the role of special sites in catalysis [67].

At the time of the work of Taylor it was very difficult to actually probe different sites on a catalytic surface by direct experiments. One thing, however, that could be investigated was the dependence of the reactivity on the crystal face, or the *structure sensitivity*. Some of the first experimental work that systematically aimed at probing structure sensitivity was carried out by Gwathmey *et al.* They studied the evolution of spherical single crystals during reactions, and were able to study the structure sensitivity from the reaction-induced faceting of their crystals [68].

The influence of defect sites such as step edges has been examined by comparing planar and stepped single-crystal surfaces. This has, e.g., been done by Yates *et al.* who used a variety of surface sensitive techniques to study the adsorption of CO on Pt [69] and Ru [70] single-crystal surfaces. This type of studies carried out by Yates *et al.*, however, relies on averaging techniques such as TPD, electron diffraction, or infrared spectroscopy, and the information on specific sites is to a certain degree only indirect. The real breakthrough in the study of defect sites came with the advent of the STM,

which is ideal for this kind of studies owing to its unique property as a true local probe with atomic resolution. The STM was first utilized in this context by Ertl and coworkers who showed that the step edges of Ru(0001) are the active sites for the NO dissociation by observing the concentration profile of the reaction products [71]. Another potentially powerful tool for the study of the reactivity of defect sites is DFT. DFT was used in combination with adsorption experiments by Dahl *et al.* to quantify the step edge effect. They found that at 500 K the rate of N₂ dissociation on Ru(0001) is at least nine orders of magnitudes higher at a step edge site than on the terraces. Within the last decade it has become more and more evident that step edges in general dominate the dissociation of diatomic molecules [70–76].

Active sites on catalysts are usually thought of as special sites of the active material. They can be the regular surface atoms or they may be sites at step edges, kinks, or even corners on faceted particles. The concentrations of these types of active sites are all increased when the catalyst particle size is reduced, and this is the typical argument for using high surface area catalysts. For some systems, however, completely new active sites may exist for very small particles, which are not found at all for larger particles. This concept that “small is different” was clearly demonstrated by the work of Haruta and Goodman on Au nanoparticles supported on TiO₂. Even though Au is known to be a very noble metal [77], Au particles with a size of less than ~ 10 nm have a high activity for CO oxidation even below room temperature [78–80]. There is no consensus as to what is the mechanism behind this enhanced reactivity of oxide-supported Au nanoparticles, and at least three effects are discussed in the literature [81]. First, quantum size effects may alter the electronic structure of small particles compared to the bulk material, and this effect can be enhanced by charge transfer between the substrate and the active metal particles [82]. Second, the metal-substrate perimeter interface may provide novel active sites for certain particle sizes [83]. Third, it is suggested that a thin film of the oxide support wets the Au nanoparticles, and thereby the reactivity of the substrate, and not the Au, is enhanced [84]. Although the mechanism is far from understood, the unique properties related to nanosized Au clusters are a clear example that catalysis is indeed nanotechnology – catalysis can only be understood through a deeper understanding at the atomic level. In this context it is obvious why the STM is an invaluable tool for the characterization of catalytically active surfaces.

The following three examples present how the STM in combination with DFT can be used to locate the active site for a surface reaction. The first example is for the hydrodesulphurization of thiophene on MoS₂ nanoclusters on Au(111), which serves as a model system for the real hydrodesulphurization catalyst. For this model system a new type of active sites is found in the form of a one-dimensional metallic edge state on the MoS₂ clusters. The second example is a “classical” example of the dissociation of a simple molecule, namely CO on Ni(111), whereas the final example deals with a more complex molecule, ethylene. In the case of ethylene, it is not a simple question of whether or not the step edges have higher reactivities than the regular facets. Since multiple reactions pathways exist for the decomposition of ethylene, the step edges may influence the different pathways in non-similar ways, which will be shown to be very important for the selectivity of this reaction.

3.2.1 Thiophene on MoS₂

Hydrotreating is the common term for a number of different catalytic processes used in the refining of crude oil. In hydrotreating catalysis, hydrogen is used to saturate unsaturated hydrocarbons and remove impurities such as S, N, O, and metals. Especially the removal of sulphur by hydrodesulphurization (HDS) has received growing attention due to the increasingly strict environmental legislation which lowers the upper limit for sulphur contents in fuels for transport applications. If sulphur is not removed during the processing of fuels, it will lead to SO₂ emissions and acid rain with severe implications for the ecological system. Much progress has been achieved within HDS processing over the last three decades, and, e.g., the emission of SO₂ in Denmark has been reduced from more than 400,000 ton in 1977 to less than 2,000 ton in 2003 [85], but even further reductions are called for and new and improved catalysts are needed to achieve this.

The catalysts most widely used for HDS consist of MoS₂ nanoparticles often promoted with Co or Ni to enhance the catalytic activity. The particles are supported on an aluminum oxide to provide a large area of contact between the reactant gases and the active material. The (0001) basal plane of MoS₂ has been found to be completely inert towards HDS [86], and from *in situ* studies it is well established that the high HDS activity of the MoS₂ particles is related to the edges of the particles [87]. Therefore, the usual surface science approach, which would be to study MoS₂ single-crystal surfaces, is of limited use for this particular catalyst. New and better model systems are thus needed to gain insight into the atomic details of the HDS catalyst from standard surface science techniques in general and STM in particular. One such model system was recently prepared and characterized by S. Helveg and J. V. Lauritsen in our group [88], and we have used this model system to examine the HDS reaction of thiophene with STM.

The model system consists of sulfided Mo nanoclusters dispersed on a Au(111) substrate, and it is described in detail in ref. [88]. The Au(111) surface is chosen as the substrate for three reasons. First, it is metallic and thus allows for STM measurements. Second, Au is rather inert and therefore the intrinsic properties of MoS₂ can be singled out. Third, the “herring bone” reconstruction of the Au(111) surface [89] acts as a template for the dispersal of the Mo nanoclusters. The nanoclusters are prepared by e-beam evaporation of Mo onto the Au(111) substrate in a background of H₂S followed by post-annealing to crystalize the clusters. This preparation leads to the formation of an array of particles shaped predominantly as triangles and displaying a relatively narrow size distribution with an average side length of 30 Å (fig. 3.1(a)), which corresponds well to the size of the active particles in the HDS catalyst [87].

Fig. 3.1(b) shows an atomically resolved STM image of a typical triangular MoS₂ cluster. From the inter-atomic distance and the height of this cluster it is associated with a single layer of MoS₂ with the (0001) basal plane parallel to the Au(111) surface [88]. MoS₂ is a layered compound consisting of slabs with hexagonally close-packed S–Mo–S layers sandwiched in a hcp stacking sequence. A ball model of the triangular cluster is shown in fig. 3.1 (c). It is noteworthy that the clusters are almost exclusively triangular, although the MoS₂ basal plane has a sixfold symmetry. This shows that one of the possible edge terminations is far more stable than the other. From comparisons between high resolution STM images such as that in fig. 3.1(b) with DFT-simulated

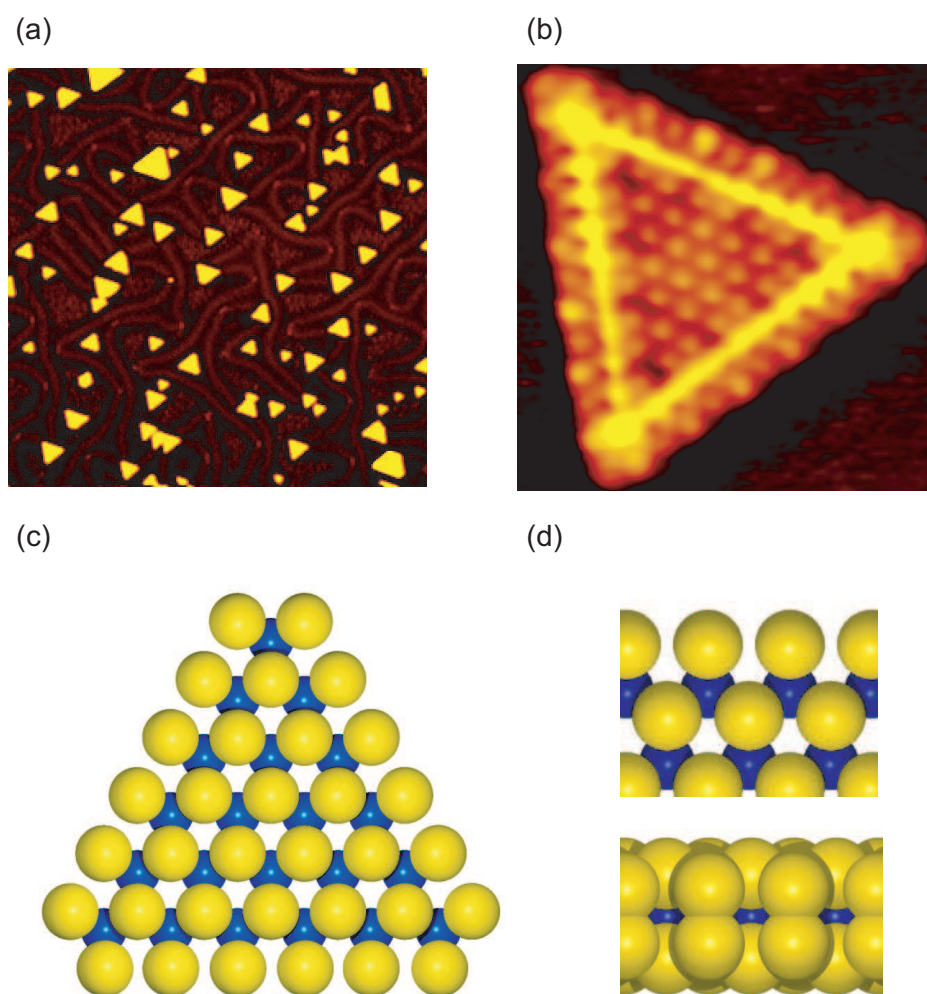


Figure 3.1: **(a)** STM image ($744 \times 721 \text{ \AA}^2$) of MoS₂ nanoclusters synthesized on a Au(111) surface in a sulfiding atmosphere. **(b)** Atomically resolved STM image ($41 \times 42 \text{ \AA}^2$) of a triangular MoS₂ nanocluster. **(c)** Ball model of a triangular MoS₂ cluster (S atoms = yellow, Mo atoms = blue). **(d)** Top and side view of the S-dimer terminated Mo edges of the MoS₂ cluster.

STM images, it is found that the triangles are terminated with the $(10\bar{1}0)$ and equivalent edges, also named the Mo edges. These Mo edges have unsaturated Mo atoms in their bulk truncation, but due to the sulfiding conditions of the preparation the Mo edges are terminated with S dimers, as shown in fig. 3.1(d) [90].

A very predominant feature of the atomically resolved STM image, which cannot

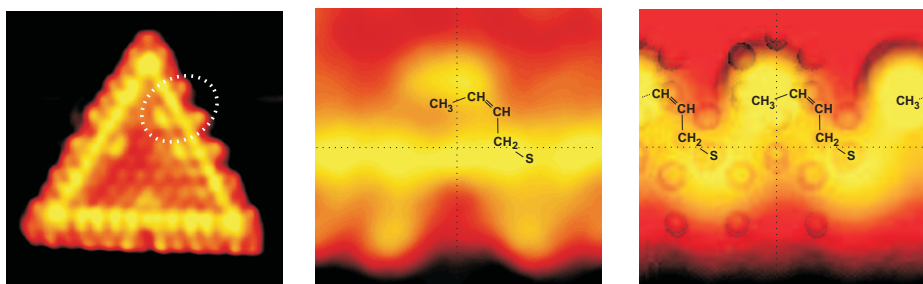


Figure 3.2: **(Left)** STM image ($50 \times 54 \text{ \AA}^2$) of MoS_2 nanoclusters after pre-exposure to atomic hydrogen followed by exposure to thiophene at 500 K. **(Middle)** Zoom-in on one of the protrusions that appear behind the bright brim of the MoS_2 nanoclusters. **(Right)** Simulated STM image of $\text{C}_4\text{H}_7\text{S}$ (*cis*-but-2-ene-thiolate) adsorbed on top of the edge of MoS_2 .

be explained by simple geometrical effects, is the appearance of the very bright brim located close to the edges of the MoS_2 triangle. Indeed it is shown from DFT calculations that the bright brim is owing to a localized metallic edge state [91]. The metallic edge state in the otherwise insulating MoS_2 cluster is the consequence of changes in the electronic structure due to the broken symmetry at the edges. This is simply the one-dimensional analogue of two-dimensional, localized metallic surface states on the surface of insulators [92]. The existence of this metallic edge state already gives a strong indication that the chemical properties of these MoS_2 nanoclusters may be very different from those of bulk MoS_2 . From the experiments with thiophene adsorption on this model system, it has become clear that this edge state indeed plays a crucial role for the high HDS activity of these MoS_2 nanoclusters.

Thiophene ($\text{C}_4\text{H}_4\text{S}$) is the simplest aromatic sulphur containing molecule found in crude oil, and for this reason it is often used as a test molecule for the HDS of aromatics, which are generally more difficult to desulphurize than, e.g., regular thiols. In our experiments we used the model system with single layer MoS_2 nanoclusters on Au(111), and exposed it to thiophene under different conditions. When exposing the MoS_2 nanoclusters to thiophene without any pretreatment we found that thiophene adsorbed at the edges. However, this is only a weak adsorption state since we could only observe it at substrate temperatures below 200 K. The situation changed when the sample was pre-exposed to atomic hydrogen, which can be shown to lead to the formation of S–H groups at the edges of the MoS_2 clusters [93]. When a pre-dosing of atomic hydrogen is followed by an exposure to thiophene at $\sim 500 \text{ K}$, we observe several protrusions inside the bright brim of the MoS_2 clusters, all accompanied by a depression on the outside of the brim. The STM image in fig. 3.2 (left) shows four of these protrusions on a single MoS_2 cluster, and fig. 3.2 (middle) shows a close-up of one of the protrusions.

Since thiophene only interacts strongly with the MoS_2 when S–H groups have been

formed at the edges by a pre-exposure to atomic hydrogen, we speculate that the observed protrusions in the STM images are owing to hydrogenated thiophene species. To confirm this, DFT calculations were carried out for a number of hydrogenated species adsorbed near the edge of a MoS₂ cluster. A C₄H₇S (*cis*-but-2-ene-thiolate) is found to be very stable, and furthermore a simulated STM image of this thiol (fig. 3.2 (right)) shows good qualitative agreement with the features observed in the STM images. From DFT the barrier for the cleavage of the C_α-S bond, which we expect to be the most difficult step in the formation of C₄H₇S, was calculated to be only 1.07 eV, and the barrier is thus easily surmounted at 500 K.

These findings show the existence of a reaction pathway for hydrogenation and the cleavage of the first C_α-S bond. The adsorbed C₄H₇S specie is a regular thiol, from which the sulphur atom is more easily removed than from sulphur-containing aromatics. This final sulphur extraction may take place at another site, such as a sulphur vacancy at the edge. It can, however, not be observed in our experiments, since any hydrogen vacancies created during the exposure to atomic hydrogen will already have recombined with sulphur atoms from thiophene prior to our experiments. The important finding in this study is the existence of a reaction pathway for the initial C_α-S bond cleavage taking place on top of the S atoms at the edge of the MoS₂ clusters. Since the basal plane of MoS₂ is inactive, the active sites for this reaction can be associated with the metallic state localized at the edges, which shows the existence of a completely new class of active sites, which may be speculated to exist also for other nanosized metalsulphide clusters. It was found experimentally that a metallic edge state also exists for Co-promoted MoS₂ nanoclusters grown on the Au(111) surface by a co-evaporation of Co and Mo in an H₂S background [94]. This provides yet another stunning example that small is different.

3.2.2 C on Ni(111)

Nickel catalysts are used for multiple purposes including the steam reforming process [95, 96], CO methanation [97], and the anode reaction in solid oxide fuel cells [27]. The formation of solid carbon on the nickel catalysts, also known as *coking*, poses a major technological challenge for industrial applications [95]. Especially in the steam forming reactions, large carbon whiskers can be grown which will eventually lead to a breakdown of the catalyst pellets, thus causing an expensive shutdown of the reactor and a replacement of the catalyst material. The growth of carbon whiskers on supported nickel catalysts has recently been shown to be related to the edges of the nickel particles [98]. We have studied the initial nucleation of carbon on the Ni(111) surface from the decomposition of CO ethylene (C₂H₄) and used the STM to obtain information on the specific role of step edges in these processes.

In the industrial catalysts several different phases of carbon may form, with whisker-like, encapsulating, and pyrolytic carbon being the most common.¹ On single-crystal surfaces, however, only two ordered structures are known. The two structures, which form above ~ 700 K and below ~ 600 K, respectively, are termed the *graphitic* and the *carbide* phases. The naming of the two phases is motivated by the similarity between

¹see ref [95] for a thorough discussion of carbon formation in steam reforming catalysis

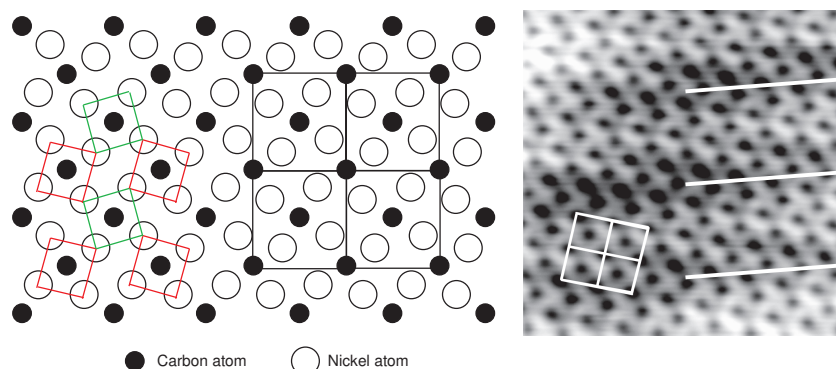


Figure 3.3: **Left:** Model of the topmost layer of the carbidic carbon phase on Ni(111). The colored squares show the (100)-like structures of the “clock reconstruction” rotated clockwise (red) and anticlockwise (green). The square unit cell of the carbon atoms is indicated with the black grid. **Right:** STM image ($45 \times 48 \text{ \AA}^2$) of the carbidic phase. Both the square unit cell and the striped structure are indicated. Figure reproduced from [102].

the Auger spectra for the surface adsorbed structures and the corresponding spectra for the bulk-terminated graphite and nickel carbide [97]. The formation of the graphitic phase leads to an inactive surface, whereas the carbidic phase does not deactivate the nickel surface to, e.g., CO methanation [97]. Even though the carbidic phase does not itself deactivate the nickel surface, it is of great importance, since it is a precursor for the graphitic phase and an onset of whisker growth. Also it has been suggested that the graphitic phase nucleates on top of the carbidic phase [99].

All our experiments were performed below 600 K, and thus only the carbidic phase is relevant for the present studies. The structure of the carbidic phase on Ni(111) has been characterized by LEED [100,101] and STM [102,103], and a model of the structure along with an STM image are shown in fig. 3.3. The adsorbed carbon atoms induce a reconstruction of the topmost layer of the Ni(111) surface with a local square (100)-like structure of the Ni atoms. These squares of four Ni atoms are rotated clockwise and anticlockwise, thus naming the structure as “the clock reconstruction”. The carbon atoms are arranged in a $c(2 \times 2)$ structure with respect to the unrotated Ni(100) geometry. The reconstructed topmost layer is incommensurate with the Ni(111) substrate, which leads to the formation of a striped appearance of the carbidic phase in the STM images, as seen in fig. 3.3 (right). These stripes can be observed in STM even when atomic resolution is not achieved, which greatly simplifies the identification of the carbidic structure in our experiments. The formation of the (100)-like “clock reconstruction” is accompanied by a 10 % mass reduction of the topmost layer of the Ni(111) surface, and thus involves a mass transport of Ni atoms.

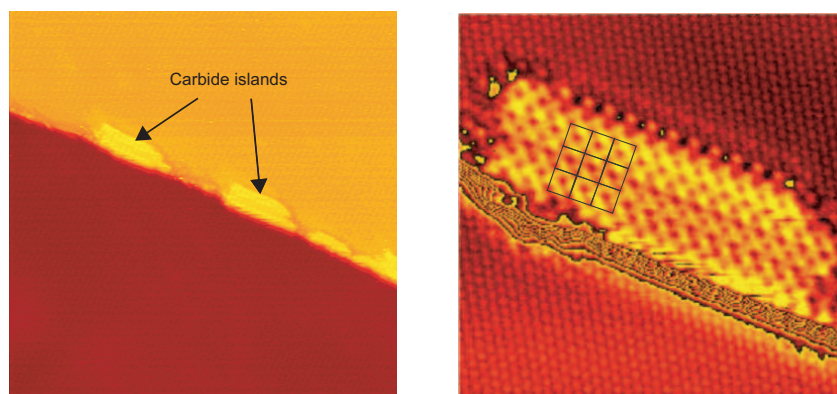


Figure 3.4: **Left:** STM image ($500 \times 500 \text{ \AA}^2$) of a Ni(111) surface after exposure to 50 L CO at 400 K. Carbide islands have nucleated along the upper step edges. **Right:** Zoom-in ($87 \times 87 \text{ \AA}^2$) on a carbide islands. The square $c(2 \times 2)$ unit mesh of the carbon atoms is superimposed.

3.2.2.1 CO dissociation on Ni(111)

When the Ni(111) surface was exposed to CO at 400 K we observed the nucleation of islands along the upper step edges. This is shown in the STM image of fig. 3.4 (left), which shows the Ni(111) surface after exposure to 50 L CO (10^{-7} torr; 500 s). The nucleation of isolated islands away from the step edges was never observed. High resolution images of the islands (fig. 3.4 (right)) reveal the quadratic, centered unit cell of the carbidic structure. The observations of the nucleation of carbide islands along the upper step edges are in excellent agreement with the STM studies of Nakano *et al.* [104]. The reason for the preferential nucleation of the carbide structure at the upper step edges is most likely the mass transport associated with the “clock” reconstruction. This mass transport is most easily accommodated at the step edges, where atoms are relatively free to move around and rearrange into a new structure. We cannot draw a conclusion about the active site for the CO dissociation based on the preferred nucleation of the carbidic islands. The non-uniform distribution of the islands along the step edges shows that the carbon atoms are mobile at the conditions of our experiments. In section 3.3.1 I will provide strong evidence that in fact only the step edge sites are active for the CO dissociation on Ni(111) at 400 K. From DFT calculations it is also found that the CO dissociation on Ni(111) follows the general trend of a substantially higher activity at the step edges than on the regular (111) facets [105, 106].

3.2.2.2 C₂H₄ dissociation on Ni(111)

By exposing the Ni(111) surface to ethylene at the lowest temperature for which decomposition is observed, one can be assured to probe only the most reactive sites. We found that an exposure to ethylene at room temperature led to the formation of a narrow brim

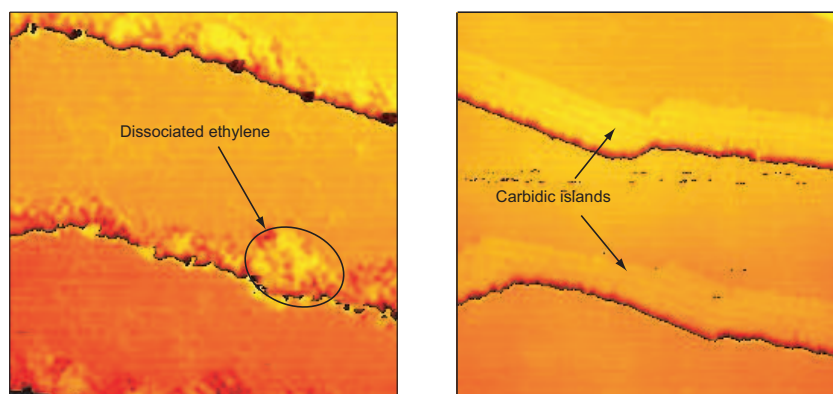


Figure 3.5: **Left:** STM image ($200 \times 200 \text{ \AA}^2$) of a Ni(111) surface after exposure to 1 L of ethylene at room temperature. Ethylene decomposes and adsorbs along the upper step edges. **Right:** STM image ($500 \times 500 \text{ \AA}^2$) of carbide islands nucleated along the upper step edges of Ni(111) upon exposure to 0.1 L of ethylene at 500 K.

of reaction products along the upper step edges on Ni(111), as can be seen in the STM image of fig. 3.5, which shows a Ni(111) surface after exposure to 1 L ($= 10^{-8}$ torr·100 s) of ethylene at room temperature. The brim, which appears in the STM images as areas of different corrugation as compared to the (111) facets, was found all along the step edges and with a width of typically no more than 40 \AA , independent of the size of the terraces. The cleanliness of the sample, and in particular that of the step edges, was checked prior to the ethylene exposure, and the formation of this brim could therefore unambiguously be associated with the ethylene adsorption. No indication of nucleation of islands on the terraces of the surface was observed upon the exposure to ethylene. When the exposure time was increased by a factor of 20 at the same ethylene pressure of 10^{-8} torr, we again observed the formation of a brim along the upper step edges, and furthermore we found that the width of this brim did not increase with increasing dosing time. From this it was concluded that the process of forming the brim is self-poisoning. Since the only adsorbates observed on the surface are the ones at the step edges, it was furthermore concluded that the mechanism behind the formation of the brim is the decomposition of ethylene at the step edge atoms. The decomposition products adsorb at the step edges and prevent further reaction. From the STM measurements at room temperature it was found that the step edges of the Ni(111) surface have a higher reactivity for ethylene decomposition than the regular atoms of the (111) facets. In this sense the decomposition of ethylene on Ni(111) follows the same trend as that observed for diatomic molecules.

Since the STM cannot distinguish between different chemical species and only the final reaction products were observed, it cannot be determined through which reaction pathway the decomposition of ethylene proceeds, e.g., whether the initial step is dehydrogenation (C–H bond breaking) or dissociation (C–C bond breaking). Since this bond

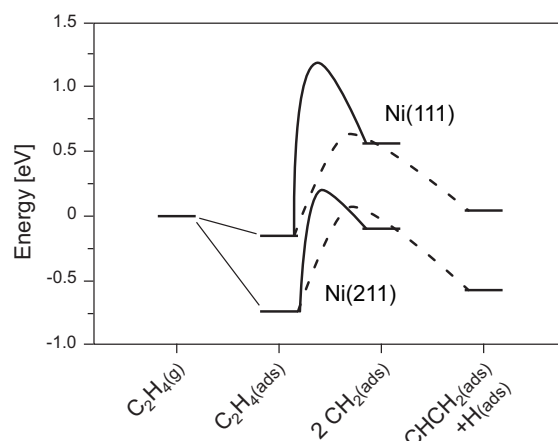


Figure 3.6: Potential energy diagram for C–C bond breaking (full line) and C–H bond breaking (dotted line) of ethylene on Ni(111) and Ni(211).

breaking selectivity will show in the overall selectivity between different end products in a given catalytic reaction involving ethylene decomposition, the issue is of great interest. The group of Jens Nørskov at DTU in Lyngby performed DFT calculations for the two possible initial steps in the decomposition reaction on both Ni(111) and the stepped Ni(211) surface. The potential energy diagram (fig. 3.6) shows that the barriers for both dehydrogenation and dissociation are indeed much lower on the stepped surface as compared to the flat surface which is in agreement with the STM measurements. Furthermore, whereas the barriers for the dehydrogenation and the dissociation are similar on Ni(211), they differ by 1 eV on the flat Ni(111) surface. This implies that an initial dissociation can only take place as long as free step edge sites are exposed, or in other words, the bond breaking selectivity of the Ni(111) surface is to a high degree controlled by the presence of free step edges. In section 3.3.1 it is shown how the availability of free step edges and thus the bond breaking selectivity can be controlled.

3.3 Changing the reactivity

Although catalysis has a history dating back to the beginning of the 20th century, surprisingly little improvement has been seen for the industrially applied catalysts. As an example the iron catalyst first introduced by Fritz Haber is almost identical to the catalyst still used today for the ammonia synthesis. The reason for this limited progress within applied catalysis originates in the limitations of the trial and error screening method for developing new catalysts, and is not an indication that there is no room for major improvements. Again the ammonia synthesis provides an astonishing example, since the naturally occurring enzyme nitrogenase catalyzes the formation of ammonia from N_2 at

ambient conditions in harsh contrast to the industrial process, which typically runs at $\sim 400^\circ\text{C}$ and ~ 100 atmospheres [107]. Attempts have been made to understand the relation between the structure of nitrogenase and its ability to produce nitrogen with the hope of producing new catalysts that mimic the superior properties found in the natural enzyme [108, 109]. The approach has, however, far from reached a point at which it is technologically applicable, and other methods have to be pursued in order to improve the efficiency of catalytic processes.

One method that can be used in situations, in which unwanted side reactions cause problems, is a partial poisoning of the catalytically active material. This is, e. g., utilized to impede graphite formation during the steam reforming reaction in the SPARG (Sulfur PAssivated ReforminG) process developed by Rostrup-Nielsen *et al.* [110, 111]. In this process trace amounts of H_2S are added to the gas feed stock. H_2S acts as a poison for the steam reforming reaction, but it is an even stronger poison for the graphite formation, and thus the selectivity is enhanced and the lifetime of the catalyst is prolonged. The addition of H_2S is not a viable solution in many applications, since H_2S also acts as an effective poison for most transition metal catalysts, which may be placed down-stream in the catalyst reactor. Rather than changing the gas composition one would prefer to change the catalyst material in such a way that a more efficient catalyst is produced. One way of changing the chemical properties of a surface is through alloying with a second metal, and alloys are in several cases known to have superior catalytic properties as compared to the pure metals [112, 113]. The approach was used by Besenbacher *et al.* to design a new steam reforming catalyst with a Au/Ni alloy as the active material [114, 115]. Au and Ni belong to a class of two component metals, which are bulk immiscible but still form stable surface alloys in which Au atoms have substituted Ni atoms in the topmost layer [116, 117]. From an interplay between STM and DFT it was shown that the presence of Au atoms in the Ni(111) surface had a destabilizing effect on graphite. This observation inspired the synthesis of an oxide-supported Au/Ni(111) alloy catalyst that proved to be superior to a similar catalyst with pure Ni as the active material. To my knowledge it is the first example in the literature, where fundamental surface science studies have led to the design of a new technical applicable catalyst.

Another, and intriguingly simple, example of catalyst design from first principles was provided by Jacobsen *et al.*, who used an interpolation in the periodic table to make an improved catalyst for the ammonia synthesis. Their principal observation was that when the ammonia activity was plotted against the nitrogen binding energy, a typical volcano curve was found with an optimal nitrogen binding energy lying in a “gap” between Fe and Ru, i.e., none of the pure elements have the optimal binding energy [118]. Their simple approach was then to form an alloy of two metals lying on each side of the maximum of the volcano curve; Mo with a too high binding energy, and Co with a too low binding energy. Using this principle they developed a “CoMo” catalyst, which experimentally turned out to indeed have a higher activity than the most active of the pure elements, Ru [119].

Despite the success of both the Au/Ni steam reforming catalyst and the CoMo ammonia synthesis catalyst, none of these have found their way to commercial use. It shows that real-world catalysis is not just about finding the most efficient catalyst with respect to activity or selectivity. Factors like the cost of the active materials and the possibility

of large-scale production play a very important role in choosing the optimal catalyst for industrial applications. Again the ammonia synthesis serves as a class room example, since iron catalysts are used, although it is well known that besides CoMo also both Ru and Os catalysts are better catalysts [120]. In the following two sections, examples will be given of how the reactivity of Ni and Pt surfaces can be modified by adding impurities or forming surface alloys, providing further insight which will hopefully help in guiding the way towards a true catalyst design from first principles.

3.3.1 Ni(111)

As discussed in the previous section the step edges of Ni(111) play an important role in the dissociation of CO. The influence of the step edges was further examined by depositing additives onto the Ni(111), which preferentially nucleate along the step edges. Since the atoms at the step edges are more under-coordinated than the regular surface atoms, adsorbates are generally expected to bind preferentially to the step edges as long as their mobility is high enough for them to actually diffuse to a step edge; an expectation that has also been confirmed theoretically for several adsorbates by Bengaard *et al.* [105]. Ag and Au are two metals which experimentally are known to nucleate into large islands at the descending step edges on the Ni(111) surface [121], which was also confirmed by the present STM experiments (see fig. 3.7(a) and 3.7(c)). To single out the influence of the step edges they should be completely blocked. This has obviously not happened after room temperature deposition since both Ag and Au grow as large islands, leaving behind free Ni atoms at large parts of the step edges. To get a complete wetting of the step edges the Ag/Ni(111) surface was post-annealed for 10 minutes at 800 K, and this indeed led to Ag atoms becoming more mobile and decorating all of the step edges, which show up as the bright brim of protrusions running along the step edge in fig. 3.7(b) (see also the inserted ball model). When the post-annealed Ag/Ni(111) surface was exposed to CO at 400 K no growth of carbidic islands was observed. This provides very strong evidence that the step edges of Ni(111) are indeed the active sites for the CO dissociation, and it also serves to show that these very reactive sites can be blocked.

Au and Ag are chemically very similar and as can be seen they show the same step flow growth at room temperature. At higher temperatures, however, the growth of Au on Ni(111) is markedly different from that of Ag. Au and Ni(111) belong to the class of two-component metals that are bulk immiscible but still form stable surface alloys. This is nicely illustrated in an atomically resolved STM image of a post-annealed Au/Ni(111) surface (fig. 3.7(d)). The dark atoms are single Au atoms substituted into the topmost layer of the Ni(111) substrate. The fact that Au is imaged as depressions by the STM, despite its larger radius than Ni, is a classical example of how the STM images a convolution of the geometrical and electronic structure of a surface. No bright brim of protrusions is found along the step edges of the post-annealed Au/Ni(111) surface. This does, however, not necessarily mean that the step edges are not decorated with Au atoms in a manner similar to that found for Ag/Ni(111). The Au atoms are imaged as depressions and one would thus not expect to be able to observe a single row of Au atoms at the step edge with the STM. Indirectly it could be shown that also Au

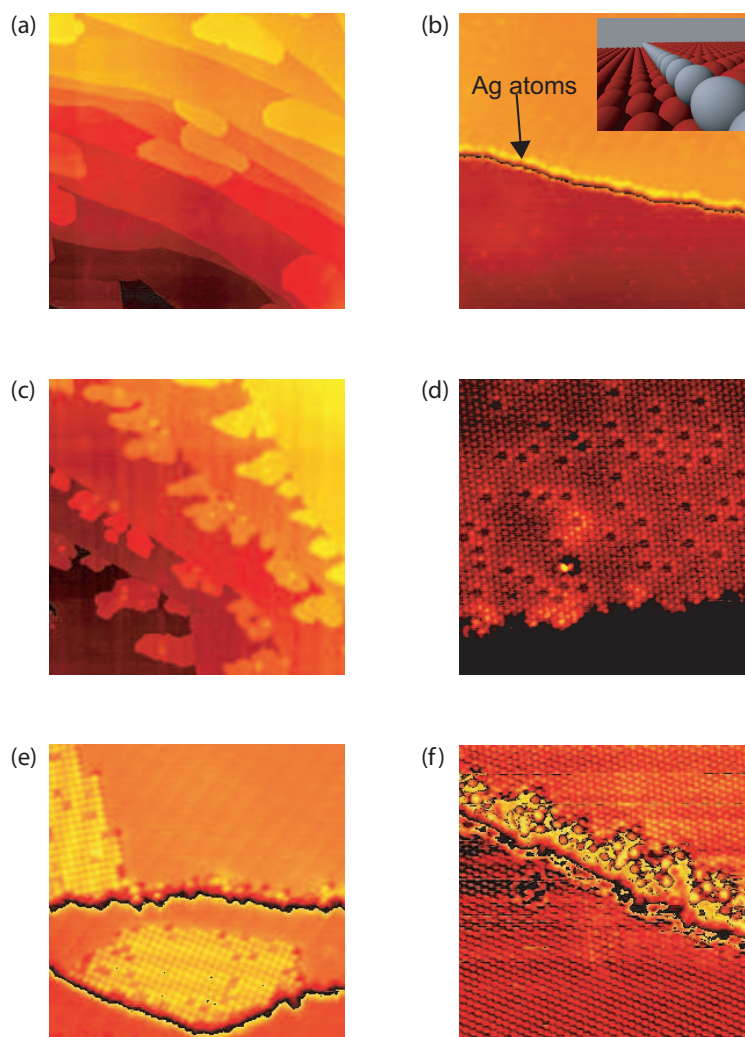


Figure 3.7: STM images showing the growth of Ag, Au, and S on the Ni(111) surface. **(a)** ($7000 \times 7000 \text{ \AA}^2$) Ag deposited at room temperature. **(b)** ($400 \times 400 \text{ \AA}^2$) Ag/Ni(111) after post-annealing at 800 K **(c)** ($2012 \times 2012 \text{ \AA}^2$) Au evaporated at room temperature. **(d)** ($100 \times 100 \text{ \AA}^2$) Au/Ni(111) after post-annealing at 800 K **(e)** and **(f)** ($100 \times 100 \text{ \AA}^2$ and $200 \times 200 \text{ \AA}^2$) Ni(111) after exposure to 5 L of H₂S at 400 K.

does indeed block the step edges for CO dissociation. This was done by exposing a Au/Ni(111) surface alloy with only ~ 0.05 ML of Au to CO at 400 K. In this experiment no formation of carbidic islands was observed (fig. 3.7), and since a random distribution of the Au would leave areas with free Ni step edge atoms, where CO would dissociate, it is concluded that Au atoms decorate the step edges of Ni(111).

A final additive that was examined in the experiments was H₂S due to its relevance as a poison for catalytic processes on Ni surfaces. The SPARG process and the poisoning effect in the steam reforming process have already been introduced, and H₂S has also been shown to act as a poison for the CO methanation (inverse steam reforming) [122]. In these old studies the influence of step edges was not considered, and with the new insight into the high reactivity of these special sites it was thus interesting to return to this sulphur poisoning effect with special emphasis on the role of the step edges. The Ni(111) surface was exposed to H₂S at 400 K, at which temperature it readily dissociates to form adsorbed S [123]. When the surface was exposed to moderate doses (5 L) of H₂S at 400 K, single sulphur atoms were found at the nickel step edges (fig. 3.7(e)) imaged as protrusions in the STM. Some of the sulfur atoms nucleated into islands found at the upper step edges (fig. 3.7(f)). These islands have an almost quadratic unit cell and are identified with the $(\sqrt{39} \times \sqrt{39})$ structure known to form above room temperature at low S coverage [124]. In agreement with this work we also observed that these islands nucleated exclusively at the step edges of Ni(111).

The sample temperature of 400 K during H₂S exposure was chosen since we wanted to subsequently expose the surface to CO at 400 K as in the experiments on pure Ni(111), Ag/Ni(111), and Au/Ni(111). By first characterizing the adsorption of H₂S at this temperature, the complexity of inducing new sulphur structures when the sample is heated to 400 K during CO exposure was avoided. The protrusions at the step edges are interpreted as the nucleation centers of the sulphur-induced reconstruction accompanying the $(\sqrt{39} \times \sqrt{39})$ structure, and it is therefore expected that the coverage of sulphur must reach a certain level before it can be observed by STM. For lower doses of H₂S we were able to prove that the step edges of Ni(111) are covered with sulphur by showing that the CO dissociation is blocked: a pre-dosing of 0.5 L H₂S at 400 K onto Ni(111) followed by exposure to 500 L CO at 400 K led to no carbon formation. These findings definitely indicate that the role of the step edges is an important factor to take into account when interpreting the role of sulphur as a poison in both the steam reforming and the CO methanation process.

It was also demonstrated that the step edges of Ni(111) could be blocked for ethylene decomposition by Ag atoms by exposing the Ag/Ni(111) surface to ethylene at room temperature and not observing any adsorbed reaction products. In the light of the importance of free step edge sites for the selectivity towards ethylene dehydrogenation/dissociation this is very interesting. By blocking all of the step edges, a Ni(111) surface on which ethylene will exclusively go through primary dehydrogenation can be created. Based on these findings a MgAl₂O₄-supported high surface area AgNi catalyst was synthesized and tested in flow reactor measurements at the Haldor Topsøe Research Laboratories. It was found that the C–C bond breaking was indeed suppressed in the hydrogenolysis of ethane by the presence of the Ag atoms in the catalyst.

The demonstration that the very reactive step edges on Ni surfaces can be blocked

even on high surface area catalysts could potentially have many practical applications. First of all it may help to impede the formation of carbon in steam reforming catalysts, and in fact this may be one of the reasons why the Au/Ni surface alloy displays an improved carbon resistance. The carbon formation is also a problem in solid oxide fuel cells, when natural gas and not pure hydrogen is used as the fuel. The AgNi catalyst could also be a possible candidate for this application, and in fact the presented results have paved the way for a joint patent with the Technical University of Denmark and Haldor Topsøe A/S.

3.3.2 Cu/Pt(111)

3.3.2.1 Background

The study of transition metal alloy catalysts dates back earlier than WWII [125], and it has long been established that alloy catalysts often are superior catalysts compared to the pure elements, both in terms of activity and selectivity [112, 113]. For a long time, however, these studies were exclusively aimed at two-component systems, which were known to form thermodynamically stable bulk phases, such as Ni and Cu [126, 127]. Sinfelt was the first to extend the studies to two-component metal systems of elements that are bulk immiscible in his experiments on Ru-Cu and Os-Cu catalysts in the dehydrogenolysis of ethane and the dehydrogenation of cyclohexane [128]. He was also the first to introduce the term bimetallic clusters in place of alloy clusters, since he wanted to include these new types of clusters comprised of two bulk-immiscible metals.

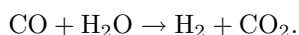
As it has already been discussed for the case of Au and Ni, a two-component system of bulk-immiscible metals may form stable surface alloys [116]. For the case of Au alloyed into a Ni surface this can be rationalized by simple arguments based on the coordination of the surface atoms. The Ni surface atoms are under-coordinated due to missing nearest neighbors and thus favor a stronger interaction with the neighboring atoms. Exactly this is achieved by substituting a neighboring Ni surface atom with a Au atom, which due to its larger atomic radius has a larger overlap with the surrounding Ni atoms thus effectively increasing their coordination number and lowering the surface energy. These simple arguments have been confirmed by extensive DFT calculations [105, 129].

In the simplest approach the mixing of two metals can be divided into four generic cases characterized by two parameters, the segregation energy and the mixing energy [130]. The segregation energy (E_{seg}) determines whether a solute will stay at the surface ($E_{seg} < 0$) or segregate into the bulk of the substrate ($E_{seg} > 0$), whereas the mixing energy (E_{mix}) discriminates between alloy formation ($E_{mix} > 0$) and phase separation ($E_{mix} < 0$). The Au on Ni system belongs to the generic class in which the solute, Au, does not segregate into the substrate, Ni ($E_{seg} < 0$), but the two metals do mix to form an alloy ($E_{mix} > 0$).

In a recent work it was shown by Greeley *et al.* that even when the segregation of the solute is favored, it tends to stay in the second layer of the substrate and thus form a subsurface alloy [46]. It was furthermore shown that certain of these subsurface alloys display very interesting chemical properties. In particular it was found that some of the

alloys bound H₂ almost as weakly as the noble metals while at the same time showing a high activity for the dissociation of H₂. This does not agree with the traditionally observed Brønsted–Evans–Polanyi relations, which predict that a lowering of the H₂ binding energy should be followed by an increase in the dissociation barrier [64]. This is just one example to illustrate that very interesting effects may appear when transition metal surface alloys are formed. In the following I will discuss alloy catalysts in relation to the water-gas shift (WGS) reaction.

The (WGS) reaction



is important to the production of high-purity hydrogen for, e.g., ammonia synthesis, and it is also vital to the production of CO-free hydrogen fuel for low-temperature fuel cells. The WGS reaction is slightly exothermic ($\Delta H = -41.1$ kJ/mol), and therefore high temperatures tend to push the equilibrium towards CO and H₂O. Low temperature is thus needed to achieve a high conversion into CO₂ and H₂, but this implies slow reaction kinetics. To deal with these two opposing temperature effects the typical industrial plants use a two-step WGS reactor in which the feed gas is sent through a high-temperature reactor followed by a low-temperature reactor [131]. The high-temperature WGS reaction is usually run at 310–450°C over an iron oxide catalyst promoted with chromium oxide, whereas the low-temperature WGS reaction is normally carried out at 210–240°C with a copper/zinc oxide/alumina catalyst [131].

Although the commercial Cu catalyst is a complex structure, and the role of the zinc oxide is not really understood, surprisingly good agreement is found when rate measurements on Cu single crystals are compared with similar measurements on the real catalyst [132]. This strongly indicates that metallic copper is the active material in the low-temperature WGS catalyst. No single rate limiting step in the WGS reaction was found in these surface science studies, although the activation of H₂O was found to be rate limiting at certain gas compositions, and in general this elementary step is closely related to the overall WGS rate. This observation is confirmed by a kinetic model of the WGS reaction, in which three rate determining steps are necessary to obtain good qualitative agreement with experimental data [133, 134].

The implementation of onboard reforming of hydrocarbons for fuel cells in automobiles is a technological challenge which cannot simply be achieved by a down scaling of the industrial WGS reactors. The use of Cu/ZnO/alumina catalysts in vehicular onboard WGS reactors is not optimal for at least two reasons. First, the size of an onboard reactor is a key parameter, and to achieve the same rate of conversion in a smaller volume will require reactions at higher temperatures for which the Cu catalysts are not suited, mainly due to sintering problems [135]. Second, Cu catalysts are pyrophoric, i. e. prone to start fires, which would of course be a great safety hazard for vehicular applications. For these reasons other WGS catalysts have been studied in the past years, and especially ceria-supported metal catalysts, e.g., Pt/ceria, have shown interesting properties [136, 137]. In light of these recent studies and the general knowledge about alloy catalysis, it is interesting to study the alloying of Cu and Pt, and in particular to study whether or not the properties of the two materials can be combined to form an optimized WGS catalyst.

Cu and Pt form stable bulk alloys, and the existence of several phases has been confirmed experimentally [138]. In particular the Cu₃Pt bulk alloy has been the interest of a number of investigations, since it can be easily grown as fcc single crystals [139, 140]. From these studies it was for example shown that the CO adsorption is site specific to Pt and Cu sites, but the adsorption is markedly changed as compared to pure Pt or pure Cu, as would be expected based on the present understanding of the physics of alloys. In our studies, however, we focused on the near surface alloys formed when small amounts of Cu is deposited onto a Pt(111) surface, since this allows for a greater variety in structures by varying the preparation parameters such as the amount of evaporated Cu and the temperature during the different stages of the preparation. This does not only enable us to perform more quantitative experiments to single out the effect of alloying. It furthermore provides for a better model catalyst since the preparation of industrial catalysts also has numerous adjustable parameters.

The growth of Cu on Pt(111) has been studied with a variety of surface science techniques [141–148]. Several studies have shown that Cu grows as pseudomorphic 2D islands on the Pt(111) substrate, and one monolayer is nearly completed before the onset of the second layer [141–143]. The diffusion of Cu into the Pt(111) substrate is observed at temperatures above ~ 525 K, and a surface alloy is formed [141, 143]. Barrett *et al.* used core-level photoemission spectroscopy to measure the shift in the Pt4f_{7/2} peak due to alloy formation and found a shift of 170 meV, which is close to that found in bulk Cu₃Pt [144]. The change in surface reactivity upon deposition of Cu has also been studied by means of CO tpd [141] and CO oxidation reaction rate measurements [145].

Holst *et al.* studied the growth of thin films of Cu on Pt(111) with STM and observed an adlayer-driven reconstruction of the Pt(111) surface after the completion of the first pseudomorphic Cu overlayer [146, 147]. The Pt(111) surface is very close to instability towards reconstruction [149], and indeed the surface is found experimentally to reconstruct at high temperatures (>1330 K) [150] or in the presence of a Pt gas-phase environment down to 400 K [151, 152]. The growth of a pseudomorphic Cu overlayer induces stress in the substrate due to the 8% lattice mismatch between Pt(111) and Cu(111), and this stress can be relieved through the incorporation of Cu atoms in the topmost layer of Pt(111), which is relatively easily accommodated owing to the instability of the Pt(111) surface. Tsay *et al.* used Auger electron spectroscopy to study the alloy formation from 1 monolayer Cu on Pt(111). They found an activation barrier for Cu diffusion into Pt(111) of 1.1 eV, and furthermore they suggested the formation of a Cu₅₀Pt₅₀ surface alloy. To date there has, however, not been any true structural characterization of the surface alloy(s) formed by the Cu on Pt(111) at elevated temperatures. In the following it will be shown that a combination of STM, CO TPD and XPS measurements with DFT calculations strongly supports a model in which a subsurface alloy is formed, i.e., Cu segregates to the second layer or deeper into the Pt(111) substrate, leaving behind a surface layer consisting purely of Pt.

3.3.2.2 STM

When Cu was evaporated onto Pt(111) at room temperature we observed the nucleation of Cu islands at the lower step edges as seen in fig. 3.8(a). The Cu islands display a

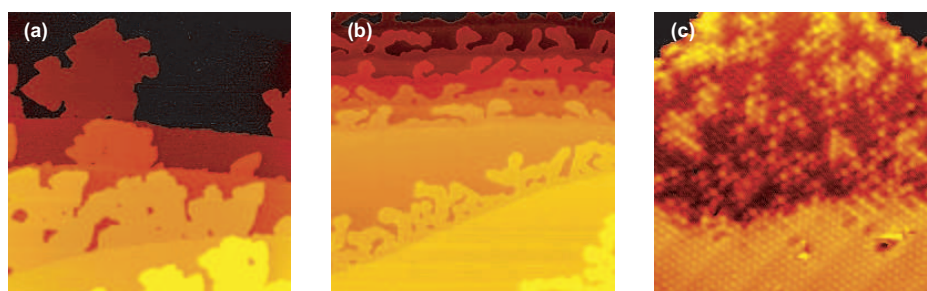


Figure 3.8: STM images of Pt(111) after evaporation of Cu at (a) room temperature ($2000 \times 2000 \text{ \AA}^2$), (b) 600 K ($2000 \times 2000 \text{ \AA}^2$), and (c) 600 K ($70 \times 70 \text{ \AA}^2$). At room temperature Cu grows as islands via step flow. At 600 K islands are formed along the step edges; these islands have a different corrugation as compared to the clean Pt(111) areas as seen in the zoom-in (c).

1×1 structure with no sign of stress lines or moiré structures for submonolayer coverage of Cu, which shows that the Cu islands grow pseudomorphically with the Pt(111) substrate at room temperature, thus confirming the findings of previous studies [141–143]. When the substrate temperature was increased to 600 K and kept there during the Cu evaporation, the nucleation of islands along the lower step edges was observed again (fig. 3.8(b)). Unlike the islands nucleated at room temperature, the corrugation of the islands was now found to be very non-uniform as compared to the Pt(111) areas. This is shown in the atomically resolved image of fig. 3.8, where both an island and a Pt(111) area are seen in the top and bottom of the image, respectively. Whereas the Pt(111) area appears as bright protrusions all with the same apparent height, the islands clearly display atoms of a different apparent height. The latter suggests that Cu atoms diffuse into the Pt(111) substrate at 600 K, which again is in agreement with literature [141, 143].

When the substrate temperature was further increased to 800 K during the Cu evaporation, the nucleation of islands at the step edges or anywhere else on the surface was no longer observed. The small insert in fig. 3.9(a) shows the surface after the evaporation of 0.3 monolayer (ML) Cu at 800 K. On a large scale the surface appears uniform and cannot be distinguished from the clean Pt(111) surface. When atomic resolution was obtained, however, it was seen that the surface atoms appeared with a very non-uniform corrugation in the STM (fig. 3.9(a)), which again indicates that the Cu atoms diffuse into the Pt(111) substrate. When the amount of evaporated Cu was increased to 1.0 ML, a new type of structure appeared as seen in the STM image of fig. 3.9(b). The new structure, which will be referred to as the *ring structure*, is a superstructure consisting of large and smaller rings arranged in a non-perfect hexagonal structure with a periodicity of ca. 100 \AA . The rings appear as bright areas in the STM images, which is seen very clearly in the atomically resolved image in fig. 3.9(c). In this image it is also seen that the atoms in the areas in between the rings have different corrugations in a similar way as observed after the evaporation of Cu at 600 K and 0.3 ML Cu at 800 K. The atoms in the

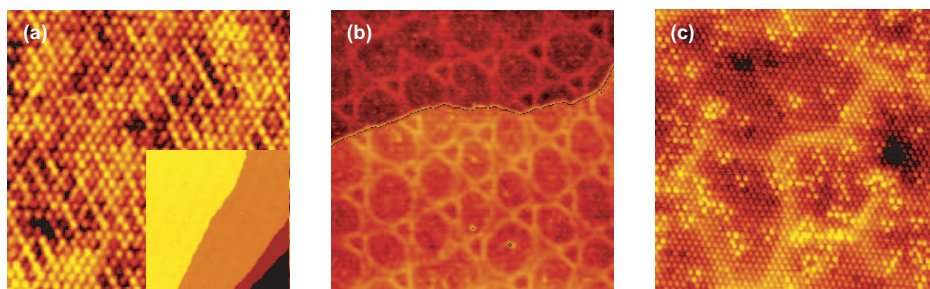


Figure 3.9: STM images obtained after evaporation of Cu at 800 K. **(a)** ($86 \times 86 \text{ \AA}^2$) 0.3 ML Cu. Cu atoms alloy into the Pt(111) substrate and form an alloy. The small insert ($475 \times 475 \text{ \AA}^2$) shows that the alloy formation is uniform across the terraces. **(b)** 1.0 ML Cu ($631 \times 631 \text{ \AA}^2$). Bright lines appear in a ring-like structure. **(c)** A zoom-in ($132 \times 132 \text{ \AA}^2$) on the ring structure shows that the atoms in between the rings have different apparent corrugation.

ring structure were always found to fit within a 1×1 grid, i.e., no dislocation structure was observed in the STM images of the ring structure.

The ring structure observed in the STM images resembles the adlayer-driven substrate reconstruction of Cu/Pt(111) observed by Holst *et al.* [146, 147] They also observed a network of bright lines in their STM images, and they associated this with a reconstruction of the Pt(111) substrate underneath the Cu adlayer. It is tempting to interpret our ring structure in terms of a similar reconstruction of a subsurface layer, which is also consistent with the fact that the topmost layer is not reconstructed (the atoms observed by STM fit within a 1×1 grid). We therefore speculate that the ring structure is caused by subsurface effects, and in particular that Cu atoms are located in the subsurface layers of the Pt(111) substrate. To directly investigate the influence of subsurface Cu on the structure observed in the STM images, we performed an experiment in which 1 ML of Cu was evaporated at room temperature followed by the evaporation of 1 ML Pt. Since the Cu atoms do not diffuse into the Pt(111) substrate at room temperature we expect the Cu and Pt to form a “sandwich” structure with the topmost layer consisting of Pt atoms on top of a subsurface layer consisting of Cu atoms.

Fig. 3.10(a) shows an STM image of the sandwich structure, and it is seen to be very similar to the ring structure formed upon evaporation of 1 ML Cu at 800 K. The most important difference between these two structures is the appearance of dark depressions in the STM images. These depressions sit in registry with the bright protrusions and are therefore associated with either atoms that due to electronic and/or geometric effects are imaged as depressions or with single vacancies in the topmost atomic layer. A post-annealing of the sandwich structure to higher and higher temperatures causes the concentration of the dark depressions to decrease, and a post-annealing at 773 K leaves the surface practically free of dark depressions (fig. 3.10(b)). Instead the corrugation of the surface becomes very similar to the one observed for the ring structure (fig. 3.9(c)),

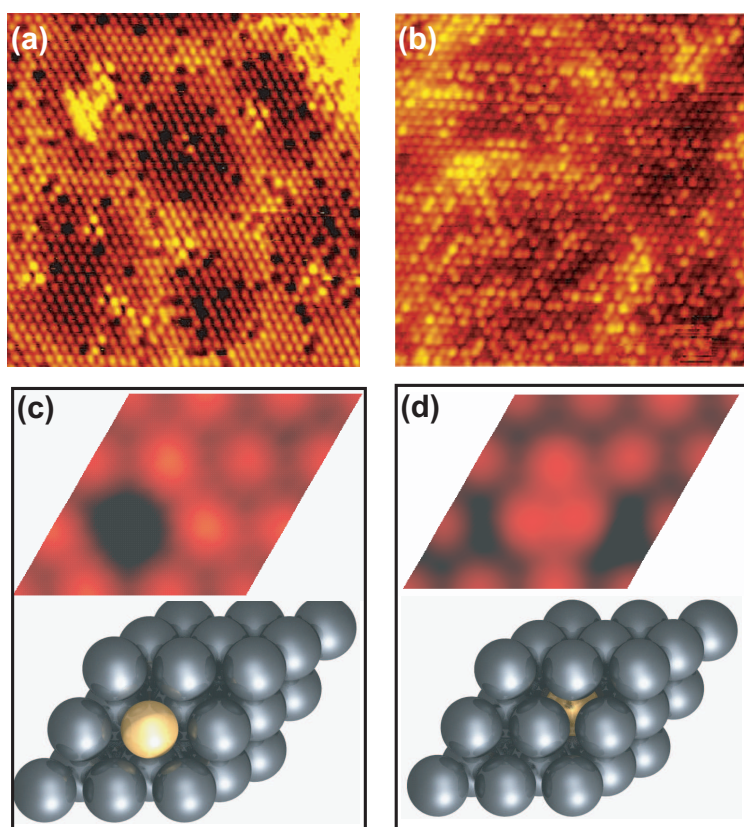


Figure 3.10: STM images ($100 \times 100 \text{ \AA}^2$) of the sandwich structure obtained by the evaporation of 1 ML Cu followed by 1 ML Pt onto Pt(111) at room temperature. **(a)** Before post-annealing. **(b)** After 10 min. of post-annealing at 773 K. **(c)** Ball model and simulated STM image of a single Cu atom (yellow) substituted for a Pt atom (grey) in the topmost layer of Pt(111) **(d)** Ball model and simulated STM image of a single Cu atom (yellow) substituted for a Pt atom (grey) in the first subsurface layer of Pt(111).

i.e., several atoms in between the rings now appear bright in the STM.

A growth mode of Pt on Cu/Pt(111), which leads to the formation of single vacancies is highly unlikely, and the depressions should thus be associated with atoms and not vacancies. The most likely growth scenario is that single Cu atoms diffuse on top of the Cu adlayer and get trapped in the growing Pt layer. Cu adatoms are highly mobile on Cu surfaces at room temperature [153], and it therefore seems reasonable to assume that they are also highly mobile on a Cu adlayer on Pt(111). This is also consistent with the disappearance of the dark atoms upon annealing, since the Cu atoms will diffuse into the subsurface layers at higher temperatures. To further support the conclusion that

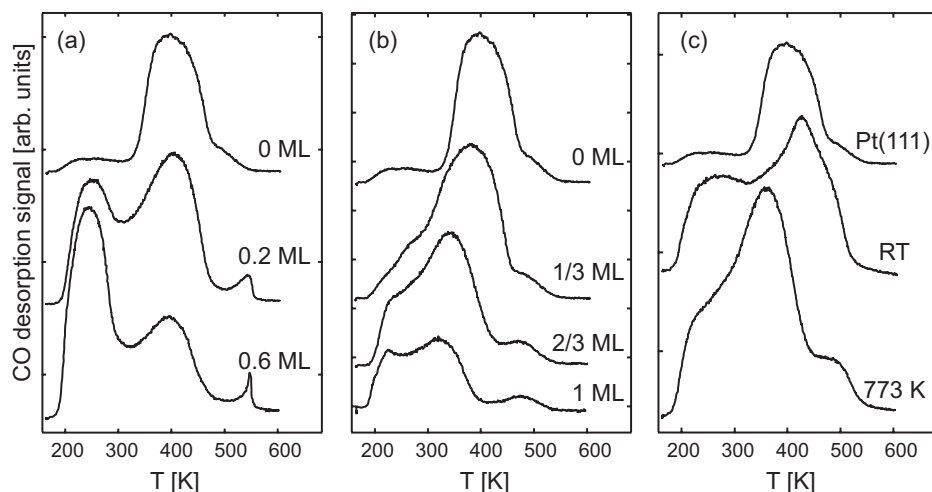


Figure 3.11: CO TPD spectra for different Cu/Pt(111) samples: **(a)** Cu/Pt(111) overlayers with submonolayer coverage of Cu evaporated at room temperature, **(b)** Cu/Pt(111) subsurface alloys prepared by evaporation of Cu at 800 K, and **(c)** Pt/Cu/Pt(111) sandwich structure prepared at room temperature before and after post-annealing.

we observe single Cu atoms trapped in the topmost layer, we compare the STM image of the sandwich structure (fig. 3.10(a)) to simulated STM images (fig. 3.10(c) and (d)), which are based on DFT calculations performed by A. U. Nilekar and M. Mavrikakis [154]. From the simulated STM images it is clearly seen that a Cu atom embedded in the topmost layer of Pt(111) is indeed imaged as a depression, whereas subsurface Cu enhances the apparent height of the above Pt atoms, which is again in good qualitative agreement with the STM images of Cu evaporated at 800 K or the sandwich structure after post-annealing. These trends in the simulated STM images remain the same when more Cu atoms are added, and furthermore the DFT calculations show that a Cu atom in the second, third, or fourth layer is favored by 0.48 eV, 0.34 eV, and 0.35 eV, respectively, as compared to Cu in the first layer [154]. Based on the STM and DFT results we thus conclude that the evaporation of Cu onto Pt(111) at 800 K leads to the formation of a subsurface alloy with no Cu residing in the surface layer.

3.3.2.3 TPD

The change in the reactivity of the Pt(111) surface caused by the deposition of Cu was examined experimentally in a series of CO TPD measurements. We started out by measuring the simplest systems, namely the Cu overlayers formed by the evaporation of Cu at room temperature. All the CO TPD spectra were obtained by exposing the sample to 10 L CO (10^{-8} torr; 1000 s) at a sample temperature of 166 K, which is the lowest obtainable temperature with the present experimental setup. Subsequently the sample

temperature was linearly increased to 600 K with a heating rate, β , of 2 K/s, while the CO desorption signal (mass 28) was monitored by the QMS.

Fig. 3.11(a) shows the CO TPD spectra for the clean Pt(111) surface as well as for 0.2 ML and 0.6 ML Cu evaporated onto Pt(111) at room temperature. The spectrum for the clean surface has a main peak with a peak temperature close to 400 K as well as a small broad peak at low temperature (~ 230 – 260 K) and a high-temperature shoulder at ~ 500 K. Pedersen *et al.* showed that the peak at 500 K increases significantly on a sputter-damaged Pt(111) [155], and the peak is therefore associated with the desorption of CO from defect sites. The small peak at low temperature is not normally observed in CO TPD spectra on Pt(111), and it is most likely caused by a desorption from the tantalum sample holder. When submonolayer coverages of Cu are deposited onto the Pt(111) substrate at room temperature, the peak at 400 K drops in intensity and a peak at 250 K is also found, which grows in intensity with increasing Cu coverage. Furthermore, a small but distinct peak shows up above 500 K. These spectra can be understood in terms of simple site blocking by the Cu adlayer atoms, i.e., the Cu atoms block the Pt sites but do not alter the properties of the free Pt atoms [141]. The small peak at high temperature is associated with defect sites as in the case of pure Pt(111).

A more interesting phenomenon than for the Cu adlayers is observed in the CO TPD spectra for the Cu/Pt(111) subsurface alloys prepared by the evaporation of Cu at 800 K. The spectra for Cu/Pt(111) subsurface alloys with varying Cu coverage are presented in fig. 3.11(b), and the spectrum for the clean Pt(111) surface is also included for reference. From these spectra it is clearly seen that the main peak at 400 K on the clean surface is shifted towards lower temperatures with increasing Cu coverage; ~ 380 K at 1/3 ML Cu, ~ 345 K at 2/3 ML Cu, and ~ 325 K at 1 ML Cu. From a crude Redhead analysis using a preexponential factor of 10^{14} s^{-1} taken from Zhdanov *et al.* [156], these peak temperatures can be converted to estimates of the CO binding energies. The estimated binding energies are given in table 3.1, and it is seen that the alloying has a strong influence on the interaction with CO, as the CO binding energy is 0.22 eV lower on the subsurface alloy with 1 ML Cu as compared to the clean Pt(111) surface.

For comparison the binding energies of CO on Pt(111) with Cu atoms substituted for Pt atoms were calculated from DFT [154], and the results are also presented in table 3.1. The values plotted are the binding energies of the most favorable adsorption sites as found from the DFT calculations. The agreement between the absolute values for the clean Pt(111) surface is not very convincing with a difference of 0.65 eV between the measured and the calculated value. This is not surprising since DFT is well known to overestimate binding energies, and in particular the CO/Pt(111) system is poorly described by DFT with respect to absolute energies [157]. The trend in the DFT calculations is, however, more reliable than the absolute numbers, since systematic errors tend to cancel out, and from the trend in the DFT calculations we can draw a very clear conclusion: substituting Cu into the topmost layer increases the binding energy of CO, whereas substituting Cu into the first subsurface layer decreases the binding energy of CO. These CO TPD measurements and DFT-calculated CO binding energies therefore add in a consistent way to the established model with the formation of a Cu/Pt(111) subsurface alloy.

In the CO TPD spectra for the Cu/Pt(111) subsurface alloys, the high-temperature

CO TPD		DFT calculations		
θ_{Cu}	E_b	θ_{Cu}	$E_b(\text{subsurface})$	$E_b^*(\text{surface})$
0 ML	1.17 eV	0 ML	1.82 eV	1.82 eV
1/3 ML	1.11 eV	1/9 ML	1.81 eV	1.95 eV
2/3 ML	1.01 eV	2/9 ML	1.80 eV	1.99 eV
1 ML	0.95 eV	3/9 ML	1.76 eV	2.06 eV

Table 3.1: CO binding energies for varying Cu coverages as found from CO TPD measurements and DFT calculations. Calculations were performed for both subsurface Cu atoms (E_b) and surface Cu atoms (E_b^*). Note that the Cu coverages in the experiments and in the DFT calculations are not directly comparable; the experimental coverage refers to the amount of Cu evaporated onto the Pt(111) substrate, whereas the theoretical coverage refers to the amount of Cu present in the surface or the first subsurface layer.

shoulder develops into a distinct peak as a consequence of the downshift of the main peak. Furthermore, a low-temperature shoulder is observed, which increases in intensity with growing Cu coverage. It is tempting to associate this peak with the CO adsorbed on Cu sites since it is located at approximately the same temperature as the low temperature peak observed for the Cu overlayers. Nevertheless, we cannot base any conclusions on this low-temperature peak for two main reasons. First, the peak does not appear to be saturated, and we would most likely need to cool to even lower temperatures during the CO exposure to locate the true position of the peak. Second, we saw from the spectrum for the clean Pt(111) surface that the CO adsorption on the sample holder gives a low temperature peak. We indeed find that the relative intensity of the low temperature peak increases when the sample is retracted further away from the opening of the QMS, which should give a stronger background signal. It thus seems most likely that the low temperature peak is an artefact due to the CO adsorption on Cu atoms evaporated onto the sample holder. This should, however, not have any implications for the conclusions relating to the position of the main peak.

The final CO TPD measurements were made on the sandwich structures prepared by the evaporation of 1 ML Cu followed by the evaporation of 1 ML Pt at room temperature. The spectrum for the as prepared sandwich structure is presented in fig. 3.11(c) along with the spectrum obtained after 10 minutes of post-annealing at 800 K of this sandwich structure. In the spectrum of the unannealed sandwich structure the main peak is shifted towards higher temperatures and thus higher CO binding energies, whereas the spectrum of the post-annealed sample bears close resemblance to that of the Cu/Pt(111) subsurface alloys prepared by the evaporation of Cu at 800 K. The DFT calculations in table 3.1 suggest that the shift towards a higher CO binding energy is due to Cu atoms being substituted into the topmost layer. The calculations supports our earlier conclusion that the dark atoms in the sandwich structure, which disappeared upon post-annealing

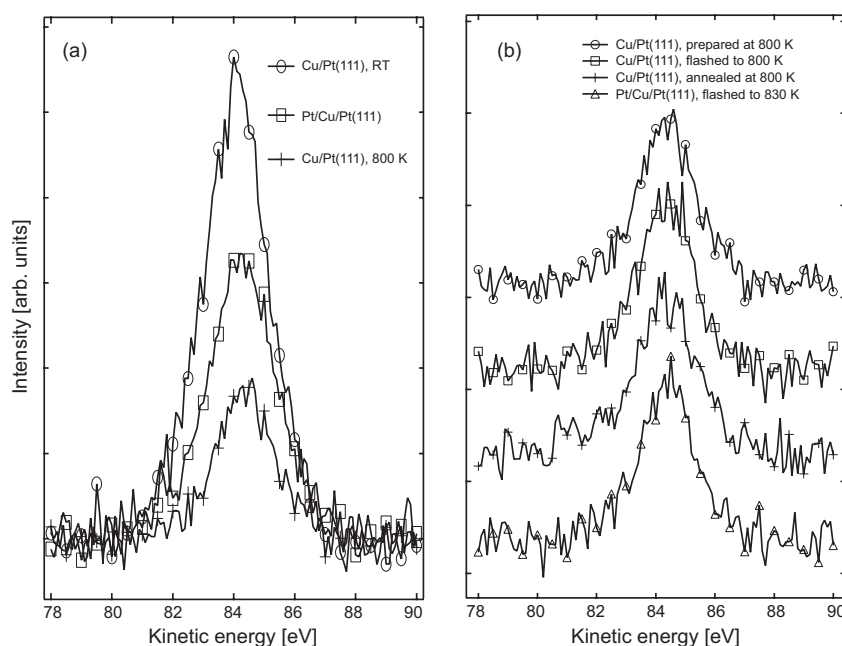


Figure 3.12: Cu3s peaks for different preparations of Cu/Pt(111). See text for details.

(fig. 3.10(a) and (b)), are single Cu atoms trapped in the topmost layer of the surface, which diffuse into the substrate during post-annealing.

3.3.2.4 XPS

Based on STM, TPD, and DFT a model has been established in which Cu/Pt(111) forms a subsurface alloy with a topmost layer consisting exclusively of Pt atoms, and it has been shown how these subsurface Cu atoms alter the chemical properties of the surface by lowering the binding energy of the CO molecules. Two important issues, however, remain to be addressed: What is the concentration of Cu in the second layer, and in the deeper layers; and is the Cu/Pt(111) subsurface alloy prepared at 800 K in thermal equilibrium or is it a kinetically hindered, unstable configuration? These issues were addressed by means of core level spectroscopy. In particular the relative intensities of the Cu3s peaks provide information on the depth profile of Cu in the various preparations.

Fig. 3.12(a) shows the Cu3s intensities corrected for the background for three different preparations of 1 ML Cu on Pt(111):

- 1 ML Cu evaporated onto Pt(111) at room temperature (Cu/Pt(111) overlayer)
- 1 ML Cu evaporated onto Pt(111) followed by the evaporation of 1 ML Pt at room temperature (Pt/Cu/Pt(111) sandwich structure)

- 1 ML Cu evaporated onto Pt(111) at 800 K (Cu/Pt(111) subsurface alloy)

The integrated intensities of the Pt/Cu/Pt(111) sandwich structure and the Cu/Pt(111) subsurface alloy relative to the Cu/Pt(111) overlayer are 0.65 and 0.30, respectively. It is thus also clear from the XPS measurements that Cu diffuses into the Pt(111) substrate, and now we see that some of the Cu diffuses deeper than the first subsurface layer as evidenced by the lower intensity of the Cu3s peak for the Cu/Pt(111) subsurface alloy.

Fig. 3.12(b) shows the Cu3s peaks for four different samples with 1 ML Cu on Pt(111), which have all been annealed to 800 K following different preparations:

- Cu/Pt(111) subsurface alloy prepared by the evaporation of 1 ML Cu at 800 K
- Cu/Pt(111) overlayer flashed to 800 K
- Cu/Pt(111) overlayer annealed 20 minutes at 800 K
- Pt/Cu/Pt(111) sandwich structure annealed to 830 K

These four spectra are indistinguishable within the experimental uncertainties, and from this we conclude that the Cu/Pt(111) subsurface alloys are formed in thermal equilibrium at 800 K, since no further diffusion is observed for the prolonged annealing at 800 K.

The depth profile of the Cu/Pt(111) subsurface alloy can be modelled from the relative intensity of the Cu3s peak with respect to the Cu/Pt(111) overlayer in combination with the energy of a Cu atom in the different layers. If we assume the Cu to be distributed in a finite number of layers, N , close to the surface, the intensity of the subsurface alloy, I , relative to the intensity of the overlayer, I_o is given by the following sum:

$$\frac{I}{I_o} = \sum_{i=1}^N c_i \cdot e^{-\frac{id}{\mu}},$$

where c_i is the concentration of Cu in the i 'th subsurface layer, μ is the inelastic mean free path of the electron, and d is the distance between adjacent atomic layers. Since the amount of Cu is relatively low, μ and d are estimated by the corresponding parameters for pure Pt(111); $\mu = 4.18 \text{ \AA}$ [158] and $d = 2.27 \text{ \AA}$. The validity of this simple model can be tested for the sandwich structure, in which $N=1$ and $c_1 = 1$. This gives a value of $\frac{I}{I_o} = 0.58$, which compares well with the experimental value of 0.65, especially when taking into account that some Cu atoms are trapped in the topmost layer in the experimentally prepared sandwich structure.

The ratio between the c_i 's in the subsurface alloy can be evaluated from the results of the DFT calculations. These showed that a Cu atom in the second, third, or fourth layer was favored by 0.48 eV, 0.34 eV, and 0.35 eV, respectively. These energies were found to be almost fully independent of the Cu coverage, and the energy for Cu in the fourth layer is assumed already to be converged to the value of a bulk substituted Cu atom [154]. Based on this, c_i is assumed to be constant for $i \geq 2$, and furthermore the ratio between c_1 and c_2 is found by assuming a Boltzman distribution of the Cu atoms:

$$\frac{c_1}{c_2} = e^{\frac{E_1 - E_2}{kT}} = e^{\frac{0.48\text{eV} - 0.35\text{eV}}{8.62 \cdot 10^{-5} \frac{\text{eV}}{\text{K}} \cdot 800\text{K}}} = 6.6$$

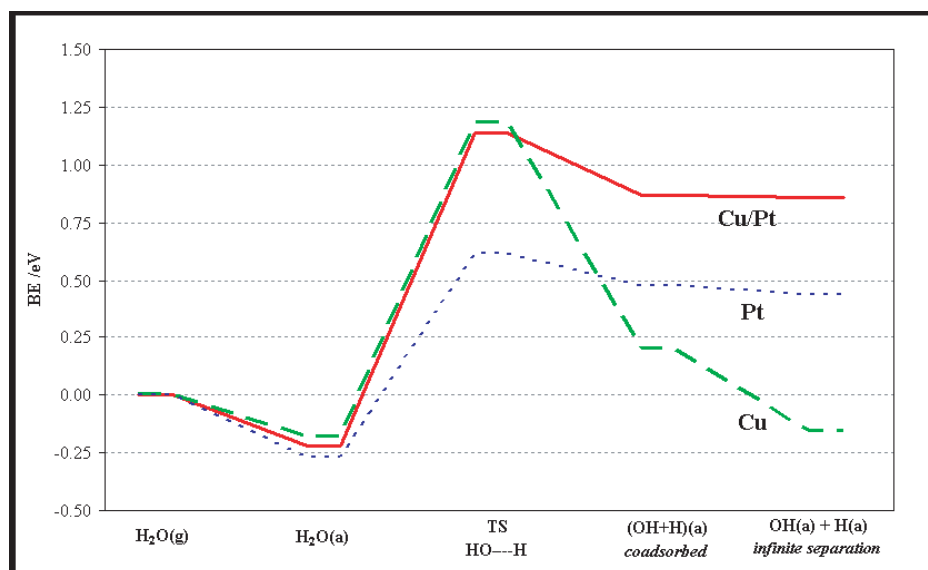


Figure 3.13: Potential energy diagram for the activation of H₂O on Cu(111), Pt(111), and Cu/Pt(111) subsurface alloy.

The concentration of Cu in the topmost layer is neglected, c_0 , since this is observed by STM to be 0, and since

$$\frac{c_0}{c_1} = e^{\frac{E_0 - E_1}{kT}} = e^{\frac{0\text{eV} - 0.48\text{eV}}{8.62 \cdot 10^{-5} \frac{\text{eV}}{\text{K}} \cdot 800\text{K}}} = 0.001$$

This gives the final expression:

$$\frac{I}{I_o} = c_1 \cdot e^{-\frac{d}{\mu}} + \frac{c_1}{6.6} \sum_{i=2}^N \cdot e^{-\frac{id}{\mu}} = c_1 \cdot e^{-\frac{d}{\mu}} + \frac{c_1}{6.6} \left(\frac{e^{-\frac{2d}{\mu}} - e^{-\frac{Nd}{\mu}}}{1 - e^{-\frac{d}{\mu}}} \right)$$

The equation should be solved under the constraint that the total amount of Cu is 1 ML:

$$\sum_{i=1}^N c_i = c_1 + \frac{N-1}{6.6} c_1 = 1 \Rightarrow c_1 = \frac{1}{1 + \frac{N-1}{6.6}}$$

The best agreement with the experimental value of $\frac{I}{I_o} = 0.30$ is found for $N = 10$, $c_1 = 0.4$ ML, and $c_2 = 0.06$ ML, and this constitutes the final model of the Cu/Pt(111) model.

3.3.2.5 Conclusion

The combination of STM, TPD, XPS, and DFT provides a comprehensive model for the formation of a Cu/Pt(111) subsurface alloy, and it is now interesting to study the

reactivity of this surface in further detail. As it was shown by CO TPD and confirmed by DFT, the interaction with CO can be “tuned” by varying the concentration of Cu in the alloy. This is in itself very interesting in relation to, e.g., anode materials in low temperature fuel cells, where this may help in overcoming the problems of CO poisoning (this will be discussed in further detail in section 4.1). As mentioned in the opening of this section, it is, however, of special interest to investigate the activity of the Cu/Pt(111) alloy for the WGS reaction, since both Cu and Pt are highly active catalysts for this process. In the DFT calculations the Cu/Pt(111) subsurface alloy was modelled by Pt(111) with a full monolayer of Cu in the first subsurface layer. In previous studies involving a series of subsurface alloys it was found that positive kinetic effects (i.e. decreased activation energies) observed at full ML subsurface alloys tend to be preserved even in the case of less than a ML solute (e.g. Cu) coverage in the subsurface layer [46]. Therefore, by choosing a high symmetry, full ML Cu/Pt(111) subsurface alloy, the key characteristics of the influence of Cu in the subsurface of Pt(111) could be elucidated.

For the comparison of the WGS activity with pure Cu, the most relevant parameter to look at is the activation of water, which is rate limiting for a relatively wide span of gas compositions and a number of the late transition metals, including Cu [132, 159]. The potential energy diagram for the activation of H₂O on Cu(111), Pt(111), and a Cu/Pt(111) subsurface alloy as calculated from DFT is shown in fig. 3.13. It is very interesting to observe that the activation barriers on Cu/Pt(111) and Cu(111) are identical, whereas the final products (adsorbed OH and H) are significantly destabilized on the Cu/Pt(111) surface as compared to Cu(111), an effect which is increased when the repulsion between OH and H is accounted for by moving them infinitely far apart. This should leave the Cu/Pt(111) surface less susceptible to poisoning by especially OH, and these calculations thus indicate that Cu/Pt(111) may have a higher WGS activity than pure Cu(111).

A detailed analysis of the WGS activity should be based on full microkinetic modelling, and we should take care in relying too heavily on the arguments just presented. For example, the barrier for the H₂O activation is seen to be much lower on Pt(111), but this surface suffers from poisoning by CO, and we cannot say whether this effect will also be important for the Cu/Pt(111) surface. Despite these precautions the Cu/Pt(111) surface definitely encourages further experimental work. In particular it would be of great interest to perform WGS rate measurements on the Cu/Pt(111) subsurface alloy and compare this with similar measurements on Cu(111). We are currently working on an experimental setup for this application, and hopefully we will be able to investigate the predictions from the DFT calculations within the nearest future.

CHAPTER 4

Surface structures at reaction conditions

In this chapter the STM is used to study several metal surfaces at high pressures relevant for catalytic processes. For the CO adsorption on Pt(111) and the NO adsorption on Pd(111) it is found that the structures formed at high pressures close to one atmosphere are similar to structures found at ultra-high vacuum conditions. For the Au/Ni(111) surface alloy, which forms the basis of, e.g., a new steam reforming catalyst, high pressures of CO are shown to induce a phase separation which is not observed at low pressure. Finally the formation of a surface oxide at high oxygen pressure on both the Pt(110) and the Ag(111) surface is studied.

4.1 Introduction

As discussed in the previous chapter the surface science approach to the study of catalysts has brought about a tremendous amount of new insight into the understanding of the fundamental mechanisms in heterogeneous catalytic processes as well as providing guidelines for the development of new and improved catalysts. One should, however, always recall that the surface science approach deals with highly idealized model systems and one needs to be somewhat precautionary when extrapolating the results to the conditions of a real working catalyst. One of the gaps between typical surface science experiments and applied catalysis is the *pressure gap* caused by the ~ 13 orders of magnitude difference in pressure from a standard surface science experiment ($\sim 10^{-10} - 10^{-6}$ mbar) to an operating catalyst ($\sim 1 - 100$ bar).

One key issue is thus to characterize the adsorption structures of the gases present during the catalytic process. The high coverage structures formed at high gas pressures and high temperatures are usually studied by performing experiments at low pressures and low temperatures, i.e., at a similar chemical potential of the gas phase molecules. This, however, only holds if entropy effects can be neglected and the adsorbed gas phase is in thermodynamical equilibrium with the gas phase. Another very important issue is whether the surface studied in surface science experiments is in fact identical to the active phase of the crystal. A very clear example that the thermodynamically stable surface in UHV may differ from the surface of the active catalyst is found in the oxidation of CO on transition metals. In UHV experiments Ru is found to be the least active of the late transition metals for CO oxidation, whereas at high pressures of oxygen a RuO₂ structure is formed, which is superior in activity to all the other metals [160, 161]. To better understand the atomic mechanism of working catalysts it is therefore essential to extend both experimental and theoretical methods to a pressure range closer to the catalytic relevant regime. In this chapter several examples will be given in which STM in combination with DFT calculations is used to study gas-surface interactions at atmospheric pressures.

4.2 The pressure gap

The importance of studying model catalysts at reaction conditions has long been realized, and already in the late 1940's Gwathmey used an optical microscope to study the morphological changes on Cu and Ni single crystals induced by reactions at atmospheric pressures [162, 163]. This *ex-situ* approach in which the model catalyst is examined after being exposed to high gas pressures and temperatures can often provide valuable information. For example Over *et al.* used *ex-situ* STM to characterize a Ru(0001) surface after CO oxidation, and they found that the formation of a RuO₂(110) surface oxide was the origin of the superior activity of Ru as a CO oxidation catalyst in excess of oxygen [160, 161]. In the case of CO oxidation on Ru(0001) the *ex-situ* measurements were adequate since the RuO₂ surface oxide is stable under UHV conditions once it has been formed. In other cases the catalyst surface may, however, undergo reversible changes during reactions, and for such catalytic systems the application of *ex-situ* studies is of

little use. In general it is highly desirable to be able to perform surface science experiments at high gas pressures or even during reactions. Over the past two decades much progress has been achieved in the development of *in-situ* surface characterization tools, and the pressure gap has been “bridged” for many catalytically relevant systems.

Most tools for the *in-situ* characterization are based on optical principles, since electron-based techniques suffer from the low mean-free path of the electrons at high gas pressures. Modern x-ray synchrotron sources provide beams which enable the use of x-ray diffraction spectroscopy (XDS) for the structure determination at high pressures [164]. High pressure (HP) XDS has been developed with success in the group of Ferrer, who have used the technique to study the high pressure induced facetting of CO/Ni(110) [165], the compression of the CO adsorption structure on Ni(111) [166], and also the hydrogenation of CO on Ni(111) [167]. Synchrotron radiation can also be used for *in-situ* x-ray absorption spectroscopy (XAS), e.g., as done by Moggridge *et al.* [168], and Ogletree *et al.* have developed an *in-situ* system for photoemission spectroscopy (PES) [169]. Laser light may also be used to obtain spectroscopic information such as vibrational frequencies of adsorbates in, e.g., sum frequency generation (SFG). SFG has been employed by Su *et al.* and Rupprechter *et al.* to study the high pressure structures of CO on Pt(111) [170, 171], and in a very recent work Lu *et al.* studied the electrochemical oxidation of CO on Pt electrodes [172, 173]. Polarization modulation infrared reflection absorption spectroscopy (PM-IRAS) is another laser-based technique which has been used, e.g., in the group of D. Wayne Goodman to study a Pd(111) car catalyst model system [174].

Despite the fact that electron spectroscopy, as mentioned, is not the optimal choice for *in-situ* studies, a transmission electron microscope (TEM) which by means of several stages of differential pumping along the electron beam allows for a local gas pressure at the sample of up to ~ 20 mbar has been developed at the Haldor Topsøe research laboratories. They have used the *in-situ* TEM to characterize the promoting effect of Ba-supported Ru catalysts which are highly active for the ammonia synthesis [175]. They have also imaged a reversible reshaping of supported Cu particles induced by elevated gas pressures [176] and have followed the growth of carbon whiskers on Ni particles in real time [98].

Although the STM uses electrons to probe the electric and morphological structure of a surface, it is not limited to low pressures since the electrons only have to tunnel through the narrow gap between the tip and the surface, and the STM is applicable in the entire pressure range from UHV to ambient, and even at higher pressures. Due to the unique degree of details that can be studied with STM and due to the limited number of surface science techniques available for an *in-situ* characterization, the STM is an invaluable tool for bridging the pressure gap. The work on HP-STM was pioneered by Salmeron and Somorjai who designed a dedicated HP chamber and used a vacuum transfer cell for the sample transfer between the UHV chamber and the HP cell [177]. Later they improved their design so that they could perform an *in-situ* transfer without loss of vacuum, and the temperature range for the STM measurements was increased to 675 K [178]. We have employed a similar design and redesigned our home-built Aarhus STM for operation in up to atmospheric gas pressures while still maintaining the high resolution and fast scanning capabilities which are characteristic for the Aarhus STM [33]. The group of

Joost Frenken has taken the application of high pressure STM one step further and has incorporated an STM into a micro reactor [179], and with this setup they have, e.g., been able to image a Pt(110) surface during a CO oxidation reaction [180]. This type of setup that combines reactivity measurements with *in-situ* surface characterization has the potential of providing hitherto unattainable information of the structure of working catalysts. It should, however, be mentioned that this is in no way a simple task, and the setup used by Frenken's group has so far not been able to produce atomic resolution due to problems with, e.g., the vibrational isolation.

From the many studies based on the *in-situ* surface characterization tools described, several examples exist that new and important phenomena occur at reaction conditions which cannot be observed in vacuum-based experiments. These effects may involve compositional and morphological changes of the active surface or the formation of surface oxide layers. An example of morphological changes of a Au/Ni(111) surface alloy induced by high pressures of CO will be presented in section 4.2.3, and surface oxide formation will be the topic of section 4.3.1 and 4.3.2. To my knowledge, however, only one example exists in the literature, where a new adsorption structure is formed at high pressures and which cannot be reproduced at low pressures. The example is that of the NO adsorption on Rh(111) reported by Rider *et al.* Using HP STM they found the existence of a (3×3) -7NO structure, which only forms in equilibrium with the gas phase at elevated pressures [181]. In all other studies of high pressure adsorbate structures, the structures observed at elevated pressures have been found to correspond to similar structures formed at low pressure and low temperature. In the following two sections I will present HP STM studies of the adsorbate structures of CO/Pt(111) and NO/Pd(111), and indeed show that for these systems we are able to bridge the pressure gap.

4.2.1 CO/Pt(111)

The interaction of CO with the Pt(111) is among the most well-studied adsorbate-metal surface systems in the whole of surface science. This great interest is due to the importance of both CO and Pt in numerous catalytic processes, such as CO oxidation, CO hydrogenation, and the activation of H₂ derived from natural gas in low-temperature fuel cells. As for most other systems of interest in surface science the number of studies on low pressure ($< \sim 10^{-6}$ torr) CO adsorption on Pt(111) by far exceeds the number of studies carried out at high pressure (up to ~ 1 bar). A very comprehensive understanding of the CO adsorption structures up to 0.5 ML formed at low pressures thus exists (see e.g. ref [182]). Above 0.5 ML several ordered CO structures have been identified on Pt(111), which can be described as either a $c(4 \times 2)$ -2CO structure (0.5 ML) or $c(4 \times 2)$ -2CO domain wall structures [183]. The group of Somorjai was the first to perform high pressure studies on CO/Pt(111), and based on HP-STM [184] and SFG [171] they suggested the existence of a new incommensurate CO structure, which had not been observed at low temperature. The results of Somorjai's group have, however, been rejected in a recent SFG study by Rupprechter *et al.* [170], and Vestergaard *et al.* in our group showed from atomically resolved HP-STM that CO at room temperature and 1 bar forms a rotated moiré pattern [185], which has in fact also been observed at 170 K and low CO pressure in a LEED study by Ertl *et al.* [186]. These studies, however, only

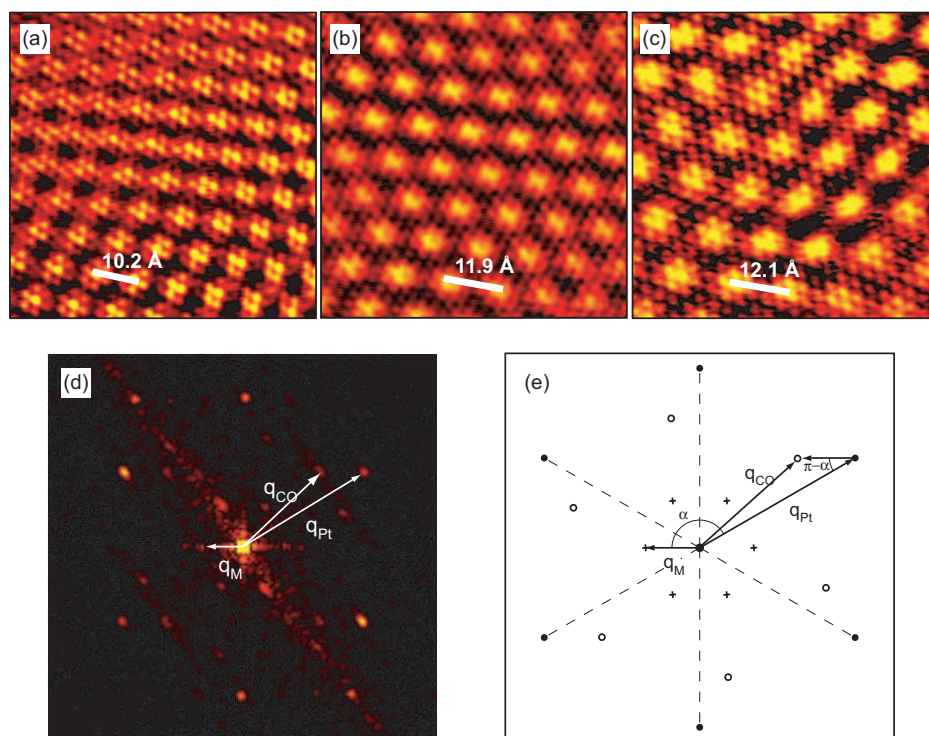


Figure 4.1: (a)-(c) STM images ($60 \times 60 \text{ \AA}^2$) of CO adsorbed on Pt(111) at room temperature and 10^{-2} torr (a), 100 torr (b), and 720 torr (c). Notice the different periodicity of the moiré structure. (d) Fourier transform of an STM image of CO/Pt(111). (e) Model showing the relationship between the reciprocal lattice vectors of the CO adsorbate structure (\vec{q}_{CO}), the Pt(111) substrate (\vec{q}_{Pt}), and the moiré pattern (\vec{q}_M).

characterize the CO adsorption structure on Pt(111) at one given pressure (1 bar), and so far no comprehensive study of the adsorption structures formed at pressures in the intermediate pressure range between UHV and 1 bar.

Using atomically resolved HP STM we studied the adsorption structure of CO on Pt(111) at room temperature over the entire pressure range from 10^{-6} –720 torr. Fig. 4.1(a-c) shows three typical STM images obtained at three different pressures. In all three STM images two different hexagonal patterns can be recognized: one corresponding to the structure of the single protrusions, and one corresponding to a periodic height modulation of the single protrusions. These are the typical features of a moiré pattern caused by the interference of an incommensurate, hexagonally close-packed adsorbate layer on a likewise hexagonally close-packed surface. A moiré is simply the two-dimensional equivalent of the beating frequency that results from adding to harmonic functions with similar frequencies.

The appearance of the two different hexagonal structures is better seen when a fast Fourier transform (fft) is made of the STM images (see fig. 4.1(d)). The application of fft to the data also ensures that the measured angles and distances are averaged over the entire STM images, thus taking full advantage of the data and minimizing the statistical errors. From a comparison with fft's of STM images of the clean Pt(111) surface it is found that depending on the CO pressure, the STM images either the adsorbed CO molecules ($p_{CO} \gtrsim 0.1$ torr) or the Pt(111) substrate ($p_{CO} \lesssim 0.1$ torr). The peaks in the fft represent the reciprocal lattice vectors of the CO adsorbate structure (\vec{q}_{CO}), the Pt(111) substrate (\vec{q}_{Pt}), and the moiré pattern (\vec{q}_M), which are related by [187]

$$\vec{q}_M = \vec{q}_{CO} - \vec{q}_{Pt},$$

as illustrated in fig. 4.1(e). In the cases where the CO molecules were imaged, the coverage of CO, θ_{CO} , can be directly determined from the fft by

$$\theta_{CO} = \left(\frac{q_{CO}}{q_{Pt}}\right)^2.$$

In the cases where the Pt(111) substrate was imaged, q_{CO} and thereby also θ_{CO} could be determined indirectly by applying the cosine relation to the model in fig. 4.1(e):

$$q_{CO}^2 = q_{Pt}^2 + q_M^2 - 2q_{Pt}q_M \cos(\pi - \alpha).$$

The CO coverage as a function of the CO pressure is shown in fig. 4.2, and it is seen that the CO coverage varies continuously over the whole pressure range from 10^{-6} –720 torr. Furthermore, it was found that the change in CO coverage is reversible, since the same CO coverage was found at a given CO pressure either by raising or lowering the pressure. These data show that CO is in equilibrium with the gas phase and the CO adsorbs in a close-packed structure which is reversibly compressed/expanded, when the pressure is increased/decreased. Although only one moiré structure has been identified at low pressure and low temperature, and although the high coverage lattice gas structures are not found at high pressure, one cannot really speak of a pressure gap for CO/Pt(111) since no new physics happens for high temperatures. Rather than a pressure gap one should consider a *temperature gap* since the observed differences between the low pressure and temperature and the high pressure and temperature are most likely due to kinetic or entropic effects.

The finding that the adsorbed CO is in equilibrium with the gas phase and that the coverage varies continuously with the pressure is of great relevance to the ongoing debate on the role of Ru promoters in Pt-based anode catalysts in low temperature fuel cells. It is well known that Pt-Ru alloy anode catalysts are more tolerant to CO impurities in the hydrogen fuel in low temperature fuel cells [188]. Two models for the role of Ru in the Pt-Ru alloy have been discussed in the literature. In the *bifunctional mechanism* the Ru atoms act as active sites for the CO oxidation, which removes the CO molecules from the surface [189]. *The ligand effect* ascribes the increased CO tolerance to a change in the electronic structure of Pt, which weakens the interaction with CO more than the interaction with H₂, thus giving an overall higher rate [190]. It has been shown both experimentally [191] and theoretically [30] that Pt overlayers on a Ru(0001)

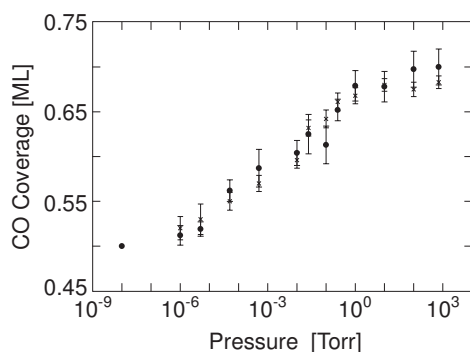


Figure 4.2: CO coverage as a function of CO pressure at room temperature.

substrate indeed lower the binding energy of CO. This will, however, only have an effect on the CO coverage if the adsorbed CO is in equilibrium with the gas phase at the conditions of the fuel cell. Our results show that the adsorbed CO is indeed in equilibrium with the gas phase at room temperature and therefore also at higher temperatures. These results thus give strong support to the ligand effect without, of course, discarding the bifunctional mechanism, and it is indeed very likely that the enhanced CO tolerance of Pt-Ru is due to a combination of the two effects.

4.2.2 NO/Pd(111)

The automotive catalyst, first implemented in the United States in 1975 and in 1986 in Europe, is without doubt the most widely known application of catalysis, and it has also received a great deal of interest within the field of surface science [174, 192]. The car catalyst simultaneously reduces NO_x to N_2 , oxidizes CO to CO_2 , and combusts unburned hydrocarbons, and for this reason it is also known as the three-way catalyst. The active material in the three-way catalyst is a precious metal or mixtures of precious metals (Pt, Rh, and Pd) supported on an oxide material [193]. When the three-way catalyst was introduced it was mainly based on Pt and Rh, but for technical and economic reasons Pd-based catalysts are preferred, which are, however, more susceptible towards poisoning by Pb and S [194]. With the recent progress in fuel pretreatment resulting in very low Pb- and S-contents, Pd is now commonly used in three-way catalysts.

From a surface science point of view the use and further development of the three-way catalyst raise many interesting issues, one of them being the interaction of NO with Pd surfaces. In particular the NO/Pd(111) system has been widely studied since the (111) facet of Pd is the predominant facet of Pd nanocrystals [195]. Conrad *et al.* were the first to study the NO/Pd(111) adsorption system in detail. By means of LEED they were able to correlate three distinct peaks in the NO TPD spectrum with three NO adsorption structures: an unordered structure with an NO coverage, θ_{NO} , of $1/4$ ML, a $c(4 \times 2)$ structure with $\theta_{\text{NO}} = 1/2$ ML, and a (2×2) structure with $\theta_{\text{NO}} = 3/4$

ML [196]. In a later study Chen and Goodman also identified a $c(8 \times 2)$ structure with $\theta_{NO} = 5/8$ ML [197]. The preferred binding site of NO has been a cause of dispute, but following recent DFT [198] and STM [199] studies the issue seems to be reconciled in a model in which NO adsorbs in threefold hollow sites (in the $c(4 \times 2)$ structure) or in a mixture of threefold hollow sites and tilted atop sites (in the $c(8 \times 2)$ and (2×2) structures).

In a very recent study Ozensoy *et al.* suggested the existence of a (3×3) structure with $\theta = 7/9$ ML at high NO pressures [200]. Since this adsorption structure has never been observed at low pressure and low temperature, the data of Ozensoy *et al.* indicates the existence of a pressure gap similar to the one observed for NO/Rh(111) by Rider *et al.* [181]. The conclusions in the work of Ozensoy *et al.* is based on PM-IRAS experiments and DFT-based simulations of the obtained spectra. Since the use of infrared spectroscopy only provides indirect evidence for the adsorption structures through the location of binding sites based on vibrational frequencies of the adsorbates, and since the agreement between the experimental data and the DFT-based simulations was far from perfect (this will be discussed in further detail after the presentation of the STM data), we decided to study the adsorption of NO on Pd(111) at elevated pressures by means of HP-STM.

Fig. 4.3(a) shows an STM image of NO adsorbed on Pd(111) at 720 torr, and a hexagonal pattern of bright protrusions is seen in this image. From the comparison of a series of images like the one in fig. 4.3(a) with images of the clean Pd(111) surface (fig. 4.3(b)), the unit cell of the hexagonal structure could be determined. As in the analysis of the CO/Pt(111) data in the previous section, the distances and directions were measured in the Fourier transformed STM images (see the small inserts in fig. 4.3(a)(b)). From the analysis it was found that the structure observed at 720 torr NO and room temperature corresponds to a (2×2) structure.

The STM images also provide information about the internal structure of the unit cell, which is best seen in the line scan in fig. 4.3(c). This line scan exhibits three distinct protrusions, which can be correlated with the three NO molecules in the unit cell of the (2×2) -3NO structure observed at low temperature and pressure, as illustrated by the ball model in fig. 4.3(d). The STM data thus clearly show that at 720 torr and room temperature NO adsorbs in a (2×2) -3NO structure which is identical to the structure of the highest NO coverage observed at low pressure and low temperature. The STM findings were supported by DFT calculations which found the (2×2) -3NO structure to be favored over the proposed (3×3) -7NO structure at the conditions of our experiments. The validity of the DFT calculations was tested by performing a similar calculation for the NO/Rh(111) system, where the (3×3) -7NO adsorption structure was indeed found to be more stable than the (2×2) -3NO structure at temperatures above ~ 300 K at an NO pressure of 0.03 torr, in striking agreement with the observations of Rider *et al.* [181]. Thus, no evidence of a pressure gap is found for the NO/Pd(111) adsorption system, and since this conclusion is at variance with the model proposed by Ozensoy *et al.* [200], I will discuss their work in further detail.

The main experimental finding in the work of Ozensoy *et al.* is a change in the relative intensities of the two peaks observed in the PM-IRAS spectra of NO/Pd(111) at 400 mbar and 300 K as compared to 13.3 mbar and 180 K. The spectra obtained

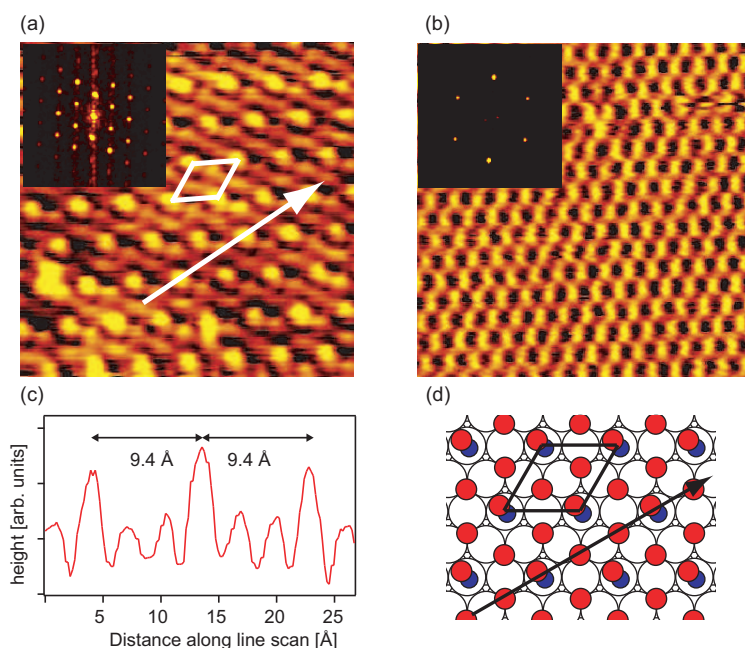


Figure 4.3: **(a)-(b)** STM images ($41 \times 41 \text{ \AA}^2$) of NO adsorbed on Pd(111) at room temperature and 720 torr **(a)** and clean Pd(111) **(b)**. The small inserts show the 2D Fourier transforms of the STM images. **(c)** Line scan (indicated by the arrow in the STM image) showing the the three NO molecules in the (2×2) unit cell; atop adsorbed NO is clearly distinguished from the threefold hollow site adsorbed NO by the apparent different heights. **(d)** Ball model of the (2×2) -3NO adsorption structure (oxygen atoms are red and nitrogen atoms blue). The (2×2) unit cell and line scan direction corresponding to those in the STM image are indicated.

at 13.3 mbar and 180 K are identical to the spectrum observed for the (2×2) -3NO structure at low pressure, and the spectrum at 400 mbar and 300 K therefore indicates the appearance of a new adsorption structure at high pressure. Based on DFT calculations they simulate the IRAS spectrum for the (3×3) -7NO structure and base their conclusion on the comparison between the experimental data and the DFT calculations. The relative amplitudes of the two peaks in the spectra are indeed similar (14% error), but the DFT-simulated spectrum finds a shift of 72 cm^{-1} for the low frequency mode, which is in poor agreement with the experimentally found shift of only 4 cm^{-1} . Based on this and the present STM and DFT findings, the proposed (3×3) -7NO structure should thus be discarded. Another explanation for the observed PM-IRAS data must be found which is compatible with the geometry of the (2×2) -3NO structure observed by STM. The change in the PM-IRAS spectrum could perhaps be due to loosely bound second layer NO which does not appear in the STM due to a high mobility, to subtle changes

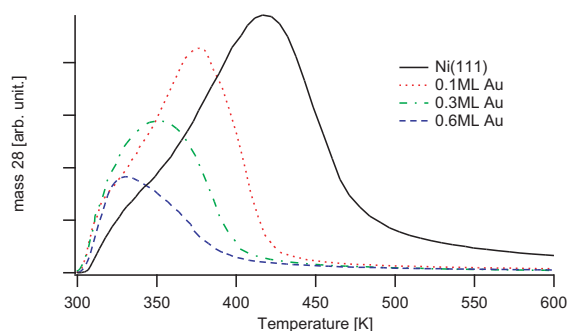


Figure 4.4: CO TPD spectra for Au/Ni(111) surface alloys with varying concentrations of Au.

in the binding geometry, or to a reconstruction of the substrate possibly induced by subsurface species. These suggestions are mere speculations, and the reconciliation of the spectroscopic data with the STM data and DFT calculations will most likely require more experimental and theoretical work, preferably by complimentary techniques.

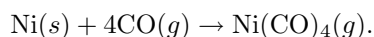
4.2.3 CO on Au/Ni(111)

The two previous sections were concerned with the adsorption of a gas molecule on a clean metal surface, and it was shown that the adsorption structures formed at high pressures and room temperature could also be found at low temperature and low pressure. The situation is, however, more complicated for the adsorption on a two-component surface, such as an alloy surface. In this case the high gas pressure may cause a compositional change in the surface layers due to a higher binding of the adsorbate to one of the components of the alloy as compared to the other. Christoffersen *et al.* used Monte Carlo simulations to describe the O₂ and CO-induced surface segregation of Ru in Pt-Ru alloy particles [201], and Greeley *et al.* studied the stability of a large number of bimetallic, near surface alloys in a H₂ atmosphere [46]. There has, however, only been very little experimental interest in the study of the adsorbate-induced segregation, and the only work I am aware of is that of Nerlov *et al.* in which their results for the methanol synthesis on Ni/Cu surfaces were rationalized in terms of a CO-induced segregation of Ni [202].

The Au/Ni(111) alloy has already been shown to be a more carbon resistant steam reforming catalyst than pure Ni [114] and to inhibit carbon formation from the dissociation of CO on Ni(111) (section 3.3.1). As another characterization of the change in the reactivity of the Ni(111) caused by the alloying with Au, a series of TPD measurements were performed on Au/Ni(111) surface alloys with varying amounts of Au. Fig. 4.4 clearly shows that an increase in the concentration of Au in the topmost layer causes a shift towards lower temperatures in the TPD spectra which shows that the CO binding energy is decreasing. These data are in excellent agreement with similar measurements

performed by Holmblad *et al.* [115]. The ability to control the CO binding energy is very interesting in relation to catalysis as also discussed for the Cu/Pt(111) alloy. One can hope that an optimal amount of Au alloyed into the topmost layer of the Ni(111) surface will decrease the reactivity of Ni in such a way that it resembles that of Pt. The development of such “cheap platinum” would have an enormous impact on the catalytic market, since platinum is perhaps the most versatile catalyst material and the rate of production of platinum cannot keep up with the present demand. The high costs of platinum is also a limiting factor in the competitiveness of the hydrogen technology, which currently strongly depends on the use of platinum catalysts. It is thus of interest both from a fundamental and a more technological point of view, to study the Au/Ni(111) surface alloy at reaction conditions. For this purpose we chose to study the influence of high pressures of CO on the Au/Ni(111) alloy, since CO is one of the most reactive gases encountered in the discussed catalytic processes and thus the one most likely to cause changes in the surface composition.

The fact that high pressures of CO indeed lead to severe morphological changes of the Au/Ni(111) surface alloys can be seen from the STM movies obtained by a repeated scanning of the same area in a CO background. Single images taken from such a movie recorded at room temperature and a CO pressure of 10 torr are shown in fig. 4.5(a-f).¹ The Au/Ni(111) sample was prepared by the evaporation of 0.3 ML Au onto Ni(111) at a substrate temperature of 800 K. As described in section 3.3.1 this causes Au atoms to substitute Ni atoms in the topmost layer. The movie shows a $1000 \times 1000 \text{ \AA}^2$ area of the surface, and therefore the single atoms are not seen; an atomically resolved STM image of the Au/Ni(111) surface alloy prior to CO exposure is inserted in fig. 4.5(a) and here the single Au atoms are clearly visible as dark depressions. Once CO is introduced into the chamber, holes start to develop at the step edges and the step edges begin to move across the surface while small clusters are nucleated behind them. The movement of the step edges is apparently induced by the removal of atoms from the topmost layer, and we suggest that the mechanism is the removal of the Ni atoms through the formation of Ni carbonyl:



Nickel carbonyl is known to form on Ni surfaces at temperatures below $\sim 525 \text{ K}$ and CO pressures above $\sim 0.1 \text{ mbar}$ [203]. Furthermore, it has been shown that the rate of carbonyl formation is greatly enhanced on Ni thin films with a high step density [204], which corresponds well with the fact that we observe the removal of surface atoms only at the step edges. The proposed model is therefore that Ni surface atoms react with gas phase CO molecules to form carbonyl which is volatile at room temperature and thus leaves the surface. The Au atoms are left on the surface and are dragged along the moving step edge until a critical size is achieved and a Au cluster is nucleated.

The proposed model was further supported by STM measurements carried out after a prolonged CO exposure at high pressure. Fig. 4.5(g) shows a Au/Ni(111) surface after exposure to 1 bar CO at room temperature, and as in the end of the movie obtained at 10 torr (fig. 4.5(f)) the surface is seen to be fully covered with clusters. A height analysis

¹The full-length movie can be seen at <http://www.phys.au.dk/spm/movies/carbonyl.mpg>

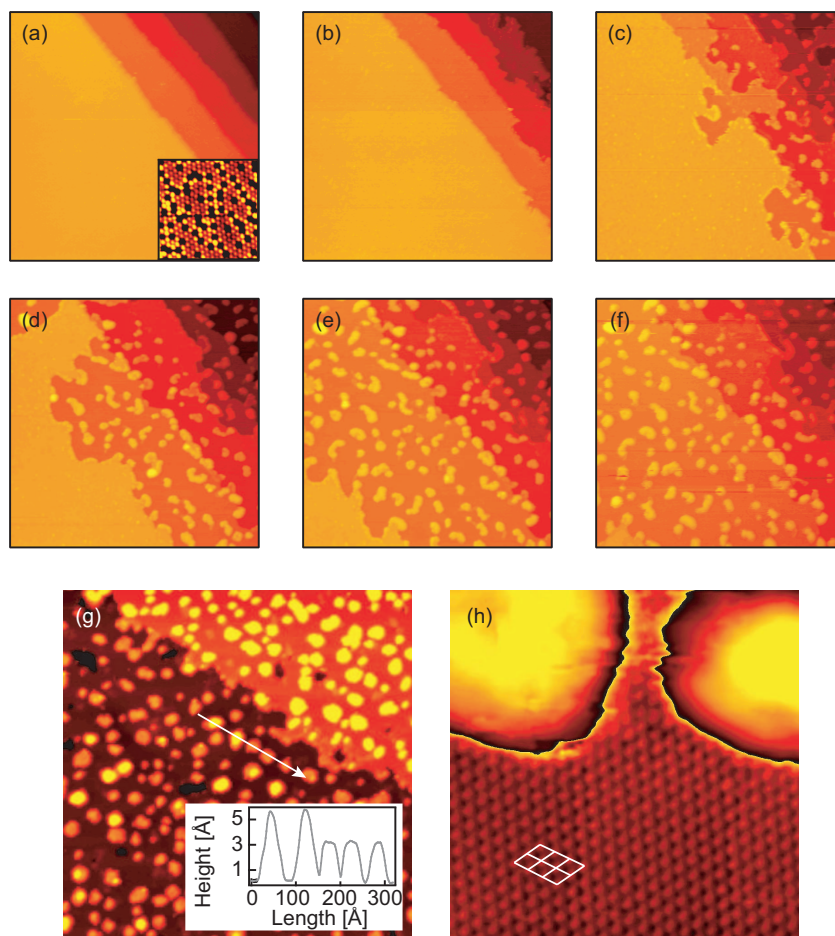


Figure 4.5: **(a)-(f)** STM images ($1000 \times 1000 \text{ \AA}^2$) of a Au/Ni(111) surface alloy after exposure to 10 torr CO for 0 min **(a)**, 25 min **(b)**, 50 min **(c)**, 75 min **(d)**, 100 min **(e)**, and 125 min **(f)**. The small insert in **(a)** is an atomically resolved STM image ($50 \times 50 \text{ \AA}^2$) of the as-prepared Au/Ni(111) surface alloy. **(g)** The Au/Ni(111) surface after exposure to 1 bar of CO at room temperature. The arrow indicates the direction of the inserted line scan. **(h)** A zoom-in ($60 \times 60 \text{ \AA}^2$) on the area between the Au clusters reveals a clean Ni(111) substrate.

of the clusters show that most islands have a height of 3.2 Å, and $\sim 10\%$ have a height of 5.6 Å (see the line scan in fig. 4.5(g)). These heights are identical to the heights of single and double-layer Au islands on Ni(111) as measured by STM. Furthermore, there is a good agreement between the coverage of the amount of Au evaporated and the coverage as calculated by assuming that the clusters consist of Au. Finally, annealing of the sample after the exposure to CO leads to the formation of a surface alloy similar to that observed prior to the CO exposure. Based on these observations it can thus be concluded that the Au/Ni(111) surface alloy undergoes a phase separation into Au clusters dispersed on a pure Ni(111) substrate at high pressures of CO at room temperature, and the mechanism behind the phase separation is the removal of the Ni atoms in the topmost layer through the formation of Ni carbonyl.

It is interesting to note from the STM data that the carbonyl formation stops almost completely once the first layer has undergone a complete phase separation, which indicates that the rate of carbonyl formation is much slower on the bare Ni(111) surface than on the Au/Ni(111) surface alloy. This was confirmed by a long-time exposure of the clean Ni(111) surface to CO at room temperature where the rate was too low to be measured by STM. The destabilization of the Ni atoms towards the carbonyl formation caused by the presence of the Au atoms was indeed confirmed by DFT calculations by Bjørk Hammer and Thorbjørn M. Pedersen as discussed in ref [VI].

The finding that high pressures of CO induce a phase separation of the Au/Ni(111) surface alloy provides an example of a fundamental pressure gap, and it underlines the importance of studying the stability of alloy surfaces at reaction conditions before extrapolating results based on UHV experiments. These experiments, however, only tested the influence of CO, and the presence of other gases or impurities or an increase in the temperature may prevent the formation of carbonyl. Preliminary experiments have indeed indicated that preexposure of the Au/Ni(111) surface alloy to H₂O prevents the formation of Ni carbonyl, most likely due to OH groups adsorbed at the step edges. The question of surface stability is particularly important for two-component (or multi-component) systems, but it will be shown in the next section that also for the pure elements the surfaces may change at high pressures, i.e., due to the formation of a surface oxide.

4.3 Oxide formation

The oxidation of metal surfaces is best known as corrosion and is most often an unwanted reaction, although in some cases it can be used for protective coatings of metals. In catalysis, and in particular for oxidation processes, the active phase of a metal may be an oxide phase as in, e.g., the already discussed case of CO oxidation on Ru(0001), where the active phase is a RuO₂(110) surface oxide [160, 161]. It is suggested that oxidation processes takes place on metal oxides via the Mars and van Krevelen mechanism in which, e.g., CO reacts with O atoms in the oxide to form CO₂ and the created O-vacancies are replenished by O₂ from the gas phase [205]. It is not clear whether the active phase of Pt during CO oxidation is an oxide or not. It has been speculated that the oscillations in the rate of CO oxidation over Pt catalysts are induced by an ox-

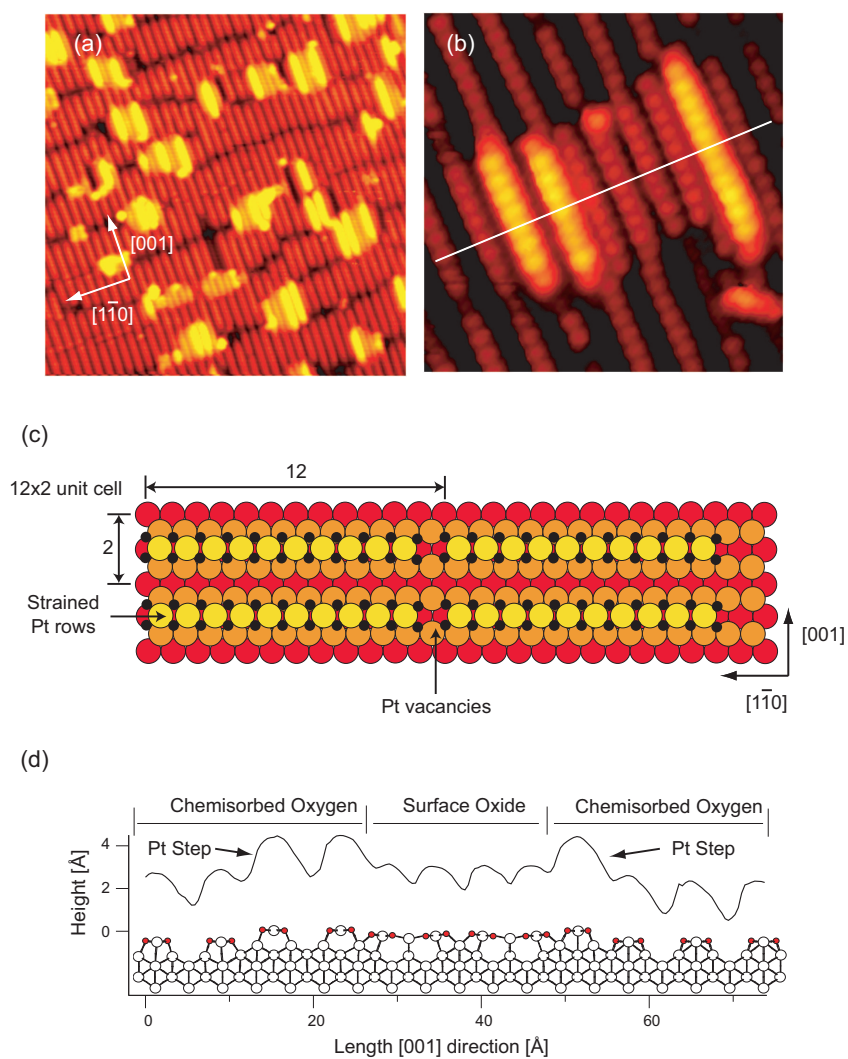


Figure 4.6: **(a)** STM image ($300 \times 300 \text{ \AA}^2$) of Pt(110) after exposure to atomic O at 500 K. **(b)** Atomically resolved STM image ($60 \times 60 \text{ \AA}^2$) of an oxide island. The white line indicates a line scan. **(c)** Ball model of the (12×2) chemisorption structure of O on Pt(110). **(d)** Comparison between the line scan across the oxide island and the oxide structure found from the DFT calculations.

idation/reduction of the Pt surface [206], and recently Hendriksen *et al.* used *in-situ* HP-STM to correlate a high CO oxidation rate over Pt(110) with a roughening of the surface which they speculated to be due to the formation of a surface oxide [180]. Hendriksen *et al.* were, however, not able to obtain atomic resolution and therefore they could not provide any structural characterization of the rough surface. Motivated by this we have studied the oxidation of Pt(110) by exposing the surface to high pressures of O₂ as well as by exposing it to atomic O.

4.3.1 O/Pt(110)

When the Pt(110) surface was exposed to either a high pressure of molecular O₂ or atomic O at room temperature, a very disordered structure was observed by STM. When the sample was subsequently annealed or when the surface was exposed to atomic O at 500 K or molecular O₂ at 355 K, a surface with ordered structures appeared in the STM, as seen in fig. 4.6(a) in which two predominant structures are found: 1) a structure consisting of bright lines aligned along the [001] direction of the rows of the Pt(110) missing row reconstructed surface; 2) a number of small islands exist on top of the striped structure. The exposure of the Pt(110) surface to atomic O at 600 K led to a surface completely covered by the striped structure, which, inspired by earlier work of Walker *et al.* [207] and Helveg *et al.* [208], was identified as a chemisorption phase with O atoms occupying every fcc sites along the protruding Pt rows (see fig. 4.6(c)). The atoms in the protruding Pt row are strained by $\sim 14\%$ compared to the substrate, which is accommodated by the creation of 2 Pt vacancies per 12 Pt atoms, and the structure is described by a (2×12) unit cell. The observed chemisorption structure is very similar to the (10×2) structure observed for O/Rh(110) [209].

Fig. 4.6(b) shows an atomically resolved STM image of one of the islands formed after exposure to atomic O at 500 K, and it is seen that the structure of the islands is quite different from that of the (12×2) structure of the substrate. The islands also have a row structure, but two different rows can be distinguished from their different apparent heights, and the inner rows were found to be compressed $\sim 29\%$ in the $[1\bar{1}0]$ direction (perpendicular to the protruding Pt rows). The imaging of these islands was only possible at a tunneling voltage $\gtrsim 1$ V which is an experimental indication of the presence of a band gap, and for this reason we associate the islands with an oxide structure. This assumption was indeed corroborated by extensive DFT calculations carried out by Wei-Xu Li, Thorbjørn M. Pedersen, and Bjørk Hammer. They investigated several structures with strained Pt rows and found a very stable surface oxide structure in which the rows were strained 25%, in good agreement with the experimentally found $\sim 29\%$. The agreement between the STM data and the DFT model is illustrated in fig. 4.6(d) where the strained rows of the islands, as observed by STM, are seen to correspond to the protruding Pt atoms of the surface oxide proposed by the DFT calculations. The bright rows at the edge of the islands are interpreted as extra rows of Pt atoms with the same (12×2) chemisorption phase as the substrate based on the fact that these rows are always found to be shifted $1/4$ of the unit cell in the $[1\bar{1}0]$ direction. Within the proposed model the Pt atoms in the islands are also found to correspond to the number of Pt vacancies created by the chemisorption of O.

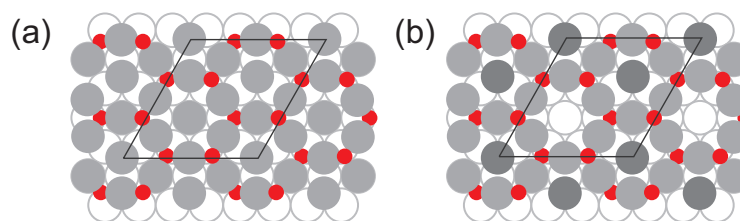


Figure 4.7: Ball models of the Ag(111) surface oxide structures proposed by (a) Rovida *et al.* and Campbell, and (b) by Carlisle *et al.* Ag atoms are grey and oxygen atoms are red. The dark grey atoms are the Ag adatoms imaged in by STM according to the model of Carlisle *et al.*

The fact that the oxide islands indeed represent a new structure was confirmed by TPD measurements carried out by Ebbe K. Vestergaard and Lars Österlund. They observed five different peaks in the TPD spectra, three of which they could assign to the three structures observed by STM: the disordered structure (formed after O exposure at room temperature), the oxide islands, and the (12×2) chemisorption phase. They furthermore found that the O-coverage associated with the disordered structure increased to as much as 8.7 ML in these experiments, for which reason this structure must be related to the formation of a bulk oxide.

Based on the DFT calculations it was found that in thermodynamical equilibrium only the chemisorption phase or the bulk oxide should exist, which means that the observed oxide islands are only a metastable structure. This is in agreement with the observation that the islands could only be prepared by O exposure at intermediate temperatures. The bulk oxide formed at room temperature might be the “rough phase” observed by Hendriksen *et al.* during the periods of the high CO oxidation rate on Pt(110) in their HP-STM experiments [180]. However, they report that the rough surface is only observed during CO oxidation and not in an O₂ atmosphere. The characterization of the active phase or phases of Pt during CO oxidation therefore still remains an open question. The present data show that, at least for the (110) facet, one should not expect to find an ordered surface oxide.

4.3.2 O/Ag(111)

Even though Ag is a noble metal it is an excellent oxidation catalyst, and Ag catalysts are used for the partial oxidation of methanol into formaldehyde and for the epoxidation of ethylene [210]. These reactions both take place under high pressures of oxygen, for which reason the interaction of high pressures of oxygen with Ag, and in particular the low surface energy (111) facet, has been studied for more than thirty years [211], and as such it was one of the very first surface oxides to be recognized. Despite three decades of experimental and theoretical efforts the structure of the active phase of Ag(111) during the oxidation processes is still debated [212, 213].

The first characterization of an oxide structure on Ag(111) was carried out by Rovida

et al. who observed a sharp 4×4 peak with LEED upon the exposure of Ag(111) to relatively high pressures of oxygen (up to 1 torr) [211, 214]. Rovida *et al.* furthermore noted that the unit cell of the (111) surface of bulk Ag_2O oxide deviates less than 1% from a 4×4 unit cell of Ag(111), and based on this observation they proposed a structural model with a thin layer of $\text{Ag}_2\text{O}(111)$ on top of the Ag(111) surface. Campbell made extensive measurements on the O/Ag(111) system, and in particular he could estimate the coverage of O in the $p(4 \times 4)$ structure to be close to $3/8$ which would be the coverage of a single trilayer of Ag_2O [215]. The model of Rovida and Campbell is shown in fig. 4.7(a). Carlisle *et al.* were the first to study the $p(4 \times 4)$ oxide phase with STM, and based on their observation of a honeycomb-like structure they proposed a revised version of the model of Rovida and Campbell [216, 217]. The model suggested by Carlisle (fig. 4.7(b)) is also based on a trilayer of Ag_2O , but every third Ag adatom in the Rovida-Campbell model is missing, i.e., the ones sitting in atop positions which gives a $\text{Ag}_{1.83}\text{O}$ stoichiometry. The $\text{Ag}_{1.83}\text{O}$ model of Carlisle *et al.* was supported by simulated STM images, and later DFT calculations found this structure to be favored over a number of other investigated structures [218–220]. At this point it seemed that the structure of the $p(4 \times 4)$ phase was fully understood, and studies on the epoxidation of ethane based on the $\text{Ag}_{1.83}\text{O}$ model were published [221]. More extensive DFT calculations have, however, shown that several other structures with a similar or even higher stability than the $\text{Ag}_{1.83}\text{O}$ structure can be found, and in particular the Ag adatoms that were suggested to be imaged by STM are unstable towards bulk diffusion [212]. From these theoretical findings it is highly unlikely that the $p(4 \times 4)$ structure observed to exist as almost complete and perfect overlayers could origin from the metastable $\text{Ag}_{1.83}\text{O}$ structure. Furthermore recent XDS experiments on the $p(4 \times 4)$ structure [213] agree very poorly with the $\text{Ag}_{1.83}\text{O}$ model of Carlisle *et al.* Based on these recent findings it seems that the structure of O on Ag(111) is still far from understood, and motivated by this we have performed STM measurements on this adsorption system.

The Ag(111) surface was studied both after exposure to molecular O_2 in the HP-cell and after exposure to atomic oxygen in the UHV chamber. A major new finding in the present work is that we find several different phases besides the well-studied $p(4 \times 4)$ structure. Fig. 4.8 shows six different phases of O/Ag(111) which have all been prepared by exposure to atomic oxygen. Panel (a) shows single O atoms chemisorbed on Ag(111) which were also observed by Carlisle *et al.* [216, 217]. The structure in panel (e) is the well-known $p(4 \times 4)$ structure, and also the structure in panel (b) was observed by Carlisle *et al.*, who ascribed it to the decomposition of the $p(4 \times 4)$ structure. The structure in panel (b) takes on a rectangular unit cell and can therefore not be described within the Woods notation for hexagonal surfaces. It can be described either in matrix form as $\begin{pmatrix} 4 & 0 \\ 5 & 5 \end{pmatrix}$ or, adapting the notation of Biberian *et al.* for a rectangular structure on fcc(111) surfaces [222], as a $(4 \times 5\sqrt{3})\text{rect}$ structure. The remaining three structures of fig. 4.8 have not been reported in the literature. Panel (c) shows a structure described as $\begin{pmatrix} 3 & 0 \\ 1 & 4 \end{pmatrix}$ in matrix form or with a $c(3 \times 5\sqrt{3})\text{rect}$ unit cell. For simplicity I shall use the term “triangle” structure for the $(4 \times 5\sqrt{3})\text{rect}$ structure and the term “long-

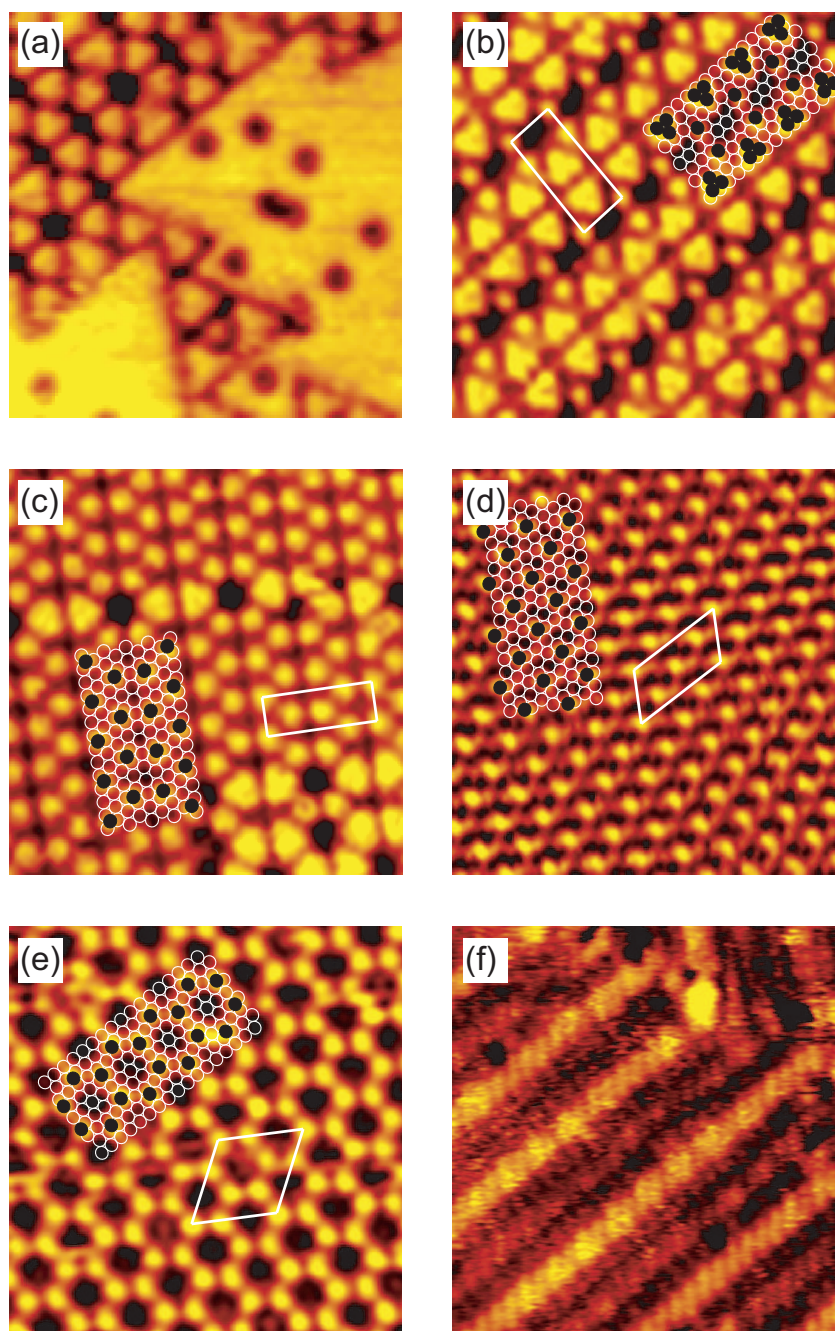


Figure 4.8: STM images (all $89 \times 90 \text{ \AA}^2$) of the different phases of O/Ag(111). **(a)** Single O atoms on Ag(111). **(b)** The triangle structure $((4 \times 5\sqrt{3})\text{rect})$. **(c)** The long-stretched structure $(c(3 \times 5\sqrt{3})\text{rect})$. **(d)** The $c(4 \times 8)$ structure. **(e)** The $p(4 \times 4)$ structure. **(f)** The striped structure. For the structures in (b)-(e) a ball model and a unit cell have been indicated in STM images. Note that the balls indicate the protrusions observed in the STM images and should not to be viewed as a model of the atomic structure.

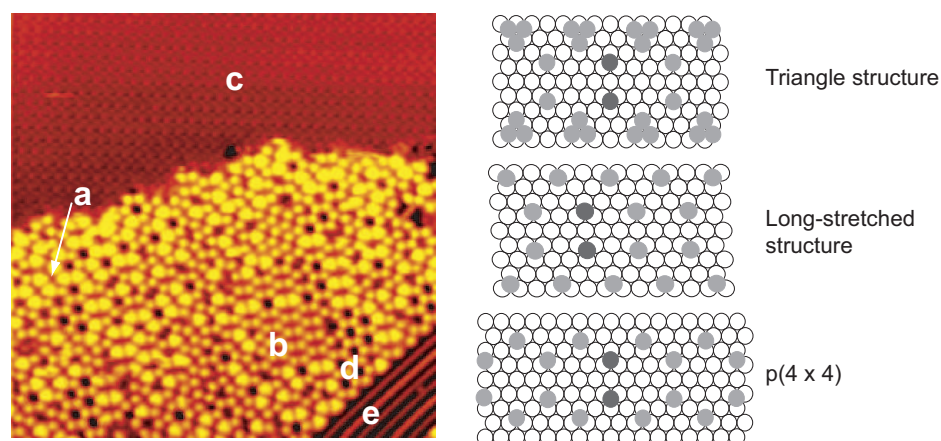


Figure 4.9: **Left:** STM image ($300 \times 300 \text{ \AA}^2$) showing the coexistence of **(a)** the triangle structure, **(b)** the long-stretched structure, **(c)** the $c(4 \times 8)$ structure, **(d)** the $p(4 \times 4)$ structure, and **(e)** the striped structure. **Right:** Ball models showing the common building block (dark grey balls) of the triangle, the long-stretched structure, and the $p(4 \times 4)$ structures.

stretched” structure for the $c(3 \times 5\sqrt{3})\text{rect}$ structure. In panel (c) the long-stretched structure is found to coexist with small patches of the triangle structure, which was very often observed in the STM images. The structure in panel (d) is a commensurate $c(4 \times 8)$ structure. The final structure which is shown in panel (f) consists of stripes running along one of the directions of the close-packed rows on the Ag(111) surface. It is generally very hard to achieve good resolution on the striped phase and the periodicity of the rows is not constant, for which reason no unit cell can be given for this structure. The striped structure is predominantly observed at high oxygen coverages, for which reason it may be speculated that it is the onset of the formation of a bulk oxide.

Whereas the single, chemisorbed O atoms are only found at low O coverages and the striped structure only at high coverages, the rest of the structures (fig. 4.8(b-e)) cannot easily be placed in a phase diagram. From the experiments with molecular O_2 the triangle structure was found to form at 1 torr and 500 K, and the long-stretched structure (co-existing with smaller areas of the triangle structure) to form at 3 torr and 500 K. The formation of the (4×4) structure required both higher temperatures and higher pressures, and it was found to form at 10 torr and 550 K. These measurements indicate that the O content increases in the order: triangle structure, long-stretched structure, and (4×4) , and furthermore that the formation of the (4×4) structure has a higher activation energy than the two other structures. The experiments with an exposure of Ag(111) to atomic O, however, showed that the phase diagram for O/Ag(111) is indeed rather complicated since the different phases in general are observed to coexist. The complexity of separating the different structures in a phase diagram is illustrated in fig. 4.9 where all of the observed phases, except for single O atoms, are found within an area of only 300×300

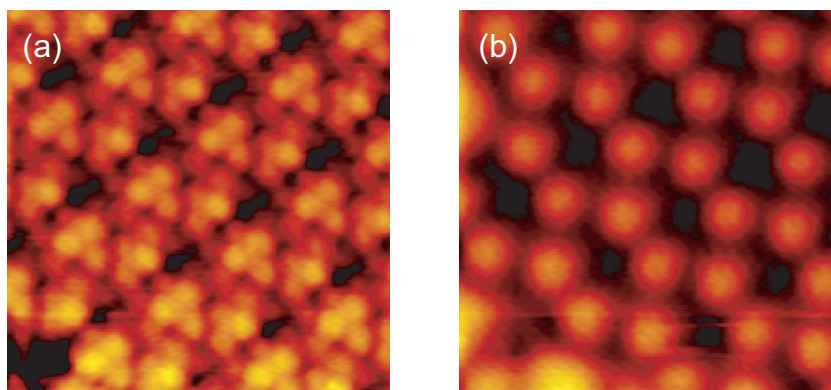


Figure 4.10: Simultaneously acquired STM images ($50 \times 50 \text{ \AA}^2$) of the long-stretched structure at (a) $V_t = -35.1 \text{ mV}$, $I_t = -0.42 \text{ nA}$, and (b) $V_t = -1790.1 \text{ mV}$, $I_t = -0.50 \text{ nA}$.

\AA^2 . At this point it should be stressed that the exposure to atomic O cannot easily be converted into an equivalent pressure of molecular O_2 for at least two reasons. First, the local pressure of atomic O at the sample was not known since only the background pressure could be measured, and second, the use of atomic O may completely change the kinetics as compared to those existing at a high pressure of O_2 . The experiments with atomic O, however, show that the different structures of O/Ag(111) must be close to each other in terms of surface energy, and that the phase diagram for O/Ag(111) is indeed more complicated than hitherto assumed.

Besides the complexity of the phase diagram, another thing that can be seen in fig. 4.9 is the apparent similarity between the triangle structure, the long-stretched structure, and the $p(4 \times 4)$ structure. In particular the three structures have the same corrugation in the STM images, and furthermore they seem to have a common building block consisting of two protrusions. Since the structures are very close in energy, it seems reasonable to expect that they should have some common structural features. A model of one of these structures should thus be able to also explain the other models, and this could potentially be a strongly validating factor for such a model.

The STM images in fig. 4.8 are not truly atomically resolved and it is thus hard to base a structural determination on such images. The experience of the $\text{Ag}_{1.83}\text{O}$ model proposed by Carlisle *et al.* clearly shows that such an approach might indeed lead to erroneous conclusions. Fig. 4.10 shows two STM images of the long-stretched structure that have been obtained simultaneously at different tunneling voltages, V_t , and tunneling currents, I_t . The image in fig. 4.10(b) is a typical image in which the building blocks of the long-stretched structure are imaged as single protrusions. The image in fig. 4.10(a), on the other hand, shows three distinct peaks in each of these building blocks. Although the STM images should not be interpreted as topographic maps, and although O atoms are inherently difficult to image with STM, the high-resolution image is certainly a strong indication that the building block of the long-stretched structure,

and hence also of the triangle structure and the $p(4 \times 4)$ structure, has a triangular shape, and one might speculate that the building block is based on a Ag trimer. This trimer building block is not compatible with the model of Rovida *et al.* and Campbell, and this is further evidence that their model needs to be revised. STM images like the one in fig. 4.10(a) and images with even higher resolution may prove capable of providing the necessary input to a new model that can be shown, primarily by DFT calculations, to be more stable than the wide range of structures that have been studied so far. Kresse *et al.* recently combined the information from high resolution STM images obtained with different tunneling parameters with DFT calculations to solve the structure of the aluminum oxide film on NiAl(110) [223]. Angelos Michaelides in the group of Matthias Scheffler is currently performing extensive DFT calculations on structures inspired by the common building block found in the present STM measurements, and hopefully this will lead to a comprehensive understanding of the oxide structure on Ag(111).

CHAPTER 5

Summary and outlook

A number of surface science studies on model systems relevant to heterogeneous catalysis has been presented in the present thesis. The overall approach in the presented studies has been the use of high-resolution and high-pressure scanning tunneling microscopy (STM) measurements in conjunction with density functional theory (DFT) calculations. The work can be grouped into two kinds of studies focusing on either the chemical properties of surfaces or on the surface structure at elevated gas pressures, and here I shall give a brief summary of the main scientific findings of my work.

In section 3.2 the active sites were identified for three specific surface reactions. For a hydrodesulphurization model catalyst consisting of MoS₂ nanoclusters grown on Au(111), a new type of active site for the C-S bond-cleavage of thiophene was found in the form of a one-dimensional, localized metallic edge state. The step edge atoms of Ni(111) were shown to have a much higher activity for the dissociation of both CO and ethylene as compared to the regular atoms of the (111) facet. In the case of ethylene decomposition, DFT calculations also showed that the lower activation barrier at the step edge as compared to the terrace is much more pronounced for the C-C bond-breaking than for the C-H bond-breaking. This implies that the step edge atoms of Ni(111) are a decisive factor for the bond-breaking selectivity between the initial dehydrogenation and dissociation.

The role of the step edge atoms on Ni(111) was further investigated in section 3.3, where it was demonstrated that the very reactive step edge atoms could selectively be blocked by the deposition of small amounts of Ag, Au, or S which all preferentially nucleate along the step edges of Ni(111). The concept of selective step edge blocking was tested on a high-surface-area AgNi catalyst which indeed showed a much lower activity for C-C bond-breaking in ethane hydrogenolysis experiments in agreement with

the predictions of the STM experiments and DFT calculations. Another approach to modifying the reactivity of a surface was pursued by the formation of a Cu/Pt(111) surface alloy. Using a combination of STM, TPD, XPS, and DFT a subsurface alloy was characterized and shown to have altered surface properties compared to clean Pt(111). In particular TPD measurements showed that the binding energy of CO on Pt(111) is reduced upon the incorporation of subsurface Cu atoms, and it was suggested that the Cu/Pt(111) subsurface alloy may be an improved catalyst for the water-gas shift (WGS) reaction.

Chapter 4 was devoted to studies at high pressures aiming at bridging the pressure gap between the conditions of standard surface science experiments and those of an operating catalyst. In the first of the studies the adsorption structure of CO on Pt(111) at room temperature was determined at elevated pressures. CO was found to adsorb in a hexagonal structure leading to the formation of a moiré superstructure, and the CO layer was reversibly compressed over the entire range from 10^{-6} torr to atmospheric pressures leading to a continuous increase in the CO coverage. Likewise, the adsorption structure of NO on Pd(111) was studied at room temperature and up to atmospheric pressure. A (2×2) -NO structure was identified which corresponds to a similar adsorption structure found in low temperature and low pressure experiments. On this basis the existence of a pressure gap for the NO/Pd(111) adsorption system was discarded. The studies of CO/Pt(111) and NO/Pd(111) both show that the structures formed at high pressures are similar to structures also formed at low temperatures and pressures, although some differences were found for the case of CO/Pt(111). These differences were ascribed to kinetic and/or entropic effects and are thus due to a temperature gap rather than a pressure gap.

For a Au/Ni(111) surface alloy the exposure to elevated pressures of CO led to severe morphological changes. The surface was observed in real time STM movies to phase separate into small Au clusters on a pure Ni(111) substrate. The mechanism behind the CO-induced phase separation was found to be the formation of volatile Ni carbonyl species which remove the Ni atoms in the topmost layer of the Au/Ni(111) surface alloy while leaving the Au atoms to nucleate into small islands on the surface. This provides an example of a surface phenomenon at high pressure which indeed would be very difficult to extrapolate from experiments performed at low pressures.

The final two studies presented in this thesis concern the formation of surface oxides on the Pt(110) and Ag(111) surfaces. In both studies surface oxides were formed by an exposure to high pressures of molecular oxygen as well as by an exposure to atomic oxygen. On Pt(110), islands of a surface oxide coexist with a high coverage chemisorbed oxygen phase. The surface oxide was only formed under certain conditions and by atomic oxygen, and the surface oxide was concluded to be a metastable phase. For oxygen on Ag(111) at least six different phases were identified, and at most temperature and pressure conditions examined two or more of these phases were found to coexist, which points to a more complex phase diagram for this system than hitherto assumed. From the STM images a common building block is suggested for at least three of the structures including the highly debated $p(4 \times 4)$ structure. High resolution images reveal a substructure of the common building block which is incompatible with previously suggested models of the $p(4 \times 4)$ structure.

The work presented in this thesis nicely illustrates that STM is indeed a valuable technique for the study of model systems relevant to heterogeneous catalysis. Besides providing new insight into some interesting problems relating to catalysis, the present works also leaves some open questions which calls for a continuation of the work. One of the natural directions to pursue is the combination of the characterization of catalyst model systems with reactivity measurements. A setup for this purpose has been developed in our group and initial measurements have been performed. This reaction cell uses a quartz capillary tube with a small leak connected to a differentially pumped mass spectrometer to detect both the reactants and products close to the surface of the sample in a small, variable temperature and pressure flow-reactor cell. Potentially, this setup can provide a very important link between the surface structure and the reactivity which is one of the key issues in the understanding of heterogeneous catalysis. It would indeed be very interesting to use the reaction cell to perform reactivity studies on some of the new two-component surface structures that have been described here, i.e., the Ag/Ni(111), Au/Ni(111), and Cu/Pt(111) surfaces. In particular the possibility of using Ag/Ni(111) or Au/Ni(111) as “cheap platinum” for, e.g., the anode reaction in low temperature fuel cells is appealing. The feasibility of this may be explored through the study of the hydrogen-deuterium exchange reaction which is an indicator of the activity towards hydrogen dissociation. These experiments may be carried out with a pure mixture of H₂ and D₂ or with a mixture of CO, H₂O, H₂, and D₂ to mimic the conditions found at a fuel cell anode. For the Cu/Pt(111) subsurface alloy it is of course a priority to measure the (WGS) activity in order to investigate the predictions of DFT which point to the Cu/Pt(111) surface as a better WGS catalyst than both pure Cu and pure Pt.

A further perspective of the present work is to extend the model systems from single-crystal surfaces to supported nanoclusters, to bridge the materials gap towards real catalysts, as it has been done for the MoS₂ hydrodesulphurization catalyst. By means of the high-pressure STM, the sintering processes, phase separation, reshaping of the nanoclusters, and more effects can be investigated at reaction conditions and correlated to reactivity measurements. For this purpose the use of atomic force microscopy (AFM) may be favored over STM since this would enable the study of insulating supports which are widely used in catalytic applications. Completely new, and potentially catalytically active surface structures may also be investigated, and in particular one could try to mimic the highly efficient catalysts found in nature by synthesizing organo-metallic surface structures which resemble the active centers of enzymes catalyzing, e.g., the production of hydrogen or ammonia. New properties may be found for such systems which are completely different from the properties known from the traditional catalysts based on transition metals, and this could potentially lead to major a breakthrough in the development of new catalysts for the future.

Bibliography

- [1] V. Smil, "Detonator of the population explosion", *Nature* **400**, 415 (1999).
- [2] <http://nobelprize.org/chemistry/laureates/1918>.
- [3] <http://nobelprize.org/chemistry/laureates/1931>.
- [4] J. Sinfelt, "Role of surface science in catalysis", *Surf. Sci.* **500**, 923 (2002).
- [5] C. Jacobsen, I. Schmidt, A. Boisen, and K. Johannsen, *Katalytisk kemi* (Holte Bogtrykkeri A/S, Lyngby, Denmark, 2002).
- [6] A. McNaught and A. Wilkinson, *The IUPAC Compendium of Chemical Terminology* (Blackwell Science, Cambridge, 1997).
- [7] G. A. Somorjai, *Surface Chemistry and Catalysis* (Wiley, New York, 1994).
- [8] G. Ertl, "Heterogeneous catalysis on atomic scale", *J. Molec. Catal. A* **182-183**, 5 (2002).
- [9] D. W. Goodman, "Model Studies in Catalysis Using Surface Science Probes", *Chemical Review* **95**, 523 (1995).
- [10] D. W. Goodman, "Correlations between Surface Science Models and "Real-World" Catalysts", *J. Phys. Chem.* **100**, 13090 (1996).
- [11] A. K. Santra and D. W. Goodman, "Oxide-supported metal clusters: models for heterogeneous catalysts", *J. Phys - Cond. Mat.* **15**, R31 (2003).
- [12] C. B. Hatfield, "Oil back on the global agenda", *Nature* **387**, 121 (1997).
- [13] J. A. Turner, "A Realizable Renewable Energy Future", *Science* **285**, 687 (1999).
- [14] M. Grätzel, "Photoelectrochemical cells", *Nature* **414**, 338 (2001).
- [15] O. Khaselev and J. A. Turner, "A Monolithic Photovoltaic-Photoelectrochemical Device for Hydrogen Production via Water Splitting", *Science* **280**, 425 (1998).
- [16] R. D. Cortright, R. R. Davda, and J. A. Dumesic, "Hydrogen from catalytic reforming of biomass-derived hydrocarbons in liquid water", *Nature* **418**, 964 (2002).
- [17] Y. Asada and J. Miyake, "Photobiological Hydrogen Production", *J. Biosci. Bioeng.* **88**, 1 (1999).
- [18] L. Schlapbach, "Hydrogen as a fuel and its storage for mobility and transport", *MRS Bull.* **27**, 675 (2002).
- [19] R. S. Irani, "Hydrogen storage: High-pressure gas containment", *MRS Bull.* **27**, 680 (2002).
- [20] J. Wolf, "Liquid-hydrogen technology for vehicles", *MRS Bull.* **27**, 684 (2002).
- [21] L. Schlapbach and A. Züttel, "Hydrogen-storage materials for mobile applications", *Nature* **414**, 353 (2001).
- [22] R. C. Bowman and B. Fultz, "Metallic Hydrides I: Hydrogen storage and other gas-phase applications", *MRS Bull.* **27**, 688 (2002).

- [23] B. Bogdanovic and G. Sandrock, "Catalyzed complex metal hydrides", *MRS Bull.* **27**, 712 (2002).
- [24] B. Bogdanovich, M. Felderhoff, S. Kaskel, A. Pommerin, K. Schlichte, and F. Schüth, "Improved Hydrogen Storage Properties of Ti-doped Sodium Alenate Using Titanium Nanoparticles as Doping Agents", *Adv. Mat.* **15**, 1012 (2003).
- [25] J. Chen, N. Kuriyama, Q. Xu, H. T. Takeshita, and T. Sakai, "Reversible Hydrogen Storage via Titanium-Catalyzed LiAlH_4 and Li_3AlH_6 ", *J. Phys. Chem. B* **105**, 11214 (2001).
- [26] H. Lee, J. Lee, D. Y. Kim, J. Park, Y.-T. Seo, H. Zeng, I. L. Moudrakovski, C. I. Ratcliffe, and J. A. Ripmeester, "Tuning clathrate hydrates for hydrogen storage", *Nature* **434**, 743 (2005).
- [27] L. Carrette, K. A. Friedrich, and U. Stimming, "Fuel Cells: Principles, Types, Fuels, and Applications", *ChemPhysChem* **1**, 162 (2000).
- [28] L. P. L. Carrette, K. A. Friedrich, A. Huber, and U. Stimming, "Improvement of CO tolerance of proton exchange membrane (PEM) fuel cells by a pulsing technique", *Phys. Chem. Chem. Phys.* **3**, 320 (2001).
- [29] L. Carrette, K. A. Friedrich, and U. Stimming, "Fuel Cells - Fundamentals and Applications", *Fuel Cells* **1**, 5 (2001).
- [30] E. Christoffersen, P. Liu, A. Ruban, H. L. Skriver, and J. K. Nørskov, "Anode Materials for Low-Temperature Fuel Cells: A Density Functional Theory Study", *J. Catal.* **199**, 123 (2001).
- [31] G. Binnig, H. Rohrer, C. Gerber, and E. Weibel, "Surface Studies by Scanning Tunneling Microscopy", *Phys. Rev. Lett.* **49**, 57 (1982).
- [32] F. Besenbacher, "Scanning tunnelling microscopy studies of metal surfaces", *Rep. Prog. Phys.* **59**, 1737 (1996).
- [33] E. Lægsgaard, L. Österlund, P. Thostrup, P. B. Rasmussen, I. Stensgaard, and F. Besenbacher, "A high-pressure scanning tunneling microscope", *Rev. Sci. Instrum.* **72**, 3537 (2001).
- [34] R. Wiesendanger, *Scanning Probe Microscopy and Spectroscopy* (Cambridge University Press, Cambridge, 1994).
- [35] E. Lægsgaard, F. Besenbacher, K. Mortensen, and I. Stensgaard, "A fully automated, 'thimble-size' scanning tunnelling microscope", *J. Microscop.* **152**, 663 (1988).
- [36] J. Tersoff and D. R. Hamann, "Theory and Application for the Scanning Tunneling Microscope", *Phys. Rev. Lett.* **50**, 1998 (1983).
- [37] J. Tersoff and D. R. Hamann, "Theory of the scanning tunneling microscope", *Phys. Rev. B* **31**, 805 (1985).
- [38] J. Bardeen, "Tunneling from a Many-Particle Point of View", *Phys. Rev. Lett.* **6**, 57 (1961).
- [39] N. D. Lang, "Vacuum Tunneling Current from an Adsorbed Atom", *Phys. Rev. Lett.* **55**, 230 (1985).
- [40] N. D. Lang, "Theory of Single-Atom Imaging in the Scanning Tunneling Microscope", *Phys. Rev. Lett.* **56**, 1164 (1986).
- [41] D. A. King, "Thermal desorption from metal surfaces: A review", *Surf. Sci.* **47**, 384 (1975).
- [42] P. A. Redhead, "Thermal Desorption of Gases", *Vacuum* **12**, 203 (1962).
- [43] A. M. Jong and J. W. Niemantsverdriet, "Thermal desorption analysis: Comparative test of ten commonly applied procedures", *Surf. Sci.* **233**, 355 (1990).
- [44] B. Hammer and J. K. Nørskov, "Theoretical Surface Science and Catalysis – Calculation and Concepts", *Adv. Catal.* **45**, 71 (2000).
- [45] J. Greeley, J. K. Nørskov, and M. Mavrikakis, "Electronic structure and catalysis on metal surfaces", *Ann. Rev. Phys. Chem.* **53**, 319 (2002).
- [46] J. Greeley and M. Mavrikakis, "Alloy catalysts design from first principles", *Nat. Mater.* **3**, 810 (2004).
- [47] P. Hohenberg and W. Kohn, "Inhomogeneous Electron Gas", *Phys. Rev.* **136**, B864 (1964).
- [48] W. Kohn and L. J. Sham, "Self-Consistent Equations Including Exchange and Correlation Effects", *Phys. Rev.* **140**, A1133 (1965).

- [49] R. O. Jones and O. Gunnarsson, "The density functional formalism, its applications and prospects", *Rev. Mod. Phys.* **61**, 689 (1989).
- [50] D. C. Langreth and M. J. Mehl, "Easily Implementable Nonlocal Exchange-Correlation Energy Functional", *Phys. Rev. Lett.* **47**, 446 (1981).
- [51] J. P. Perdew, J. A. Chevary, S. H. Vosko, K. A. Jackson, M. R. Pederson, D. J. Singh, and C. Fiolhais, "Atoms, molecules, solids, and surfaces: Applications of the generalized gradient approximation for exchange and correlation", *Phys. Rev. B* **46**, 6671 (1992).
- [52] J. P. Perdew, K. Burke, and M. Ernzerhof, "Generalized Gradient Approximation Made Simple", *Phys. Rev. Lett.* **77**, 3865 (1996).
- [53] Y. Zhang and W. Yang, "Comment on "Generalized Gradient Approximation Made Simple" ", *Phys. Rev. Lett.* **80**, 890 (1998).
- [54] B. Hammer, L. B. Hansen, and J. K. Nørskov, "Improved adsorption energetics within density-functional theory using revised Perdew-Burke-Ernzerhof functionals", *Phys. Rev. B* **59**, 7413 (1999).
- [55] D. Vanderbilt, "Soft self-consistent pseudopotentials in a generalized eigenvalue formalism", *Phys. Rev. B* **41**, 7892 (1990).
- [56] K. Reuter and M. Scheffler, "Composition, structure, and stability of RuO₂(110) as a function of oxygen pressure", *Phys. Rev. B* **65**, 035406 (2001).
- [57] M. W. Chase, *NIST-JANEF Thermochemical Tables*, 4th ed. (American Chemical Society, Washington, DC, 1998).
- [58] K. Reuter and M. Scheffler, "First-Principles Atomistic Thermodynamics for Oxidation Catalysis: Surface Phase Diagrams and Catalytically Interesting Regions", *Phys. Rev. Lett.* **90**, 046103 (2003).
- [59] K. Reuter and M. Scheffler, "Composition and structure of the RuO₂(110) surface in an O₂ and CO environment: Implications for the catalytic formation of CO₂", *Phys. Rev. B* **68**, 045407 (2003).
- [60] P. Stoltze, "Microkinetic simulation of catalytic reactions", *Prog. Surf. Sci.* **65**, 65 (2000).
- [61] P. Stoltze and J. K. Nørskov, "Bridging the "Pressure Gap" Between Ultrahigh-Vacuum Surface Physics and High-Pressure Catalysis", *Phys. Rev. Lett.* **55**, 2502 (1985).
- [62] K. Reuter, D. Frenkel, and M. Scheffler, "The Steady State of Heterogeneous Catalysis, Studied by First-Principles Statistical Mechanics", *Phys. Rev. Lett.* **93**, 116105 (2004).
- [63] K. Honkala, A. Hellman, I. N. Remediakis, A. Logadottir, A. Carlsson, S. Dahl, C. H. Christensen, and J. K. Nørskov, "Ammonia synthesis from first-principles calculations", *Science* **307**, 555 (2005).
- [64] T. Bligaard, J. K. Nørskov, S. Dahl, J. Matthiesen, C. H. Christensen, and J. Sehested, "The Brønsted-Evans-Polanyi relation and the volcano curve in heterogeneous catalysis", *J. Cat.* **224**, 206 (2004).
- [65] J. K. Nørskov, T. Bligaard, A. Logadottir, S. Bahn, L. B. Hansen, M. Bollinger, H. Bengaard, B. Hammer, Z. Sljivančanin, M. Mavrikakis, Y. Xu, S. Dahl, and C. J. H. Jacobsen, "Universality in heterogeneous catalysis", *J. Cat.* **209**, 275 (2002).
- [66] H. S. Taylor, "A theory of the catalytic surface", *Proc. R. Soc. London Ser. A* **108**, 105 (1925).
- [67] B. Hammer, "Special sites at noble and late transition metal catalyst", *Catal. Today*, submitted, 2005.
- [68] A. T. Gwathmey and R. E. Cunningham, "The influence of crystal face in catalysis", *Adv. Cat.* **10**, 57 (1958).
- [69] J. T. Yates Jr., "Surface chemistry at metallic step defect sites", *J. Vac. Sci. Tech. A* **13**, 1359 (1995).
- [70] T. Zubkov, G. A. Morgan Jr., J. T. Yates Jr., O. Köhlert, M. Lisowski, R. Schillinger, D. Fick, and H. J. Jänsch, "The effect of atomic steps on adsorption and desorption of CO on Ru(109)", *Surf. Sci.* **526**, 57 (2003).
- [71] T. Zambelli, J. Winterlin, J. Trost, and G. Ertl, "Identification of the "Active Sites" of a Surface-Catalyzed Reaction", *Science* **273**, 1688 (1996).
- [72] S. Dahl, A. Logadottir, R. C. Egeberg, J. H. Larsen, I. Chorkendorff, E. Törnquist, and J. K. Nørskov, "Role of Steps in N₂ Activation on Ru(0001)", *Phys. Rev. Lett.* **83**, 1814 (1999).

- [73] B. Hammer, "Bond Activation at Monatomic Steps: NO Dissociation at Corrugated Ru(0001)", *Phys. Rev. Lett.* **83**, 3681 (1999).
- [74] Z. P. Liu and P. Hu, "General Rules for Predicting Where a Catalytic Reaction Should Occur on Metal Surfaces: A Density Functional Theory Study of C–H and C–O Bond Breaking/Making on Flat, Stepped, and Kinked Metal Surfaces", *J. Am. Chem. Soc.* **125**, 1958 (2003).
- [75] P. Gambardella, Z. Sljivancanin, B. Hammer, M. Blanc, K. Kuhnke, and K. Kern, "Oxygen Dissociation at Pt Steps", *Phys. Rev. Lett.* **87**, 056103 (2001).
- [76] I. M. Ciobică and R. A. v. Santen, "Carbon Monoxide Dissociation on Planar and Stepped Ru(0001) Surfaces", *J. Phys. Chem. B* **107**, 3808 (2003).
- [77] B. Hammer and J. Nørskov, "Why gold is the noblest of all the metals", *Nature* **376**, 238 (1995).
- [78] M. Haruta, S. Tsubota, T. Kobayashi, H. Kageyama, M. J. Genet, and B. Delmon, "Low-Temperature Oxidation of CO over Gold Supported on TiO₂, α -Fe₂O₃ and Co₃O₄", *J. Catal.* **144**, 175 (1993).
- [79] M. Haruta, "Size- and support-dependency in the catalysis of gold", *Catal. Today* **36**, 153 (1997).
- [80] M. Valden, S. Pak, X. Lai, and D. W. Goodman, "Structure sensitivity of CO oxidation over model AuTiO₂ catalysts", *Catal. Lett.* **56**, 7 (1998).
- [81] M. Haruta, "Catalysis of Gold Nanoparticles Deposited on Metal Oxides", *CATTECH* **6**, 102 (2002).
- [82] M. Valden, X. Lai, and D. W. Goodman, "Onset of Catalytic Activity of Gold Clusters on Titania with the Appearance of Nonmetallic Properties", *Science* **281**, 1647 (1998).
- [83] L. M. Molina, M. D. Rasmussen, and B. Hammer, "Adsorption of O₂ and oxidation of CO at Au nanoparticles supported by TiO₂(110)", *J. Chem. Phys.* **120**, 7673 (2004).
- [84] M. A. Bollinger and M. A. Vannice, "A kinetic and DRIFTS study of low-temperature carbon monoxide oxidation over Au–TiO₂ catalysts", *Appl. Catal. B* **8**, 417 (1996).
- [85] <http://www.oil-forum.dk>.
- [86] M. Daage and R. R. Chianelli, "Structure–Function Relations in Molybdenum Sulfide Catalysts: The "Rim-Edge" Model", *J. Catal.* **149**, 414 (1994).
- [87] H. Topsøe, B. S. Clausen, and F. E. Massoth, in *Hydrotreating Catalysis*, Vol. 11 of *Catalysis, Science and Technology*, edited by J. R. Anderson and M. Boudart (Springer-Verlag, Berlin, 1996).
- [88] S. Helveg, J. V. Lauritsen, E. Lægsgaard, I. Stensgaard, J. K. Nørskov, B. S. Clausen, H. Topsøe, and F. Besenbacher, "Atomic-Scale Structure of Single-Layer MoS₂ Nanoclusters", *Phys. Rev. Lett.* **84**, 951 (2000).
- [89] J. V. Barth, H. Brune, G. Ertl, and R. J. Behm, "Scanning tunneling microscopy observations on the reconstructed Au(111) surface: Atomic structure, long-range superstructure, rotational domains, and surface defects", *Phys. Rev. B* **42**, 9307 (1990).
- [90] J. V. Lauritsen, M. V. Bollinger, E. Lægsgaard, K. W. Jacobsen, J. K. Nørskov, B. S. Clausen, H. Topsøe, and F. Besenbacher, "Atomic-scale insight into structure and morphology changes of MoS₂ nanoclusters in hydrotreating catalysts", *J. Catal.* **221**, 510 (2004).
- [91] M. V. Bollinger, J. V. Lauritsen, K. W. Jacobsen, J. K. Nørskov, S. Helveg, and F. Besenbacher, "One-Dimensional Metallic Edge States in MoS₂", *Phys. Rev. Lett.* **87**, 266104 (2001).
- [92] A. Zangwill, *Physics at Surfaces* (Cambridge University Press, Cambridge, 1988).
- [93] J. V. Lauritsen, M. Nyberg, J. K. Nørskov, B. S. Clausen, H. Topsøe, E. Lægsgaard, and F. Besenbacher, "Hydrodesulfurization reaction pathways on MoS₂ nanoclusters revealed by scanning tunneling microscopy", *J. Catal.* **224**, 94 (2004).
- [94] J. V. Lauritsen, S. Helveg, E. Lægsgaard, I. Stensgaard, B. S. Clausen, H. Topsøe, and F. Besenbacher, "Atomic-Scale Structure of Co-Mo-S Nanoclusters in Hydrotreating Catalysts", *J. Catal.* **197**, 1 (2001).
- [95] J. R. Rostrup-Nielsen, in *Catalytic Steam Reforming*, Vol. 5 of *Catalysis, Science and Technology*, edited by J. R. Anderson and M. Boudart (Springer-Verlag, Berlin, 1983).
- [96] J. R. Rostrup-Nielsen and T. Rostrup-Nielsen, "Large-scale hydrogen production", *CATTECH* **6**, 150 (2002).

- [97] D. W. Goodman, R. D. Kelley, T. E. Madey, and J. T. Yates, "Kinetics of the Hydrogenation of CO over a Single Crystal Nickel Catalyst", *J. Catal.* **63**, 226 (1980).
- [98] S. Helveg, C. Lopez-Cartes, J. Sehested, P. L. Hansen, B. S. Clausen, J. R. Rostrup-Nielsen, F. Abild-Pedersen, and J. K. Nørskov, "Atomic-scale imaging of carbon nanofibre growth", *Nature* **427**, 426 (2004).
- [99] G. R. Darling, J. B. Pendry, and R. W. Joyner, "A theoretical study of the structure and reactivity of carbon and graphite layers on nickel surfaces", *Surf. Sci.* **221**, 69 (1989).
- [100] J. J. McCarroll, T. Edmonds, and R. C. Pitkethly, "Interpretation of a Complex Low Energy Electron Diffraction Pattern: Carbonaceous and Sulphur-containing Structures on Ni(111)", *Nature* **223**, 1260 (1969).
- [101] D. E. Gardin, J. D. Batteas, M. A. Van Hove, and G. A. Somorjai, "Carbon, nitrogen, and sulfur on Ni(111): formation of complex structures and consequences for molecular decomposition", *Surf. Sci.* **296**, 25 (1993).
- [102] C. Klink, I. Stensgaard, F. Besenbacher, and E. Lægsgaard, "An STM study of carbon-induced structures on Ni(111): evidence for a carbide-phase clock reconstruction", *Surf. Sci.* **342**, 250 (1995).
- [103] C. Klink, PhD thesis, University of Aarhus, 1994.
- [104] H. Nakano and J. Nakamura, "Carbide-induced reconstruction initiated at step edges on Ni(111)", *Surf. Sci.* **482-485**, 341 (2001).
- [105] H. S. Bengaard, J. K. Nørskov, J. Sehested, B. Clausen, L. P. Nielsen, A. M. Molenbroek, and J. R. Rostrup-Nielsen, "Steam Reforming and Graphite Formation on Ni Catalysts", *J. Catal.* **209**, 365 (2002).
- [106] T. Li, B. Bhatia, and D. S. Sholl, "First-principles study of C adsorption, O adsorption, and CO dissociation on flat and stepped Ni surfaces", *J. Chem. Phys.* **121**, 10241 (2004).
- [107] T. H. Rod and J. K. Nørskov, "The surface science of enzymes", *Surf. Sci.* **500**, 678 (2002).
- [108] B. Hinnemann and J. K. Nørskov, "Structure of the FeFe-cofactor of the iron-only nitrogenase and possible mechanism for dinitrogen reduction", *Phys. Chem. Chem. Phys.* **6**, 843 (2004).
- [109] B. Hinnemann and J. K. Nørskov, "Chemical activity of the nitrogenase FeMo cofactor with a central nitrogen ligand: Density functional study", *J. Am. Chem. Soc.* **126**, 3920 (2004).
- [110] J. R. Rostrup-Nielsen, "Sulfur-Passivated Nickel Catalysts for Carbon-Free Steam Reforming of Methane", *J. Catal.* **85**, 31 (1984).
- [111] J. H. Larsen and I. Chorkendorff, "From fundamental studies of reactivity on single crystals to the design of catalysts", *Surf. Sci. Rep.* **35**, 163 (1999).
- [112] J. H. Sinfelt, *Bimetallic catalysts, Discoveries, Concepts, and Applications* (Wiley, New York, 1983).
- [113] V. Ponec, "Alloy catalysts: the concepts", *Appl. Catal. A* **222**, 31 (2001).
- [114] F. Besenbacher, I. Chorkendorff, B. S. Clausen, B. Hammer, A. M. Molenbroek, J. K. Nørskov, and I. Stensgaard, "Design of a Surface Alloy Catalyst for Steam Reforming", *Science* **279**, 1913 (1998).
- [115] P. M. Holmblad, J. H. Larsen, and I. Chorkendorff, "Modification of Ni(111) reactivity toward CH₄, CO and D₂ by two-dimensional alloying", *J. Chem. Phys.* **104**, 7289 (1996).
- [116] L. P. Nielsen, F. Besenbacher, I. Stensgaard, E. Lægsgaard, C. Engdahl, P. Stoltze, K. W. Jacobsen, and J. K. Nørskov, "Initial Growth of Au on Ni(110): Surface Alloying of Immiscible Metals", *Phys. Rev. Lett.* **71**, 754 (1993).
- [117] L. P. Nielsen, PhD thesis, University of Aarhus, 1995.
- [118] A. Logadottir, T. H. Rod, J. K. Nørskov, B. Hammer, S. Dahl, and C. J. H. Jacobsen, "The Brønsted-Evans-Polanyi Relation and the Volcano Plot for Ammonia Synthesis over Transition Metal Catalysts", *J. Cat.* **197**, 229 (2001).
- [119] C. J. H. Jacobsen, S. Dahl, B. S. Clausen, S. Bahn, and J. K. Logadottir, A. Nørskov, "Catalyst Design by Interpolation in the Periodic Table: Bimetallic Ammonia Synthesis Catalysts", *J. Am. Chem. Soc.* **123**, 8404 (2001).

- [120] A. Azaki and K. Aika, in *Catalysis, Science and Technology*, edited by J. R. Anderson and M. Boudart (Springer-Verlag, Berlin, 1981).
- [121] F. Besenbacher, L. P. Nielsen, and P. T. Sprunger, in *The Chemical Physics of Solid Surfaces and Heterogeneous Catalysis*, edited by D. A. King and D. P. Woodruff (Elsevier Science Publishers, Amsterdam, 1997).
- [122] D. W. Goodman, "Chemisorption and Reactivity Studies of H₂ and CO on Sulfided Ni(100)", *Surf. Sci. Lett.* **105**, L265 (1981).
- [123] L. Ruan, I. Stensgaard, F. Besenbacher, and E. Lægsgaard, "Observation of a Missing-Row Structure on an fcc (111) Surface: The (5√3×2)S Phase on Ni(111) Studied by Scanning Tunneling Microscopy", *Phys. Rev. Lett.* **71**, 2963 (1993).
- [124] V. Maurice, N. Kitakatsu, M. Siegers, and P. Marcus, "Low-coverage sulfur induced reconstruction of Ni(111)", *Surf. Sci.* **373**, 307 (1997).
- [125] J. H. Long, J. C. W. J. C. W. Frazer, and E. Ott, "The Activity and Crystal Structures of Mixed Metal Catalysts", *J. Am. Chem. Soc.* **56**, 1101 (1934).
- [126] R. J. Best and W. W. Russell, "Nickel, Copper and Some of their Alloys as Catalysts for Ethylene Hydrogenation", *J. Am. Chem. Soc.* **76**, 838 (1954).
- [127] J. H. Sinfelt, J. L. Carter, and D. J. C. Yates, "Catalytic hydrogenolysis and dehydrogenation over copper-nickel alloys", *J. Catal.* **24**, 283 (1972).
- [128] J. H. Sinfelt, "Supported "bimetallic cluster" catalysts", *J. Catal.* **29**, 308 (1973).
- [129] H. S. Bengaard, PhD thesis, Technical University of Denmark, 2001.
- [130] A. Christensen, A. V. Ruban, P. Stoltze, K. W. Jacobsen, H. L. Skriver, J. K. Nørskov, and F. Besenbacher, "Phase diagrams for surface alloys", *Phys. Rev. B* **56**, 5822 (1997).
- [131] C. Rhodes, G. J. Hutchings, and A. M. Ward, "Water-gas shift reaction: finding the mechanistic boundary", *Catal. Today* **23**, 43 (1995).
- [132] C. T. Campbell and K. A. Daube, "A Surface Science Investigation of the Water-Gas Shift Reaction on Cu(111)", *J. Catal.* **104**, 109 (1987).
- [133] C. V. Ovesen, P. Stoltze, J. K. Nørskov, and C. T. Campbell, "A Kinetic Model of the Water-Gas Shift Reaction", *J. Catal.* **134**, 445 (1992).
- [134] N. Schumacher, A. Boisen, S. Dahl, A. A. Gokhale, L. C. Kandoi, S. Grabow, J. A. Dumesic, M. Mavrikakis, and I. Chorkendorff, "Trends in low-temperature water-gas shift reactivity on transition metals", *J. Catal.* **229**, 265 (2005).
- [135] M. V. Twigg and M. S. Spencer, "Deactivation of supported copper metal catalysts for hydrogenation reactions", *Appl. Catal. A* **212**, 161 (2001).
- [136] G. Jacobs, E. Chenu, P. M. Patterson, L. Williams, D. Sparks, G. Thomas, and B. H. Davis, "Water-gas shift: comparative screening of metal promoters for metal/ceria systems and role of the metal", *Appl. Catal. A* **258**, 203 (2004).
- [137] S. Hilaire, X. Wang, T. Luo, R. J. Gorte, and J. Wagner, "A comparative study of water-gas-shift reaction over ceria-supported metallic catalysts", *Appl. Catal. A* **258**, 271 (2004).
- [138] *Binary Alloy Phase Diagrams*, 2nd ed., edited by Massalski (AMS International, Ohio, 1992), Vol. 2.
- [139] U. Schneider, G. R. Castro, and K. Wandelt, "Adsorption on ordered Cu₃Pt(111): site selectivity", *Surf. Sci.* **287-288**, 146 (1993).
- [140] C. Becker and K. Wandelt, "Coadsorption of CO and Hydrogen on the Cu₃Pt(111) Surface", *Zeitschrift für Physikalische Chemie* **198**, 87 (1997).
- [141] R. C. Yeates and G. A. Somorjai, "The growth and alloy formation of copper on the platinum (111) and stepped (553) crystal surfaces; characterization by Leed, AES, and CO thermal desorption", *Surf. Sci.* **134**, 729 (1983).
- [142] M. L. Shek, P. M. Stefan, I. Lindau, and W. E. Spicer, "Photoemission study of the adsorption of Cu on Pt(111)", *Phys. Rev. B* **27**, 7277 (1983).

- [143] M. T. Paffett, C. T. Campbell, T. N. Taylor, and S. Srinivasan, "Cu adsorption on Pt(111) and its effects on Chemisorption: A comparison with electrochemistry", *Surf. Sci.* **154**, 284 (1985).
- [144] N. T. Barrett, R. Belkhou, J. Thiele, and C. Guillot, "A core-level photoemission spectroscopy study of the formation of surface alloy Cu/Pt(111): comparison with Pt/Cu(111)", *Surf. Sci.* **331-333**, 776 (1995).
- [145] M. Kolodziejczyk, R. E. R. Colen, M. Berdau, B. Delmon, and J. H. Block, "CO oxidation on a copper-modified Pt(111) surface", *Surf. Sci.* **375**, 235 (1997).
- [146] B. Holst, M. Nohlen, K. Wandelt, and W. Allison, "The growth of ultra thin Cu-films on Pt(111), probed by helium atom scattering and scanning tunnelling microscopy", *Surf. Sci.* **377-379**, 891 (1997).
- [147] B. Holst, M. Nohlen, K. Wandelt, and W. Allison, "Observation of an adlayer-driven substrate reconstruction in Cu-Pt(111)", *Phys. Rev. B* **58**, R10195 (1998).
- [148] J. S. Tsay, T. Mangel, and K. Wandelt, "Kinetic study of the formation of a surface-confined Cu₅₀Pt₅₀ alloy", *Thin Solid Films* **397**, 152 (2001).
- [149] R. J. Needs, M. J. Godfrey, and M. Mansfield, "Theory of surface stress and surface reconstruction", *Surf. Sci.* **242**, 215 (1991).
- [150] A. R. Sandy, S. G. J. Mochrie, D. M. Zehner, G. Grübel, K. G. Huang, and D. Gibbs, "Reconstruction of the Pt(111) Surface", *Phys. Rev. Lett.* **68**, 2192 (1992).
- [151] M. Bott, M. Hohage, T. Michely, and G. Comsa, "Pt(111) Reconstruction Induced By Enhanced Pt Gas-Phase Chemical-Potential", *Phys. Rev. Lett.* **70**, 1489 (1993).
- [152] M. Hohage, T. Michely, and G. Comsa, "Pt(111) network reconstruction: structure, growth and decay", *Surf. Sci.* **337**, 249 (1995).
- [153] M. Giesen-Seibert, R. Jentjens, M. Poensgen, and H. Ibach, "Time dependence of step fluctuations on vicinal Cu(1 1 19) surfaces investigated by tunneling microscopy", *Phys. Rev. Lett.* **71**, 3521 (1993).
- [154] A. U. Nilekar and M. Mavrikakis, unpublished results.
- [155] M. Ø. Pedersen, S. Helveg, A. Ruban, E. Lægsgaard, J. K. Nørskov, and F. Besenbacher, "How a gold substrate can increase the reactivity of a Pt overlayer", *Surf. Sci.* **426**, 395 (1999).
- [156] V. P. Zhdanov, P. J., and Z. Knor, "Preexponential Factors for Elementary Surface Processes", *Catal. Rev. - Sci. Eng.* **30**, 501 (1988).
- [157] P. J. Feibelman, B. Hammer, J. K. Nørskov, F. Wagner, M. Scheffler, R. Stumpf, R. Watwe, and J. Dumesic, "The CO/Pt(111) puzzle", *J. Phys. Chem. B* **105**, 4018 (2001).
- [158] "NIST standard reference database 71".
- [159] A. A. Gokhale, L. C. Kandoi, S. Grabow, and M. Dumesic, J. Mavrikakis, "In preparation", .
- [160] H. Over, Y. D. Kim, A. P. Seitsonen, S. Wendt, E. Lundgren, M. Schmid, P. Varga, A. Morgante, and G. Ertl, "Atomic-Scale Structure and Catalytic Reactivity of the RuO₂(110) Surface", *Science* **287**, 1474 (2000).
- [161] H. Over and M. Muhler, "Catalytic CO oxidation over ruthenium - bridging the pressure gap", *Prog. Surf. Sci.* **72**, 3 (2003).
- [162] H. Leidheiser and A. T. Gwathmey, "The Catalytic Reaction of Hydrogen and Oxygen on Plane Faces of a Single Crystal of Copper", *J. Am. Chem. Soc.* **70**, 1200 (1948).
- [163] H. Leidheiser and A. T. Gwathmey, "The Selective Deposition of Carbon on the (111) Face of a Nickel Crystal in the Catalytic Decomposition of Carbon Monoxide", *J. Am. Chem. Soc.* **70**, 1206 (1948).
- [164] P. Bernard, K. Peters, J. Alvarez, and S. Ferrer, "Ultrahigh vacuum/high pressure chamber for surface x-ray diffraction experiments", *Rev. Sci. Instrum.* **70**, 1478 (1999).
- [165] K. F. Peters, C. J. Walker, P. Steadman, O. Robach, H. Isern, and S. Ferrer, "Adsorption of carbon monoxide on Ni(110) above atmospheric pressure investigated with surface X-ray diffraction", *Phys. Rev. Lett.* **86**, 5325 (2001).

- [166] C. Quiros, O. Robach, H. Isern, P. Ordejon, and S. Ferrer, "Compressibility of CO adsorbed on Ni(111) from 10^{-6} mbar to 1.2 bar ambient CO pressures investigated with X-ray diffraction", *Surf. Sci.* **522**, 161 (2003).
- [167] M. Ackermann, O. Robach, C. Walker, C. Quiros, H. Isern, and S. Ferrer, "Hydrogenation of carbon monoxide on Ni(111) investigated with surface X-ray diffraction at atmospheric pressure", *Surf. Sci.* **557**, 21 (2004).
- [168] G. D. Moggridge, T. Rayment, R. M. Ormerod, M. A. Morris, and R. M. Lambert, "Spectroscopic Observation Of A Catalyst Surface In A Reactive Atmosphere At High-Pressure", *Nature* **358**, 658 (1992).
- [169] D. F. Ogletree, H. Bluhm, G. Lebedev, C. S. Fadley, Z. Hussain, and M. Salmeron, "A differentially pumped electrostatic lens system for photoemission studies in the millibar range", *Rev. Sci. Instrum.* **73**, 3872 (2002).
- [170] G. Rupprechter, T. Dellwig, H. Unterhalt, and H. J. Freund, "High-pressure carbon monoxide adsorption on Pt(111) revisited: A sum frequency generation study", *J. Phys. Chem. B* **105**, 3797 (2001).
- [171] X. C. Su, P. S. Cremer, Y. R. Shen, and G. A. Somorjai, "Pressure dependence (10^{-10} – 700 Torr) of the vibrational spectra of adsorbed CO on Pt(111) studied by sum frequency generation", *Phys. Rev. Lett.* **77**, 3858 (1996).
- [172] P. Guyot-Sionnest, "The mature years of Sum-Frequency Generation are ahead", *Surf. Sci.* **585**, 1 (2005).
- [173] G. Q. Lu, A. Lagutchev, D. D. Dlott, and A. Wieckowski, "Quantitative vibrational sum-frequency generation spectroscopy of thin layer electrochemistry: CO on a Pt electrode", *Surf. Sci.* **585**, 3 (2005).
- [174] E. Ozensoy, C. Hess, and D. W. Goodman, "Understanding the catalytic conversion of automobile exhaust emissions using model catalysts: CO+NO reaction on Pd(111)", *Topics Catal.* **28**, 13 (2004).
- [175] T. W. Hansen, J. B. Wagner, P. L. Hansen, S. Dahl, H. Topsøe, and C. J. H. Jacobsen, "Atomic-resolution in situ transmission electron microscopy of a promoter of a heterogeneous catalyst", *Science* **294**, 1508 (2001).
- [176] P. L. Hansen, J. B. Wagner, S. Helveg, J. R. Rostrup-Nielsen, B. S. Clausen, and H. Topsøe, "Atom-Resolved Imaging of Dynamic Shape Changes in Supported Copper Nanocrystals", *Science* **295**, 2053 (2002).
- [177] B. J. McIntyre, M. Salmeron, and G. A. Somorjai, "A Variable Pressure Temperature Scanning Tunneling Microscope For Surface Science And Catalysis Studies", *Rev. Sci. Instrum.* **64**, 687 (1993).
- [178] J. A. Jensen, K. B. Rider, Y. Chen, M. Salmeron, and G. A. Somorjai, "High pressure, high temperature scanning tunneling microscopy", *J. Vac. Sci. Technol. B* **17**, 1080 (1999).
- [179] P. B. Rasmussen, B. L. M. Hendriksen, H. Zeijlemaker, H. G. Ficke, and J. W. M. Frenken, "The "reactor STM": A scanning tunneling microscope for investigation of catalytic surfaces at semi-industrial reaction conditions", *Rev. Sci. Instrum.* **69**, 3879 (1998).
- [180] B. L. M. Hendriksen and J. W. M. Frenken, "CO oxidation on Pt(110): Scanning tunneling microscopy inside a high-pressure flow reactor", *Phys. Rev. Lett.* **89**, 046101 (2002).
- [181] K. B. Rider, K. S. Hwang, M. Salmeron, and G. A. Somorjai, "Structure and dynamics of dense monolayers of NO adsorbed on Rh(111) in equilibrium with the gas phase in the Torr pressure range", *Phys. Rev. Lett.* **86**, 4330 (2001).
- [182] J.-S. McEwen, S. H. Payne, H. J. Kreuzer, M. Kinne, R. Denecke, and H.-P. Steinrück, "Adsorption and desorption of CO on Pt(111): a comprehensive analysis", *Surf. Sci.* **545**, 47 (2003).
- [183] B. N. J. Persson, M. Tushaus, and A. M. Bradshaw, "On the nature of dense CO adlayers", *J. Chem. Phys.* **92**, 5034 (1990).
- [184] J. A. Jensen, K. B. Rider, M. Salmeron, and G. A. Somorjai, "High Pressure Adsorbate Structures Studied by Scanning Tunneling Microscopy: CO on Pt(111) in Equilibrium with the Gas Phase", *Phys. Rev. Lett.* **80**, 1228 (1998).

- [185] E. K. Vestergaard, P. Thostrup, T. An, E. Lægsgaard, I. Stensgaard, B. Hammer, and F. Besenbacher, "Comment on "High Pressure Adsorbate Structures Studied by Scanning Tunneling Microscopy: CO on Pt(111) in Equilibrium with the Gas Phase"", *Phys. Rev. Lett.* **88**, 259601 (2002).
- [186] G. Ertl, M. Neumann, and K. M. Streit, "Chemisorption of CO on the Pt(111) surface", *Surf. Sci.* **64**, 393 (1977).
- [187] E. K. Vestergaard, PhD thesis, University of Aarhus, 2004.
- [188] H. F. Oetjen, V. M. Schmidt, U. Stimming, and F. Trila, "Performance data of a proton exchange membrane fuel cell using H₂/CO as fuel gas", *J. Electrochem. Soc.* **143**, 3838 (1996).
- [189] H. A. Gasteiger, N. Markovic, P. N. Ross, and E. J. Cairns, "Carbon monoxide electrooxidation on well-characterized platinum-ruthenium alloys", *J. Phys. Chem.* **98**, 617 (1994).
- [190] H. Igarashi, T. Fujino, Y. M. Zhu, H. Uchida, and M. Watanabe, "CO Tolerance of Pt alloy electrocatalysts for polymer electrolyte fuel cells and the detoxification mechanism", *Phys. Chem. Chem. Phys.* **3**, 306 (2001).
- [191] F. Buatier de Mongeot, M. Scherer, B. Gleich, E. Kopatzki, and R. J. Behm, "CO adsorption and oxidation on bimetallic Pt/Ru(0001) surfaces - a combined STM and TPD/TPR study", *Surf. Sci.* **411**, 249 (1998).
- [192] B. Kasemo, S. Johansson, H. Persson, P. Thormählen, and V. P. Zhdanov, "Catalysis in the nm-regime: manufacturing of supported model catalysts and theoretical studies of the reaction kinetics", *Topics Catal.* **13**, 43 (2000).
- [193] R. J. Farrauto and R. M. Heck, "Catalytic converters: state of the art and perspectives", *Catal. Today* **51**, 351 (1999).
- [194] M. Shelef and R. W. McCabe, "Twenty-five years after introduction of automotive catalysts: what next?", *Catal. Today* **62**, 35 (2000).
- [195] K. H. Hansen, T. Worren, S. Stempel, E. Lægsgaard, M. Baumer, H. J. Freund, F. Besenbacher, and I. Stensgaard, "Palladium nanocrystals on Al₂O₃: Structure and adhesion energy", *Phys. Rev. Lett.* **83**, 4120 (1999).
- [196] H. Conrad, G. Ertl, J. Küppers, and E. E. Latta, "Interaction Of NO And O₂ With Pd(111) Surfaces. I.", *Surf. Sci.* **65**, 235 (1977).
- [197] P. J. Chen and D. W. Goodman, "Ordered High Coverage No Overlayers On Pd(111)", *Surf. Sci.* **297**, L93 (1993).
- [198] D. Loffreda, D. Simon, and P. Sautet, "Vibrational frequency and chemisorption site: a DFT-periodic study of NO on Pd(111) and Rh(111) surfaces", *Chem. Phys. Lett.* **291**, 15 (1998).
- [199] K. H. Hansen, Z. Sljivancanin, B. Hammer, E. Lægsgaard, F. Besenbacher, and I. Stensgaard, "An STM and DFT study of the ordered structures of NO on Pd(111)", *Surf. Sci.* **496**, 1 (2002).
- [200] E. Ozensoy, C. Hess, D. Loffreda, P. Sautet, and D. W. Goodman, "Formation of a high coverage (3 × 3) NO phase on Pd(111) at elevated pressures: Interplay between kinetic and thermodynamic accessibility", *J. Phys. Chem. B* **109**, 5414 (2005).
- [201] E. Christoffersen, P. Stoltze, and J. K. Nørskov, "Monte Carlo simulations of adsorption-induced segregation", *Surf. Sci.* **505**, 200 (2002).
- [202] J. Nerlov, S. Sckerl, J. Wambach, and I. Chorkendorff, "Methanol synthesis from CO₂, CO and H₂ over Cu(100) and Cu(100) modified by Ni and Co", *Appl. Catal. A* **191**, 97 (2000).
- [203] P. de Groot, M. Coulon, and K. Dransfeld, "Ni(CO)₄ formation on single Ni crystals: reaction kinetics and observation of surface faceting induced by the reaction", *Surf. Sci.* **94**, 204 (1980).
- [204] V. K. Medvedev, R. Borner, and N. Kruse, "Nickeltetracarbonyl formation on non-equilibrium Ni surfaces", *Surf. Sci.* **401**, L371 (1998).
- [205] C. Doornkamp and V. Ponec, "The universal character of the Mars and Van Krevelen mechanism", *J. Mol. Catal. A* **162**, 19 (2000).
- [206] J. E. Turner, B. C. Sales, and M. B. Maple, "Oscillatory oxidation of Co over a Pt catalyst", *Surf. Sci.* **103**, 54 (1981).

- [207] A. V. Walker, B. Klotzer, and D. A. King, "Dynamics and kinetics of oxygen dissociative adsorption on Pt110(1×2)", *J. Chem. Phys.* **109**, 6879 (1998).
- [208] S. Helveg, H. T. Lorensen, S. Horch, E. Laegsgaard, I. Stensgaard, K. W. Jacobsen, J. K. Norskov, and F. Besenbacher, "Oxygen adsorption on Pt(110)-(1×2): new high-coverage structures", *Surf. Sci.* **430**, L533 (1999).
- [209] E. Vesselli, C. Africh, A. Baraldi, G. Comelli, F. Esch, and R. Rosei, "(10×2) strained reconstruction induced by oxygen adsorption on the Rh(110) surface", *J. Chem. Phys.* **114**, 4221 (2001).
- [210] R. A. van Santen and P. C. E. Kuipers, "The Mechanism of Ethylene Epoxidation", *Adv. Catal.* **35**, 265 (1987).
- [211] G. Rovida, F. Pratesi, M. Maglietta, and E. Ferroni, "Effects of Oxygen on Silver Surface Structure", *J. Vac. Sci. Tech.* **9**, 796 (1972).
- [212] A. Michaelides, K. Reuter, and M. Scheffler, "When seeing is not believing: Oxygen on Ag(111), a simple Adsorption System?", *J. Vac. Sci. Tech.*, submitted (2005).
- [213] A. Stierle, A. Reicho, N. Kasper, I. Costina, and H. Dosch, "In-situ study of the interaction of O₂ with Ag(111)", *Abstracts of CECAM Workshop: In-situ atomic scale characterization of surfaces under high pressures: recent advances in experiment and theory* (2004).
- [214] G. Rovida, F. Pratesi, M. Maglietta, and E. Ferroni, "Chemisorption of oxygen on the silver (111) surface", *Surf. Sci.* **43**, 230 (1974).
- [215] C. T. Campbell, "Atomic and molecular oxygen adsorption on Ag(111)", *Surf. Sci.* **157**, 43 (1985).
- [216] C. I. Carlisle, D. A. King, M. L. Bocquet, J. Cerda, and P. Sautet, "Imaging the surface and the interface atoms of an oxide film on Ag111 by scanning tunneling microscopy: Experiment and theory", *Phys. Rev. Lett.* **84**, 3899 (2000).
- [217] C. I. Carlisle, T. Fujimoto, W. S. Sim, and D. A. King, "Atomic imaging of the transition between oxygen chemisorption and oxide film growth on Ag111", *Surf. Sci.* **470**, 15 (2000).
- [218] A. Michaelides, M. L. Bocquet, P. Sautet, A. Alavi, and D. A. King, "Structures and thermodynamic phase transitions for oxygen and silver oxide phases on Ag111", *Chem. Phys. Lett.* **367**, 344 (2003).
- [219] W. X. Li, C. Stampfl, and M. Scheffler, "Why is a noble metal catalytically active? The role of the O-Ag interaction in the function of silver as an oxidation catalyst", *Phys. Rev. Lett.* **90**, 256102 (2003).
- [220] W. X. Li, C. Stampfl, and M. Scheffler, "Subsurface oxygen and surface oxide formation at Ag(111): A density-functional theory investigation", *Phys. Rev. B* **67**, 045408 (2003).
- [221] M. L. Bocquet, A. Michaelides, D. Loffreda, P. Sautet, A. Alavi, and D. A. King, "New insights into ethene epoxidation on two oxidized Ag (111) surfaces", *J. Am. Chem. Soc.* **125**, 5620 (2003).
- [222] J. P. Biberrian and M. A. Van Hove, "A new model for CO ordering at high coverages on low index metal surfaces: A correlation between LEED, HREELS and IRS: II. CO adsorbed on fcc (111) and hcp (0001) surfaces", *Surf. Sci.* **138**, 361 (1984).
- [223] G. Kresse, M. Schmid, E. Napetschnig, M. Shishkin, L. Kohler, and P. Varga, "Structure of the ultrathin aluminum oxide film on NiAl(110)", *Science* **308**, 1440 (2005).

Acknowledgements

The work presented in my thesis is not the result of my work alone, but rather it is the outcome of a fruitful interaction with a large number of coworkers. At this point it is therefore a great pleasure to acknowledge all the persons who with their excellent scientific insights and warm personalities have helped me mature both as a scientist and as a person over the past four years.

First of all I want to thank my supervisor Flemming Besenbacher for his enthusiastic guidance throughout the entire course of my PhD studies. His ability to lead the group into new and exciting areas of research and to create a unique scientific environment is amazing, and I have gained immensely from his foresighted supervision. Erik Lægsgaard is highly appreciated for his technical support in the laboratory.

A warm thanks is given to all the members of the scanning probe microscopy group for helping to make the everyday life at the institute a pleasant experience. In particular I want to acknowledge the people who have taken part in the experimental part of my work: Toshu An, Jan Knudsen, Jeppe V. Lauritsen, Sarah Longwitz, Jesper Matthiesen, Joachim Schnadt, and Ebbe K. Vestergaard. In particular I am grateful to Ebbe K. Vestergaard and Joachim Schnadt who have acted as my mentors during the first and last part of my PhD studies, respectively. Both of them are extremely talented physicists, and they have provided invaluable support and guidance which has aided the scientific outcome of my work tremendously.

I have had the the pleasure to collaborate with some of the world-leading groups within theoretical surface science, and I am thankful for the contributions from: Wei Xu Li, Thorbjørn M. Pedersen, Jian-Guo Wang, and Bjørk Hammer at the University of Aarhus, Karoliina Honkala and Jens K. Nørskov at the Technical University of Denmark, and Anand Nilekar and Manos Mavrikakis at the University of Wisconsin-Madison. I have also enjoyed a stimulating collaboration with Søren Dahl and Bjerne S. Clausen at Haldor Topsøe A/S.

Finally I want to express my gratitude to those who helped me during the writing process. Jeppe V. Lauritsen, Peter Thostrup, and Ebbe K. Vestergaard read parts of the thesis, and in particular Joachim Schnadt is thanked for a thorough reading and for numerous suggestions that have helped in improving the linguistics as well as the scientific content. Jeanette Dandanell is acknowledged for proof reading the entire thesis.

I

Chemistry of one-dimensional metallic edge states in MoS₂ nanoclusters

J V Lauritsen¹, M Nyberg², R T Vang¹, M V Bollinger²,
B S Clausen³, H Topsøe³, K W Jacobsen², E Lægsgaard¹,
J K Nørskov² and F Besenbacher¹

¹ Department of Physics and Astronomy, Centre for Atomic-Scale Materials Physics (CAMP) and the Interdisciplinary Nanoscience Centre (iNANO), University of Aarhus, DK-8000 Aarhus C, Denmark

² Department of Physics and Centre for Atomic-Scale Materials Physics (CAMP), Technical University of Denmark, DK-2800 Lyngby, Denmark

³ Haldor Topsøe A/S, Nymøllevej 55, DK-2800 Lyngby, Denmark

E-mail: fbe@phys.au.dk

Received 23 January 2003

Published 5 February 2003

Online at stacks.iop.org/Nano/14/385

Abstract

Nanostructures often have unusual properties that are linked to their small size. We report here on extraordinary chemical properties associated with the edges of two-dimensional MoS₂ nanoclusters, which we show to be able to hydrogenate and break up thiophene (C₄H₄S) molecules. By combining atomically resolved scanning tunnelling microscopy images of single-layer MoS₂ nanoclusters and density functional theory calculations of the reaction energetics, we show that the chemistry of the MoS₂ nanoclusters can be associated with one-dimensional metallic states located at the perimeter of the otherwise insulating nanoclusters. The new chemistry identified in this work has significant implications for an important catalytic reaction, since MoS₂ nanoclusters constitute the basis of hydrotreating catalysts used to clean up sulfur-containing molecules from oil products in the hydrodesulfurization process.

 This article features online multimedia enhancements

1. Introduction

For the transition-metal oxides and sulfides, which are two important classes of catalytically active materials, the chemical activity is often explained in terms of the geometric coordination of surface atoms. This has led to the concept of ‘coordinatively unsaturated sites’ (CUS) or anion vacancies as a description of the chemically or photocatalytically active sites [1, 3–6]. These are low-coordination point defects with a high affinity towards bond formation. It is generally accepted that such vacancies play an important role in the catalytic activity of the MoS₂-based catalysts used in hydrodesulfurization (HDS) [1, 2]. In the present paper we have found a new kind of chemical activity associated with fully sulfur-saturated active sites on two-dimensional MoS₂ nanoclusters. We can relate this chemistry to highly localized metallic electron states located at the perimeter of triangularly

shaped nanoclusters, and suggest that such electronic states, which will dominate in nanosized clusters, may constitute a new class of active centres in heterogeneous catalysis.

Our approach exploits recent progress in the synthesis of a relevant model system for hydrotreating catalysts [7, 8]. We can nucleate and grow ~30 Å wide MoS₂ nanoclusters (see figure 1(A)), and the scanning tunnelling microscope (STM) has given us the first direct images of the detailed atomic structure. When synthesized on an inert Au(111) substrate, the MoS₂ clusters consist of a single S–Mo–S layer, in which the Mo atoms are coordinated in a trigonal prismatic geometry to six S atoms. The clusters have a triangular morphology, and from an interplay with theory the detailed edge structure was determined as (10 $\bar{1}$ 0) Mo edges fully saturated with S dimers [7, 9]. Of particular interest, we find in the STM images a characteristic bright brim extended all the way around the edge of the nanoclusters (figure 1(A)). It can

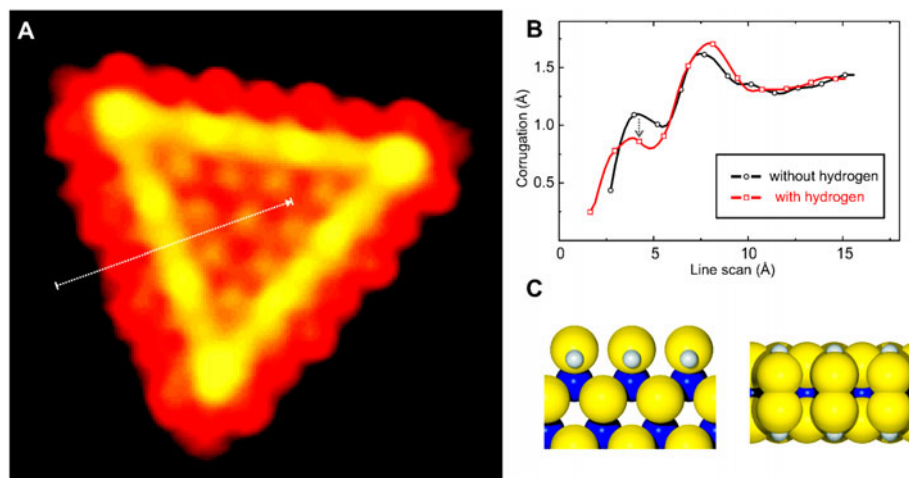


Figure 1. MoS₂ nanocluster synthesized on Au(111) and the effect of atomic hydrogen on the edges. (A) Atom-resolved STM image ($I_t = 0.86$ nA, $V_t = -1250$ mV, $32 \text{ \AA} \times 33 \text{ \AA}$) of a sulfided MoS₂ nanocluster. The bright brim of the high electronic state density extended around the cluster is associated with the existence of metallic edge states [7, 9]. (B) Upon treatment of the clusters with atomic H (H_2 dissociated on a hot W filament, $T_{\text{sample}} \cong 600$ K), S–H groups are formed on the edge. This is observed in experimental STM images as a downshift of the outermost edge protrusions relative to the bright edge state corresponding to $-0.20 \pm 0.07 \text{ \AA}$ shown by the line scans. In accordance with this, STM simulations show that adsorption of hydrogen leaves the appearance of the edge essentially unaltered except for the small downshift of the outermost row [22]. (C) Ball models of the configuration in which hydrogen adsorbs on the fully sulfided edges, shown in a top and side view representation (S: yellow; Mo: blue; H: grey).

be associated with a one-dimensional metallic electron state at the edge of the otherwise insulating MoS₂ nanoclusters, in which electrons are strongly localized perpendicularly to the edge, but delocalized along the direction of the cluster edges [9]. It has long been realized that the basal plane of MoS₂ is catalytically inactive [10], and that the activity in the HDS process is associated somehow with the edges terminating the clusters [1, 2, 11, 12]. Here we study on the atomic scale the interaction of individual thiophene ($\text{C}_4\text{H}_4\text{S}$) molecules with the MoS₂ nanoclusters, allowing us to explore the chemical properties of the edges. Thiophene is the simplest aromatic sulfur-containing molecule which occurs naturally in oil fractions, and for that reason it has been widely used to test the ability of a catalyst to remove sulfur [13–16]. This choice of catalyst model system enables us with the STM to pinpoint the active sites on the metallic edge states of the MoS₂ nanoclusters and reveal signatures of possible reaction intermediates, while our density functional theory (DFT) calculations help identify these and elucidate the reaction pathway and energetics.

2. Methods and materials

The experiments were performed in a standard ultrahigh-vacuum (UHV) chamber, with base pressure below 1×10^{-10} mbar, equipped with a home-built, variable-temperature STM [17]. The Au(111) substrate is chosen as the model catalyst substrate since it is chemically rather inert and furthermore offers the characteristic ‘herringbone’ surface reconstruction as an ideal template for dispersing MoS₂ into 20–30 Å wide nanoclusters. The detailed synthesis of MoS₂ nanoclusters on Au(111) to form a realistic model catalyst system for hydrodesulfurization was described previously [7]. Thiophene (99% purity, Aldrich) was processed by repeated cycles of freeze–pump–thaw purification and admitted to the UHV environment through a leak-valve. A tube of stainless steel di-

rected the flux onto the sample, which was held at temperatures in the range from 173 K to ~ 500 K. STM images were recorded at room temperature, except for the low-temperature measurements which were recorded below 200 K.

Density functional theory (DFT) calculations were performed within the generalized gradient approximation using ultrasoft pseudopotentials to describe the ion cores [18, 19]. The edge of the MoS₂ nanoclusters was modelled by a stripe of MoS₂, four Mo atoms wide (six for simulations of STM images), and the unit cell along the stripe was either two or three Mo long. All structures are completely relaxed and transition states are located using the nudged elastic band method [20]. The Kohn–Sham orbitals were expanded in plane waves with a cut-off energy of 25 Ryd, and eight special k -points in the k_x -direction. STM images were simulated within the Tersoff–Hamann formalism [21].

3. Results and discussion

On exposing the fully sulfided single-layer MoS₂ nanoclusters to thiophene at room temperature, no binding of thiophene could be observed. On lowering the temperature of the sample below 200 K, however, individual thiophene molecules situated near the edges on top of single-layer MoS₂ nanoclusters are observed in STM images (not shown). This indicates a flat η^5 -like adsorption geometry of thiophene on top of the bright brim associated with the metallic edge state. Heating the sample slightly above 200 K results in desorption of the molecules, from which we conclude that this configuration is a weakly adsorbed state with a non-covalent character, and hence presumably of little catalytic relevance. In the present context, we emphasize, however, that thiophene binds more strongly to the metallic edge state than to the basal plane of the MoS₂ nanocluster.

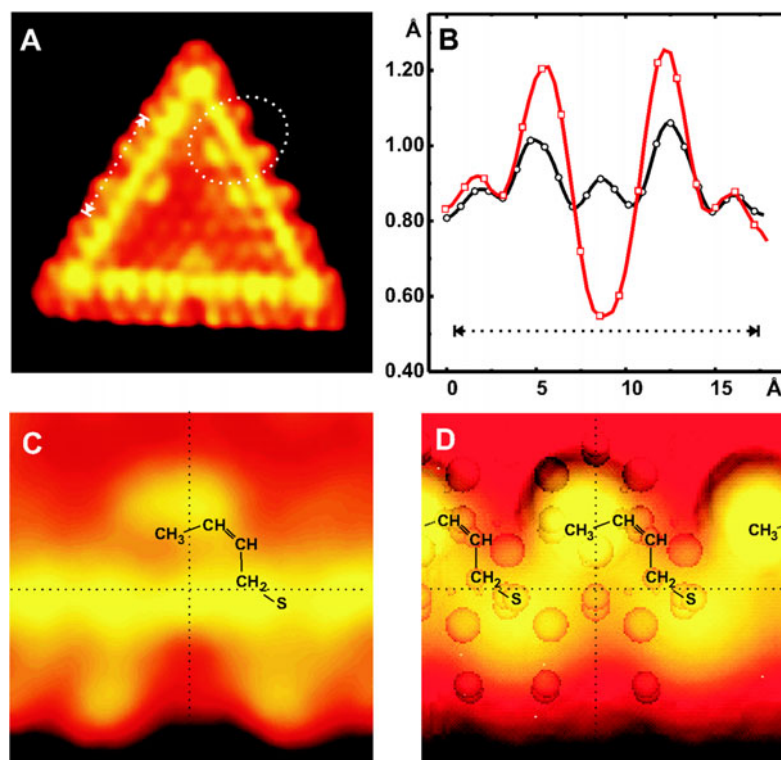


Figure 2. Thiophene is adsorbed onto a triangular MoS₂ nanocluster pre-exposed to atomic hydrogen. (A) Atom-resolved STM image ($I_t = 0.50$ nA, $V_t = -331$ mV) showing species adsorbed at sites on the metallic edge states. The image dimensions are $50 \text{ \AA} \times 54 \text{ \AA}$. Compared to the cluster edges in figure 1, a ‘bean-like’ structure is seen in a position adjacent to the bright brim and the intensity of the nearby edge protrusions is shifted. (B) STM line scans along the nearby edge protrusions of the clean edge (black) and an edge with a molecule adsorbed on the edge state (red). A decrease of $\sim 0.4 \text{ \AA}$ of the protrusion located in front of the bean-like structure is observed, together with an increase of $\sim 0.2 \text{ \AA}$ at the two neighbouring protrusions. We associate this with changes in the LDOS due to molecule adsorption. (C) Cut-out from the STM image in (A) illustrating the features associated with each molecule. (D) Simulated STM image from the DFT calculations of the structure, with individual molecules adsorbed in a repeated geometry along the edge. The hydrogenated thiophenic species, C₄H₇S (*cis*-but-2-ene-thiolate), coordinated to the edge state primarily through the terminal S atom is seen to reproduce the details of the experimental STM image.

We observe a much stronger binding of thiophene *only* when the MoS₂ nanoclusters (see figure 2(A)) are exposed to *atomic hydrogen* prior to thiophene dosing. The thiophene was dosed directly after the atomic H treatment while the sample was still hot (~ 500 K). A ‘bean-like’ structure is observed in the STM image (figure 2(C)) in the row adjacent to the bright brim of the cluster, which can be associated with individual molecules coordinated to the metallic edge state. From a line scan along the edge of the MoS₂ nanocluster (see figures 2(A), (B)) we can furthermore conclude that the ‘bean-like’ feature is always accompanied by a decrease in intensity (0.4 \AA) at the edge protrusion located in front of the ‘bean-like’ structure, and a slight increase (0.2 \AA) of the two neighbouring protrusions with respect to the Mo edge without the thiophene. Additionally, a closer inspection of STM images like that shown in figure 2(C) reveals that the ‘bean-like’ feature is slightly asymmetric with respect to the corresponding edge depression.

Since thiophene adsorbs at higher temperatures ($T > 200$ K) only when the clusters are pre-exposed to atomic hydrogen, we conclude that the hydrogen apparently changes the chemical properties of the MoS₂ clusters substantially. We have studied the interaction of atomic hydrogen with the MoS₂ clusters further and find that hydrogen adsorbs near the

cluster edges. From STM height corrugations (figure 1(B)) of the cluster edges measured with and without the H pre-treatment, we find a relative downshift in the intensity of the edge protrusions compared to the electronic edge state corresponding to a height of $\approx -0.20 \text{ \AA}$. We associate this effect in the STM images with a change in the local electronic structure near the edge due to adsorbed H. This is supported by DFT calculations on the fully sulfided Mo edge with hydrogen adsorbed in the configurations shown by the ball model in figure 1(C). STM simulations are in qualitative accordance with the STM image and reproduce the observed downshift of the outermost row [22]. According to our DFT calculations the H atoms adsorbed on the S dimers are marginally unstable (energy of $+0.03$ eV) relative to molecular H₂. We suggest that an energy barrier prevents the desorption of H under the conditions of our experiments, and since this implies a similar barrier for dissociative adsorption of H₂, this also explains the need experimentally to pre-dissociate H₂. A thermodynamical treatment using energies from the DFT calculations shows that H atoms are indeed abundant at the edges during industrial hydrotreating conditions [23], and the high temperatures should also allow dissociation to occur easily. The use of atomic hydrogen in our experiments can therefore be viewed as a simple way of providing hydrogen atoms at the high

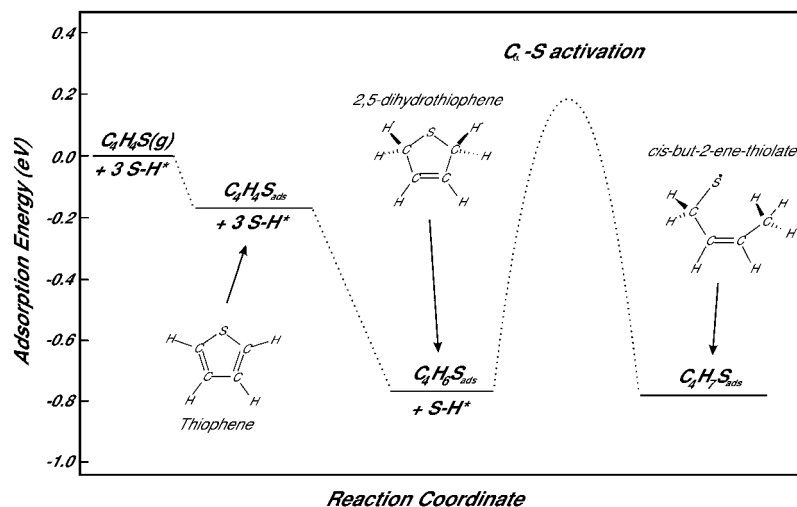


Figure 3. Energy diagram showing the reaction path of thiophene adsorbed on the metallic edge state of MoS₂. The energies are in electron volts, and are calculated relative to gas phase thiophene and H adsorbed on the MoS₂ edge (+0.03 eV). The diagram displays the most relevant intermediate steps in the hydrogenation of thiophene and subsequent C_α-S bond cleavage. The schematic molecules illustrate the geometric configurations associated with thiophene species adsorbed on top of the MoS₂ edge before, during, and after C_α-S bond cleavage. Note that the barrier associated with this reaction step is rather low (1.07 eV). The final configuration is C₄H₇S (*cis*-but-2-ene-thiolate).

chemical potential found under industrial reaction conditions. Previously, *in situ* infra-red spectroscopy measurements have indeed indicated that S-H groups are present at the edges of MoS₂ clusters under reaction conditions [24]. In view of the observed change in reactivity of the clusters upon atomic hydrogen pre-treatment, we thus propose that the S-H groups formed adjacent to the metallic edge state of MoS₂ facilitate the hydrogenation reaction and that the adsorbed species observed with STM (figure 2(A)) are hydrogenated thiophene derivatives.

In accordance with the low-temperature STM results and earlier estimates of thiophene desorption temperatures on supported MoS₂ catalyst particles [25], our DFT calculations show that thiophene does indeed interact very weakly (~0.2 eV in figure 3) with the fully sulfided Mo edges of MoS₂. Since the STM experiments show that S-H groups are needed here for a strong interaction, we have performed DFT calculations of different hydrogenated species derived from thiophene; see figure 3. It is found that a C₄H₇S (*cis*-but-2-ene-thiolate) species coordinated through the terminal sulfur atom to edge S atoms is very stable and shows a good accordance with the STM results. The adsorbed thiolates are illustrated in the simulated STM image (figure 2(D)), and the features associated with each molecule are seen to reproduce several of the most important features found in the STM image (figure 2(C)), including the shifted intensity of the three outermost protrusions near the molecular adsorption site. The asymmetry of the ‘bean-like’ structure is also reproduced in the simulated STM images and is seen to be associated with the ring-opened carbon chain of the thiolate, the end-group of which is imaged with a higher intensity.

Figure 3 shows the proposed reaction pathway leading to the adsorbed C₄H₇S state. We have included a calculation of the activation barrier for what we assume is the most difficult step on this path, the C_α-S bond cleavage. It is interesting to note that the associated barrier is rather modest (~1 eV). This means that, at the temperature (~500 K) where we

adsorb thiophene, equilibrium between C₄H₇S and thiophene in the gas phase is easily achieved. The same will of course also be true for industrial hydrotreating conditions [1]. The barrier for the reverse reaction (see figure 3) is, however, large enough that thiophene is not desorbed during imaging at room temperature, in accordance with our experimental observation. The final configuration associated with a ring-opened thiolate structure absorbed on the cluster edge is simply an ordinary thiol. After the first C_α-S bond in thiophene has been broken, the sulfur is much more reactive and the final extrusion may take place at another site on the cluster to complete the HDS process. Such sites are most probably sulfur vacancies (coordinatively unsaturated metal atoms) located at the MoS₂ edges [1, 7, 11]. It is likely that this will require surface diffusion of the thiolates along the edge (or through the gas phase) to such vacancies for the final step in the overall reaction process. From a consecutive sequence of STM images such as figure 2(A) (so-called STM movies), we indeed observe a high mobility at room temperature of the adsorbed thiolate species (see movie 1) supporting the notion that the reactivity may involve a two-step process. At present, we have not observed the last step directly, since the STM experiment captures the model catalyst in a quenched situation, not favouring the further reaction of thiolates. Unlike under real catalytic conditions, the number of available vacancies has become depleted due to the recombination with other thiols prior to imaging. Nevertheless, the reaction of thiolates is not expected to be difficult at reaction conditions since thiols are typically much more reactive than thiophenes.

We have thus identified a new route for activating a relatively inert, sulfur-containing molecule such as thiophene. It takes place by hydrogenation of the double bonds followed by a C_α-S bond breaking. Remarkably, the completely sulfur-saturated Mo edge is able not only to hydrogenate the C-C double bonds in the presence of S-H groups but also to break the C_α-S bond of the hydrogenated thiophene. All the processes take place on top of the sulfur atoms of the

MoS₂ structure with no direct interaction with the Mo atoms. We associate this interesting chemistry with the metallic edge states of the MoS₂ nanocrystals, since we find no indication of chemical activity, experimentally or theoretically, at the S atoms on the basal plane of the MoS₂ structures. The metallic states associated with S atoms at the edges, on the other hand, have the ability to donate and accept electrons and thus act as catalytic sites just like ordinary metal surfaces. We suggest that the chemical activity associated with sites on the metallic edge states may be of general importance, providing a route for the hydrogenation of aromatics, which is an integral part of hydrotreating catalysis [1, 2]. In fact, as the demands for cleaner transport fuels grow, it is of increasing importance to be able to hydrogenate averse aromatic compounds [1, 2, 26, 27] and the new atomistic insight may aid the design of the next-generation hydrotreating catalysts. Generally, nanoparticles have inherently different electronic properties, and thus reactivity, to their macroscopic counterparts. So far, no general description of the reactivity of nanoclusters has been available, but the approach presented here should be applicable to inorganic nanoclusters on conducting substrates in general, and may therefore provide a breakthrough in our understanding of nanoscale reactivity.

Acknowledgments

We acknowledge stimulating discussions with S Helveg. This work was supported by the Danish National Research Foundation through the Centre for Atomic-Scale Materials Physics (CAMP). JVL acknowledges support from the Interdisciplinary Centre for Catalysis (ICAT).

References

- [1] Topsøe H, Clausen B S and Massoth F E 1996 *Hydrotreating Catalysis, Science and Technology* vol 11, ed J R Anderson and M Boudart (Berlin: Springer)
- [2] Prins R 1997 *Handbook of Heterogeneous Catalysis* ed G Ertl, H Knözinger and J Weitkamp (Wienheim: VCH) p 1908
- [3] Ertl G 2001 *J. Mol. Catal. A* **128** 5–16
- [4] Over H *et al* 2000 *Science* **287** 1474–6
- [5] Schaub R *et al* 2001 *Phys. Rev. Lett.* **87** 6104
- [6] Linsebigler A, Lu G and Yates J T J 1995 *Chem. Rev.* **95** 735–58
- [7] Helveg S *et al* 2000 *Phys. Rev. Lett.* **84** 951–4
- [8] Lauritsen J V *et al* 2001 *J. Catal.* **197** 1–5
- [9] Bollinger M V *et al* 2001 *Phys. Rev. Lett.* **87** 196803/1
- [10] Salmeron M, Somorjai G A, Wold A, Chianelli R and Liang K S 1982 *Chem. Phys. Lett.* **90** 105
- [11] Byskov L S, Nørskov J K, Clausen B S and Topsøe H 1999 *J. Catal.* **187** 109–22
- [12] Raybaud P, Hafner J, Kresse G, Kasztelan S and Toulhoat H 2000 *J. Catal.* **189** 129–46
- [13] Angelici R J 2001 *Organometallics* **20** 1259–75
- [14] Kishan G, Coulier L, de Beer V H J, van Veen J A R and Niemantsverdriet J W 2000 *J. Catal.* **196** 180–9
- [15] Rodriguez J A, Dvorak J, Capitano A T, Gabelnick A M and Gland J L 1999 *Surf. Sci.* **429** L462–8
- [16] Wiegand B C and Friend C M 1992 *Chem. Rev.* **92** 491
- [17] Lægsgaard E, Besenbacher F, Mortensen K and Stensgaard I 1988 *J. Microsc.* **152** 663–9
- [18] Perdew J P *et al* 1992 *Phys. Rev. B* **46** 6671–87
- [19] Hammer B and Nørskov J K 2001 *Adv. Catal.* **45** 71–129
- [20] Jonsson H, Mills G, Jacobsen K W, Berne B J, Ciccotti G and Coker D F 1998 *Classical and Quantum Dynamics in Condensed Phase Simulations* (Singapore: World Scientific) pp 385–404
- [21] Tersoff J and Hamann D R 1985 *Phys. Rev. B* **31** 805–13
- [22] Bollinger M V, Jacobsen K W and Nørskov J K 2003 *Phys. Rev. B* at press
- [23] Lauritsen J V *et al* 2003 in preparation
- [24] Topsøe N-Y and Topsøe H 1993 *J. Catal.* **139** 641–51
- [25] Tarbuck T L, McCrea K R, Logan J W, Heiser J L and Bussell M E 1998 *J. Phys. Chem. B* **102** 7845–57
- [26] Derouane E G 2001 *Cattech* **5** 214–25
- [27] Whitehurst D D, Isoda T and Mochida I 1998 *Adv. Catal.* **42** 345–471

II



CO Desorption Rate Dependence on CO Partial Pressure over Platinum Fuel Cell Catalysts

J. C. Davies¹, R. M. Nielsen¹, L. B. Thomsen¹, I. Chorkendorff^{1*}, Á. Logadóttir², Z. Lodziana², J. K. Nørskov², W. X. Li³, B. Hammer³, S. R. Longwitz⁴, J. Schnadt⁴, E. K. Vestergaard⁴, R. T. Vang⁴ and F. Besenbacher⁴

¹ Interdisciplinary Center for Catalysis (ICAT), Department of Physics, Department of Chemical Engineering, Technical University of Denmark, Building 312, DK-2800 Lyngby, Denmark

² Center for Atomic-Scale Materials Physics (CAMP), Department of Physics, Technical University of Denmark, Building 307, DK-2800 Lyngby, Denmark

³ Interdisciplinary Nanoscience Center and Institute of Physics and Astronomy, University of Aarhus, Ny Munkegade, DK-8000 Aarhus C, Denmark

⁴ Center for Atomic-Scale Materials Physics (CAMP), Interdisciplinary Nanoscience Center, and Department of Physics and Astronomy, University of Aarhus, DK-8000 Aarhus C, Denmark

Received October 16, 2003; accepted March 18, 2004

Abstract

Carbon monoxide adsorption on high area platinum fuel cell catalysts was investigated. Isotopic exchange experiments were performed to determine the exchange rate (k) of CO under different partial pressures of CO (p_{CO}) in argon. A linear dependence of $\ln(k)$ with $\ln(p_{\text{CO}})$ was observed. This pressure dependence of the rate of exchange is explained by considering a change in surface coverage of CO with different CO pressures and a subsequent reduction in the CO binding energy as demonstrated by Density Functional The-

ory (DFT) calculations. High Pressure Scanning Tunneling Microscopy (HP STM) studies on the Pt(111) surface have also displayed a pressure dependency of the coverage consistent with this data. The relevance of these observations to the Polymer Electrolyte Membrane Fuel Cell (PEMFC) anode reaction is discussed.

Keywords: Co-Tolerance, Ligand Effect, PEM Fuel Cell, Platinum, Ruthenium

1 Introduction

Proton Exchange Membrane Fuel Cells (PEMFC) are the most likely fuel cells to achieve commercialisation for automotive purposes due to their low operating temperatures and their inherent properties of being lightweight, producing high current densities and containing no corrosive materials [1]. At the anode of the fuel cell hydrogen dissociation and oxidation to protons occurs. This electrode is generally platinum-based due to the high current densities obtained [2, 3] and its inherent stability within fuel cell operating conditions. The protons formed then pass through a proton conducting membrane to the supported platinum cathode where they combine with oxygen to form water. If the hydrogen feed to the anode is to be produced at reasonable prices, inline reformation of a

hydrocarbon species, e.g., methanol, is a viable option. Reforming methanol by partial oxidation or steam reforming produces a hydrogen feed which can contain approximately 1% CO, along with 25% CO₂. It is very difficult to remove this CO entirely and as little as 20 ppm of CO is known to poison the hydrogen oxidation reaction at the anode by binding strongly to the platinum surface [4]. It has been shown that by alloying platinum with ruthenium the anode tolerance to CO can be increased [5]. Currently, there are two proposed mechanisms for this promotion:

i) The bifunctional effect [6, 7]: It can be demonstrated that alloying Pt and Ru (with an optimal ratio of 50:50)

[*] Corresponding author, ib.chorkendorff@fysik.dtu.dk

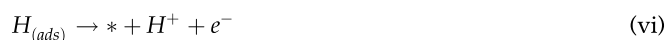
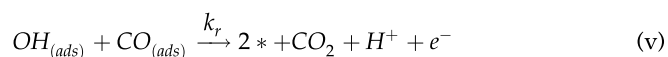
reduces the overpotential required for the oxidation of pure CO to CO₂ by water [8–12]. This reduction in overpotential is due to the more facile dissociation of water on ruthenium. This mechanism has been further elucidated on model alloy systems prepared in vacuum and then investigated electrochemically [13–15] and also theoretically [16–18].

- ii) The ligand effect [1, 19–21]: Here, alloying ruthenium with platinum alters the chemical properties of the surface platinum atoms. It has been found both experimentally [14, 22] and theoretically [16–18, 23–26] that the Pt-CO bond strength in a platinum/ruthenium alloy is significantly reduced compared to that on pure platinum.

In the situation where CO oxidation occurs in the presence of hydrogen, it has been suggested that there may be a combined mechanism where both of the above processes are relevant [6, 27].

An important question in connection with the unravelling of the two possible mechanisms is whether CO from the reactant stream is in equilibrium with CO on the surface. If this is the case, then the ligand effect must be a factor, a weaker CO bond must lead to a lower CO coverage. This of course does not preclude a contribution from the bifunctional effect.

This can be expressed using the following kinetic description of the processes occurring at a fuel cell anode:



It can be seen that steps (ii) and (v) are the only two involving CO. At steady state the coverage of CO will be governed by the following equation:

$$\frac{d\theta_{CO}}{dt} = k_a p_{CO}(1 - \theta_{CO}) - k_d \theta_{CO} - k_r \theta_{CO} = 0$$

or

$$\theta_{CO} = \frac{k_a p_{CO}}{k_a p_{CO} + k_d + k_r} = \frac{k_a p_{CO}}{k_a p_{CO} + k_d} \times \left(\frac{1}{1 + \frac{k_r}{k_a p_{CO}}} \right) \quad (1)$$

Rearranging this equation, it can be shown that the steady state coverage of CO on the surface can be expressed as two terms, the first of which is the coverage determined by the CO adsorption equilibrium, whilst the second term is a correction due to the effect of CO oxidation. From this second term it can be determined that for the rate of oxidation of CO

to play a significant role it would have to be large compared to the combined rates of adsorption and desorption.

It is with this in mind that the equilibrium rates of desorption will be determined during the course of this paper.

The adsorption of CO on platinum is a thoroughly researched area, but the majority of surface studies are limited to the high vacuum regime. In nanoscale platinum particles the (111) face is favoured at the surface, hence this system will be treated in detail here. Ertl et al. have studied the adsorption of CO at 170 K on Pt(111) by LEED and TPD [28]. A diffuse ($\sqrt{3} \times \sqrt{3}$)R30° LEED pattern was observed for an overlayer of $\theta \leq 0.33$ and spectroscopic evidence from EELS [29, 30] and RAIRS [31] experiments have shown that, at this coverage, only linear CO is present ($\sim 2110 \text{ cm}^{-1}$). At a coverage of $\theta \leq 0.5$ this transforms into a $c(4 \times 2)$ overlayer with both linear and bridge-bound species present in a 1:1 ratio [31]. The presence of a $c(4 \times 2)$ structure below $\theta = 0.5$ is explained by island formation of the adsorbed species. Further splitting of the $c(4 \times 2)$ structure is observed up to a saturation coverage of 0.67.

Recently, work has been performed by several groups in an attempt to bridge the pressure gap in this regime. Besenbacher et al. have observed CO overlayers on Pt(111) in the high pressure regime by STM [32]. A maximum coverage of 0.68 ML was again obtained leading to the conclusion that raising the pressure was equivalent to lowering the temperature, as long as the thermodynamic equilibrium structure remains kinetically accessible. Sum Frequency Generation studies by Rupprechter et al. observed a 40% increase in the intensity of the linear bound CO from the $c(4 \times 2)$ structure to the saturation coverage. The coverage dependence on the binding energy of the CO on Pt(111) is well known under these pressure regimes. Ertl et al. observed an initial adsorption energy of 138 kJ mol^{-1} at room temperature, reducing to 62 kJ mol^{-1} at the saturation coverage of 0.67 [28]. Microcalorimetry experiments by Yeo et al. have also demonstrated a shift in the heat of adsorption from a value of 183 kJ mol^{-1} at a coverage of 0.05 ML down to a value of 75 kJ mol^{-1} at a coverage of 0.75 ML [33].

In previous studies, which were concerned with investigating the replacement of C¹³O preadsorbed by gaseous C¹²O on polycrystalline platinum [34] no effect of changing pressure was observed, but these experiments were performed in a low pressure regime ($1.5\text{--}4.6 \times 10^{-7}$ mbar). However, a dependence on temperature was observed. A value of 90 kJ mol^{-1} for the activation energy was obtained leading to a rate of desorption of $3.50 \times 10^{-9} \text{ mol m}^{-2} \text{ s}^{-1}$.

An isothermal kinetic study of hydrogen induced CO displacement has previously been performed by Parker et al. [35]. They observed that chemisorbed CO could be completely removed from the Pt(111) surface at temperatures from 318–348 K and hydrogen pressures above 2.6×10^{-2} mbar. In this temperature range only a fraction of the CO is removed by thermal desorption. They proposed that repulsive interactions between the CO and atomic hydrogen lead to lower values of the desorption activation energy.

It will be demonstrated, by isotopic exchange experiments and DFT calculations, that there is a significant relationship between the pressure of CO above a platinum catalyst surface and the subsequent desorption rate, binding energy and coverage of the CO. These observations will be used to elucidate the mechanism for fuel cell anode catalysis.

2 Experimental

Experiments were performed on the system given in Figure 1. The sample used was a commercial membrane electrode assembly or MEA (Electrochem. Inc.) consisting of a Nafion[®] 115 membrane, both sides of which were mounted with Toray carbon paper impregnated with the highly dispersed platinum catalyst. The catalyst loading was 1 mg cm^{-2} and the total area of each carbon electrode 5 cm^2 . The electrode was mounted in a stainless steel cell between brass connecting flow field plates.

For the purposes of the experiments presented, the system was used in a flow mode and only one electrode was used for adsorption experiments, i.e., open circuit mode with pure argon flow on the cathode side. The gas content was investigated using a quartz tube sniffer connected to a mass spectrometer [36]. The gas dosing system allowed for fast interchange between a variety of different gases. The highest available gas purities were always used. All experiments

were performed at room temperature and no humidification was used in the gas streams.

Measurements were also performed on a Pt(111) single crystal using a combination of a UHV STM and a high pressure STM with the facility for *in situ* scanning over a range of 13 orders of magnitude of pressure from 10^{-10} mbar up to 1 bar. The system used for these studies is described in detail elsewhere [37].

3 Calculations

To calculate adsorption energies Density Functional Theory (DFT) calculations were used. The DFT calculations were based on a plane-wave expansion of the wave functions, a RBPE description of exchange and correlation effects [38], and ultra-soft pseudopotentials [39]. Plane waves with kinetic energies of up to 25 Ry were used. The self-consistent electron density was determined by iterative diagonalization of the Kohn-Sham Hamiltonian, Fermi-population of the Kohn-Sham states ($k_B T = 0.1 \text{ eV}$), and Pulay mixing of the resulting electronic density [40]. All total energies have been extrapolated to $k_B T = 0 \text{ eV}$. The Pt(111) surface was studied and was modelled with 4 layer slabs and with 6 layers of vacuum between the slabs. A fcc structure with a lattice constant of $a = 4.02 \text{ \AA}$ was used. The CO and the top-most Pt layer were allowed to relax.

The aim of the study was to find the adsorption energy of CO at different coverages. To obtain these differences in coverage the adsorption energy was calculated using several different surface unit cells, (1×1) ($\theta = 1.0$), (2×2) ($\theta = 0.25$), $(\sqrt{3} \times \sqrt{3})R30^\circ$ ($\theta = 0.33$), $c(4 \times 2)$ ($\theta = 0.5$) and a unit cell containing 13 CO molecules ($\theta = 0.68$) as is shown in Ref. [32]. The k points used in the calculations for the Pt(111) surface are a regular grid of $4 \times 4 \times 1$ and $6 \times 6 \times 1$ for the coverages $\theta = 0.25$, 0.333. For $\theta = 0.5$ and 1.0, 4 and 54 special k points were used. One special k point was used to find the CO adsorption energy at $\theta = 0.68$.

CO on Pt(111)

The rich experimental evidence of the adsorption properties of CO on Pt(111) are summarised in Figure 2 together with the calculated integral heats of adsorption, E_{ads}^{int} . A strong coverage dependence of E_{ads}^{int} is evident irrespective of the experimental method used. Theoretical predictions give a slightly larger coverage dependence.

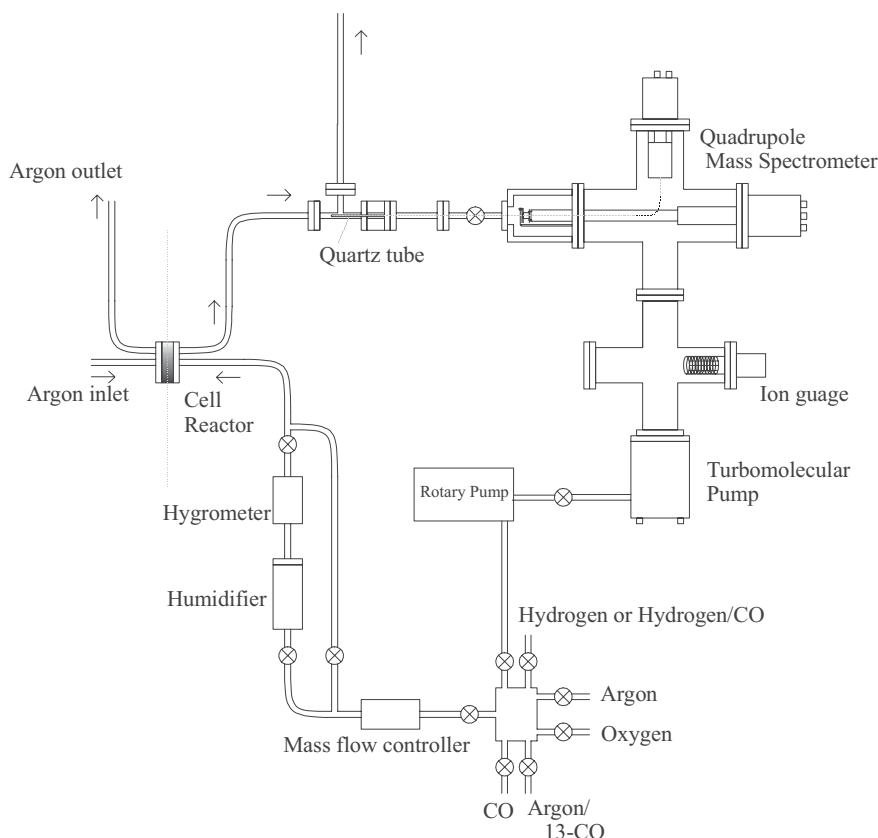


Fig. 1 Apparatus used for flow data measurement.

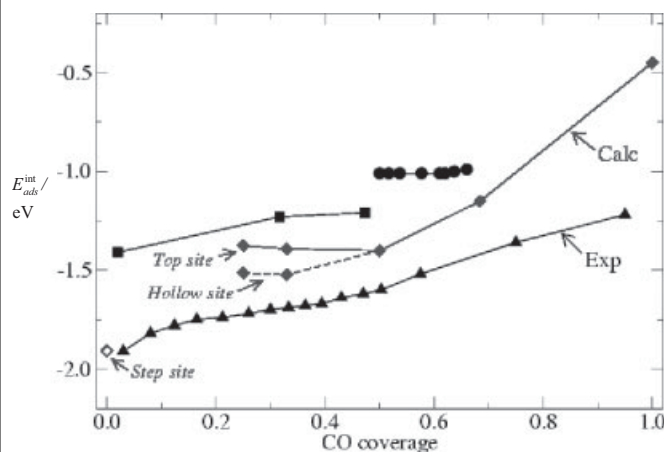


Fig. 2 The integrated enthalpies for CO adsorption (E_{ads}^{int}) at different coverages. The DFT results (diamonds) are compared to three different sets of experimental results (triangles, circles and squares) taken from [33], where differential enthalpies have been changed to integrated enthalpies for comparison with the calculated results. The enthalpy for CO adsorbed at a step site (open diamond) is taken from [41].

4 Results and Discussion

Initially, the Pt catalyst used was characterised experimentally by adsorption with CO, and subsequent oxidation with O₂. CO was dosed on the high area catalyst surface by exposure of the surface to a flow of CO at 1 bar pressure for approximately 15 min. (hereby ensuring saturation coverage). The flow of CO was then replaced by an argon flow for a time of 20 min. to remove background CO, and was subsequently titrated with O₂. The m/z 44 profile was measured during oxygen exposure and a CO₂ production profile could also be measured in the mass spectrometer (Figure 3). From this it was necessary to subtract a background arising from

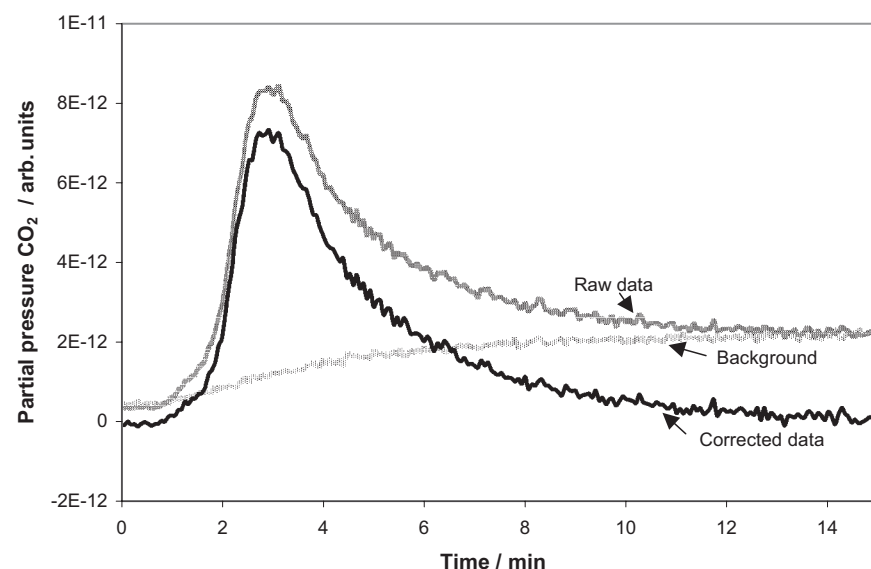


Fig. 3 The evolution of CO₂ arising from the titration of adsorbed CO with 1 bar of O₂. The subtraction of the background obtained due to reaction of oxygen in the mass spectrometer is also shown.

CO₂ formed by oxygen reaction within the mass spectrometer. This background was measured by switching from pure argon to O₂ over a catalyst previously oxygen passivated. In this manner no response is expected from the catalyst and the signal observed is solely due to an increased background of CO₂ in the mass spectrometer, due to the increased pressure of oxygen. From the area of the corrected peak the number of moles of CO₂ can be determined, and then, making certain assumptions, an overall surface area for the catalyst can be approximated. If it is assumed that the saturation coverage is 0.68, as observed on Pt(111), then a surface area of 0.58 m² is obtained. Assuming that the particles are spherical then an average particle size of ~2.5 nm is obtained. It should be noted that 0.68 is the coverage calculated on Pt(111) at 1 bar CO pressure, and that, as shall be demonstrated within the course of this article, the coverage after exposure to 1 bar pressure of Ar for a period of 20 min. will be lower than this value. However, as a direct value cannot be measured, 0.68 was determined to be accurate enough for the purpose of determining the approximate particle size and total surface area.

The next stage was to investigate the stability of overlayers of adsorbed C¹³O on exposure to flows of certain gases and gas mixtures in order to determine the exchange rate for CO from small platinum particles under these conditions.

Firstly, an overlayer of adsorbed CO was exposed to a flow of argon for differing lengths of time and the CO was then titrated with O₂ and the relative coverage obtained (Figure 4). This was in order to determine that there was no effect due to the oxidation of small levels of contaminant species in the pure gases. It can be seen that the coverage decreases to a limiting value after about 4 h, but after this time stabilises and no further reduction is observed. The latter observation is in good agreement with the traditional view of CO poisoning in the PEMFC by a strongly bound overlayer. Note that the depletion in CO coverage is also shown, as observed in the situation where there is oxygen present in the gas stream at a fixed level of contamination. Here, the depletion of CO due to oxidation by contaminant oxygen is strongly observed.

It is not known whether the observation of a decrease in coverage within the first few hours is a real effect or due to the readsorption of some CO from the background (in these experiments where CO is dosed at 1 bar, a slowly decaying background of CO is observed). However, this could tentatively be ascribed to CO in a higher coverage regime at a pressure of 1 bar, slowly desorbing down to its equilibrium level at a pressure of 1 bar of argon, which appears to be attained after a few hours, particularly as the ratio of the highest and lowest cov-

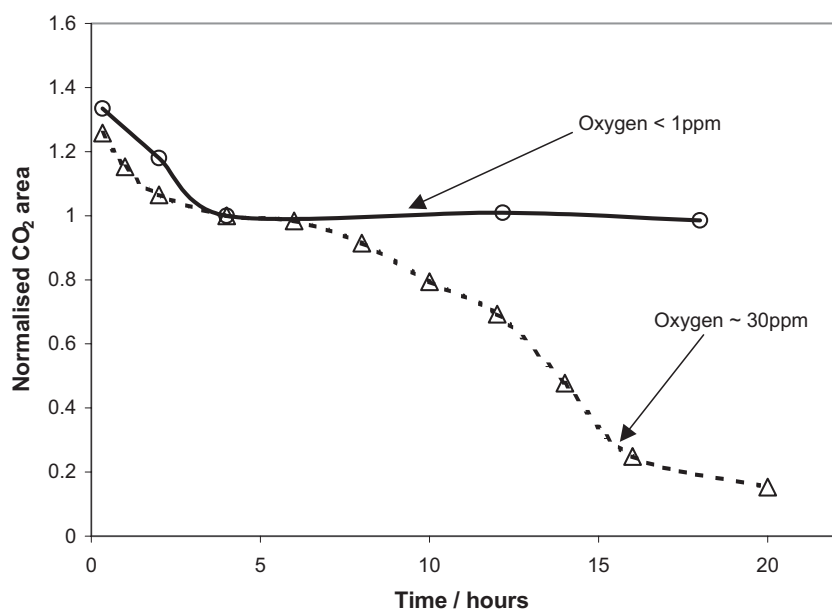


Fig. 4 Plot of normalised CO_2 peak area against time of exposure. CO is dosed at 1 bar, then replaced by a flow of argon. After a given exposure time the remaining CO is titrated with O_2 to produce CO_2 . Data is shown for an oxygen-free and oxygen contaminated system.

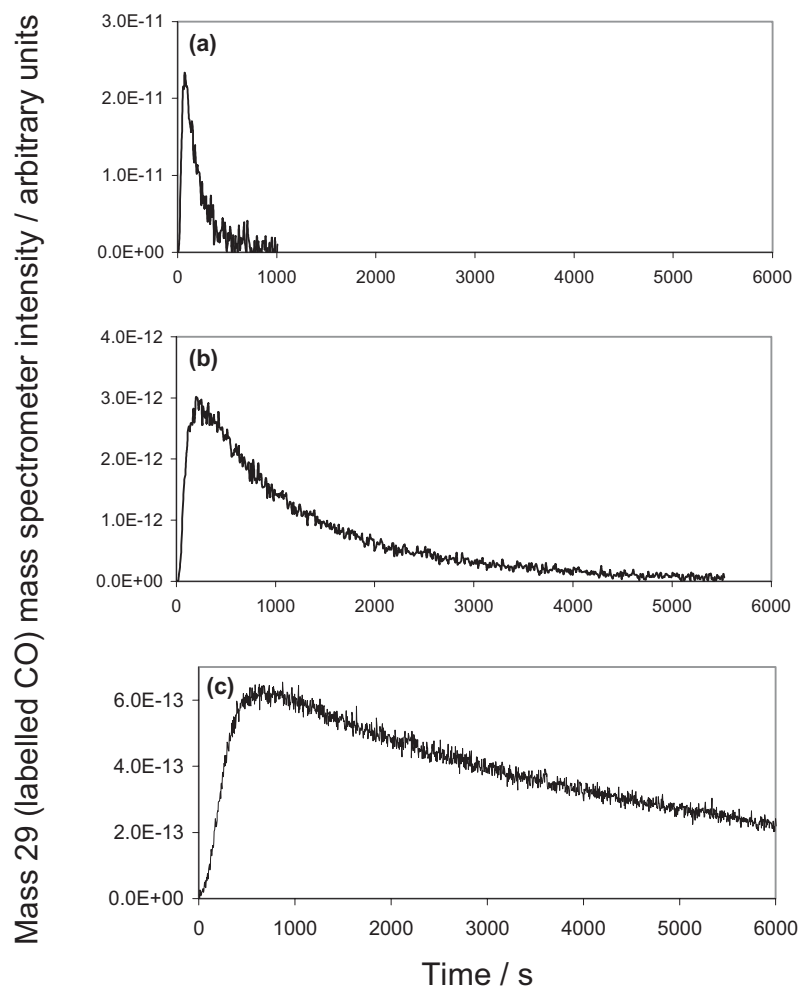
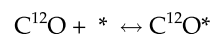


Fig. 5 Plots showing C^{13}O desorption in flows of: (a) 1 bar CO, (b) 1000 ppm CO in argon and (c) 100 ppm CO in argon from the platinum electrocatalyst.

erages observed is approximately the same as the ratio between the coverage observed by Besenbacher et al. at 1 bar CO of 0.68 [32] and the coverage observed under vacuum on Pt(111) of 0.5 [32].

Secondly, an overlayer of C^{13}O was adsorbed on the platinum surface and a stream of pure C^{12}O (1% C^{13}O) was passed over the surface at 12 ml min^{-1} . The level of C^{13}O in the exit stream was monitored and it was found that the C^{13}O was almost entirely removed after 10 min. Reducing the C^{12}O content in the stream to 1000 ppm C^{12}O in argon lead to a reduction of the rate of removal of C^{13}O from the surface. In addition, a similar exchange experiment was performed for 100ppm CO in argon, a concentration which is not unlike that of the fuel cell supply gas [1]. Figure 5 shows the measured traces for desorbing C^{13}O in these experiments. Figure 6 shows a plot of $\ln(\theta)$ versus time including additional data for a C^{12}O overlayer exposed to 1% C^{13}O , and a C^{13}O overlayer exposed to a flow of pure hydrogen. It can be seen that at room temperature virtually no CO desorbs in the time period of 10,000 seconds in pure hydrogen, which seems reasonable, considering that hydrogen interacts more weakly with platinum than CO does. This was confirmed by titrating the remaining C^{13}O with oxygen after the period of hydrogen exposure. In contrast Gland et al. have determined that at 318–348 K the presence of hydrogen at a pressure of $\sim 3 \text{ mbar}$ strongly influences the desorption of CO on a Pt(111) single crystal [35]. No observable desorption rate is seen under these conditions within the detection limit of the experiments.

The kinetic regime for this system is as follows, where * represents an adsorption site:



From this the following kinetic expressions can be derived:

$$\frac{d\theta_{\text{C}^{12}\text{O}}}{dt} = k_2^+ P_{\text{C}^{12}\text{O}} \theta_* - k_2^- \theta_{\text{C}^{12}\text{O}} \quad (2)$$

$$\frac{d\theta_{\text{C}^{13}\text{O}}}{dt} = k_1^+ P_{\text{C}^{13}\text{O}} \theta_* - k_1^- \theta_{\text{C}^{13}\text{O}} \quad (3)$$

$$\theta_* = 1 - \theta_{\text{C}^{13}\text{O}} - \theta_{\text{C}^{12}\text{O}} \quad (4)$$

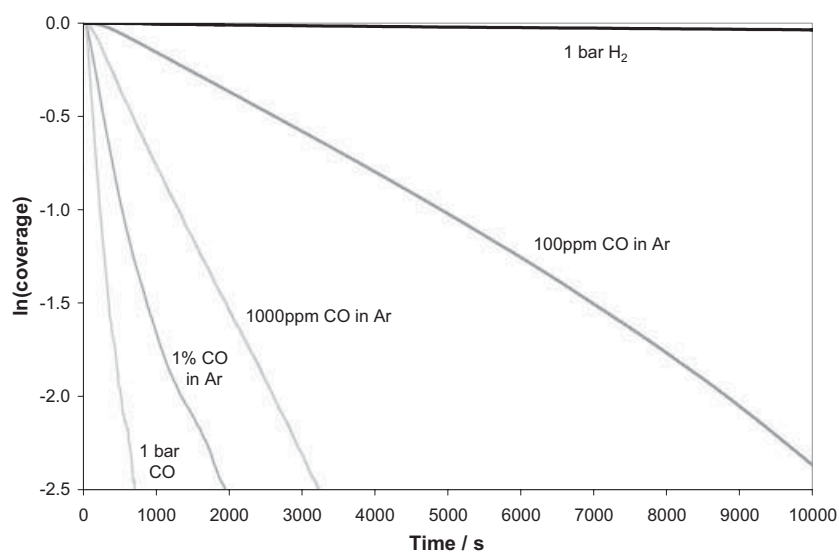


Fig. 6 Plot of \ln of the normalised coverage versus time for a preadsorbed overlayer of $C^{13}O$ under flows of various gases and gas mixtures.

For a simple model it is necessary to assume that the pressure of $C^{13}O$ above the surface is zero, although 1% of the gas adsorbing will in fact be $C^{13}O$ from the natural abundance of C^{13} . It is also assumed that, over the flow rate range used for these experiments (12–15 ml min), there is no readsorption of desorbed $C^{13}O$.

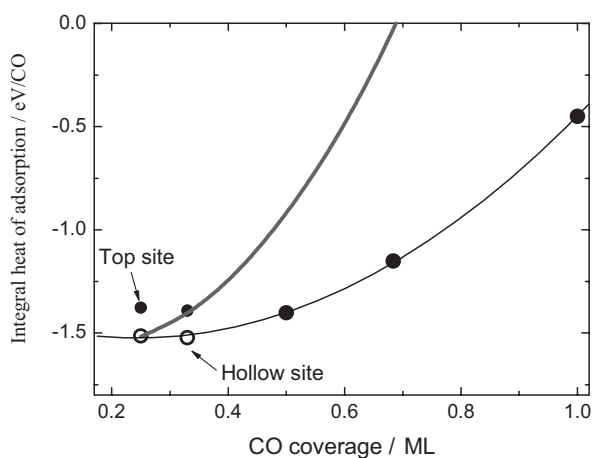


Fig. 7 The integral heats of adsorption for CO on Pt(111) at different coverages calculated using DFT. The lower thin line is the second order polynomial fit to the most stable adsorption configuration whilst the upper thick line gives the differential heat of adsorption.

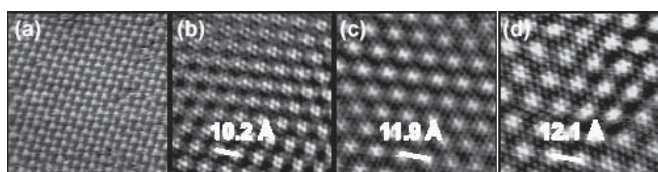


Fig. 8 STM images ($75 \times 75 \text{ \AA}$) of CO adsorption structures on Pt(111) at different CO pressures. (a) 1.33×10^{-7} mbar, (b) 1.33×10^{-2} mbar, (c) 133 mbar, (d) 960 mbar. Notice the change in the periodicity of the Moiré superstructure on (b)–(d).

Hence Eq. (3) reduces to:

$$\frac{d\theta_{C^{13}O}}{dt} = -k_1^- \theta_{C^{13}O} \quad (5)$$

resulting in:

$$\theta_{C^{13}O} = \theta_{C^{13}O}^0 e^{-k_1^- t} \quad (6)$$

Thus the gradient of a plot of $\ln(\theta)$ vs. t , as observed in Figure 6, is a direct measurement of the rate of exchange.

The change in the rate of desorption for different partial pressures of CO (cf. Figure 6) necessarily derives from a change in the bonding energy of the CO. From these calculations on Pt(111) it is believed that a sharp decrease in the differential heat of adsorption of CO occurs for coverage above 0.5 ML (see Figure 7). Increasing the partial pressure of CO above the surface leads to a

subsequent increase in coverage and the strongly repulsive lateral interactions that result lead to a significant increase in the rate of desorption.

In addition, the pressure dependence of the CO saturation coverage on Pt(111) was directly observed by *in situ* high pressure (HP) scanning tunnelling microscopy (STM). The combination of the home-built Aarhus [42] UHV STM with a novel HP STM (described in detail elsewhere [37]) facilitated *in situ* scanning on Pt(111) in a CO atmosphere over 13 orders of magnitude of pressure, ranging from 10^{-10} mbar up to 1 bar.

The CO adsorption structure was characterized at varying CO pressures. At 10^{-10} mbar and at temperatures slightly below room temperature ($-28 \text{ }^\circ\text{C}$) the $c(4 \times 2)$ commensurate overlayer was found (Figure 8a) [43], that can also be observed by LEED on room temperature samples [28]. Increasing the CO pressure to $> 6.7 \times 10^{-5}$ mbar results in the formation of a new CO adsorption structure (Figure 8b–d), in which a hexagonal superstructure with a periodicity of 3–4.5 times the periodicity of the substrate platinum is observed. Such a hexagonal superstructure has previously been found at 1 bar of CO on Pt(111) [32] in the form of a so-called Moiré structure. Such a superstructure arises from the interference between the hexagonally packed Pt surface and the hexagonally packed CO overlayer, which is rotated with respect to the Pt. Further details will be published elsewhere [44].

The reversibility of the formation of these CO Moiré structures was investigated by performing experiments where a given CO pressure was reached following different routes, either by lowering the pressure from a higher value or by increasing the pressure from a lower value. In both types of experiments the same CO adsorption structure was found. This implies that the Moiré structure changes reversibly and continuously with CO pressure. The latter is illustrated in Figure 9, in which the periodicity of the Moiré superstructure relative to the platinum substrate has been plotted for differ-

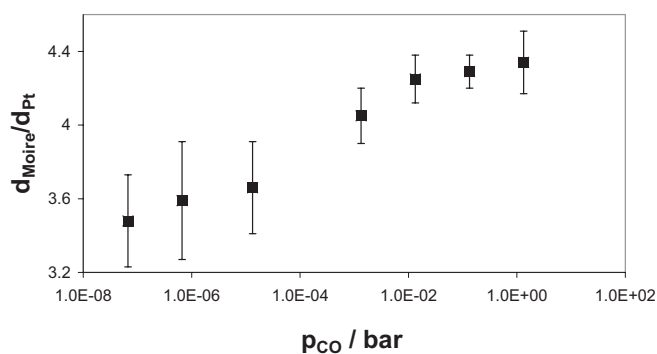


Fig. 9 The periodicity of the Moiré superstructure as a function of the CO pressure. $d_{Moiré}$ is the distance between adjacent Moiré patterns and d_{Pt} is the nearest-neighbour distance of the atoms on the Pt(111) surface.

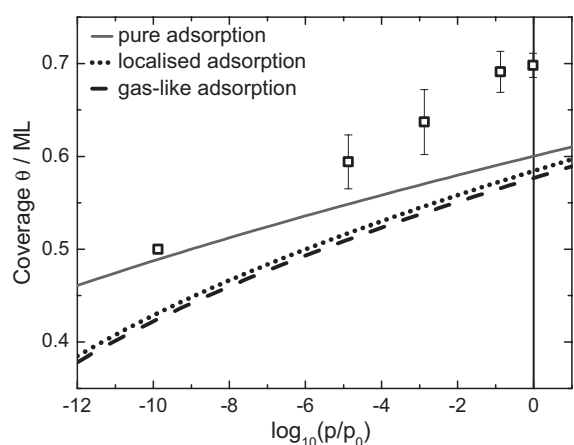


Fig. 10 The experimental data shows the CO coverage versus the CO pressure as measured with the HP STM. Also shown is the calculated equilibrium coverage of CO on the Pt(111) surface at room temperature (see text). The solid line represents the adsorption model not including any effects related to the statistics of CO adsorption on the surface. The dotted line is for the lattice gas model, and the dashed line represents a model of the mobile CO at the surface.

ent CO pressures. From high resolution STM images, such as those in Figure 8, the CO distance can be directly extracted by counting the individual CO molecules, and in this way the CO coverage can be determined as a function of the CO pressure. This has been plotted in Figure 10, where a clear pressure dependence of the CO coverage is observed.

5 Model of Adsorption

Calculated adsorption properties of CO provide a good starting point for the construction of a simple model of adsorption kinetics, which will be further used to compare with the experimental data presented above.

The equilibrium chemical potential of CO in the gas phase must be equal to that of the adsorbed state ($\mu_{gas} = \mu_{ads}$). From microscopic theory the chemical potential of an ideal gas

$$\mu_{gas} = -k_B T \frac{\partial \ln(Q_g)}{\partial N_g}$$

is given by:

$$\begin{aligned} \mu_{gas} &= -k_B T \ln \left(\frac{(2\pi M k_B T)^{3/2} k_B T}{h^3 p_0} \right) + \mu_{vib-rot} + k_B T \ln \left(\frac{p}{p_0} \right) \\ &= -TS_0 + k_B T \ln \left(\frac{p}{p_0} \right) \end{aligned} \quad (7)$$

where Q_g is the partition function for the ideal CO gas and $M = (m_O + m_C)$ is the mass of the gas molecule, h is Planck's constant, $\mu_{vib-rot}$ are the contribution from the vibrational and rotational degrees of freedom, and p and p_0 are the actual and standard pressures, respectively. The entropic term can be calculated from the microscopic model. The lengthy formulas for rotational and vibrational modes can be found in good textbooks [45]. Also, S_0 can be found in standard thermodynamic tables [46] and for CO $S_0 = 197 \text{ J kmol}^{-1}$ at standard thermodynamic conditions.

The chemical potential of adsorbed CO depends on the specific model used to describe adsorption. Two extreme cases are usually considered: localized adsorption, where adsorbed molecules are fixed at the adsorption sites (thus do not move on the surface) and mobile adsorption, where the adsorbent is free to move on the surface. It is safe to assume that the properties of CO are somewhere between these extremes. The chemical potential of adsorbed CO consists of contributions from the particular lattice statistics (μ_{stat}), vibrational properties ($\mu_{frus-vib}$) and both surface and mutual CO interaction (μ_{int}).

$$\mu_{ads} = \mu_{int} + \mu_{stat} + \mu_{frus-vib} \quad (8)$$

To determine the chemical potential of adsorbed CO the coverage $\theta = \frac{N}{M} = \frac{N_a}{A}$ is introduced where N molecules are adsorbed on M available sites, or they cover an area N_a of the total surface area available, A . The interaction part of the free energy can be determined directly from the DFT calculations, as the coverage dependence of $E_{ads}(\theta)$ is known (see Figure 7). Hence:

$$\begin{aligned} \mu_{int} &= -k_B T \frac{\partial \ln((q_{ads})^N)}{\partial N} \\ &= -k_B T \frac{\partial \ln \exp(-NE_{ads}^{int}(\theta)/k_B T)}{\partial N} \\ &= k_B T \frac{\partial NE_{ads}^{int}(\theta)/k_B T}{\partial N} = \left(E_{ads}^{int}(\theta) + \theta \frac{\partial E_{ads}^{int}(\theta)}{\partial \theta} \right) = E_{ads}^{diff} \end{aligned} \quad (9)$$

which is simply the differential heat of adsorption. This treatment of the interaction is purely phenomenological, as the details of the interaction energy are not considered, which is an obvious limitation, but there is a great advantage to this approach, which is that the model can be solved analytically.

In the case of localised adsorption, all gas translational and rotational degrees of freedom are lost in favour of frustrated vibrational modes of the adsorbed CO molecule. This part of the chemical potential can be written as:

$\mu_{frus-vib} = -k_B T \ln(q_{frus-vib})$, where the vibrational partition function runs over all modes:

$$q_{frus-vib} = \sum_i \exp(-\varepsilon_i/2k_B T) / [1 - \exp(-h\nu_i/k_B T)].$$

Finally the statistics of the adsorbed phase give the configurational entropy for the localised adsorption:

$$\mu_{stat} = -k_B T \partial \ln \left(\frac{M}{(M-N)N} \right) / \partial N = -k_B T \ln \left(\frac{\theta}{1-\theta} \right).$$

Notice that this is a standard expression for lattice models, but it is also valid for mobile adsorption, as long as the finite size of CO is taken into account. In the limit of point molecules the formula reduces to that of a 2-dimensional ideal gas. If CO is mobile at the surface, a very reasonable assumption as there is only a very small difference between the CO adsorption energies at different surface sites, then this has to be taken into account, and an additional term enters the free energy, equivalent to the pressure in a 3-dimensional gas and equal to $k_B T \frac{\theta}{1-\theta}$.

The chemical potential of adsorbed CO equals:

$$\mu_{ads} = E_{ads}^{int}(\theta) + \theta \frac{\partial E_{ads}^{int}(\theta)}{\partial \theta} + \mu_{stat} + \mu_{frus-vib} \quad (10)$$

and the last term varies with the adsorbent properties.

$$\mu_{stat} = k_B T \ln \left(\frac{\theta}{1-\theta} \right) \text{ for localised adsorption and}$$

$$\mu_{stat} = k_B T \ln \left(\frac{\theta}{1-\theta} \right) + k_B T \left(\frac{\theta}{1-\theta} \right) \text{ for mobile adsorption.}$$

In the latter case $\mu_{frus-vib}$ will be the normal $\mu_{vib-rot}$.

To find the equilibrium CO coverage the differential heat of adsorption needs to be calculated, which can be done easily by approximating discrete points from DFT by a simple continuous function. The approximation by the second order polynomial is shown on Figure 7, and it is used in further considerations. The equilibrium temperature of the diluent gas (argon) and the surface ensures that effects related to direct energy transfer between impinging molecules and adsorbed CO is of minor importance.

The calculated equilibrium CO coverage on the Pt(111) surface at various pressures is shown with the experimental data in Figure 10. The three lines represent three different models for the adsorbent. Note that there is a very small difference between the two extreme adsorption statistics, and an almost linear regime in all interesting pressure ranges. The precise determination of CO coverage is beyond the scope of the present paper, but comparing to existing literature fairly good agreement is found. From the STM data presented in this paper and in Ref. [32] a room temperature coverage of 0.68 ML at ambient pressure, and around 0.5 ML in UHV, are observed. A simplistic mean field model as presented above is not able to predict the formation of superstructures, such as the $c(4 \times 2)$ structure observed for CO on Pt(111). This is one of the reasons why the calculated equilibrium CO coverage is lower than the experimental.

Determination of the desorption rate, k , is now very simple, as the desorption mechanism is governed simply by Eq. (6). The standard desorption rate at equilibrium is given by: $k_1^- = \nu(\theta) \exp\left(-\frac{E_{act}(\theta)}{k_B T}\right)$, where $\nu(\theta)$ is the prefactor, and $E_{act}(\theta)$ is the activation energy.

If CO adsorption is not activated then $E_{act} = E_{ads}^{diff}$.

For CO on Pt(111), however, Steckel et al. [47] have shown that at a coverage above 0.6 ML a barrier for desorption appears. While it is very small, 0.1 eV for 0.6 ML, the magnitude of this barrier grows to 0.5 eV at 1 ML. One might argue, that such a high coverage is not possible for such a system as CO on Pt(111), but the existence of a barrier, however small, at a coverage around 0.6 ML influences the desorption process. The activation barrier is given by $E_{act} = -E_{ads}^{diff} + \xi E_{ads}^{diff}$, and $0 < \xi < 1$ is a continuous function of the coverage.

By assuming that there is a chemical equilibrium between the adsorbed CO and the CO in the gas phase Eq. (7) and (10) can be equated, i.e.:

$$\begin{aligned} \mu_g &= \mu_{ads} \\ \Rightarrow \ln \left(\frac{p}{p_0} \right) - \frac{S_0}{k_B} &= \frac{E_{ads}^{int}(\theta)}{k_B T} + \frac{\theta}{k_B T} \frac{\partial E_{ads}^{int}(\theta)}{\partial \theta} + \frac{\mu_{stat}}{k_B T} + \frac{\mu_{frus-vib}}{k_B T} \\ \Rightarrow \frac{E_{ads}^{diff}(\theta)}{k_B T} &= \ln \left(\frac{p}{p_0} \right) + \frac{\mu_{rest}}{k_B T} \end{aligned}$$

where all the terms with small coverage dependence have been collected in the term μ_{rest} . Now, utilising the fact that the activation energy can be expressed in terms of the adsorption energy and that $\ln(k_1^-) = \ln(\nu(\theta)) - \frac{E_{act}(\theta)}{k_B T}$ then:

$$\begin{aligned} \ln(k_1^-) &= \ln(\nu(\theta)) - \frac{E_{act}(\theta)}{k_B T} \\ &= \ln(\nu(\theta)) + (1-n) \ln \left(\frac{p}{p_0} \right) + (1-n) \frac{\mu_{rest}}{k_B T} \\ &= (1-n) \ln \left(\frac{p}{p_0} \right) + \alpha \end{aligned}$$

A relationship between the pressure and the rate constant is arrived at, where coefficients $(1-n)$ and α come from Figure 10. The slope of the linear relation depends on the coverage dependence of the activation energy, which is usually taken as minus the adsorption energy.

This means that the coverage dependence of the activation energy is weaker than the adsorption energy. The relation between p and k is presented in Figure 11. The absolute location along the k axis is determined by the prefactor, ν , and a value of $\nu = 10^{17}$ gives good agreement with the experimental data.

It is then possible to convert the rates observed for CO desorption to equivalent current densities that would be required to oxidise the same amount of CO. The case at 1 bar of CO was considered where an average desorption rate of $6.52 \times 10^{-3} \text{ s}^{-1}$ was obtained.

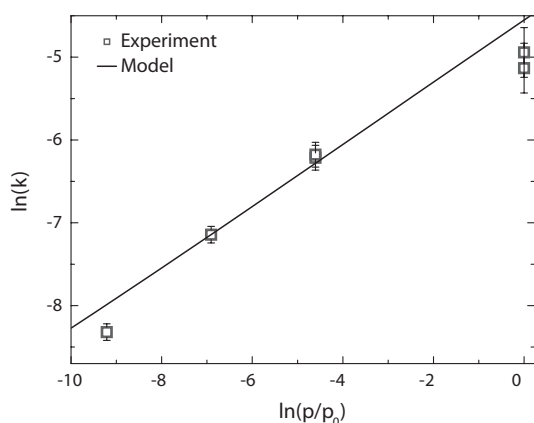


Fig. 11 Plot of the rate of $C^{13}O$ desorption versus the pressure of $C^{12}O$ above the surface. Squares represent experimental data whilst the solid line is from the simple model described in the text.

If a prefactor of 10^{17} is assumed, an activation energy can be found from the expression:

$$k_{des} = \nu e^{-\frac{E_{des}(\theta)}{k_b T}} \quad (10)$$

A value of 1.13 eV is obtained.

By substituting back into Eq. 10, extrapolated values for the rate of desorption of CO at 62 °C and 80 °C can be obtained. As the number of sites per square centimetre is 1.50×10^{15} for close-packed Pt(111) and the number of electrons per oxidised CO molecule is 2, then these rates can be converted to equivalent oxidation currents:

$$\text{At } 25 \text{ }^\circ\text{C} \quad k = 6.5 \times 10^{-3} \text{ s}^{-1}; \quad j = 3.1 \times 10^{-3} \text{ mA cm}^{-2}$$

$$\text{At } 62 \text{ }^\circ\text{C} \quad k = 0.85 \text{ s}^{-1}; \quad j = 0.41 \text{ mA cm}^{-2}$$

$$\text{At } 80 \text{ }^\circ\text{C} \quad k = 6.3 \text{ s}^{-1}; \quad j = 3.0 \text{ mA cm}^{-2}$$

Using a value for the prefactor of 10^{13} s^{-1} the value of the desorption energy reduces to 0.90 eV and the following values for k and j are obtained:

$$\text{At } 25 \text{ }^\circ\text{C} \quad k = 6.5 \times 10^{-3} \text{ s}^{-1}; \quad j = 3.1 \times 10^{-3} \text{ mA cm}^{-2}$$

$$\text{At } 62 \text{ }^\circ\text{C} \quad k = 0.31 \text{ s}^{-1}; \quad j = 0.14 \text{ mA cm}^{-2}$$

$$\text{At } 80 \text{ }^\circ\text{C} \quad k = 1.5 \text{ s}^{-1}; \quad j = 0.73 \text{ mA cm}^{-2}$$

To determine the effect this would have on the fuel cell anode mechanism, it is necessary to compare these rates with values directly measured for the CO oxidation

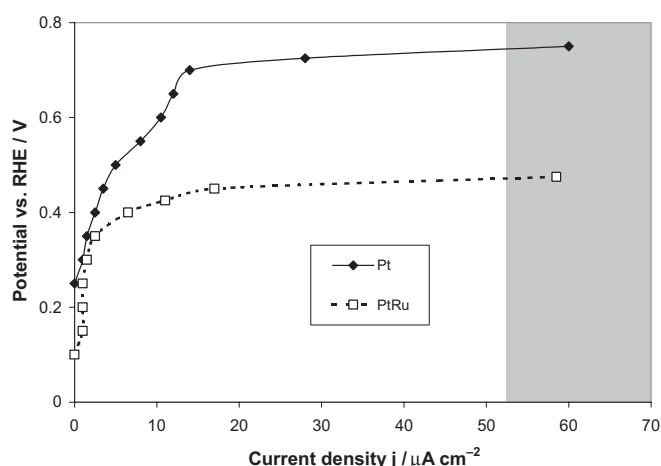


Fig. 12 Experimentally observed polarisation curve for CO (100%) oxidation at 62 °C on a platinum/ruthenium surface alloy electrode with the relative surface ratio of 50:50, reproduced from Ref. [12]. The shaded region shows the calculated range of equivalent current densities obtained from the experimental CO desorption rate for 100% CO, on varying the prefactor from 10^{13} to 10^{17} , and extrapolated to 62 °C.

rates at the given temperatures as governed by the relationship shown earlier in Eq. (1). Figure 12 shows the potential required to provide a current density, j , for the oxidation of pure CO at 25 °C calculated from experimental data [12]. If it can be shown that the equivalent current densities calculated above would require significant overpotentials, which are not observed as potential losses for the fuel cells operating at these temperatures then the desorption rate must be significant compared to the oxidation rate under the operating conditions of the fuel cell.

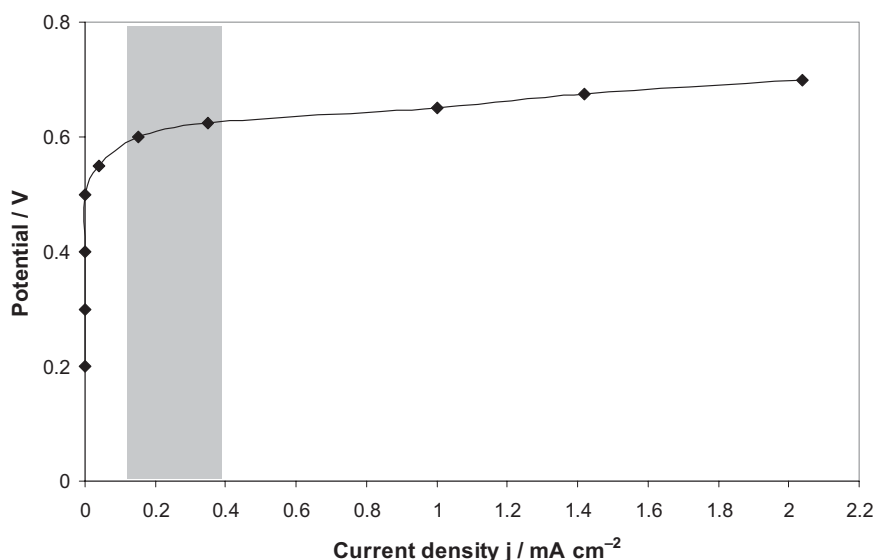


Fig. 13 Experimentally observed polarisation curve for CO (2% in argon) oxidation at 62 °C on a platinum/ruthenium surface alloy electrode with the relative surface ratio of 50:50 (reproduced from Ref. [12]). The shaded region shows the calculated range of equivalent current densities obtained from the experimental CO desorption rate for 1% CO in argon, on varying the prefactor from 10^{13} – 10^{17} , and extrapolated to 62 °C. The upper limit is $150 \mu\text{A cm}^{-2}$ and is not shown on this plot.

If the data for the rate of CO desorption on pure Pt, and the rate of oxidation of pure CO on a platinum/ruthenium 50:50 surface alloy are compared, then it can be seen that, for the oxidation rate to match the desorption rate ($j = 0.12 \text{ mA cm}^{-2}$) then an overpotential of $\sim 0.6 \text{ V}$ would be required. On pure platinum this value would be even higher.

If a similar treatment for the data at 1% CO in Ar is conducted for a prefactor of 10^{17} and at a temperature of $62 \text{ }^\circ\text{C}$, a current density of $j = 0.15 \text{ mA cm}^{-2}$ is observed whereas for a prefactor of 10^{13} , $j = 0.053 \text{ mA cm}^{-2}$. This gives a possible range for the current density obtained.

Again comparing to the data of Gasteiger et al. [12] in Figure 13, obtained for the pure oxidation of 2% CO in argon at $62 \text{ }^\circ\text{C}$ and comparing directly to our figure of between $53\text{--}150 \mu\text{A cm}^{-2}$ it can be seen that an overpotential of at least 0.7 V would be required on pure platinum and an overpotential of 0.45 V required on PtRu to provide the same rate of removal of CO by oxidation.

Therefore this would suggest that the rate of desorption is indeed significant in comparison to the rate of oxidation observed in the fuel cell gas stream. That is to say, that at overpotentials below those designated by the grey areas in Figures 12 and 13, the rate of desorption of CO will exceed the rate of electrochemical oxidation and the surface coverage would be determined by the thermal equilibrium coverage. The only reservation can be, whether the presence of water in the gas stream significantly reduces the CO desorption rate, and this is the subject of an ongoing study. It seems likely, however, that the dry gas phase behaviour will be a closer model to the behaviour in the humidified fuel cell set-up than that observed in solution where some limitation on the exchange rate is likely.

6 Conclusions

It has been shown from CO isotope exchange experiments that there is a significant CO exchange rate on platinum fuel cell catalysts at room temperature. Moreover, this rate of desorption is strongly dependent on the pressure of CO in the feed gas to the fuel cell.

DFT calculations have demonstrated that increasing the pressure of CO above the platinum surface leads to an increase in the coverage of CO on the surface and a concomitant drop in the binding energy for CO. The coverage dependency on pressure has been demonstrated using a high pressure STM from the range of ultra-high vacuum up to 1 bar.

Furthermore, it has been demonstrated that adsorbed CO is not caused to desorb by a stream of hydrogen at room temperature.

It is believed that in a fuel cell running under normal conditions at $80 \text{ }^\circ\text{C}$ the partial pressure of CO in the feed gas will strongly affect the CO coverage, binding energy and subsequent desorption rate, and that these factors are all intricately linked in the mechanism leading to the improved tolerance of the fuel cell.

Furthermore, it has been demonstrated that the rate of desorption is indeed significant compared to the rate of oxidation observed in a fuel cell.

Acknowledgements

The Centre for Atomic-scale Materials Physics (CAMP) is sponsored by the Danish National Research Foundation. The present project was in part funded by the Danish Research Councils. Computational resources were provided by Dansk Center for Supercomputing.

References

- [1] G. Hoogers, D. Thompsett, *CATTECH* **1999**, *3*, 106.
- [2] R. A. Lemons, *J. Power Sources* **1990**, *29*, 251.
- [3] W. Vogel, J. Lundquist, P. Ross, P. Stonehart, *Electrochim. Acta* **1975**, *20*, 79.
- [4] H. Igarashi, T. Fujino, M. Watanabe, *J. Electroanal. Chem.* **1995**, *391*, 119.
- [5] H. F. Oetjen, V. M. Schmidt, U. Stimming, F. Trila, *J. Electrochem. Soc.* **1996**, *143*, 3838.
- [6] M. Watanabe, S. Motoo, *J. Electroanal. Chem.* **1975**, *60*, 267.
- [7] S. Motoo, M. Watanabe, *J. Electroanal. Chem.* **1979**, *98*, 203.
- [8] H. A. Gasteiger, N. Markovic, P. N. Ross, E. J. Cairns, *J. Phys. Chem.* **1994**, *98*, 617.
- [9] H. A. Gasteiger, P. N. Ross, E. J. Cairns, *Surf. Sci.* **1993**, *293*, 67.
- [10] H. A. Gasteiger, N. Markovic, P. N. Ross, E. J. Cairns, *Electrochimica Acta* **1994**, *39*, 1825.
- [11] H. A. Gasteiger, N. Markovic, P. N. Ross, *J. Phys. Chem.* **1995**, *99*, 8290.
- [12] H. A. Gasteiger, N. Markovic, P. N. Ross, *J. Phys. Chem.* **1995**, *99*, 16757.
- [13] J. C. Davies, B. E. Hayden, D. J. Pegg, *Electrochimica Acta* **1998**, *44*, 1181.
- [14] J. C. Davies, B. E. Hayden, D. J. Pegg, *Surf. Sci.* **2000**, *467*, 118.
- [15] J. C. Davies, B. E. Hayden, M. E. Rendall, D. J. Pegg, *Surf. Sci.* **2002**, *496*, 110.
- [16] M. T. M. Koper, T. E. Shubina, R. A. van Santen, *J. Phys. Chem. B* **2002**, *106*, 686.
- [17] T. E. Shubina, M. T. M. Koper, *Electrochimica Acta* **2002**, *47*, 3621.
- [18] P. Liu, A. Logadottir, J. K. Nørskov, *Electrochimica Acta* **2003**, *48*, 3731.
- [19] H. Igarashi, T. Fujino, Y. M. Zhu, H. Uchida, M. Watanabe, *Phys. Chem. Chem. Phys.* **2001**, *3*, 306.
- [20] M. Watanabe, Y. M. Zhu, H. Igarashi, H. Uchida, *Electrochemistry* **2000**, *68*, 244.
- [21] P. Wolohan, P. C. H. Mitchell, D. Thompsett, S. J. Cooper, *J. Mol. Catal. A.* **1997**, *119*, 223.
- [22] R. J. Behm, *Acta Physica Polonica A.* **1998**, *93*, 259.

- [23] Q. Ge, S. Desai, M. Neurock, K. Kourtakis, *J. Phys. Chem. B* **2001**, *105*, 9533.
- [24] M.-S. Liao, C. R. Cabrera, Y. Ishikawa, *Surf. Sci.* **2000**, *445*, 267.
- [25] Y. Ishikawa, M.-S. Liao, C. R. Cabrera, *Surf. Sci.* **2002**, *513*, 98–110.
- [26] E. Christoffersen, P. Liu, A. Ruban, H. L. Skriver, J. K. Nørskov, *J. Catal.* **2001**, *199*, 123.
- [27] M. Watanabe, M. Shibata, S. Motoo, *J. Electroanal. Chem.* **1986**, *206*, 197.
- [28] G. Ertl, M. Neumann, K. M. Streit, *Surf. Sci.* **1977**, *64*, 393.
- [29] W. D. Mieher, L. J. Whitman, W. Ho, *J. Chem. Phys.* **1989**, *91*, 3228.
- [30] H. Steininger, S. Lehwald, H. Ibach, *Surf. Sci.* **1982**, *123*, 264.
- [31] B. E. Hayden, A. M. Bradshaw, *Surf. Sci.* **1983**, *125*, 787.
- [32] E. K. Vestergaard, P. Thostrup, T. An, E. Lægsgaard, I. Stensgaard, B. Hammer, F. Besenbacher, *Phys. Rev. Lett.* **2002**, *88*, 259601.
- [33] Y. Y. Yeo, L. Vattuone, D. A. King, *J. Chem. Phys.* **1997**, *106*, 392.
- [34] T. Matsushima, *Surf. Sci.* **1979**, *79*, 63.
- [35] D. H. Parker, A. D. Fisher, J. Colbert, B. E. Koel, J. L. Gland, *Surf. Sci.* **1991**, *258*, 75.
- [36] B. Kasemo, *Rev. Sci. Instrum.* **1979**, *50*, 1602.
- [37] E. Lægsgaard, L. Österlund, P. Thostrup, P. B. Rasmussen, I. Stensgaard, F. Besenbacher, *Rev. Sci. Instrum.* **2001**, *72*, 3537.
- [38] B. Hammer, L. B. Hansen, J. K. Nørskov, *Phys. Rev. B* **1999**, *59*, 7413.
- [39] D. Vanderbilt, *Phys. Rev. B* **1990**, *41*, 7892.
- [40] G. Kresse, J. Furthmüller, *Comput. Mat. Sci.* **1996**, *6*, 15.
- [41] M. Mavrikakis, B. Hammer, J. K. Nørskov, *Phys. Rev. Lett.* **1998**, *81*, 2819.
- [42] F. Besenbacher, *Reports on Progress in Physics* **1996**, *59*, 1737.
- [43] M. Ø. Pedersen, M.-L. Bocquet, P. Sautet, et al., *Chemical Physics Letters* **1999**, *299*, 403.
- [44] E. K. Vestergaard, R. T. Vang, J. Schnadt, S. Longwitz, F. Besenbacher, in preparation.
- [45] T. L. Hill, *An Introduction to Statistical Thermodynamics*, Addison-Wesley, Reading, USA, **1960**.
- [46] *CRC Handbook of Chemistry and Physics*, 64th ed. (Eds. R. C. Weast), CRC, Boca Raton, FL, **1985**.
- [47] J. A. Steckel, A. Eichler, J. Hafner, *Phys. Rev. B* **2003**, *68*, 85416.

III

High-Coverage Structures of Carbon Monoxide Adsorbed on Pt(111) Studied by High-Pressure Scanning Tunneling Microscopy[†]

Sarah R. Longwitz,^{‡,§} Joachim Schnadt,[‡] Ebbe Kruse Vestergaard,[‡] Ronnie T. Vang,[‡] Erik Lægsgaard,[‡] Ivan Stensgaard,[‡] Harald Brune,[§] and Flemming Besenbacher^{*‡}

Interdisciplinary Nanoscience Center (iNANO) and Department of Physics and Astronomy, University of Aarhus, 8000 Aarhus C, Denmark, Institut de Physique des Nanostructures, Ecole Polytechnique Fédérale de Lausanne, 1015 Lausanne, Switzerland

Received: February 20, 2004

High-pressure scanning tunneling microscopy was used to study the room-temperature adsorption of CO on a Pt(111) single-crystal surface in equilibrium with the gas phase. The coverage was found to vary continuously, and over the entire range from 10^{-6} -760 Torr pressure-dependent moiré patterns were observed, characteristic of a hexagonal or nearly hexagonal CO overlayer. Two different pressure ranges can be distinguished: below 10^{-2} Torr, the moiré lattice vector is oriented along a 30° high-symmetry direction of the substrate, corresponding to a pressure-dependent rotation of the CO overlayer with respect to the (1×1) Pt surface lattice, while above 10^{-2} Torr, the CO layer angle is independent of the pressure. This behavior is analyzed in terms of the interplay of the repulsive CO-CO interaction potential and the substrate potential.

Introduction

Few adsorbate systems have received as much attention as carbon monoxide on transition-metal surfaces. The enormous interest originates from the system's relevance to catalysis, since CO takes part in many important reactions such as CO hydrogenation and oxidation and the Fischer-Tropsch synthesis¹ and transition-metal particles are the most common catalytic materials for these reactions. Notwithstanding these beneficial interactions, carbon monoxide is also an unwanted poison molecule in, e.g., the hydrogen feed for low-temperature fuel cells produced from hydrocarbons.² Since all these aspects can be traced back to adsorbate-surface interactions, it is important to acquire a thorough understanding of the properties of the adsorption of CO on transition-metal surfaces.

To date, an impressively detailed knowledge has been gained on the adsorption of CO on Pt(111) under ultrahigh vacuum (UHV) conditions (see, e.g., refs 3, 4, and 5). The relevance of this understanding to industrial catalytic conditions has however been questioned.^{6,7} The divergence of experimental and theoretical results for systems under UHV and catalytic or realistic pressures, respectively, has been designated "the pressure gap", which has to be bridged (see, e.g., ref 8). Therefore the development of surface-sensitive techniques that are capable of working at elevated pressures has renewed the interest in the CO/Pt(111) system, and a number of recent high-pressure studies have addressed the subject using different techniques.^{6,7,9,10} These studies revealed that carbon monoxide forms a hexagonal overlayer on Pt(111) at atmospheric pressure and room temperature. Two different structures were proposed, one close to a (4×4) -9CO nonrotated structure,⁷ the other one compatible with a $(\sqrt{19} \times \sqrt{19})$ R23.4°-13CO commensurate structure.¹⁰ The latter structure has also been proposed for the adsorption of CO in an electrochemical cell at 0-0.2 V electrode potential.¹¹ In contrast, under UHV and low-temperature condi-

tions, a series of nonhexagonal commensurate structures is observed.^{3,4,12} These are the $c(4 \times 2)$ or $(\sqrt{3} \times 2)\text{rect}(\theta)^{1/2}$, where θ is the coverage (ref 13)) and $c(\sqrt{3} \times 5)\text{rect}(\theta)^{3/5}$, $(\sqrt{3} \times 3)\text{rect}(\theta)^{2/3}$, and $c(\sqrt{3} \times 7)\text{rect}(\theta)^{5/7}$ structures; the latter three can be cast in a unified picture in which unit stripes of the $c(4 \times 2)$ structure separated by domain walls of higher, structure-specific CO density.⁴ It is not yet clear, however, whether these lattice gas structures represent global or local minima of the potential energy surface.

While it was shown that a hexagonal CO overlayer can also be produced under vacuum conditions when the sample is cooled sufficiently,^{3,10} the understanding of the atomic-scale details of the room-temperature adsorption structures of CO on Pt(111) over the entire pressure range from UHV pressures up to atmospheric pressure is still incomplete. In particular, no study has been able to unambiguously determine the adsorbate structure for the complete pressure range from UHV to one atmosphere.

For the present study we used high-resolution scanning tunneling microscopy (STM) to unravel the room-temperature adsorption structures of CO/Pt(111). At all pressures above 10^{-6} Torr, we observed moiré patterns characteristic of the formation of a hexagonal CO overlayer on the hexagonal Pt(111) surface. The superposition of the two hexagonal lattices leads to a beating phenomenon resulting in the moiré pattern. A one-dimensional analogy is given by the sum of two sine functions with slightly different frequencies. At low CO pressures, up to 10^{-2} Torr, the moiré pattern is characterized by a lattice vector oriented along one of the high-symmetry directions of the substrate, while at higher CO pressures, a rotation of the pattern is observed. In the following, we discuss these results in the context of existing theories and compare them to available UHV low-temperature data and results obtained in electrochemical cells.

Experimental Section

The experiments were performed in a UHV chamber equipped with a home-built Aarhus scanning tunneling microscope as well as UHV standard equipment for sample cleaning and charac-

[†] Part of the special issue "Gerhard Ertl Festschrift".

^{*} To whom correspondence may be addressed. E-mail: fbe@phys.au.dk.

[‡] University of Aarhus.

[§] Ecole Polytechnique Fédérale de Lausanne.

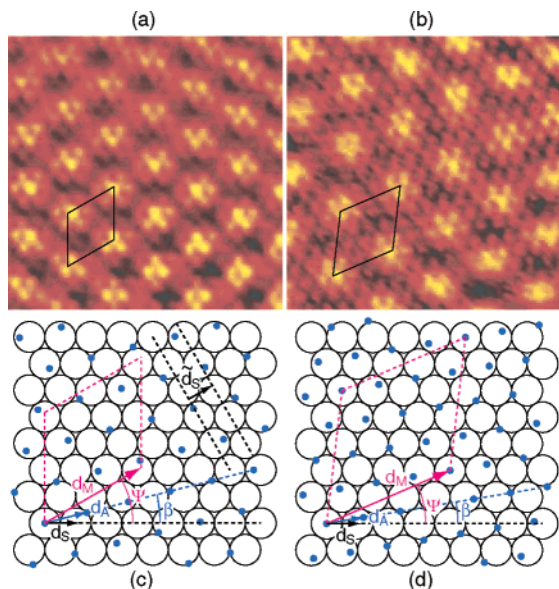


Figure 1. STM images of $55 \times 55 \text{ \AA}^2$ and corresponding ball models showing moiré superstructures of CO on Pt(111) at room temperature. (a) Incommensurate structure at $p = 10^{-2}$ Torr, $I_t = 1.06$ nA, $V_t = 8.2$ mV. (b) $p = 720$ Torr, $I_t = 1.27$ nA, $V_t = 4.9$ mV. The images a and b are aligned so that the bulk $[1\bar{1}0]$ direction is oriented along the x axis. The image treatment comprised frequency filtering and interpolation. In the ball models in c and d, the open circles represent Pt atoms and the dark blue dots CO molecules. The rotational angles β between the substrate and adsorbate lattices and Ψ between the substrate and moiré lattices are indicated. The moiré unit cell with lattice constant d_M is also shown. (c) Incommensurate structure at 10^{-2} Torr. $\Psi = 30^\circ$, $\beta = 10.4^\circ$, $d_M/d_S = 3.6$. \vec{d}_S is the real space equivalent of the reciprocal vector \vec{q}_S observed in the fast Fourier transform (cf. Figure 2). \vec{d}_S is rotated by 30° from \vec{d}_S , and the length relationship is $\vec{d}_S = \sqrt{3}d_S/2$. (d) Commensurate ($\sqrt{19} \times \sqrt{19}$) R23.4°-13CO structure at 720 Torr. $\Psi = 23.4^\circ$, $\beta = 9.5^\circ$, $d_M/d_S = 4.4$.

terization.¹⁴ Connected to this chamber is a gold-plated cell containing the newly developed Aarhus high-pressure scanning tunneling microscope.¹⁵ With this, STM experiments can be carried out at pressures of up to 760 Torr of pure gases or gas mixtures. Sample transfer between the systems takes place under clean conditions, i.e., without removing the sample from the vacuum. The gas exposure system of the high-pressure cell has been designed to avoid nickel-carbonyl ($\text{Ni}(\text{CO})_4$) formation, which is of utmost importance when working with CO. For that purpose, the gas line has been constructed primarily using copper tubing instead of stainless steel. Furthermore, just prior to the inlet, the CO is passed through an activated high surface area carbon powder filter heated to ~ 400 K, over which the Ni-carbonyls dissociate, leaving the Ni behind. The efficiency of this system was checked by performing Auger electron spectroscopy after extended high-pressure CO exposure and subsequent pump-out.

The sample was cleaned in the UHV chamber following standard sample cleaning procedures: 30 min 800 eV Ar^+ sputtering, followed by an annealing procedure (in case of severely contaminated samples, 10 min annealing at 800 K in 10^{-7} Torr O_2 plus 3 min annealing at 1000 K in UHV, otherwise just UHV anneal). The experiments at low and medium pressure (up to 5×10^{-4} Torr) were then performed in the UHV chamber, while those at higher pressures up to 760 Torr were performed in the high-pressure cell. For pressures between 0.1 and 100 Torr, electric discharges between the closely spaced piezo electrodes may occur. We thus always work at a total pressure of close to 760 Torr in the high-pressure cell. Because of its

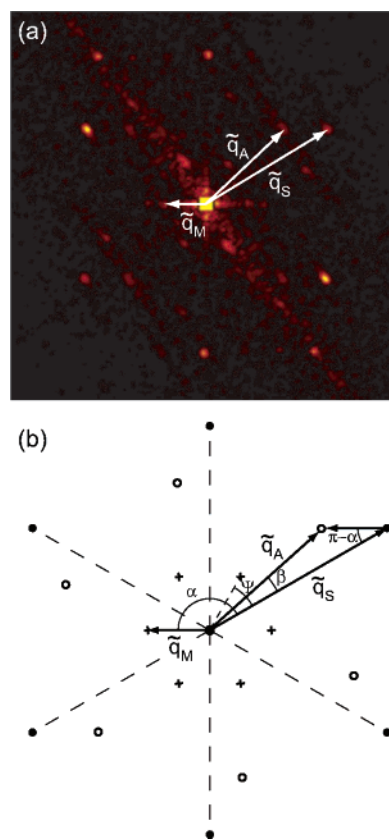


Figure 2. (a) FFT of an STM image of a CO/Pt(111) moiré pattern (5×10^{-7} Torr). (b) Relationship between the reciprocal lattice vectors. Here the filled circles represent the substrate lattice, the empty circles correspond to the adsorbate lattice, and the crosses correspond to the resulting moiré pattern. The observed vectors \vec{q}_M , \vec{q}_S , and \vec{q}_A are rotated by 30° from the vectors \vec{q}_M , \vec{q}_S , and \vec{q}_A used in the analysis, and the vector lengths are related via $\tilde{q}_x = 2q_x/\sqrt{3}$, where $x = M, S, A$. The moiré vector \vec{q}_M is equal to the difference vector $\vec{q}_M = \vec{q}_A - \vec{q}_S$ and hence also $\vec{q}_M = \vec{q}_A - \vec{q}_S$.

unreactive nature, ultrapure argon as commercially available is used for backfilling from the desired CO pressure up to the working pressure.

Results

Figure 1 shows two typical STM images of CO adsorbed on Pt(111) at room temperature. Image a was recorded at a CO pressure of 10^{-2} Torr, image b at 720 Torr. In both images, two hexagonal structures coexist, one with a short and one with a longer periodicity. The short-periodicity hexagonal lattice is the image of either the Pt(111) substrate (panel a) or the CO overlayer (panel b), while the long-periodicity lattice (the moiré lattice) is characterized by the periodic height modulation induced by the superposition of the hexagonal CO adsorbate layer and the Pt(111) surface.¹⁶ Similar images, all of which exhibited moiré patterns, were obtained at the other investigated pressures.

We observed quite generally that we could not image the CO molecules at pressures below 0.1 Torr (at room temperature), but instead we sampled the underlying Pt(111) substrate, as in Figure 1a. The measurement of the moiré pattern with a hexagonal shape, however, proves the presence of a hexagonal CO overlayer. The invisibility of CO adsorbed on Pt and other metal surfaces in STM is known to occur under certain conditions (see, e.g., refs 18, 19, and 20).

Performing fast Fourier transforms (FFT) on the STM images allowed us to measure the periodicities and angles of the

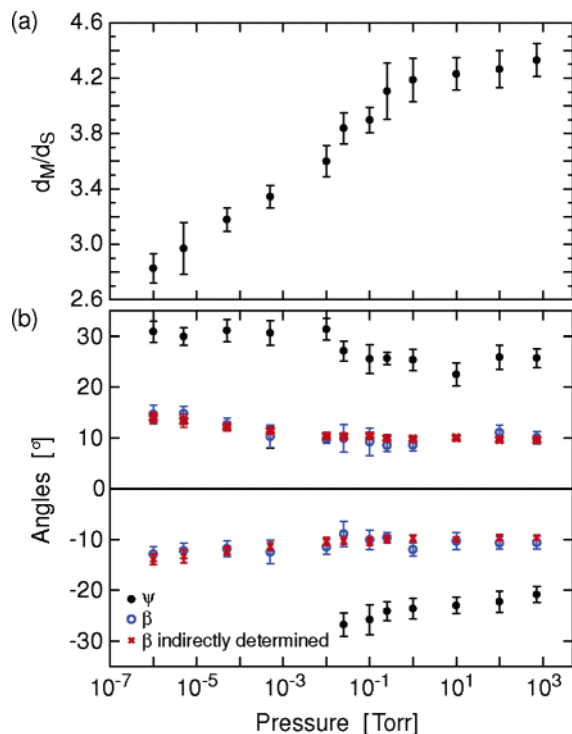


Figure 3. (a) Moiré lattice constant d_M for a CO layer on Pt(111) as a function of CO partial pressure. d_M is normalized with respect to the substrate lattice constant d_S . (b) Rotational angles between the substrate and the moiré lattice Ψ (filled symbols) and the substrate and adsorbate lattice β (open symbols). β can also be calculated from d_M , d_S , and Ψ (crosses).²¹ In those cases, where two equivalent domains were observed (rotation of the moiré and adsorbate lattices by $\pm\Psi$ and $\pm\beta$ with respect to the substrate $[1\bar{1}0]$ direction, respectively), the angles for both domains are given.

observed structure. A typical FFT is shown in Figure 2a, and a sketch of the relevant parameters is shown in Figure 2b. These are the reciprocal lattice vectors \vec{q}_M of the moiré lattice, \vec{q}_A of the adsorbate lattice, and \vec{q}_S of the substrate lattice, which are related to each other by virtue of $\vec{q}_M = \vec{q}_A - \vec{q}_S$. This set of reciprocal vectors \vec{q}_x translates into the set \vec{q}_x ($x = M, S, A$), where \vec{q}_x are the reciprocal space vectors of the real space vectors \vec{d}_x used in Figure 1 and in the analysis below, by a rotation of 30° and by virtue of $\vec{q}_x = 2q_x/\sqrt{3}$. Hence $\vec{q}_M = \vec{q}_A - \vec{q}_S$. Ball models showing the real space vectors are given in panels c and d of Figure 1. \vec{d}_M and \vec{d}_A form angles Ψ and β , respectively, relative to the $[1\bar{1}0]$ direction of the substrate. From Figure 2a, it is seen that the adsorbate lattice vector can be determined even if the adsorbates are not visible in the STM image, since the moiré spots appear as satellites around the substrate spots.²¹ The substrate spots can be identified unambiguously by comparison to the Fourier transforms of images taken on the clean Pt(111) crystal.

Figure 3 shows these parameters as a function of the CO partial pressure ranging from 10^{-6} to 760 Torr. In panel a, the moiré superlattice constant d_M is plotted in units of the Pt(111) substrate nearest neighbor distance $d_S = 2.77 \text{ \AA}$. In panel b, the filled circles refer to the rotation angle Ψ between the substrate and moiré lattice and the open circles to the rotation angle β between the substrate and adsorbate lattice. In addition, crosses indicate values for β which were derived from the moiré parameters only as described in ref 21. The procedure proved to be useful in case of barely visible satellites and gave additional confidence, since these values coincide with the β values determined directly from the images within the measurement uncertainty. From Figure 3b, we can identify two regimes

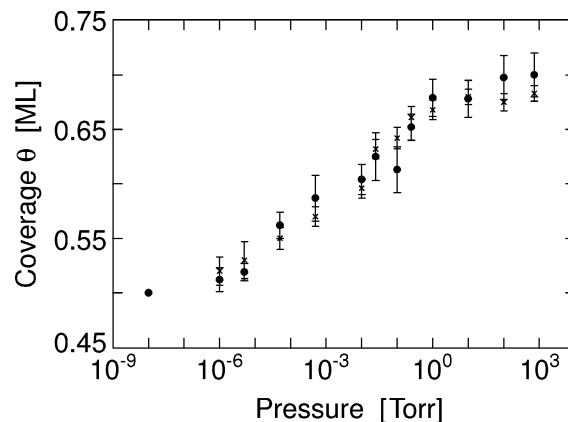


Figure 4. CO coverage θ on Pt(111) as a function of CO background pressure. The filled circles indicate values, which were directly determined from the STM images, while the indirectly determined values²¹ are indicated by crosses.

with different types of incommensurate moiré superstructures. In the pressure range from 10^{-6} to 10^{-2} Torr, we observe a moiré pattern, which is rotated by a fixed angle of $\Psi = 30^\circ$ with respect to the Pt(111) substrate, whereas the adsorbate angle β decreases from about 14° to 10° . At the same time, the lattice constant of the moiré pattern changes approximately linearly with the logarithm of the CO pressure. At CO pressures above 10^{-2} Torr, Ψ decreases, while β remains approximately constant at about 10° . Close to atmospheric pressure, the moiré lattice constant d_M approaches a fixed saturation value.

In panels c and d of Figure 1, a schematic model of the CO structures observed at 10^{-2} and 720 Torr is given. The ball model in panel c was created with the Ψ , d_M , d_A , and β values from the measurement. The structure at 720 Torr is compatible with a $(\sqrt{19} \times \sqrt{19})$ R23.4°-13CO commensurate structure, and the corresponding values were used in panel d.

Knowledge of the substrate and adsorbate lattice constants allows one also to determine the CO coverage, which is given by $\theta = (d_S/d_A)^2 = (q_A/q_S)^2$. Figure 4 shows how the coverage increases continuously with CO pressure in the range of 10^{-8} – 10^3 Torr. Toward atmospheric pressures, the CO coverage saturates due to the increasingly repulsive CO–CO interaction. We confirmed that the variation of the CO coverage was reversible by first exposing the sample to a CO pressure of 760 Torr and then adjusting the pressure to a lower value. The structural parameters were the same as for a sample that was exposed to the lower pressure only. The results for the CO coverage are in good agreement with the previously determined CO coverages at 10^{-8} Torr ($\theta = 0.5$)³ and 760 Torr ($\theta = 0.68$).¹⁰ The CO coverage given for 10^{-8} Torr corresponds to the $c(4 \times 2)$ structure observed in low-energy electron diffraction (LEED).^{3,22}

Discussion

From Figure 4, the coverage of CO on Pt(111) at room temperature is seen to vary continuously (and reversibly, as outlined above) over the pressure range from 10^{-6} to 760 Torr. The observed CO structures were hexagonally ordered. The finding of a continuous variation of the CO coverage with pressure and the observation of hexagonal, ordered overlayer structures for all pressures above 10^{-6} Torr is in contrast to the CO/Pt(111) lattice gas structures found in the same coverage range at lower pressures and temperatures.^{3,4,12} The formation of lattice gas structures would lead to a phase diagram with alternating regimes of ordered and disordered CO overlayers.⁴

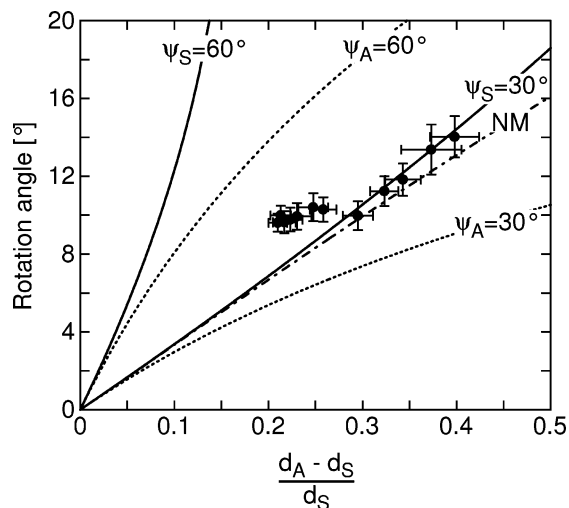


Figure 5. Rotation angle between CO adsorbate layer and Pt(111) substrate as a function of the lattice misfit between d_A and d_S , $(d_A - d_S)/d_S$. The solid and short-dashed lines indicate the theoretical high-symmetry solutions of ref 35 and the dashed–dotted line marked NM the harmonic approximation of ref 29 for a Lennard-Jones system. Ψ_S is the rotation angle of the moiré superlattice with respect to the substrate. Ψ_A is the rotation angle of the moiré superlattice with respect to the adsorbate.

Nevertheless, a true pressure gap is not observed for the CO/Pt(111) system since cooling of the sample to approximately 170 K leads to an increase in CO coverage and the formation of a hexagonal CO overlayer similar to that at 760 Torr.¹⁰

The formation of moiré structures has been observed previously for a large variety of adsorbate systems. For example, moiré patterns for CO overlayers have been reported for the Ni(111),²³ Ag(111),²⁴ and graphite²⁵ substrates and, at a pressure of ~ 760 Torr, also for the CO/Pt(111) system.^{7,10} Generally, the occurrence of moiré patterns can always be expected when the adsorbate lateral repulsive potential V_1 balances or exceeds the corrugation ΔU of the adsorbate–substrate interaction potential. In the $V_1 \gg \Delta U$ and infinite lattice limit, the resulting structure can be viewed as a mere superposition of two perfect, in this case hexagonal, lattices of the substrate and adsorbate, respectively. Because of the small difference in the adsorbate and substrate lattice constants, a long-periodicity (given by the moiré wave vector) height modulation is then observed.¹⁶

In the case $V_1 \approx \Delta U$, the situation is more complicated and has received considerable theoretical interest.^{26–36} The various theories predict an alignment of the moiré vector in preferred directions if the molecules are able to relax their positions with respect to the perfect hexagonal overlayer lattice^{26–32} and/or if the system has a finite size.^{33–36} References 33–36 put forward a “high-symmetry hypothesis” according to which the adsorbate layer rotates by an angle β such that the resulting incommensurate moiré superlattice is either oriented along a high-symmetry direction of the substrate or along a high-symmetry direction of the adsorbate layer. Numerical calculations showed that these situations correspond to an energy minimum, since the number of adsorbates in or close to low-energy sites is maximized.^{34,35,36} The maximization is solely due to a finite-size effect, with relaxation only resulting in a second-order correction.

In Figure 5 the rotation angle β of the CO lattice with respect to the Pt substrate as a function of the lattice misfit $(d_A - d_S)/d_S$ is compared to the high-symmetry (30 and 60°) solutions relevant for the (111) surface. For comparison, we also show, marked NM, the theoretical harmonic approximation³⁷ solution

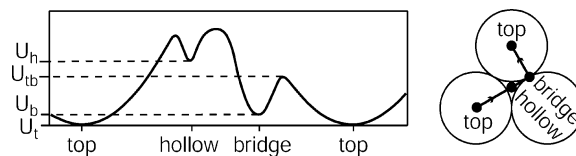


Figure 6. Qualitative potential energy curve for an isolated CO molecule on Pt(111) along the lines connecting the top, bridge and hollow sites.

derived for a Lennard-Jones system in refs 26 and 29. (The longitudinal and transverse sound velocities c_L and c_T are the only system parameters which enter into the solution. For a two-dimensional hexagonal lattice they are related to each other by $c_L = \sqrt{3}c_T$.) For misfit values between 0.3 and 0.4, i.e., coverages below 0.6 monolayers, the experimental data points are found to be in good agreement with the $\Psi_S = 30^\circ$ solution found from the high-symmetry hypothesis, i.e., the moiré vector aligns with the 30° high-symmetry direction of the substrate (which corresponds to the $[1\bar{2}1]$ direction). For misfit values lower than 0.3, however, a deviation from the theoretical lines is observed. As the compression of the CO layer continues, i.e., for lower values of $(d_A - d_S)/d_S$, β remains constant at approximately 10° within the error bars, whereas Ψ decreases from 30° to about $\pm 24^\circ$ (cf. Figure 3b).

The alignment of the moiré vector with the 30° substrate direction indicates that the particular rotation of the adsorbate layer is due to the finite size of the substrate.^{35,36} The role of the substrate boundaries is played by the substrate steps, which are oriented along the $[1\bar{1}0]$ and equivalent directions. It would be interesting to confirm this result in experiments using samples with varying step density.

As established above, the moiré vector does not align with any of the substrate high-symmetry directions at pressures above 10^{-2} Torr. The energy gain associated with this transition (see discussion below) thus does not give a sufficiently high impetus to achieve the rotation. We can analyze the situation in further detail by taking the form of the substrate interaction potential U and the strength of the lateral interaction V_1 into account. The exact form of V_1 has not yet been determined (see refs 38–41), but an approximation is given by the semiempirical CO–CO pairwise interaction potential in ref 42. A qualitative sketch of U is given in Figure 6, and Table 1 reproduces some potential parameters, derived from the semiempirical single-molecule potential curve⁴³ of ref 42. The top sites are energetically most favorable, followed by the bridge sites.^{3–5} Here we assume that the maximum of the potential energy barrier U_{tb} between top and bridge sites lies below the local potential energy minimum U_h at hollow sites, in agreement with the calculations in ref 38 and the experimental findings of ref 11. As a consequence, the hollow sites are not occupied over the entire investigated pressure range, in agreement with the results of ref 11. The observation of a hexagonal superstructure is not contradicted, since we expect the positions of the adsorbed CO molecules to be relaxed with respect to a perfect hexagonal overlayer. In addition, the area of the near-hollow sites amounts to a relatively small fraction of the total surface area only, so that these sites do not necessarily have to be occupied in a close-to-hexagonal overlayer.

Relevant for a comparison of the lateral interaction energy and the corrugation of the substrate potential are the barriers between the different sites. In the analysis, we have to take into account that the measurements are carried out at room temperature. A crude estimation for the effective barrier height is derived by assuming parabolic and isotropic oscillators. The resulting values for the effective barriers between the bridge

TABLE 1: Parameters of the Employed Substrate Interaction Potential and the Lateral Interaction (All Energies Are Given in meV)^a

T(K)	U_t	U_b	U_{tb}	$\langle U_t \rangle$	$\langle U_b \rangle$	$\Delta U_{tb-t} \equiv U_{tb} - \langle U_t \rangle - U_t$	$\Delta U_{tb-b} \equiv U_{tb} - \langle U_b \rangle - U_b$	$V_l(\theta = 0.5)$	$V_l(\theta = 0.6)$
0	0	60	300	6	37	294	203	200	290
300	0	60	300	72	60	248	180	200	290

^a ΔU_{tb-t} and ΔU_{tb-b} represent effective barrier heights relative to the mean energy of the molecule inside the potential wells, which were assumed to be parabolic. These effective barrier heights are derived assuming isotropic oscillators with energies $\langle U_{t,b} \rangle = \hbar\omega_{t,b} + \hbar\omega_{t,b}/(\exp(\hbar\omega_{t,b}/kT) - 1)$, where $\hbar\omega_t = 48 \text{ cm}^{-1}$ and $\hbar\omega_b = 300 \text{ cm}^{-1}$ are the vibrational motion frequencies in the top and bridge positions, respectively.⁴² The values defining the potentials (U_t , U_b , U_{tb} , and V_l) have been taken to be temperature independent.

and on-top sites, $\Delta U_{tb-t} \equiv U_{tb} - \langle U_t \rangle - U_t$, as seen from the on-top potential-energy minimum and $\Delta U_{tb-b} \equiv U_{tb} - \langle U_b \rangle - U_b$ as seen from the bridge minimum, are given in Table 1. ΔU_{tb-t} and ΔU_{tb-b} represent the room-temperature effective barrier heights relative to the mean energy of the molecule inside the potential wells (see the Table caption), which were assumed to be parabolic, while U_t , U_b , and U_{tb} are the parameters of the potential energy surface for the on-top and bridge sites and the barrier between these (cf. Figure 6).⁴² For the on-top sites, the lateral repulsion energy V_l is smaller than the barrier height ΔU_{tb-t} at the onset of the high-symmetry moiré phase with $\theta \approx 0.5$. At $\theta \approx 0.6$, corresponding to the rotational transition at 10^{-2} Torr, V_l is essentially equal to ΔU_{tb-t} . In contrast, the barrier as seen from the bridge sites, ΔU_{tb-b} , is found to be smaller than the lateral repulsion V_l over the entire coverage range of 0.5–0.6. This indicates that the occupation of top sites is decisive for the formation of the high-symmetry moiré phase at lower CO pressures.

At pressures above 10^{-2} Torr, the orientation of the moiré superstructure along the high-symmetry direction $\Psi = 30^\circ$ is not maintained. Hence, the rotation concomitant with such an alignment is not favorable anymore, and instead, the CO adsorbate layer keeps a constant orientation with respect to the substrate. In this pressure regime, the lateral repulsion exceeds the barrier height between the on-top and bridge position, irrespective of whether these are measured with reference to the bridge (ΔU_{tb-b}) or on-top site (ΔU_{tb-t}). Hence the tendency of the CO molecules to occupy (near) top sites is reduced. We therefore propose that the increasing dominance of the lateral repulsion over the barrier height ΔU_{tb-t} causes the deviation from the high-symmetry direction just above 10^{-2} Torr.

However, close to 760 Torr, the occupation of top sites again becomes decisive, namely, for the formation of a commensurate ($\sqrt{19} \times \sqrt{19}$) R23.4°-13CO structure. In this commensurate structure, a very high number of CO molecules can sit exactly on top sites. We note that the electrochemical study of Villegas and Weaver¹¹ indicates that going from a negative to a slightly positive sample bias leads to a switching from a (2×2) -3CO structure to the ($\sqrt{19} \times \sqrt{19}$) R23.4°-13CO system. The rotation concomitant with such a transformation indicates an enhanced stability of the ($\sqrt{19} \times \sqrt{19}$) structure. Together with the present results, this finding suggests that the occupancy of a high number of on-top sites to some extent can outweigh the lateral repulsion even at high coverages.

The energy gain due to the formation of the commensurate ($\sqrt{19} \times \sqrt{19}$) R23.4°-13CO structure is judged to be higher than the energy gain that would result from a reorientation of the incommensurate moiré superstructure along $\Psi = 30^\circ$ just above 10^{-2} Torr. We suggest that above 10^{-2} Torr the lateral forces are sufficient to exceed the corrugation of the substrate potential. Hence a simple reorientation along a high-symmetry direction is prevented but not the formation of a particularly stable commensurate structure.

Summary

In conclusion, we have determined the room-temperature surface structure of CO on Pt(111) over the entire pressure range of 10^{-6} –760 Torr. For all pressures, the formation of a hexagonal or quasi-hexagonal CO overlayer is observed, showing that for CO/Pt(111) a true pressure gap cannot be established. Nevertheless, extreme care has to be taken when relating UHV results to systems operating under realistic conditions such as atmospheric pressure. One has to consider (a) the existence of different commensurate vacuum structures on cooled samples (see, e.g., refs 3 and 4) and (b) the subtle differences between the reported hexagonal structures in terms of the adsorbate layer rotation angle.

In further detail, the CO adsorbate layer is continuously compressed with increasing pressure, resulting in a continuous coverage variation from 0.5 to 0.7. The orientation of the moiré superlattice, whose formation is due to the superposition of the hexagonal adsorbate layer with the hexagonal substrate, is pressure dependent. First, for coverages between ~ 0.5 and 0.6, the moiré pattern is rotated by 30° with respect to the $[1\bar{1}0]$ direction of the Pt(111) substrate. The orientation can be explained in terms of a maximum occupation of high-binding energy sites for a substrate of finite size,^{35,36} where the size is given by the surface terraces. Second, at a coverage of 0.6, the system undergoes a rotational phase transition. Above this coverage, the rotation angle of the adsorbate layer with respect to the substrate does not change anymore. We explain this behavior in terms of an increasing importance of the repulsive lateral molecular interaction, which starts to dominate over the corrugation of the substrate interaction potential. A quantitative analysis based on previous results⁴² supports our explanation.

References and Notes

- (1) *Handbook of Heterogeneous Catalysis*; Ertl, G., Knözinger, H., Weitkamp, J., Eds.; Wiley-VCH: Weinheim, 1997; Vols. 1–5.
- (2) See, e.g., ref 1, Vol. 4, p 2094.
- (3) Ertl, G.; Neumann, M.; Streit, K. M. *Surf. Sci.* **1977**, *64*, 393.
- (4) Persson, B. N. J.; Tüshaus, M.; Bradshaw, A. M. *J. Chem. Phys.* **1990**, *92*, 5034.
- (5) McEwen, J.-S.; Payne, S.; Kreuzer, H. J.; Kinne, M.; Denecke, R.; Steinrück, H.-P. *Surf. Sci.* **2003**, *545*, 47.
- (6) Su, X.; Cremer, P. S.; Ron Shen, Y.; Somorjai, G. A. *Phys. Rev. Lett.* **1996**, *77*, 3858.
- (7) Jensen, J. A.; Rider, K. B.; Salmeron, M.; Somorjai, G. A. *Phys. Rev. Lett.* **1998**, *80*, 1228.
- (8) Ertl, G. *Angew. Chem., Int. Ed. Engl.* **1990**, *29*, 1219.
- (9) Rupprechter, G.; Dellwig, T.; Unterhalt, H.; Freund, H.-J. *J. Phys. Chem. B* **2001**, *105*, 3797.
- (10) Kruse Vestergaard, E.; Thostrup, P.; An, T.; Lægsgaard, E.; Stensgaard, I.; Hammer, B.; Besenbacher, F. *Phys. Rev. Lett.* **2002**, *88*, 259601.
- (11) Villegas, I.; Weaver, M. J. *J. Chem. Phys.* **1994**, *101*, 1648.
- (12) Biberian, J. P.; van Hove, M. A. *Surf. Sci.* **1984**, *138*, 361.
- (13) Here we define the coverage θ as the number of CO molecules per substrate surface atom.
- (14) Besenbacher, F. *Rep. Prog. Phys.* **1996**, *59*, 1737.
- (15) Lægsgaard, E.; Österlund, L.; Thostrup, P.; Rasmussen, P. B.; Stensgaard, I.; Besenbacher, F. *Rev. Sci. Instrum.* **2001**, *72*, 3537.

(16) Note that the observation of a moiré pattern in STM in general is due to a combination of electronic and geometric effects. In fact, it has been argued that the imaging of moiré patterns in STM is not due to the modulation of the topography, but to (three-dimensional) tunneling from the buried interface.¹⁷ In this model, the enhanced visibility of the moiré pattern is explained in terms of the larger decay length of the long-periodicity wave function, which is associated with the moiré lattice and which is produced by multiple scattering. The exact imaging mechanism is not important in the present context though, since the presence of a moiré pattern unambiguously proves the presence of a (nearly) hexagonal CO adsorbate layer.

(17) Kobayashi, K. *Phys. Rev. B* **1996**, *53*, 11091.

(18) Ramos, M. M. D.; Stoneham, A. M.; Sutton, A. P.; Pethica, J. B. *J. Phys.: Condens. Matter* **1990**, *2*, 5913.

(19) Thostrup, P.; Kruse Vestergaard, E.; An, T.; Lægsgaard, E.; Besenbacher, F. *J. Chem. Phys.* **2003**, *118*, 3724.

(20) Sprunger, P. T.; Besenbacher, F.; Stensgaard, I. *Chem. Phys. Lett.* **1995**, *243*, 439.

(21) In some cases, the satellites were not visible in the STM. In these cases, and as an additional confirmation to the others, the CO lattice parameters can be inferred from the measured moiré superlattice parameters. From Figure 2b, one can derive the following formula:

$$q_A = (q_S^2 + q_M^2 - 2q_S q_M \cos(\pi - \alpha))^{1/2} \quad (1)$$

$$\sin \beta = \frac{q_M}{q_A} \sin(\pi - \alpha) \quad (2)$$

$$\pi - \alpha = \frac{\pi}{3} - \Psi \quad (3)$$

Ψ is taken to be the smallest positive angle between the substrate and moiré lattices. This set of equations allows a determination of all relevant angles and lattice vectors.

(22) The LEED images observed by Ertl et al.³ exhibit clear spots at temperatures below and more diffuse spots at room temperature, which points to some degree of overlayer disorder at room temperature. The clear LEED pattern can be recovered by sample cooling, and hence the coverage is the same in both cases ($\theta = 0.5$).

(23) Quiros, C.; Robach, O.; Isern, H.; Ordejon, P.; Ferrer, S. *Surf. Sci.* **2003**, *522*, 161.

(24) Leatherman, G. S.; Diehl, R. D. *Langmuir* **1997**, *13*, 7063.

(25) Steele, W. *Chem. Rev.* **1993**, *93*, 2355.

(26) Novaco, A. D.; McTague, J. P. *Phys. Rev. Lett.* **1977**, *38*, 1286.

(27) Villain, J. *Phys. Rev. Lett.* **1978**, *41*, 36.

(28) Novaco, A. D. *Phys. Rev. B* **1979**, *19*, 6493.

(29) McTague, J. P.; Novaco, A. D. *Phys. Rev. B* **1979**, *19*, 5299.

(30) Shiba, H. *J. Phys. Soc. Jpn.* **1979**, *46*, 1852.

(31) Shiba, H. *J. Phys. Soc. Jpn.* **1980**, *48*, 211.

(32) Villain, J.; Gordon, M. B. *Surf. Sci.* **1983**, *125*, 1.

(33) Grey, F.; Bohr, J. In *Phase Transitions in Surface Films 2*; Taub, H., Torzo, G., Lauter, H., Fain, S. C., Eds.; Plenum Press: New York, 1991; NATO ASI Series, Series B, Physics, Vol. 267, p 83.

(34) Grey, F.; Bohr, J. *Appl. Surf. Sci.* **1993**, *65–66*, 35.

(35) Grey, F.; Bohr, J. *Europhys. Lett.* **1992**, *18*, 717.

(36) Bohr, J.; Grey, F. *Condens. Matter News* **1992**, *1*, 12.

(37) Anharmonic extensions of the theory of Novaco and McTague have also been formulated, see refs 27, 28, and 32.

(38) van Beurden, P.; Verhoeven, H. G. J.; Kramer, G. J.; Thijsse, B. J. *Phys. Rev. B* **2002**, *66*, 235409.

(39) Jennison, D. R.; Schultz, P. A.; Sears, M. P. *Phys. Rev. Lett.* **1996**, *77*, 4828.

(40) Brako, R.; Šokčević, D. *Surf. Sci.* **2000**, *469*, 185.

(41) Petrova, N.; Yakovkin, I. *Surf. Sci.* **2002**, *519*, 90.

(42) Schweizer, E.; Persson, B. N. J.; Tüshaus, M.; Hoge, D.; Bradshaw, A. M. *Surf. Sci.* **1989**, *213*, 49.

(43) Ref 44 indicates that for CO/Pt(111) density functional calculations (DFT) deliver *qualitatively* wrong results for the potential-energy surface. While this statement subsequently has been softened^{45–48} or disputed,⁴⁹ DFT results are not reliable for our purposes, and we have to use results from less advanced methods.

(44) Feibelman, P. J.; Hammer, B.; Nørskov, J. K.; Wagner, F.; Scheffler, M.; Stumpf, R.; Watwe, R.; Dumesic, J. *J. Phys. Chem. B* **2001**, *105*, 4018.

(45) Grinberg, I.; Yourdshahyan, Y.; Rappe, A. M. *J. Chem. Phys.* **2002**, *117*, 2264.

(46) Geschke, D.; Baştuğ, T.; Jacob, T.; Fritzsche, S.; Sepp, W.-D.; Fricke, B.; Varga, S.; Anton, J. *Phys. Rev. B* **2001**, *64*, 235411.

(47) Gil, A.; Clotet, A.; Ricart, J. P.; Kresse, G.; García-Hernández, M.; Rösch, N.; Sautet, P. *Surf. Sci.* **2003**, *530*, 71.

(48) Kresse, G.; Gil, A.; Sautet, P. *Phys. Rev. B* **2003**, *68*, 073401.

(49) Olsen, R. A.; Philipsen, P. H. T.; Baerends, E. J. *J. Chem. Phys.* **2003**, *119*, 4522.

IV

Oxidation of Pt(110)

W. X. Li,¹ L. Österlund,^{1,2} E. K. Vestergaard,¹ R. T. Vang,¹ J. Matthiesen,¹
T. M. Pedersen,¹ E. Lægsgaard,¹ B. Hammer,¹ and F. Besenbacher¹

¹*Interdisciplinary Nanoscience Center (iNANO), Center for Atomic-scale Materials Physics (CAMP),
and Department of Physics and Astronomy, University of Aarhus, DK 8000 Aarhus C, Denmark.*

²*Dep. Environment and Protection, FOI NBC Defense, SE 901 82 Umeå, Sweden.*

(Dated: August 13, 2004)

Using scanning tunneling microscopy (STM) and temperature programmed desorption (TPD) we investigate the Pt(110) surface under strongly oxidizing conditions involving either high-pressure O₂ or atomic oxygen exposure. At low temperatures, only disordered Pt oxide structures are observed. After annealing ordered surface oxide islands are observed to coexist with a highly stable reconstructed (12×2)-O chemisorption structure. From density functional theory (DFT) calculations a model for the surface oxide phase is revealed. The phase is found to be meta-stable, and its presence is explained in terms of stabilizing defects in the chemisorption layer and reduced Pt mobility.

PACS numbers: 68.37.Ef,68.43.Bc,68.47.Gh,81.65.Mq

Oxide formation on transition metal (TM) surfaces is important in many disciplines including surface coatings in materials science and supported metal particles in heterogeneous catalysis. Considerable advances have recently been made in the microscopic understanding of oxide formation on TM surfaces [1–4]. Knowledge of the microscopic state of a metal surface is essential for a description of physiochemical processes at the surface. For instance, a catalytic oxidation reaction may proceed completely differently over a metallic surface (e.g. via a Langmuir-Hinshelwood mechanism) as compared to over an oxide surface (e.g. via a Mars-van Krevelen mechanism)[5]. So far, most studies have focused on the close-packed 4d TM surfaces. Depending on the TM, either bulk or surface oxides are formed under high O₂ pressures. To the right in the transition metal series, the oxide formation becomes thermodynamically less favored, and in some cases, the substantial reconstructions associated with the formation of the oxides have been found to set up kinetic restrictions [6, 7].

Many open questions remain in the field, including differences between the 4d and other TM elements, as well as between open and close-packed surfaces. To address these issues, we present here a combined experimental and theoretical investigation of the oxide formation on an open 5d TM element, Pt(110). Platinum is chosen since it is one of the technologically most important catalysts, used e.g. for emission cleaning, and its oxide, PtO₂, is a well-known hydrogenation catalyst. Despite this, the fundamental understanding of the Pt oxide formation is lacking. Previous ultra-high vacuum (UHV) studies have shown that the Pt(110) surface, which in the clean state reconstructs to a (1×2) missing row structure, exhibits a variety of surface structures upon O₂ exposures [8, 9]. Recently, a disordered phase was reported to develop on Pt(110) under O₂ rich conditions during CO oxidation, and this was interpreted as being due to oxide formation [10]. In this Letter we reveal, by an interplay between

STM and TPD experiments and DFT calculations, the atomic-scale structure of high-coverage oxygen structures on the Pt(110) surface, including the formation of platinum oxide. Furthermore, we determine under what conditions the oxide exists. The experimental setup is described elsewhere [11, 12]. High-pressure O₂ exposures were made in a dedicated high-pressure cell, and a thermal gas cracker source was employed for atomic O dosing at UHV compatible pressures.

When Pt(110) is exposed at room temperature to either atomic O under UHV conditions (Fig. 1a) or to high pressures of O₂ (inset), a disordered overlayer structure develops. The structure exhibits weak ordering along the [110] direction at low O exposures, with the Pt(110)-(1×2) structure discernible underneath. With increasing O exposures, all traces of the original surface structure are, however, erased.

New, ordered structures are observed after brief annealing, or when O exposure is performed at elevated temperatures. Dosing O at 500 K (Fig. 1b) results in two surface phases. Guided by previous studies and by our TPD and DFT results below, one of the phases, which consists of [110]-oriented stripes aligned along the [001] direction, is concluded to be the saturation of the O chemisorption phase [8, 9]. The other phase consists of a novel island structure, which is discussed in detail below. When dosing at even higher temperatures, 600 K (Fig. 1d), only the chemisorption phase remains. High-resolution images (Fig. 1d, bottom-left) unambiguously show that this is a structure built from (n ×2) units, where n is very narrowly peaked around 12, for which reason we shall refer to it as a (12×2) structure. Each (12×2) repeat unit contains a stripe with 10 distinct protrusions separated by ~ 4 Å wide and ~ 0.5 Å deep depressions. These depressions are deeper and more narrow than those observed in the domain structures found at lower O coverage, where the Pt(110) surface remains intact [8, 9], and the depressions are accordingly assigned

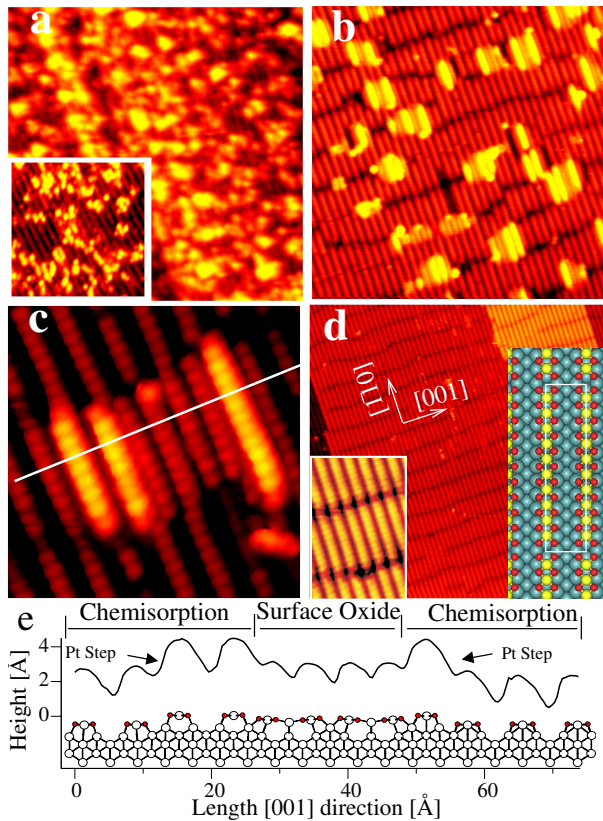


FIG. 1: STM images of the Pt(110) surface after exposure to a) 5 min atomic O at 298 K ($300 \times 300 \text{ \AA}^2$). Inset: 0.01 mbar O_2 for 10 min at 355 K ($150 \times 150 \text{ \AA}^2$). (b) 60 min atomic O at 500 K ($300 \times 300 \text{ \AA}^2$). (c) 60 min atomic O at 500 K. High-resolution image ($60 \times 60 \text{ \AA}^2$) of surface oxide island. The middle part of the island reveals a surface oxide while the protruding stripes are 2nd layer Pt rows with chemisorbed O. (d) 75 min atomic O at 600 K ($500 \times 500 \text{ \AA}^2$). Insets: high-resolution image ($46 \times 77 \text{ \AA}^2$) of the chemisorption phase and associated ball model of the (12×2) -22 O chemisorption structure. (e) Line scan along the white line in (c) and ball model based on the DFT calculations presented below. All STM measurements were made in UHV at 298 K with $I=1.5\text{--}2 \text{ nA}$, $V=1\text{--}1.75 \text{ V}$.

to vacancies, where two Pt atoms have been pushed out between neighboring stripes [13]. The remaining Pt atoms are expanded $\sim 14 \%$ in the $[1\bar{1}0]$ direction and our DFT modelling indicates a strong adsorption of 22 O atoms per stripe [14]. A similar (10×2) O structure has been observed on Rh(110) [15].

STM imaging of the small islands that appear after O exposure at 500 K (Fig. 1c) or following high pressure O_2 exposures at 355 K is only possible at bias voltages $\geq 1 \text{ V}$, indicating that the electronic structure of the islands is associated with a band gap. It is therefore reasonable to associate these islands with patches of surface oxide phase. Our calculations below further substantiate this assignment. The oxide islands appear to consist of stripes similar to those in the (12×2) structure with a similar ex-

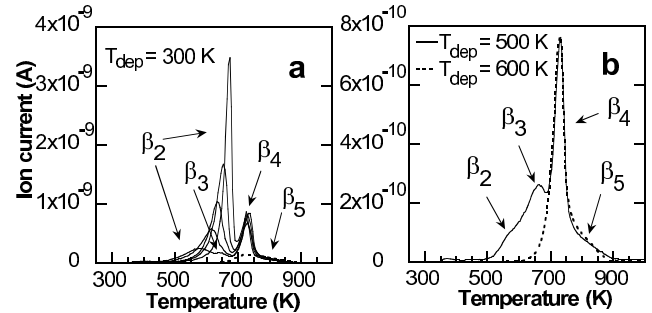


FIG. 2: (a) TPD spectra of O_2 obtained after 5 to 20 min atomic O exposures at 300 K, corresponding to 4.4, 5.0, 5.7, 7.3 and 8.7 ML, as well as after 500 L O_2 exposure (1.2 ML, dashed line). An additional weak peak (β_1) appears at $\sim 400 \text{ K}$ at the highest exposures (not shown). (b) TPD spectra obtained after atomic O exposure at 500 K and 600 K, respectively. Heating rate: 2.5 K/s .

pansion along $[1\bar{1}0]$. The stripes are, however, shifted by half a Pt-Pt separation in the $[1\bar{1}0]$ direction. Within the islands, some stripes protrude higher $\sim 1.4 \text{ \AA}$ compared to the other stripes in the islands $\sim 0.4 \text{ \AA}$ (Fig. 1e) with respect to the (12×2) structure. These stripes are typically found at the $[001]$ edges of the islands, but in a few cases also inside the islands, proving that the brightness is not a result of an electronic edge state. Moreover, they are always shifted $\pm 1/4$ of the (12×2) cell in the $[001]$ direction. These stripes are therefore attributed to 2nd layer Pt rows with chemisorbed O atoms. For the less protruding stripes within the islands, a 29 % compression in the $[001]$ direction is observed. The projected surface area covered by islands ($\sim 16 \%$) at 500 K corresponds well to the amount of Pt removed from the lattice to form the (12×2) superstructure (2 out of 12 Pt atoms), and indicates that the surface oxide islands are formed by rearrangement of such Pt atoms. The surface containing only the chemisorption phase after deposition at 600 K appears smoother with larger terraces than the clean Pt(110) surface, which typically exhibits a periodic buckling along the $[001]$ direction with a high step density along $[1\bar{1}0]$ [16]. This indicates that the Pt atoms from the formation of vacancies between the stripes are mobile at 600 K and bind to the step edges instead of forming surface oxide islands.

Figure 2 shows TPD spectra obtained after atomic O and O_2 exposures (all O desorbs associatively as O_2). The peak at 730 K (β_4) with the high temperature shoulder at $\sim 800 \text{ K}$ (β_5) is associated with O_2 desorbing from the (12×2) structure and defect sites, respectively [9]. TPD spectra obtained after O exposure at 600 K confirmed this. In such spectra (Fig. 2b, dashed line) only the β_4 and β_5 peaks are revealed, which corresponds to the STM images (Fig. 1d) exhibiting only the (12×2) chemisorption structure. The β_4 peak is accordingly used for absolute coverage calibration (corresponding to

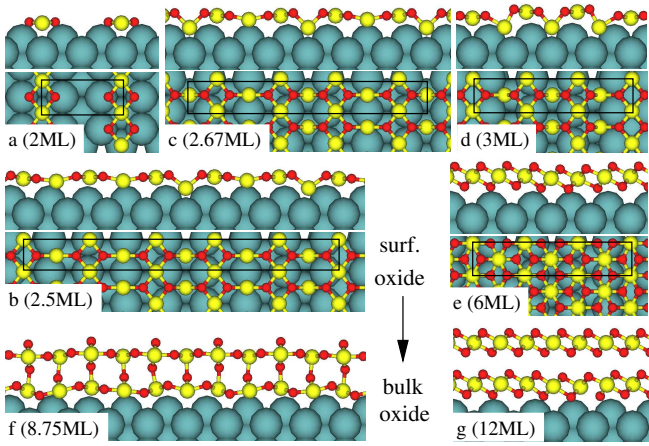


FIG. 3: Ball-and-stick models of (a) the chemisorption, (b-e) surface oxide, and (f-g) thicker oxide structures modelled with DFT. Red, yellow, and blue spheres: oxygen, oxidic, and metallic platinum atoms.

22/12=1.83 ML). The β_4 peak is stronger than the corresponding TPD peak obtained after low-pressure O_2 exposures (500 L, red line in Fig. 2a) due to the completion of the (12 \times 2) structure. A prominent TPD peak (β_2) builds up at 560 K and shifts to 680 K after 20 min atomic O exposure at 300 K, and is the main TPD peak at high O exposures, where the integrated area shows an O uptake corresponding to 8.7 ML. Such high O coverages clearly indicate that bulk oxides are formed upon extended O exposure at RT conditions. Similar TPD spectra have been reported for O_3 /Pt(111) [17], thus suggesting similarities for the high-coverage oxygen structures on the two Pt surfaces. The β_2 peak is substantially reduced or absent after O exposure at 500 and 600 K, respectively (Fig. 2b). After dosing at 500 K, a peak at 650 K (β_3) is clearly visible. Since this TPD peak correlates with the presence of the islands observed in Fig. 1b+c, we assign β_3 to the decomposition of these islands.

We start the account of our DFT calculations [18] by addressing the (12 \times 2) structure. On Pt(110)(1 \times 2) oxygen adsorbs in FCC sites along the Pt ridge causing a build-up of stress [8]. From the presented STM images we found that the stress is relieved by a \sim 14 % expansion of the Pt-Pt interatomic distance along the [1 $\bar{1}$ 0] direction on the ridges. In order to describe this with an affordable computational scheme, we focus on the middle (1 \times 2) section of the structure and expand the whole Pt(110) by 14 % in the [1 $\bar{1}$ 0] direction prior to the introduction of oxygen [19]. The resulting chemisorption structure (Fig. 3a) has a formation energy/O atom with respect to $O_2(g)$, ΔE_O , which is -1.57 eV (Fig. 4A).

The formation energies of the three bulk Pt oxides, PtO, α -PtO₂ and β -PtO₂, are calculated to be $\Delta E_O = -0.41$, -0.62 and -0.64 eV per O, respectively, in agreement with experimental evidence of α and β -PtO₂ being the most stable oxides with a formation energy of -0.69

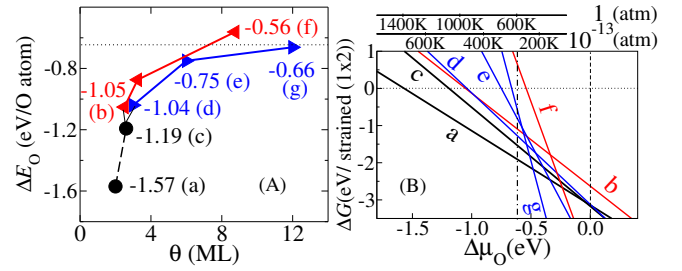


FIG. 4: (A) The formation energy per O atom, ΔE_O , as a function of O coverage. Extra Pt atoms are taken from bulk reservoirs. (B) Formation free energy per (strained) surface (1 \times 2) area with respect to $\Delta\mu_O$. The reference point (dotted vertical line) is $\mu_O = 1/2E_{O_2}$, while the dot-dashed vertical line corresponds to the heat of formation of α -PtO₂. Temperature scales at two typical pressures of O_2 have been indicated.

eV[20]. Inspired by the compressed islands in Fig. 1c, we have calculated the structure and stability of the chemisorption structure compressed by 20, 25, and 33 % in the [001] direction (Fig. 3b-d). The structure compressed by 20 % (Fig. 3b) takes the form of a β -PtO₂(110) surface (strained -0.8% and +2.5% in the in-plane directions) stripped from weakly bound bridging O. The structures compressed 25 % and 33 % are both very stable. The former (Fig. 3c) has no bulk oxide analogue, while the latter (Fig. 3d) adopts the form of the PtO(100) surface, strained -2.0% and +2.5% in-plane. The Pt density in the structure of Fig. 3d is the same as in the α -PtO₂(0001) surface (when strained -1.7% and +3.0% in-plane) meaning that the addition of O atoms would lead to a single (tri-)layer structure of the α -PtO₂ (Fig. 3e) without long-range Pt rearrangement. Second layers of the β and α -PtO₂ oxides can be added (Fig. 3f-g), whereby the average O-binding approaches the formation energy of the bulk oxides (Fig. 4A).

To investigate the expected state of the surface under varying oxidation conditions we turn to the formation *free* energy per (1 \times 2) unit area, $\Delta G = (\Delta E_O - \Delta\mu_O) \times n_O$, where $\Delta\mu_O$ is the change in the chemical potential of oxygen due to temperature and pressure, and n_O is the number of O atoms in the (strained) (1 \times 2) cell [4, 21]. From ΔG it is clear (Fig. 4B) that in the thermodynamic limit, our calculations predict formation of bulk oxide for $\Delta\mu_O > -0.64$ eV and formation of the 2 ML chemisorption structure at lower $\Delta\mu_O$'s. The surface oxide structures are meta-stable and must be stabilized e.g. by defects and/or kinetic restrictions. Referring to Fig. 1b, we note that the surface oxide islands are indeed found in conjunction with imperfections in the (12 \times 2) structure. Furthermore, the surface oxide islands are only found at temperatures, 500 K, where Pt diffusion to the step edges (as seen at 600 K) is suppressed, meaning that Pt atoms ejected from the ridges are locally available at an energetically lower cost than Pt atoms from the bulk reservoir.

In constructing the model of an oxide island in Fig. 1e, we have used the surface oxide structure of Fig. 3c since this structure has a low ΔG at high temperatures and a compression (25%) close to the measured (29%). The assignment of the β_3 TPD peak to the surface oxide islands is now further corroborated by (i) the qualitative finding that the structure of Fig. 3c does not support bulk oxide growth, explaining why the peak neither grows nor shifts with O uptake, and by (ii) the quantitative finding of 0.5 ± 0.1 ML O in the β_3 peak. With a 16 % island coverage this implies a local O coverage of 3.1 ± 0.6 ML within the islands, which compares well with the 2.67 ML in the structure of Fig. 3c.

In contrast to the β_3 peak, the β_2 peak grows with increasing O coverage and shifts to higher temperatures. We already assigned this peak to oxide growth on experimental grounds, and from the DFT results we see that both the α -PtO₂ and the β -PtO₂ phase are candidates for the 3D oxide structure. The crossing in Fig. 2 of the leading edges of the β_2 peaks indicate an increasing barrier for decomposition with increasing O uptake. This is consistent with an increasing differential binding energy (the energy required to remove the *first* O atom) for which we e.g. calculate 1.04 eV for the α -PtO₂ surface oxide (Fig. 3e), and 1.79 eV for the thicker oxide (Fig. 3g), further supporting our assignment of the β_2 peak to bulk oxide growth.

To place our finding of a metastable surface oxide on Pt(110) in a more general context, we note that in order to form a stable surface oxide, the chemisorption phase and the surface oxide phase must coexist (their ΔG 's must cross) at a $\Delta\mu_{\text{O}}$ for which the bulk oxide has not formed yet. To split the effect of studying 4d vs. 5d and dense vs. open surfaces, we have performed calculations for the Pd(110) surface assuming similar chemisorption (Fig. 3a) and surface oxide (Fig. 3c) structures as for Pt(110). A major difference between the 4d and 5d TMs is the cohesive energy which is systematically larger for the 5d TMs (e.g. 3.89 eV for Pd and 5.84 eV for Pt). In our calculations, the cohesive energy enters the surface oxide formation energies (since metal atoms are taken from the bulk reservoir) while it does not enter the chemisorption energies. Yet, comparing Pd(110) and Pt(110), we calculate very similar energetics (on Pd, the chemisorption and surface oxide phases are only 0.27 and 0.32 eV/O weaker than on Pt) meaning that the great difference in cohesive energies is compensated by an enhanced metal-oxygen binding for the Pt system. This rational also explains the similar oxide formation energies for PdO and PtO₂ (experimentally: -0.88 eV/O and -0.69 eV/O at standard conditions).

We thus attribute the finding of the only metastable surface oxides on Pt(110) and Pd(110) to the openness of these surfaces, which allows for a particularly (numerically) high ΔG for the chemisorption phase. In fact, at for example $\Delta\mu_{\text{O}} = -0.4$ eV (cor-

responding ~ 417 K at 1 atm.), we calculate a ΔG of -91 meV/Å² and -70 meV/Å² for the chemisorption phases over Pt(110) and Pd(110) which is to be compared to -67 meV/Å², -39 meV/Å², -24 meV/Å², and -6 meV/Å² for Rh(111) [7], Pd(111) [2], Pd(100) [6], and Ag(111) [4] at 0.25 ML, the latter three systems (with small ΔG 's) all having stable surface oxides. The favorable chemisorption of oxygen in every FCC site on either side of the close-packed ridge of the (110) surface is responsible for the (numerically) large ΔG , which in turn leaves little room for an improved binding in a surface oxide, thereby moving the point of phase coexistence far into the region of a stable bulk oxide.

We acknowledge the financial support from the Danish Natural Research Foundation through the Center for Atomic-scale Materials Physics (CAMP), support from the Danish Research Councils, Dansk Center for Supercomputing, and NorFA (010153).

-
- [1] H. Over *et al.*, *Science* **287**, 1474 (2000).
 - [2] E. Lundgren *et al.*, *Phys. Rev. Lett.* **88**, 246103 (2002).
 - [3] C. I. Carlisle *et al.*, *Phys. Rev. Lett.* **84**, 3899 (2000).
 - [4] W. X. Li *et al.*, *Phys. Rev. Lett.* **90**, 256102 (2003).
 - [5] C. Doornkamp and V. Ponec, *J. Mol. Catal. A* **162**, 19 (2000)
 - [6] E. Lundgren *et al.*, *Phys. Rev. Lett.* **92**, 046101 (2004).
 - [7] J. Gustafson *et al.*, *Phys. Rev. Lett.* **92**, 126102 (2004).
 - [8] S. Helveg *et al.*, *Surf. Sci.* **430**, 533 (1999).
 - [9] A. V. Walker and D. A. King, *J. Phys. Chem.* **109**, 6879 (1998).
 - [10] B. L. M. Hendriksen and J. W. M. Frenken, *Phys. Rev. Lett.* **89**, 046101 (2002).
 - [11] L. Österlund *et al.*, *Phys. Rev. Lett.* **86**, 460 (2001).
 - [12] E. Lægsgaard *et al.*, *Rev. Sci. Instrum.* **72**, 3537 (2001).
 - [13] In the oxygen structures studied by Helveg *et al.* no Pt atoms were pushed out from the close-packed ridges.
 - [14] O binds differentially with 1.76 eV (1.59 eV) at middle (terminal) positions in the (12×2)-22 O structure, as estimated from calculations using (6×2) cells.
 - [15] E. Vesselli *et al.*, *J. Chem. Phys.* **114**, 4221 (2001).
 - [16] T. Gritsch *et al.*, *Surf. Sci.* **257**, 297 (1991).
 - [17] N. A. Saliba *et al.*, *Surf. Sci.* **419**, 79 (1999).
 - [18] Perdew-Wang 91 exchange correlation, ultra-soft pseudopotentials and plane waves cut off at 25 Ry are used. The slabs consist of five atomic layers of Pt(110), three of them fully relaxed, supporting O on one side. (8×8/*N*) **k**-point grids are used for surface Brillouin zone sampling for (1×*N*), *N* = 2, 4, 8 surface cells.
 - [19] The present model with 2 ML per strained (1×2) Pt(110) unit shows differential O binding of 1.72 eV close to the values obtained when including mismatch between the Pt ridge and the Pt(110) [14].
 - [20] *The Oxide Handbook*, Ed. G.V. Samsonov (IFI/Plenum, New York 1973).
 - [21] K. Reuter and M. Scheffler, *Phys. Rev. B* **65**, 035406 (2002).

V

Controlling the catalytic bond-breaking selectivity of Ni surfaces by step blocking

RONNIE T. VANG¹, KAROLIINA HONKALA², SØREN DAHL³, EBBE K. VESTERGAARD¹,
JOACHIM SCHNADT¹, ERIK LÆGSGAARD¹, BJERNE S. CLAUSEN³, JENS K. NØRSKOV²
AND FLEMMING BESENBACHER^{1*}

¹Interdisciplinary Nanoscience Center (iNANO), Center for Atomic-scale Materials Physics (CAMP), and Department of Physics and Astronomy, University of Aarhus, DK-8000 Aarhus C, Denmark

²Center for Atomic-scale Materials Physics (CAMP), and Department of Physics, Technical University of Denmark, DK-2800 Lyngby, Denmark

³Haldor Topsøe A/S, Nymøllevej 55, DK-2800 Lyngby, Denmark

*e-mail: fbe@inano.dk

Published online: 23 January 2005; doi:10.1038/nmat1311

The reactivity of catalytic surfaces is often dominated by very reactive low-coordinated atoms such as step-edge sites^{1–11}. However, very little knowledge exists concerning the influence of step edges on the selectivity in reactions involving multiple reaction pathways. Such detailed information could be very valuable in rational design of new catalysts with improved selectivity. Here we show, from an interplay between scanning tunnelling microscopy experiments and density functional theory calculations, that the activation of ethylene on Ni(111) follows the trend of higher reactivity for decomposition at step edges as compared with the higher-coordinated terrace sites. The step-edge effect is considerably more pronounced for the C–C bond breaking than for the C–H bond breaking, and thus steps play an important role in the bond-breaking selectivity. Furthermore, we demonstrate how the number of reactive step sites can be controlled by blocking the steps with Ag. This approach to nanoscale design of catalysts is exploited in the synthesis of a new high-surface-area AgNi alloy catalyst, which is tested in hydrogenolysis experiments.

The idea that special active sites can control the reactivity of an atomic surface dates back to the pioneering work of Taylor¹. Traditionally, the influence of step edges has been investigated by comparing the reactivity of planar and stepped atomic surfaces, using integrating techniques (for example, reaction rate studies or thermal desorption spectroscopy^{2–4}). The scanning tunnelling microscope (STM) with its unique imaging capabilities has proven to be a very powerful tool for identifying the active sites on metal surfaces, as first demonstrated by Ertl and co-workers⁵ for NO dissociation on Ru(0001). With the advent of density functional theory (DFT) calculations, it became evident that the difference in

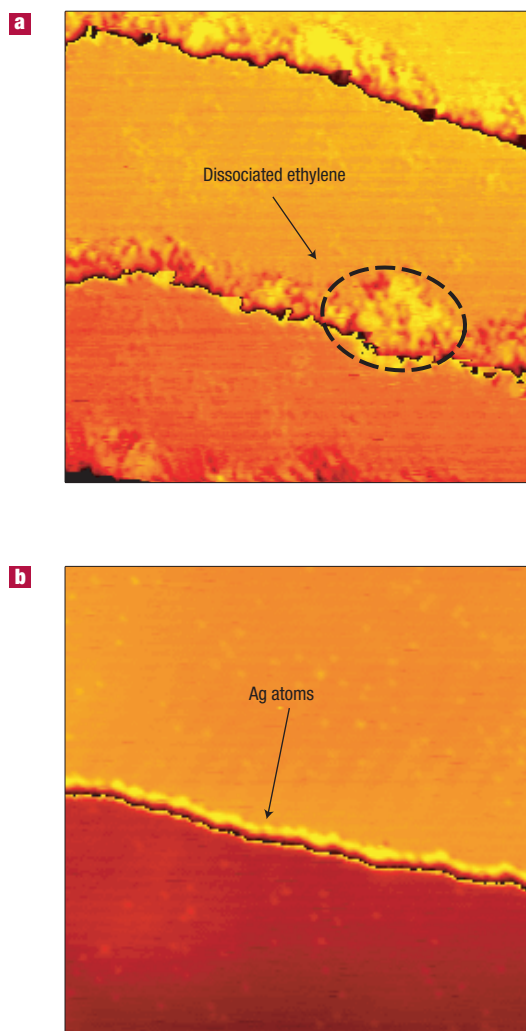


Figure 1 Ethylene decomposition on Ni(111) and Ag/Ni(111). **a**, STM image ($200 \times 200 \text{ \AA}^2$) of a Ni(111) surface after exposure to ethylene (10^{-8} torr; 100 s) at room temperature. A brim of decomposed ethylene is formed along the step edges. **b**, STM image ($400 \times 400 \text{ \AA}^2$) of a Ni(111) surface with the step edges blocked by Ag atoms. No decomposition of ethylene is observed on this modified surface.

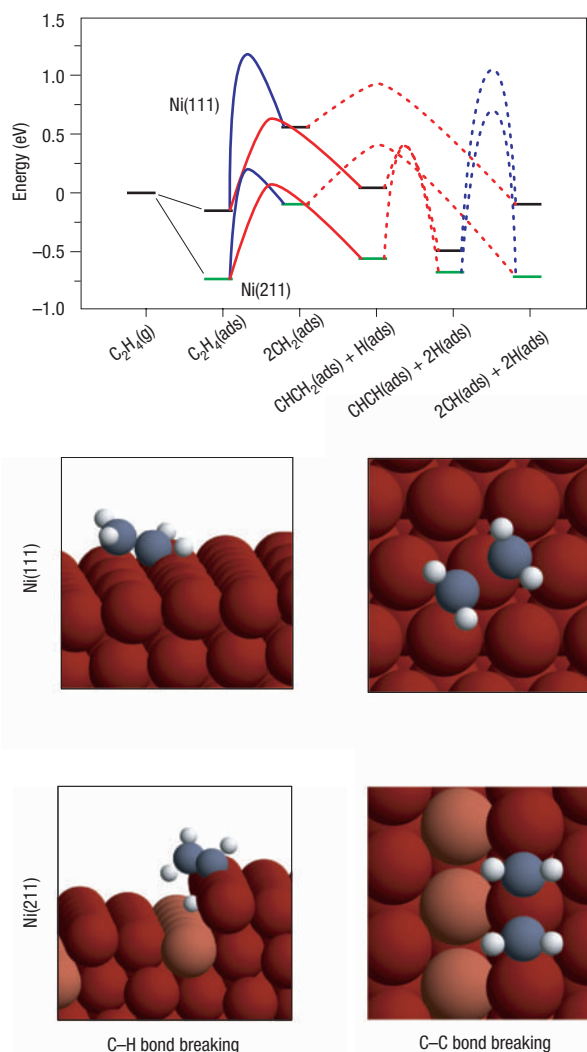


Figure 2 Potential energy diagram for ethylene decomposition on Ni(111) and stepped Ni(211). The diagram shows the activation barriers for C–C bond breaking—dissociation (blue line); and C–H bond breaking—dehydrogenation (red line) on both Ni(111) and Ni(211). The activation barrier for CH_2 dehydrogenation is for one CH_2 . The adsorption of different reaction intermediates is marked with black (green) lines on the Ni(111) (Ni(211)) surface. Below, the transition-state structures for dissociation and dehydrogenation are shown on the two different surfaces.

reactivity between terraces and steps can be enormous, and it was confirmed experimentally⁶ that the rate of N_2 dissociation is at least nine orders of magnitude larger at steps than on close-packed terraces on Ru(0001) at 500 K. The DFT calculations also showed the effect to be present for a number of other diatomic molecules^{7–11}. However, due to the simple structure of the molecules, these studies have only probed the reactivity of the surfaces. It is highly desirable also to have information about the specific role of step edges in reactions for which more than one possible reaction pathway exists. In the present study we have considered the initial step of the decomposition of ethylene (C_2H_4) on Ni(111) in order to gain a detailed knowledge of the influence of the step edges on the rate of C–H and C–C bond breaking. In the end, this bond-breaking selectivity determines the selectivity that can be observed in the macroscopic kinetics—for instance, as the difference in dehydrogenation and hydrogenolysis rates.

Figure 1a shows an STM image of the Ni(111) surface after a 100-s exposure to 10^{-8} torr ethylene at room temperature. The image clearly shows how ethylene has induced a brim with a significantly different corrugation compared with that of the (111) facets along the steps of the surface. The ethylene-induced brim structure was observed exclusively at the upper steps. We never found nucleation of ethylene-induced islands on the terraces of the surface after ethylene exposure. The width of the brim did not increase when the exposure time was increased by a factor of 20, which shows that the process is self-poisoning. As seen from the STM image (Fig. 1a), the self-poisoning is caused by selective adsorption at the step edges, and free step sites are thus needed for the process of forming the brim. If the brim were to be caused by molecularly adsorbed ethylene one would expect the width of the brim to increase with increasing ethylene exposure, which is not consistent with the experimental findings. Furthermore, no brim was observed when the sample was exposed to ethylene at 200 K, indicating that an activation barrier is associated with the formation of the brim. We thus conclude that the formation of the brim is caused by ethylene that has partly or fully decomposed at the step sites.

We calculated the activation barriers for the dissociation (C–C bond breaking) and dehydrogenation (C–H bond breaking) of ethylene both on the flat Ni(111) and the stepped Ni(211) surface. The potential energy diagram is shown in Fig. 2, and from this the binding of ethylene at a step site was found to be favoured by 0.6 eV over binding to a regular terrace site. For all possible intermediates we found adsorption at the upper steps to be the most stable configuration in agreement with the experimental finding. The results showed that the energies of the transition states for ethylene dissociation and dehydrogenation at the steps were both lower by more than 0.5 eV compared with the lowest barrier (dehydrogenation) on the flat Ni(111) surface, thus confirming the high reactivity of the step sites consistent with the present STM findings. Furthermore, the potential-energy diagram showed that the reduction in the height of the activation barrier, when comparing step sites with terrace sites, was considerably more pronounced for dissociation than for dehydrogenation. An indication of the origin of this difference can be obtained by considering the structure of the transition states, see Fig. 2. For C–H bond breaking the transition state is over a single Ni atom both on the (111) surface and at the step. For C–C bond breaking, in contrast, the transition state is somewhat different in the two cases. On the (111) surface, the CH_2 groups end up in the three-fold sites, whereas at the step the final states are the two-fold sites, reflecting the fact that the Ni step-edge atoms are more reactive than those behind the step. The distance between CH_2 in the two-fold sites of the final state at the step is shorter than the distance between the three-fold sites of the final state on the terrace. This means that the CH_2 groups are stabilized at an earlier point on the dissociation path, and the barrier becomes lower. The results in Fig. 2 show that the barriers for C–C and C–H bond breaking for adsorbed ethylene become comparable at the step. We note that the reaction steps following dehydrogenation of C_2H_4 lead to intermediates with larger C–C bond strength, which should result in larger energy barriers for C–C bond breaking. This is illustrated for CH–CH bond breaking in the figure (dotted lines). The main effect of the step is therefore to open C–C bond breaking at the level of adsorbed C_2H_4 .

As shown by the DFT calculations, the selectivity of the Ni(111) surface towards ethylene dissociation/dehydrogenation is to a great extent determined by the ratio of the number of steps to terrace atoms, which implies that the selectivity of a Ni(111) surface may be controlled by regulating the availability of free step sites.

Comparison of the dehydrogenation barrier to the higher dissociation barrier on the flat Ni(111) terrace indicates at least partial ethylene dehydrogenation before C–C bond breaking, which

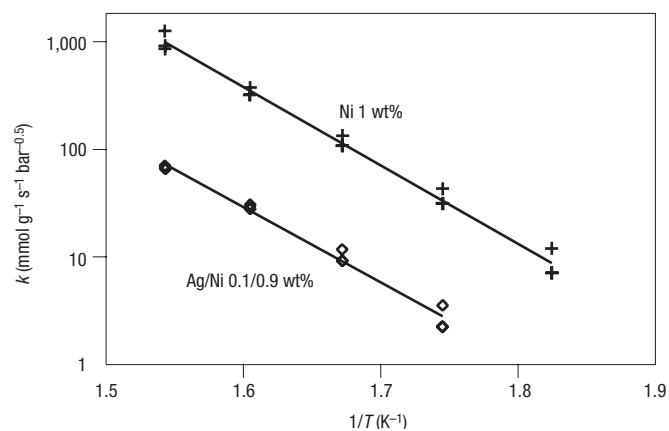


Figure 3 Arrhenius plot of the rate constant for ethane hydrogenolysis over Ni/MgAl₂O₄ and Ag/Ni/MgAl₂O₄. The rate constant (k) of ethane hydrogenolysis is approximately one order of magnitude lower on Ag/Ni/MgAl₂O₄ as compared with Ni/MgAl₂O₄, whereas the activation energy (slope of the Arrhenius plot) is similar.

has also been observed experimentally¹². By blocking the step sites one can thus prevent C–C bond breaking and selectively control the formation of CHCH₂.

In order to pursue this strategy we investigated the possibility of blocking the steps by the use of small amounts of Ag, which is known from previous STM studies¹³ to nucleate preferentially at the step edges of Ni(111). Figure 1b shows an STM image of a Ni(111) surface after room-temperature deposition of Ag and post-annealing at 800 K. As seen in the STM image, this procedure led to a Ni(111) surface with all step sites being covered by Ag atoms. To demonstrate that Ag does in fact lower the reactivity of the step sites, we subsequently exposed the Ag/Ni sample to 10⁻⁸ torr ethylene for 100 seconds at room temperature. In this case, no ethylene-induced brim structure was observed at the step edges (or on the terraces). We thus both provided further evidence that the step atoms are the active sites for decomposition of ethylene on the Ni(111) surface at room temperature, and demonstrated the possibility of blocking these sites.

To take the next step and bridge the gap between the fundamental surface science results and applied catalysis, we synthesized a new high-surface-area oxide-supported AgNi alloy catalyst and tested it for the hydrogenolysis of ethane, which is the simplest reaction used to probe the activity for C–C bond breaking (see, for example, ref. 14). Figure 3 summarizes the results of the integral flow-reactor measurements performed on both a pure and a Ag-modified Ni high-surface-area catalyst. From the data, it is evident that the addition of Ag to the Ni catalyst led to a decrease in the rate constant for ethane hydrogenolysis by approximately an order of magnitude. It was, however, also seen that the apparent activation energy (the slope of the curves) was the same for the two catalysts, which strongly indicates that the active sites on the two catalysts are the same. From this observation together with the STM and DFT results we conclude that the decrease in the rate constant was caused by Ag atoms partly covering the Ni step edges. It seems highly plausible that not all step sites are blocked, when taking into account the high degree of complexity of the supported high-surface-area catalyst as compared to the well-defined Ni(111) single-crystal surface on which a complete blocking of all the step sites could be achieved with a relatively low amount of Ag.

In conclusion, we are now closer to a better understanding of the role of step atoms in catalytic processes involving the decomposition of complex molecules. In general, one cannot just simply view the step atoms as more reactive sites but also consider the relative

increase in reactivity between different reaction pathways. The step atoms may thus, to a high degree, control the selectivity in a given catalytic process. Such knowledge gained from fundamental surface science experiments could become a powerful tool in the nanoscale design of new and improved catalysts.

METHODS

The STM experiments were conducted in an ultrahigh vacuum (UHV) chamber with the home-built Aarhus STM^{15,16}. The sample was exposed to ethylene by backfilling the chamber while the sample was kept at a constant temperature. Subsequently, the sample was transferred to the STM and all STM images were recorded at room temperature.

The spin-polarized DFT calculations were carried out using the dacapo code¹⁷, we used the RPBE¹⁸ generalized gradient correction self-consistently, and the core electrons of all the atoms were treated with Vanderbilt ultrasoft pseudopotentials¹⁹. All calculations used a six-atom Ni surface unit cell (corresponding to coverage of 1/6) and the equivalent of three Ni(111) layers.

Two different methods were applied to determine the transition states. In some cases the transition state was localized constraining the C–C distances (or C–H distances) and relaxing all other degrees of freedom. In cases, where we did not know the location of the transition state we used the nudged elastic band method²⁰ to determine the transition state.

The high-surface-area Ni catalyst for the integral flow reactor measurements was prepared by incipient wetness impregnation of an MgAl₂O₄ support with Ni(NO₃)₂(aq), and the Ag/Ni catalyst was similarly prepared by incipient wetness impregnation of AgNO₃(aq) on the reduced Ni catalyst. Following the impregnation steps the catalysts were dried and subsequently calcined at 450 °C. The metal content in the samples was verified by inductive coupled plasma analysis. The ethane (C₂H₆) hydrogenolysis experiments were performed in an integral plug flow reactor, a U-tube made of quartz, with an inner diameter of 4 mm. The reactor, with a pressure of about 1.0–1.2 bar, was loaded with 200 mg of catalyst, 150–300 μm sieved fraction, which was fixed between two quartz wool wads. Each run started with a reduction of the catalyst in hydrogen (100 ml min⁻¹ NTP) at 500 °C for 1 hour. Five different feed-gas compositions were used, 2–3.5% ethane and 15–30% hydrogen in a He flow, at temperatures from 200–400 °C. The conversion was determined by measuring the concentration of methane in the exit gas employing a calibrated mass spectrometer. Methane was the only product detected.

Received 16 June 2004; accepted 1 November 2004; published 23 January 2005.

References

- Taylor, H. S. A theory of the catalytic surface. *Proc. R. Soc. London Ser. A* **108**, 105–111 (1925).
- Gwathmey, A. T., Cunningham, R. E. The influence of crystal face in catalysis. *Adv. Catal.* **10**, 57–95 (1958).
- Somorjai, G. A. *Surface Chemistry and Catalysis* (Wiley, New York, 1994).
- Yates, J. T. Jr, Surface chemistry at metallic step defect sites. *J. Vac. Sci. Technol. A* **13**, 1359–1367 (1995).
- Zambelli, T., Wintterlin, J., Trost, J. & Ertl, G. Identification of the “active sites” of a surface-catalyzed reaction. *Science* **273**, 1688–1690 (1996).
- Dahl, S. *et al.* Role of steps in N₂ activation on Ru(0001). *Phys. Rev. Lett.* **83**, 1814–1817 (1999).
- Nørskov, J. K. *et al.* Universality in heterogeneous catalysis. *J. Catal.* **209**, 275–278 (2002).
- Liu, Z. P. & Hu, P. General rules for predicting where a catalytic reaction should occur on metal surfaces: A density functional theory study of C–H and C–O bond breaking/making on flat, stepped, and kinked metal surfaces. *J. Am. Chem. Soc.* **125**, 1958–1967 (2003).
- Zubkov, T. *et al.* The effect of atomic steps on adsorption and desorption of CO on Ru(109). *Surf. Sci.* **526**, 57–71 (2003).
- Gambardella, P. *et al.* Oxygen dissociation at Pt steps. *Phys. Rev. Lett.* **87**, 056103 (2001).
- Cioabica, I. M. & van Santen, R. A. Carbon monoxide dissociation on planar and stepped Ru(0001) surfaces. *J. Phys. Chem. B* **107**, 3808–3812 (2003).
- Lehwald, S. & Ibach, H. Decomposition of hydrocarbons on flat and stepped Ni(111) surfaces. *Surf. Sci.* **89**, 425–445 (1979).
- Besenbacher, F., Nielsen, L. P. & Sprunger, P. T. In *The Chemical Physics of Solid Surfaces and Heterogeneous Catalysis* Vol. 8 (eds King, D. A. & Woodruff, D. P.) Ch. 10 (Elsevier, Amsterdam, 1997).
- Sinfelt, J. H. *Bimetallic Catalysts, Discoveries, Concepts, and Applications* (Wiley, New York, 1983).
- Lægsgaard, E., Besenbacher, F., Mortensen, K. & Stensgaard, I. A fully automated, “thimble-size” scanning tunnelling microscope. *J. Microsc.* **152**, 663–669 (1988).
- Besenbacher, F. Scanning tunnelling microscopy studies of metal surfaces. *Rep. Prog. Phys.* **59**, 1737–1802 (1996).
- <http://www.fysik.dtu.dk/CAMPOS>
- Hammer, B., Hansen, L. B. & Nørskov, J. K. Improved adsorption energetics within density-functional theory using revised Perdew–Burke–Ernzerhof functionals. *Phys. Rev. B* **59**, 7413–7421 (1999).
- Vanderbilt D. Soft self-consistent pseudopotentials in a generalized eigenvalue formalism. *Phys. Rev. B* **41**, 7892–7895 (1990).
- Jónsson, H., Mills, G. & Jacobsen, K. W. In *Classical and Quantum dynamics in Condensed Phase Simulations* (eds Berne, B. J., Ciccotti, G. & Coker, D. F.) Ch. 16 (World Scientific, Singapore, 1998).

Acknowledgements

We acknowledge the financial support from the European Union through the contract HPRN-CT-2002-00170.

Correspondence and requests for materials should be addressed to F. B.

Competing financial interests

The authors declare that they have no competing financial interests.

Adsorbate-induced alloy phase-separation: A direct view by high-pressure scanning tunneling microscopy

Ebbe K. Vestergaard, Ronnie T. Vang, Jan Knudsen, Thorbjørn M. Pedersen, Toshu An, Erik Lægsgaard, Ivan Stensgaard, Bjørk Hammer, and Flemming Besenbacher*
*Interdisciplinary Nanoscience Center (iNANO) and Department of Physics and Astronomy,
University of Aarhus, DK 8000 Aarhus C, Denmark.*

The influence of high pressures of carbon monoxide (CO) on the stability of a Au/Ni(111) surface alloy has been studied by high-pressure scanning tunneling microscopy. We show that CO induces a phase separation of the surface alloy at high pressures, and by means of time-lapsed STM movies we find that Ni atoms are removed from the surface layer during the process. Density functional theory calculations reveal the thermodynamic driving force for the phase separation to be the Au-induced compression of the CO overlayer with a resulting CO-CO repulsion. Furthermore, the atomistic mechanism of the process is shown to be kink-site carbonyl formation and evaporation which is found to be enhanced by the presence of Au.

PACS numbers:

There is an increasing awareness of the fact that chemical reactivity of bimetallic catalysts can be radically different from the reactivity of either of the elemental component metal catalysts [1–9]. In the past the main focus has been on the class of binary metal systems that form thermodynamically stable, ordered or random bulk alloys. Recently, however, it has been shown that another class of very interesting, so-called surface alloy systems exists that do mix and form alloys in the surface layer, although the constituent metals are bulk immiscible. The prospects of designing novel catalysts with improved chemical properties, both with respect to the overall activity and not least the selectivity, has spurred a lot of scientific interest in alloy systems. It has been demonstrated that we are today approaching an era where knowledge gained from fundamental surface science studies on alloys may lead to the nanoscale design of new and improved high surface area industrial catalysts [8].

One issue, which remains to be addressed is, however, whether such alloy systems are stable when the pressure gap between the idealized, well-controlled low vacuum conditions for typical fundamental model studies and the high gas pressures at industrially relevant catalytical conditions is bridged. Adsorption-induced effects on alloy surfaces have previously been observed. Segregation of the more reactive species in bimetallic alloys has, e.g., been investigated under reaction conditions [10, 11], and bimetallic overlayers have been found to exhibit morphological changes upon exposure to adsorbates [12].

Based on an interplay of fast-scanning, high resolution STM and DFT calculations we will show in this letter that adsorption-induced phase-separation may indeed occur when the surface alloy is exposed to high pressures of a reactive gas. In the past it has been shown that Au atoms alloyed into the topmost layer of Ni(111) significantly modify the reactivity of the neighboring nickel atoms, thereby rendering the AuNi alloy an interesting candidate for catalytic applications [8, 13]. With the fast-

scanning capabilities of our high-pressure scanning tunneling microscope (HP-STM) we have studied the AuNi alloy system when exposed to high pressures of CO, and from real-time STM movies we have followed the dynamics of the phase-separation. DFT calculations reveal that the underlying atomistic process is the formation of Ni-carbonyls at step edges. The Au atoms are found to accelerate this process owing to an increased CO-CO repulsion at high pressures.

The experiments were performed in a UHV chamber (base pressure $\sim 1 \cdot 10^{-10}$ mbar) equipped with a dedicated HP-STM situated in a HP-cell attached directly to the chamber. Further details of the HP-cell and gas dosing are described elsewhere [14, 15]. The Ni(111) crystal was prepared by several sputtering and annealing cycles (2 keV Ar⁺ followed by 800 K annealing in UHV for 10 minutes) and characterized by STM in UHV to check the cleanliness. Au was evaporated onto the sample at room temperature (RT) from a home-built evaporator. Under these conditions, Au islands nucleate at the Ni steps, and the Au coverage is easily determined by STM measurements. Alloying of Au into the topmost Ni-layer was subsequently facilitated by annealing the sample to 800 K for 10 minutes. Fig. 1a shows an example of an STM image of the Au/Ni(111) surface alloy. For clarity, the Au coverage in this particularly chosen image is rather low. Au is imaged as depressions in the alloy as previously described [8]. In all the high-pressure experiments the Au coverage was kept at 0.3 ± 0.1 ML. DFT calculations were performed using a super cell, plane wave (25 Ry) and ultra-soft pseudopotential approach with exchange-correlation effects described within the revised Perdew, Burke, Ernzerhof (RPBE) form [16].

When the Au/Ni(111) surface alloy is exposed at room temperature (RT) to 1000 mbar of CO, dramatic morphological changes are observed. The surface is observed to be covered with small irregular clusters, persisting even after the high-pressure CO is pumped away (See fig. 1b).

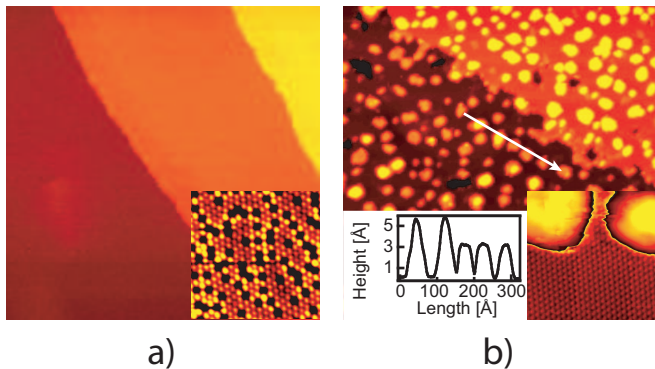


FIG. 1: (a) STM image ($800 \times 800 \text{ \AA}^2$) of Au/Ni(111) after annealing (alloy formation). Inset: Atomic-resolution image ($50 \times 50 \text{ \AA}^2$) of the Au/Ni(111) surface alloy. The Au atoms are imaged as depressions. (b) STM image ($1000 \times 1000 \text{ \AA}^2$) of Au/Ni(111) after exposure to 1000 mbar of CO, in which case the surface is observed to be covered with islands. The line scan (indicated by the white arrow) shows islands of two different heights. Inset: Atomic resolution of an area between the Au islands ($60 \times 60 \text{ \AA}^2$) reveals a clean Ni(111) surface.

A zoom-in on the flat regions between the clusters reveals the clean Ni surface with no Au alloyed into the topmost layer (Insert in Fig. 1b) [17], but subsequent annealing at 800 K under UHV conditions restores the original AuNi surface alloy, thus indicating that Au is still present in the surface region after the high-pressure CO exposure. From an analysis of the island height distribution in the STM images we find that most islands have an apparent height of 3.2 \AA , while $\sim 10\%$ have a height of 5.6 \AA (See inserted line scan in figure 1b). The 3.2 \AA corresponds well to the height measured for Au islands on Ni(111) after RT evaporation, and are therefore ascribed to monolayer islands of Au. The height difference between the two types of islands is 2.4 \AA , which agrees with the step height of Au(111) (2.35 \AA), and the taller islands are thus associated with double-layer Au islands. Assuming that the clusters consist entirely of Au, we estimate a Au coverage of $0.24 \pm 0.04 \text{ ML}$ after high-pressure CO exposure, which is in good agreement with the initial coverage of $0.32 \pm 0.04 \text{ ML}$ [18]. Based on the above experimental findings we hence conclude that all the observed clusters must be Au clusters, and that the alloy has undergone a complete phase-separation.

Lowering the CO pressure to 7-53 mbar, the phase separation slowed down sufficiently that we were able to follow its dynamics by acquiring STM movies. Figure 2 shows a series of STM images picked from such an STM movie acquired at a CO pressure of 13 mbar [19]. The movie reveals that the Au cluster formation starts at the Ni steps. Ni atoms are removed and Au clusters are nucleated and left behind in the wake of the moving step. The process is non-uniform; on each step a large fraction of the Ni atoms is removed from the terrace in certain

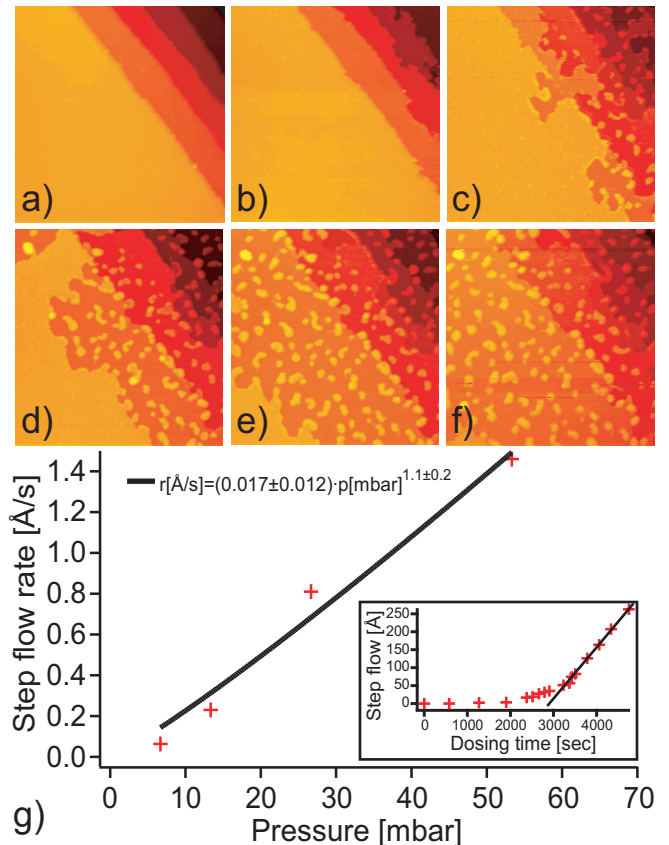


FIG. 2: (a)-(f) STM images ($1000 \times 1000 \text{ \AA}^2$) taken from an STM movie recorded in 13 mbar CO. Time of exposure: (a) 0 min, (b) 25 min, (c) 50 min, (d) 75 min, (e) 100 min, (f) 125 min. (g) Plot of the reaction rate of Ni removal (carbonyl formation) taken from the linear part of step flow graphs (see insert).

areas, whereas other areas are nearly intact after a given time. Apparently, the Ni atoms removed from the step edge leave the surface since no nucleation of Ni islands is ever observed. The removal of Ni atoms is best explained in a model where Ni-carbonyl molecules are formed and desorb from the surface, as we will discuss below.

To quantify the rate of removal of Ni atoms and the concomitant nucleation of Au clusters, the average movement of the Ni steps (step flow) is determined as a function of time (see insert in Fig. 2g). Even though the process is not uniform, this quantity still contains information about the general evolution of the phase separation. The phase separation is characterized by an *incubation* period in which the step edges do not move, followed by a transition to a region where the step edges move with an approximately constant velocity. The incubation time varies largely across the surface, but the final velocity of the step flow can reasonably be used as a parameter for describing the reaction rate on the surface. In Fig. 2g, the reaction rate (final step flow velocity) is plotted as a function of pressure, and we observe that the

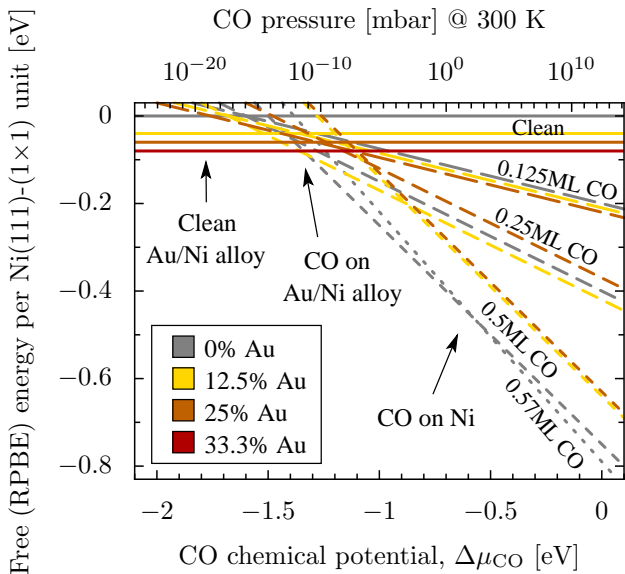


FIG. 3: Free energies of several CO molecules adsorbed on pure Ni and alloyed AuNi surfaces (Au/Ni ratio = 0.125, 0.250, or 0.333). The four horizontal lines represent surfaces with zero CO coverage. At low $\Delta\mu_{\text{CO}}$ (below ca -1.45 eV) the clean AuNi alloys (no CO adsorbed) are thermodynamically favored, while CO adsorbed on pure Ni surfaces are favored at higher potentials ($\Delta\mu_{\text{CO}}$ above ca -1.3 eV). At $\Delta\mu_{\text{CO}} \simeq -1.35$ eV CO adsorbed on AuNi is favored.

rate at which Ni atoms are removed scales as a power law as a function of the CO pressure with a reaction order of 1.1 ± 0.2 , i.e. a linear dependence of the CO pressure within the uncertainty of the data.

The removal of Ni atoms from the step edges does not stop after the completion of the phase separation, and even on the clean Ni(111) surface (no Au deposited), we find that atoms are removed at high pressures of CO. The step flow on the pristine Ni(111) surface is, however, severely reduced compared to on the AuNi alloy, and a similar quantification of the rate of Ni removal has therefore not been possible.

To track the atomic origin of the AuNi phase separation, we have performed DFT calculations investigating both the thermodynamics and kinetics of the process. In Fig. 3 we present the surface free energy of Ni(111) and the AuNi surface alloyed with different Au loads and CO coverages. In equilibrium, the lowest free energy curve dictates the thermodynamically preferred surface state at a given CO chemical potential, $\Delta\mu_{\text{CO}}$, i.e. as a function of the temperature and CO partial pressure [20]. Figure 3 shows that at $\Delta\mu_{\text{CO}}$ above -1.3 eV, it becomes preferable to phase separate the alloy constituents. The Ni becomes CO covered, while the Au does not (in the calculations, only the bulk cohesive energy of Au is used). Our DFT calculations thus confirm that the phase separation of AuNi should happen for high CO chemical potentials. High potentials can be achieved either by having

low temperatures or high pressures. Experimentally, only the latter shows phase separation, possibly due to slow kinetics at low temperatures.

The calculations further reveal the reason for the phase separation; the Au atoms bind the CO about 1 eV weaker than the Ni atoms. On the alloy, the adsorbed CO's thus relocate away from the Au atoms and effectively become slightly compressed on the Ni atoms. The energy of compression can be calculated on Ni(111) by comparing the stability of the optimum CO structure with that of the compressed structure. At e.g. 0.5 ML CO coverage, the compression caused by 12.5 % Au corresponds to an energy cost of 0.14 eV per CO (= 0.56 eV per Au), which out-weighs the calculated 0.33 eV alloying energy of Au in Ni(111).

Inspired by the removal of nickel atoms inducing the phase separation of AuNi at high pressures of CO, a model based on nickel carbonyl ($\text{Ni}(\text{CO})_4$) formation is presented in the following. Nickel carbonyl formation is a well-known process capable of dissolving Ni atoms from Ni surfaces during exposure to high pressures of CO [23–25], and the process is furthermore utilized industrially for the refinement of nickel (the so-called Mond process [26]). The formation of carbonyls has previously been found to occur with a measurable rate at pressures above $\sim 10^{-1}$ mbar and temperatures below ~ 525 K [23, 25], which overlaps the investigated pressure and temperature range in our experiments (>7 mbar, room temperature). Also, steps and defects have been found to play a dominant role for the reaction rate of the nickel carbonyl formation [25], which further corroborates the idea that the observed removal of nickel atoms from step edges in our experiments is correlated with the formation of carbonyl species. A variety of CO reaction orders for carbonyl formation on nickel crystals and powders have been reported in the literature with values ranging from 0.63 to 2.9 [23, 24]. Our extracted reaction order of ~ 1 is thus compatible with these earlier findings, and we therefore propose that the phase separation of the AuNi surface alloy occurs because of the formation of nickel carbonyl species at the step edges, and that these species are volatile and leave the surface. Due to the removal of atoms, the step edge moves and Au atoms diffuse along the step edge to form clusters, which are eventually left behind on the new terrace.

The observed incubation time and non-uniformness of the phase separation could indicate that certain specific sites are the only “active sites” for carbonyl formation at the step edges. Au atoms are known from DFT calculations to wet the Ni steps [27], and initially no free Ni step atoms are thus available. We therefore reasonably associate the incubation time with atomic rearrangements to create free low-coordinated Ni sites, e.g. kink sites [25]. To investigate the atomistic mechanism of the subsequent AuNi de-alloying and the reason for the Au promotion of Ni removal, the elementary steps of the carbonyl for-

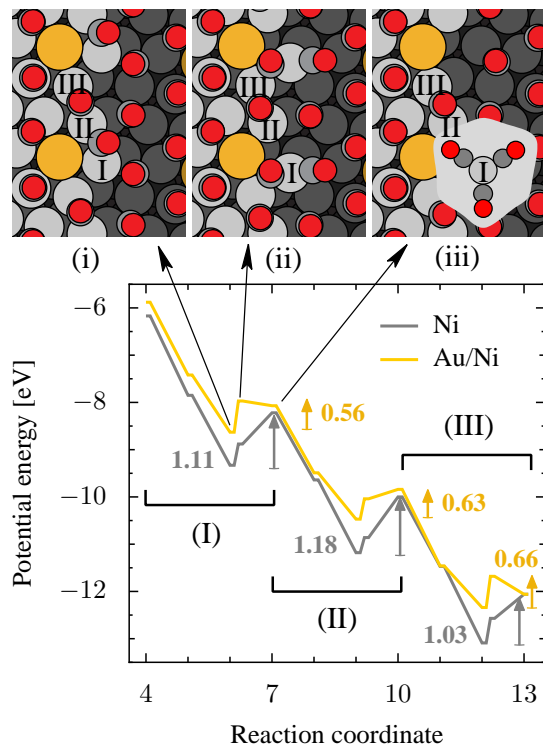


FIG. 4: Top panel: Top view of different configurations during the removal of the first Ni (tagged by I): (i) the fully CO adsorbed surface, (ii) the formation of a $\text{Ni}(\text{CO})_2$ intermediate, and (iii) the formation and desorption of the $\text{Ni}(\text{CO})_3$ intermediate. Bottom panel: Potential energy as the three Ni atoms (I, II, and III) are removed on a pure Ni surface (gray) and on a AuNi alloy surface (gold), respectively. Each tick on the x axis represents a CO taken from the gas phase.

mation have been addressed by DFT calculations. Two series of calculations were performed: kink-Ni removal from a CO-covered Ni(754) surface with and without a substituted Au atom. In both cases, the CO coverage is 0.57 ML, adapting the adlayer geometry reported by Eichler [22]. The Au is substituted at a Ni site inside the Ni(111) terrace to model the situation after the initial Au-plated Ni steps have started retracting, meaning that the steps are mainly Ni. The substituted Ni site is chosen to be that of atop CO bonding, and the CO overlayer is rearranged locally at the kink and step sites as to accommodate the CO elsewhere.

Figure 4 gives the structure and energetics of sequential CO adsorption and $\text{Ni}(\text{CO})_3$ desorption until three consecutive kink-Ni atoms have been removed. The initial situation is thought to be the surface right after the desorption of a carbonyl from the kink site. The empty CO sites in the CO overlayer are filled with strongly bound CO on Ni and with less strongly bound CO on AuNi. On both surfaces, the Ni can detach slightly ($\sim 0.8\text{\AA}$) from the kink site with two CO's residing atop. This rearrangement is associated with a minor energy cost both with and without Au. Now the final state en-

ergy of attaching a third CO to this complex and bringing the carbonyl into the gas phase turns out to be more or less the same for pure Ni as for AuNi. However, since the CO's were less strongly bound on the AuNi than on Ni, the reaction energy for the $\text{Ni}(\text{CO})_3$ formation calculated from the initial state (the fully CO-covered surfaces), becomes much larger for pure Ni than for AuNi. This holds true for all three kink-Ni atoms removed, meaning that the result is insensitive to the details of the CO pattern right at the kink sites. The calculations offer a general explanation of the faster carbonyl formation on AuNi, namely that the CO compression (that originates from the presence of Au) leads to a CO destabilization that enables more exothermic and hence possibly less activated pathways towards the carbonyl formation. Once $\text{Ni}(\text{CO})_3$ is desorbed, the formation of $\text{Ni}(\text{CO})_4$ in the gas-phase is associated with a further 1.04 eV energy release.

With our presented high-pressure studies of CO on Au/Ni(111) we have shown an example of chemical attack and destruction of a surface alloy, which only occurs at pressures well above what is usually studied in the UHV-based surface science model systems. Through DFT calculations we have provided evidence for a model explaining the observed phase separation, where Ni carbonyl formation is responsible for the removal of the Ni atoms in the surface layer.

We acknowledge financial support from the Danish Research Council and computational resources from Dansk Center for Scientific Computing.

* Corresponding author: fbe@inano.dk

- [1] J. Greeley *et al.*, *Nature Materials* **3**, 810 (2004).
- [2] J. R. Kitchin *et al.*, *Phys. Rev. Lett.* **93**, 156801 (2004).
- [3] F. Buatier de Mongeot *et al.*, *Surf. Sci.* **411**, 249 (1998).
- [4] J. A. Rodriguez, *Surf. Sci. Rep.* **24**, 223 (1996).
- [5] R. C. Yeates *et al.*, *Surf. Sci.* **134**, 729 (1983).
- [6] C. Xu *et al.*, *J. Phys. Chem.* **98**, 585 (1994).
- [7] C. T. Campbell, *Ann. Rev. Phys. Chem.* **41**, 775 (1990).
- [8] F. Besenbacher *et al.*, *Science* **279**, 1913 (1998).
- [9] M. Schmid *et al.*, *Phys. Rev. Lett.* **70**, 1441 (1993).
- [10] J. Nerlov *et al.*, *Appl. Catal. A* **191**, 97 (2000).
- [11] E. Christoffersen *et al.*, *J. Catal.* **199**, 123 (2001).
- [12] K. Pohl *et al.*, *Nature* **397**, 238 (1999).
- [13] P. M. Holmblad *et al.*, *J. Chem. Phys.* **104**, 7289 (1996).
- [14] E. Lægsgaard *et al.*, *Rev. Sci. Instrum.* **72**, 3537 (2001).
- [15] P. Thostrup *et al.*, *J. Chem. Phys.* **118**, 3724 (2003).
- [16] B. Hammer *et al.*, *Phys. Rev. B* **59**, 7413 (1999).
- [17] The STM image was obtained at tunneling conditions where the adsorbed CO was swept away by the tip.
- [18] The initial coverage of Au was determined from the step-nucleated Au islands prior to alloying. The small drop in Au coverage arises from bulk diffusion of Au at the initial 800 K annealing during the formation of the alloy.
- [19] The movie can be seen in its full length at <http://www.phys.au.dk/camp/movies/carbonyl.mpg>

- [20] The AuNi surface alloy was composed of a spin-polarized 4-layer Ni(111) slab (two bottom layers fixed). Entropy effects are solely included for gas phase CO [21]. For the CO overlayers on Ni(111) we have used the most stable structures at various coverages found by Eichler [22].
- [21] K. Reuter *et al.*, Phys. Rev. B **68**, 045407 (2003).
- [22] A. Eichler, Surf. Sci. **526**, 332 (2003).
- [23] P. de Groot *et al.*, Surf. Sci. **94**, 204 (1980).
- [24] K. Lascelles *et al.*, Surf. Sci. **125**, L67 (1983).
- [25] V. K. Medvedev *et al.*, Surf. Sci. **401**, L371 (1998).
- [26] L. Mond *et al.*, J. Chem. Soc. **57**, 749 (1890).
- [27] H. S. Bengaard *et al.*, J. Catalysis **209**, 365 (2002).

VII

The Adsorption Structure of NO on Pd(111) at High Pressures Studied by STM and DFT

Ronnie T. Vang, Jian-Guo Wang, Jan Knudsen, Joachim Schnadt, Erik Lægsgaard, Ivan Stensgaard, and Flemming Besenbacher*

Interdisciplinary Nanoscience Center (iNANO) and Department of Physics and Astronomy, UniVersity of Aarhus, DK-8000 Aarhus C, Denmark

Received: May 13, 2005; In Final Form: June 23, 2005

Using a combination of scanning tunneling microscopy (STM) and density functional theory (DFT) calculations, we study the adsorption structure of NO on Pd(111) at pressures of up to 720 Torr. From atomically resolved STM images, we identify, at high pressures, only the (2×2) -3NO structure, which is identical with the highest NO-coverage structure found at low pressure and low temperature. DFT calculations confirm that the (2×2) -3NO structure is indeed the most stable adsorption structure at high pressures. Contrary to recent suggestions in the literature, we therefore conclude that we find no evidence for a (3×3) -7NO structure on Pd(111) at high NO pressure.

The adsorption of gas molecules on metal surfaces is at the very heart of heterogeneous catalysis, and the study of adsorption structures on single-crystal surfaces is fundamental to the understanding of catalytic systems. Therefore, numerous adsorption structure studies have been carried out in the past, and an enormous insight has been gained into the structures formed by most gases on clean metal surfaces at standard ultrahigh vacuum (UHV) conditions.¹ However, it has been argued that the structures found under standard surface science conditions (low temperatures and low pressures) might not resemble those found at typical reaction conditions (high pressures and high temperatures), and the existence of a so-called pressure gap has been discussed.² Such a pressure gap may occur as a consequence of a kinetic hindrance that does not allow for the thermodynamic favorable structure to form at very low temperatures, or entropic effects can lead to the stabilization of new structures at higher temperatures. These effects are difficult to fully take into account when extrapolating UHV results to the relevant reaction conditions. Experimental input is therefore needed in order to elucidate which adsorption structures are the ones of technological interest for a given reaction.

Several techniques are available for exploring adsorption structures at high gas pressure such as scanning tunneling microscopy (STM),³⁻⁸ transmission electron microscopy (TEM),⁹ X-ray diffraction spectroscopy (XDS),¹⁰ sum-frequency generation (SFG),¹¹ and polarization modulation infrared reflection absorption spectroscopy (PM-IRAS).¹² Recently, we have demonstrated the capability of STM to resolve the adsorption structures formed by CO on Pt(111)^{4,5} and Pt(110),³ and H₂ on Cu(110)⁸ surfaces at nearly atmospheric pressures. For all systems, it was shown that the structures found at elevated pressures were identical to structures formed at lower pressures and lower temperatures (i.e., no indications of a pressure gap were revealed for these systems). However, in electrochemical experiments, high adsorbate coverages have been observed,

which cannot be reproduced at low-pressure conditions,¹³ high oxygen pressures are for certain systems found to lead to the formation of oxide structures,^{6,14,15} and high adsorbate coverage can cause a segregation of the more reactive of the components of a surface alloy.^{16,17} One system that displays a true pressure gap, meaning that new adsorption structures are formed on a pure metal at elevated pressures, which are not formed at lower pressures and temperatures, is the NO/Rh(111) adsorption system as reported by Rider et al., who identified a (3×3) -7NO adsorption structure, which forms in equilibrium with the gas phase only at elevated NO pressures.⁷

In a very recent publication, Ozensoy et al. suggest the existence of a similar pressure gap for NO adsorption on Pd(111).¹⁸ On the basis of PM-IRAS data, the authors propose that a (3×3) -7NO structure with an NO coverage of 7/9 monolayer (ML) is also formed at elevated NO pressures on the Pd(111) surface. As for Rh(111), this structure has never been observed at lower pressures and temperatures for which the highest-coverage NO structure is the (2×2) -3NO structure with a coverage of 3/4 ML.¹⁹⁻²³ However, the evidence for the (3×3) structure from vibrational spectroscopy is indirect with respect to a genuine structural determination. We therefore decided to complement these PM-IRAS data with HP-STM data to explore the existence of a (3×3) -7NO adsorption structure.

In the present letter, we find from atomically resolved STM experiments that at room temperature and high NO pressures of up to 720 Torr only the (2×2) -3NO structure is formed. The STM results are supported by state-of-the-art ab initio DFT calculations. We therefore conclude that the NO/Pd(111) system does not provide a pressure gap between standard low-pressure conditions and high-pressure conditions. The origin of the apparent discrepancy of the present STM and DFT results with the recent PM-IRAS data will be briefly discussed.

The experiments were performed in a combined UHV and high-pressure (HP) system comprising a UHV chamber (base pressure $\approx 1 \times 10^{-10}$ Torr) equipped with the home-built

* To whom correspondence should be addressed. E-mail: fbe@inano.dk.

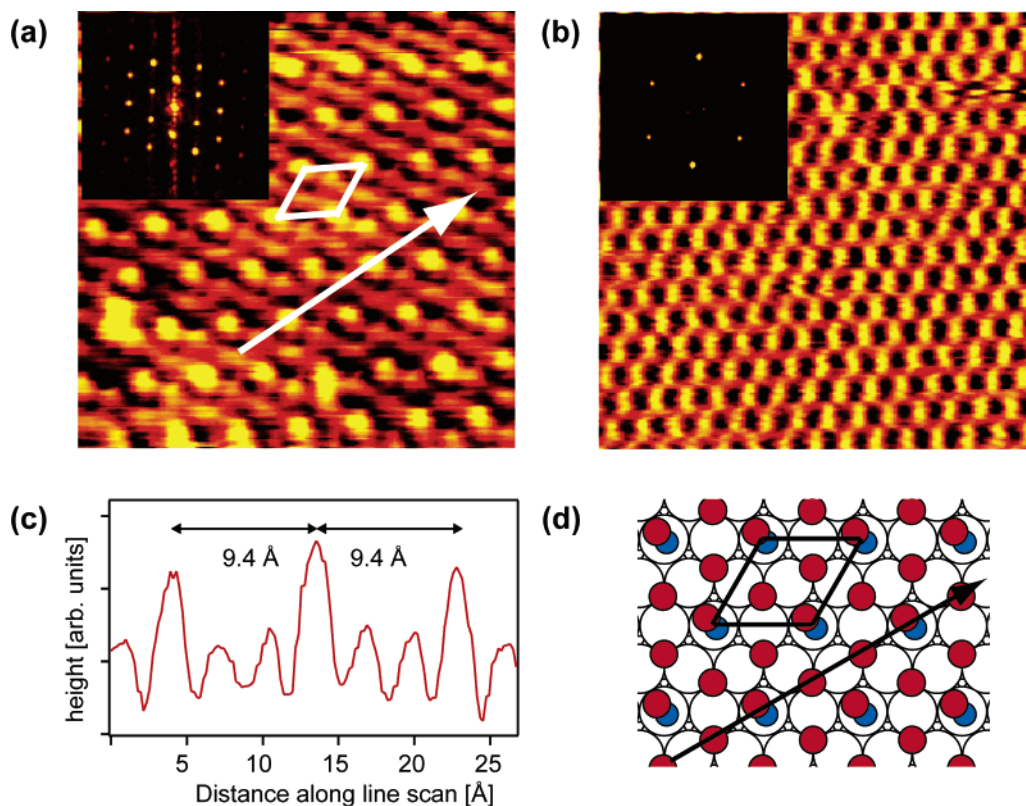


Figure 1. (a) STM image ($41 \times 41 \text{ \AA}^2$) of NO on Pd(111) obtained at room temperature in a background of 720 Torr of NO; the (2×2) unit cell and a line scan direction are indicated (small insert: 2D Fourier transform). (b) STM image ($41 \times 41 \text{ \AA}^2$) of a clean Pd(111) surface (small insert: 2D Fourier transform). (c) Line scan showing the three NO molecules in the unit cell; atop adsorbed NO is clearly distinguished from threefold hollow site adsorbed NO by their different apparent heights. (d) Ball model of the $p(2 \times 2)$ -3NO structure on Pd(111) (oxygen atoms are red, and nitrogen atoms are blue). The (2×2) unit cell and line scan direction corresponding to those in the STM image are indicated.

Aarhus STM²⁴ and standard surface analysis tools. The sample can be transferred under UHV conditions from the main chamber to a separate HP cell equipped with a home-built in situ HP-STM with a design similar to the Aarhus STM.²⁵ Through a gas-handling system, the HP cell can be filled with up to 1 atm of a mixture of ultra-clean gases, and STM images can be obtained in situ. The inner parts of the HP cell as well as the metal parts of the STM are gold-coated in order to avoid any reactions occurring on the chamber walls at the high-pressure conditions. High-purity NO (Messer 99.5%) was used for the NO exposure experiments; further purification, which is important for HP studies, was performed by leading the gas through a copper coil submerged in an ethanol slush kept at approximately $-100 \text{ }^\circ\text{C}$ during the gas inlet.

The Pd(111) single crystal was cleaned by sputtering (1 keV) and annealing (900 K) cycles, and the cleanliness was confirmed by STM images showing a (1×1) Pd(111) structure with no impurities. Although the STM has no chemical specificity, it offers a higher sensitivity than almost all other techniques, and even individual impurities (e.g., at the step edges) can easily be detected from high-resolution STM images.

The DFT calculations were performed using the DACAPO code with ultrasoft pseudopotential and a plane-wave basis set (cutoff energy 25 Rydbergs).²⁶ Exchange-correlation (XC) effects were described with the GGA-RPBE functional.²⁶ The Pd(111) surface was modeled by a four-layer slab. The two lower Pd layers were kept fixed, whereas the upper two layers and the NO molecules were relaxed until the total sum of residual forces was below 0.05 eV/\AA . In this study, we investigated two structures, (2×2) -3NO and (3×3) -7NO, corresponding to $3/4$ ML and $7/9$ ML NO coverages, respectively. The k -points meshes of the surface Brillouin-zone

integration were 6×6 and 4×4 , respectively. In addition to the DFT results, which can be regarded as zero-temperature, zero-pressure findings, we used statistical mechanics to calculate the (T, p) phase diagram.^{27,28} The chemical potential of all of the related surface species are functionals of the temperature T and pressure p , and by determining the (T, p) phase diagram, information on the adsorption phases from UHV to high-pressure conditions was obtained, whereby we are able to bridge the pressure gap. The surface free energy of a certain surface species can be defined as

$$\gamma(T, p) = (G_{\text{NO/Pd(111)}} - G_{\text{Pd(111)}} - N\mu_{\text{NO}})/A \quad (1)$$

The $G_{\text{NO/Pd(111)}}$ and $G_{\text{Pd(111)}}$ are the free energies of the investigated NO/Pd surface species and the clean Pd(111) reference system. They can be replaced by the DFT calculated total energies $E_{\text{NO/Pd(111)}}$ and $E_{\text{Pd(111)}}$, since the vibrational and entropic contributions of $G_{\text{NO/Pd(111)}}$ and $G_{\text{Pd(111)}}$ are very small. The chemical potential of NO is dependent on the temperature and pressure and is given by

$$\mu_{\text{NO}} = E_{\text{NO}}^{\text{total}} + \tilde{\mu}_{\text{NO}}(T, P^0) + k_{\text{B}}T \ln\left(\frac{P_{\text{NO}}}{P^0}\right) \quad (2)$$

P^0 is the atmospheric pressure, and $\tilde{\mu}_{\text{NO}}(T, P^0)$ includes the contribution from rotation and vibration of the molecule, as well as the ideal-gas entropy at 1 atm. Finally, we define $\Delta\mu_{\text{NO}}$ as $\mu_{\text{NO}} - E_{\text{NO}}^{\text{total}}$. All of the experimental values were taken from the JANAF thermochemical tables.²⁹

The NO adsorption structure was explored by in situ scanning at room temperature in a background pressure of NO. Figure 1a shows an STM image obtained at an NO pressure of 720

TABLE 1: Chemisorption Energies and Structural Parameters for the (2×2) -3NO and (3×3) -7NO Adsorption Structures on Rh(111) and Pd(111)

	Rh(111)		Pd(111)	
	(2×2) -3NO	(3×3) -7NO	(2×2) -3NO	(3×3) -7NO
E_{ads} (eV/per NO)	1.68	1.65	1.17	1.07
$d_{(\text{metal}-\text{N})}$ (\AA)-atop	1.78	1.80	1.98	1.98
$d_{(\text{metal}-\text{N})}$ (\AA)-fcc	2.07–2.08	2.04–2.12	2.12–2.14	2.10–2.17
$d_{(\text{metal}-\text{N})}$ (\AA)-hcp	2.05–2.08	2.04–2.14	2.10–2.12	2.15–2.20
$\alpha_{\text{Pd}-\text{N}-\text{O-atop}}$	163°	153°	129°	130°

Torr. A hexagonal pattern of bright protrusions is observed in this STM image (the unit cell is indicated with white lines). The STM was calibrated from high-resolution images of the clean Pd(111) surface (see Figure 1b), and from a detailed comparison of the close-packed directions and nearest-neighbor distances on the clean Pd(111) surface, we conclude that the hexagonal structure formed upon HP NO exposure fits nicely with a (2×2) structure. The (2×2) structure is also very distinct in the comparison of the 2D Fourier transform of the NO adsorption structure and of the clean Pd(111) surface (see the small inserts in Figure 1a,b). In the line scan in Figure 1c, the distance between two adjacent bright protrusions is measured to be 9.4 \AA , which is very close to the ideal distance of $\sqrt{12} \times 2.76 \text{ \AA} = 9.56 \text{ \AA}$ for a (2×2) structure on Pd(111) (Pd–Pd nearest neighbor distance = 2.76 \AA). We then conclude that the observed NO adsorption structure fits with a (2×2) structure within the uncertainty of the calibration of the STM (a few percent).

A similar (2×2) -3NO structure is observed at low pressure and low temperature. This structure has been studied by STM, HREELS, IR vibrational spectroscopy, LEED, UPS, TDS, work function measurements, and DFT calculations and is characterized as a (2×2) -3NO structure with a 1:2 mixture of tilted atop and threefold hollow-site adsorbed NO with an NO coverage of 3/4 ML.^{19–23} A ball model of this (2×2) -3NO structure is shown in Figure 1d with a (2×2) unit cell superimposed. By comparing this to the structure observed by STM in Figure 1a, it is evident that the bright protrusions in the STM image can be associated with the tilted atop adsorbed NO molecules. Furthermore, it is evident from the line scan in Figure 1c that we can distinguish two types of protrusions in the STM image by their different apparent heights. A line scan along the same direction is also indicated in the ball model, and this shows that the less bright protrusions coincide with the threefold hollow-site adsorbed NO molecules. We performed experiments at several NO pressures ranging from 200 Torr to 720 Torr, and we never observed any other structures than the $p(2 \times 2)$ -3NO. On the basis of our STM measurements, we thus conclude that the (2×2) -3NO adsorption structure is the only one formed at room temperature and up to 720 Torr NO pressure.

To confirm that the (2×2) -3NO structure indeed is more stable than the (3×3) -7NO structure proposed by Ozensoy et al. at the pressure and temperature conditions of our experiments, we performed DFT calculations for these two adsorption structures. From the calculations, we found the adsorption energies per NO molecule to be -1.17 eV and -1.07 eV for the (2×2) -3NO and (3×3) -7NO structures, respectively (the results of the DFT calculations are summarized in Table 1). The adsorption energy for the (2×2) -3NO structure is consistent with results reported from our group in a previous study, in which several ordered structures formed under UHV conditions were characterized by STM and DFT.²³ The lower adsorption energy per NO molecule indicates that theory also finds the (2×2) -3NO structure to be the most stable one. A

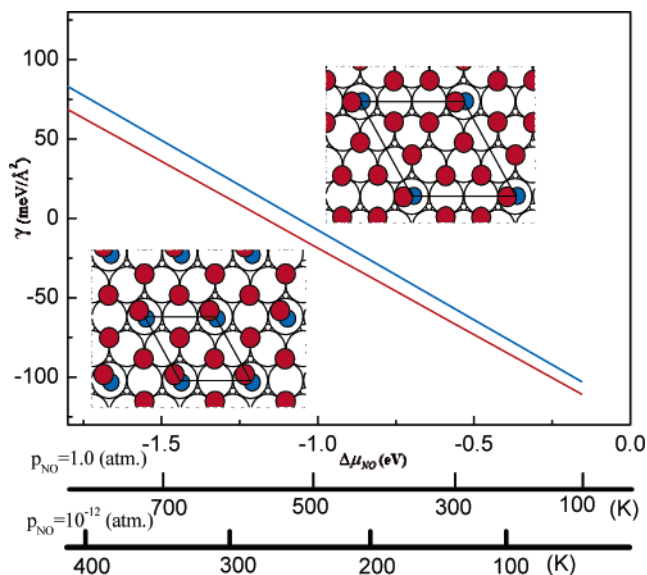


Figure 2. Surface free energies for the (2×2) -3NO (red line) and (3×3) -7NO (blue line) adsorption structures on Pd(111). Temperature axes are shown for NO pressures of 1 atm and 1×10^{-12} atmosphere.

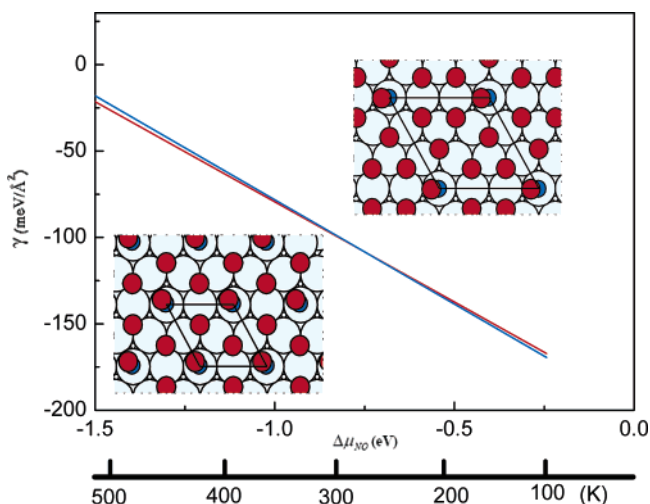


Figure 3. Surface free energies for the (2×2) -3NO (red line) and (3×3) -7NO (blue line) adsorption structures on Rh(111). Temperature axis is shown for an NO pressure of 0.03 Torr.

similar conclusion is in fact also reached in the theoretical part of the paper of Ozensoy et al.¹⁸ As mentioned earlier, the DFT calculations assume zero temperature and pressure and are, thus, not directly compatible with our experimental results. To extend the theoretical results to the experimental conditions, we calculated the surface free energies for the two NO adsorption structures. The results of these calculations are shown in Figure 2, from which we conclude that the (3×3) -7NO is unstable for all practical temperature and pressure conditions. In particular, we find that the free surface energy of the (2×2) -3NO structure is 9.46 meV/\AA^2 lower than that of the (3×3) -7NO structure at the conditions of our STM measurements (300 K and 720 torr NO pressure).

The validity of the DFT calculations was judged by performing similar calculations for the (2×2) -3NO and (3×3) -7NO adsorption structures on Rh(111) to investigate whether these calculations are in agreement with the experimental findings of Rider et al.⁷ The free energy diagram (Figure 3) indeed shows that for Rh(111) the (3×3) -7NO adsorption structure becomes thermodynamically favored at high NO chemical potential. At

an NO pressure of 0.03 Torr, we find that the transition temperature between the two structures is very close to room temperature. This is in excellent agreement with the results of Rider et al.⁷ and provides strong support to the validity of the DFT calculational scheme. The results of the DFT calculations also suggest an explanation for the different behavior of NO adsorption on Pd(111) vs Rh(111). The absolute binding energies per NO molecule are significantly higher on Rh(111) than on Pd(111) for both the (2 × 2) structure (1.68 eV vs 1.17 eV) and the (3 × 3) structure (1.65 eV vs 1.07 eV). This implies that NO is more likely to form higher-coverage structures on Rh(111) than on Pd(111), thus rationalizing the experimental findings in the present work and the work of Rider et al.

From our results, we find no direct explanation as to why the PM-IRAS spectrum changes at high NO pressure, as observed by Ozensoy et al.¹⁸ On the basis of the present STM and DFT results, we discard the proposed (3 × 3)-7NO adsorption structure, and it therefore still remains to be settled how to interpret these PM-IRAS data. In conclusion, we find strong evidence from both STM and DFT that the most stable adsorption structure of NO on Pd(111) at room temperature and 720 Torr is the (2 × 2)-3NO structure, and thus, no pressure gap exists between high-pressure and standard low-pressure conditions.

Acknowledgment. Prof. D. Wayne Goodman is acknowledged for stimulating discussions. The Danish Research Councils and Dansk Center for Scientific Computing are acknowledged for financial and computational support.

References and Notes

- (1) Somorjai, G. A. *Introduction to Surface Chemistry and Catalysis*; John Wiley & Sons: New York, 1994.
- (2) Ertl, G. *Angew. Chem., Int. Ed. Engl.* **1990**, *29*, 1219.
- (3) Thostrup, P.; Vestergaard, E. K.; An, T.; Lægsgaard, E.; Besenbacher, F. *J. Chem. Phys.* **2003**, *118*, 3724.

- (4) Longwitz, S. R.; Schnadt, J.; Vestergaard, E. K.; Vang, R. T.; Lægsgaard, E.; Stensgaard, I.; Brune, H.; Besenbacher, F. *J. Phys. Chem. B* **2004**, *108*, 14497.
- (5) Vestergaard, E. K.; Thostrup, P.; An, T.; Lægsgaard, E.; Stensgaard, I.; Hammer, B.; Besenbacher, F. *Phys. Rev. Lett.* **2002**, *88*, 259601.
- (6) Hendriksen, B. L. M.; Frenken, J. W. M. *Phys. Rev. Lett.* **2002**, *89*.
- (7) Rider, K. B.; Hwang, K. S.; Salmeron, M.; Somorjai, G. A. *Phys. Rev. Lett.* **2001**, *86*, 4330.
- (8) Osterlund, L.; Rasmussen, P. B.; Thostrup, P.; Lægsgaard, E.; Stensgaard, I.; Besenbacher, F. *Phys. Rev. Lett.* **2001**, *86*, 460.
- (9) Hansen, P. L.; Wagner, J. B.; Helveg, S.; Rostrup-Nielsen, J. R.; Clausen, B. S.; Topsøe, H. *Science* **2002**, *295*, 2053.
- (10) Peters, K. F.; Walker, C. J.; Steadman, P.; Robach, O.; Isern, H.; Ferrer, S. *Phys. Rev. Lett.* **2001**, *86*, 5325.
- (11) Rupprechter, G.; Dellwig, T.; Unterhalt, H.; Freund, H. J. *J. Phys. Chem. B* **2001**, *105*, 3797.
- (12) Ozensoy, E.; Hess, C.; Goodman, D. W. *Top. Catal.* **2004**, *28*, 13.
- (13) Villegas, I.; Weaver, M. J. *J. Chem. Phys.* **1994**, *101*, 1648.
- (14) Li, W. X.; Österlund, L.; Vestergaard, E. K.; Vang, R. T.; Matthiesen, J.; Pedersen, T. M.; Lægsgaard, E.; Hammer, B.; Besenbacher, F. *Phys. Rev. Lett.* **2004**, *93*, 146104.
- (15) Over, H.; Muhler, M. *Prog. Surf. Sci.* **2003**, *72*, 3.
- (16) Nerlov, J.; Sckerl, S.; Wambach, J.; Chorkendorff, I. *Appl. Catal., A* **2000**, *191*, 97.
- (17) Christoffersen, E.; Liu, P.; Ruban, A.; Skriver, H. L.; Nørskov, J. K. *J. Catal.* **2001**, *199*, 123.
- (18) Ozensoy, E.; Hess, C.; Loffreda, D.; Sautet, P.; Goodman, D. W. *J. Phys. Chem. B* **2005**, *109*, 5414.
- (19) Loffreda, D.; Simon, D.; Sautet, P. *Chem. Phys. Lett.* **1998**, *291*, 15.
- (20) Conrad, H.; Ertl, G.; Kuppers, J.; Latta, E. E. *Surf. Sci.* **1977**, *65*, 235.
- (21) Chen, P. J.; Goodman, D. W. *Surf. Sci.* **1993**, *297*, L93.
- (22) Bertolo, M.; Jacobi, K. *Surf. Sci.* **1990**, *226*, 207.
- (23) Hansen, K. H.; Slijivancanin, Z.; Hammer, B.; Lægsgaard, E.; Besenbacher, F.; Stensgaard, I. *Surf. Sci.* **2002**, *496*, 1.
- (24) Lægsgaard, E.; Besenbacher, F.; Mortensen, K.; Stensgaard, I. *J. Microsc. (Oxford, UK)* **1988**, *152*, 663.
- (25) Lægsgaard, E.; Österlund, L.; Thostrup, P.; Rasmussen, P. B.; Stensgaard, I.; Besenbacher, F. *Rev. Sci. Instrum.* **2001**, *72*, 3537.
- (26) Hammer, B.; Hansen, L. B.; Nørskov, J. K. *Phys. Rev. B* **1999**, *59*, 7413.
- (27) Reuter, K.; Scheffler, M. *Phys. Rev. B* **2003**, *68*, 045407.
- (28) Reuter, K.; Scheffler, M. *Phys. Rev. Lett.* **2003**, *90*, 046103.
- (29) Chase, M. W. *NIST-JANAF Thermochemical Tables*, 4th ed.; American Chemical Society: Washington, DC, 1998.

VIII

CO dissociation on Ni(111): Step blocking by Ag, Au, and S

Ronnie T. Vang, Ebbe K. Vestergaard,¹ Erik Lægsgaard,
Ivan Stensgaard, and Flemming Besenbacher^{*}

*Interdisciplinary Nanoscience Center (iNANO), and Department of Physics and
Astronomy, University of Aarhus, DK-8000 Aarhus, Denmark*

Abstract

We present results on the dissociative adsorption of carbon monoxide (CO) on a Ni(111) single crystal surface studied by high-resolution scanning tunneling microscopy (STM). We find that the dissociation of CO leads to the nucleation of carbidic islands along the upper step edges at temperatures above ~ 375 K. The influence of three different additives (Ag, Au, and S) is explored. All three are shown to nucleate preferentially at the step edges of Ni(111). The pre-adsorption of these additives completely prevents CO dissociation. We conclude that the step edge atoms are the active sites for CO dissociation at 400 K and that these active sites can be effectively blocked by Ag, Au, or S.

Key words: Scanning tunneling microscopy, Surface chemical reaction, Nickel, Carbon monoxide, Steps, Single crystal surfaces

1 Introduction

The dissociation of CO on nickel surfaces is of great interest within heterogeneous catalysis due to its importance for the steam reforming process [1,2] and CO methanation (inverse steam reforming) [3]. In the steam reforming reaction the dissociation of CO on nickel catalysts can lead to a carbon build-up (coking) and the formation of carbon whiskers. Such a carbon build-up, that

^{*} Corresponding author. Tel.: +45 8942 3604; fax: +45 8942 3690

Email address: fbe@inano.dk (Flemming Besenbacher).

URL: www.inano.dk/besenbacher (Flemming Besenbacher).

¹ Present address: Department of Chemistry, Box 351700, University of Washington, Seattle WA 98195-1700, USA

eventually will lead to a breakdown of the catalyst, is e. g. one of the major problems with the nickel-based catalysts widely used for the steam reforming process [1]. Goodman *et al.* showed that adsorbed sulfur on Ni(111) inhibits the CO methanation reaction in which the dissociation of CO is a vital step [4]. Rostrup-Nielsen *et al.* found that sulfur also acts as a poison for the steam reforming process, but as an even stronger poison for the carbon formation during the reforming process [5]. These ideas were used to develop the SPARG (Sulphur PAssivated ReforminG) process, in which trace amounts of H₂S are added to the feed gas of the steam reforming reactor to reduce the formation of carbon whiskers. The addition of H₂S to the feed gas is, however, not suitable for many applications, since sulphur acts as a poison for most transition metal catalysts, which may be encountered down stream in the reactor. Another approach for preventing carbon formation is to alloy Au atoms into the topmost layer of the nickel surface. The Au/Ni(111) surface alloy has been shown to impede the formation of carbon and thus extend the lifetime of the catalyst [6].

Owing to the importance of CO methanation and in particular the steam reforming process, much effort has been put into both experimental and theoretical studies of the interaction of CO with nickel surfaces [7–12]. On single crystal surfaces two ordered carbon structures are observed, namely the carbidic structure (below ~ 600 K) and the graphitic structure (above ~ 600 K) [3,13]. A number of studies have shown that the defect sites at the step edges play an important role in the dissociation of CO. Nakano *et al.* compared the Ni(111) surface with the stepped Ni(977) surface and showed that the latter has a higher activity for CO dissociation [14,15]. Also, from density functional theory calculations a higher reactivity for CO dissociation of the step edge atoms is found as compared to the regular terrace atoms of Ni(111) [16,17]. In the classic studies by Goodman *et al.* and Rostrup-Nielsen *et al.*, the poisoning effect of S was explained in terms of long range electronic effects (adsorbed S deactivates several neighboring Ni atoms) and ensemble effects (an ensemble of Ni atoms make up the active site), but the specific role of special active sites was not discussed. In a recent study we showed that the step edges of Ni(111) play a very important role in the decomposition of ethylene, and we demonstrated how we could control the bond-breaking selectivity by selectively blocking the step edges with Ag [18]. DFT calculations suggest that similar effects of step blocking may be expected for the adsorption of Au and S on Ni(111) [16].

Here we show from high-resolution STM studies that CO dissociates exclusively at the step edges of Ni(111) at 400 K. Furthermore, we show that Ag, Au, and S atoms all nucleate preferentially at the step edges and efficiently block the dissociation of CO on the Ni(111) surface.

2 Experimental

All STM experiments were performed in an ultrahigh vacuum (UHV) chamber equipped with standard sample preparation and surface science analysis tools, and a home-built Aarhus STM [19,20]. The Ni(111) crystal was exposed to high purity CO (Praxair 99.997%) by backfilling the chamber with the sample kept at a constant temperature. Subsequently the sample was allowed to cool to room temperature before being transferred to the STM.

The crystal was cleaned on a daily basis by sputtering (2 keV Ar⁺) and annealing (800 K) cycles, and when necessary oxidation/reduction (10⁻⁷ torr O₂/H₂ at 573 K) cycles were performed. The cleanliness of the sample was checked by STM on several different areas. Although the STM possesses no chemical specificity, high-resolution, atom-resolved STM images offer a much higher sensitivity to surface impurities than conventional electron-based techniques. In this way the concentration of impurities was estimated to be very low, and especially the cleanliness of the atomic steps could be verified, which is important for the conclusions concerning dissociation and nucleation at step edge sites.

3 Results and discussion

3.1 CO dissociation on Ni(111)

When the Ni(111) surface was exposed to CO at 400 K we observed the nucleation of islands along the upper step edges. This is shown in the STM image of Figure 1(a), which shows the Ni(111) surface after exposure to 50 L CO (10⁻⁷ torr; 500 s). No nucleation of isolated islands away from the step edges was observed. High-resolution images of the islands (fig. 1(b)) reveal a structure with a quadratic $5 \times 5 \text{ \AA}^2$, centered unit cell, which is characteristic of the carbide structure formed on Ni(111). The carbide structure has been thoroughly described in earlier studies [13], and we will not go into details in the present study. The observations of the nucleation of carbide islands along the upper step edges are in excellent agreement with the STM studies of Nakano *et al.*[15] The reason for the preferential nucleation of the carbide structure at the upper step edges is most likely the 10 % mass reduction that is associated with the reconstruction of the topmost layer of the Ni(111) surface, induced by the adsorbed carbon atoms. The mass transport is most easily accommodated at the step edges, where atoms are relatively free to move around and rearrange into a new structure. So far we cannot conclude anything about the active site for CO dissociation based on the preferred

nucleation of the carbide islands. The non-uniform distribution of the islands along the step edges shows that the carbon atoms are mobile at the conditions of our experiments. Below we will give strong evidence that only the step edges are in fact active in the dissociation of CO on Ni(111) at 400 K. Prior to this, however, we show that it is possible to estimate the CO dissociation barrier based on STM measurements. This was done by exposing the Ni(111) surface to 5 L CO at different sample temperatures and observing the temperature at which carbide islands were first detected. As can be seen from the series of STM images in fig. 2, carbide islands start to nucleate at temperatures above ~ 375 K. From this onset temperature we can find the dissociation barrier by assuming that the reaction rate, r , follows a first order Arrhenius behavior [21]:

$$r = \nu \cdot \theta \cdot e^{-\frac{E_a}{k_B T}},$$

where ν is the pre-exponential factor, θ the CO coverage, E_a the activation energy, k_B the Boltzman constant, and T the absolute temperature. For observations to occur in the timescale of our experiments the rate must be of the order of 1 event per second. The coverage can be approximated by a Langmuir adsorption isotherm [21]:

$$\frac{\theta}{\theta_0} = \frac{kP}{1+kP},$$

$$\text{where } k = \frac{N_A}{\sigma_0 \sqrt{2\pi MRT}} \cdot \tau_0 \cdot \exp\left(\frac{\Delta H_{ads}}{RT}\right)$$

Here $\frac{\theta}{\theta_0}$ is the degree of coverage, P the CO pressure, N_A the Avogadro number, σ_0 the saturation coverage, M the molecular weight, R the gas constant, τ_0 the residence time, and ΔH_{ads} is the heat of adsorption for CO on Ni(111). For the heat of adsorption we use the calorimetric data of Stuckless *et al.*, which give a value for the heat of adsorption of ~ 120 kJ/mol in the range from 0 to 0.5 ML [12]. If we now take the saturation adsorption structure to be the c(4 × 2)-2CO with a coverage of 0.5 ML CO, and take 10^{-12} s as a typical value of τ_0 [21], we find a CO coverage very close to saturation ($\frac{\theta}{\theta_0} = 0.99$) at a CO pressure of 10^{-8} torr, and we thus use 0.5 ML for the CO coverage. The coverage along the step edges may be higher than on the terraces due to the stronger binding of CO to the step edges, but this effect is irrelevant to our crude estimation.

If we finally approximate the pre-exponential factor with a typical value of $\nu = 10^{12} \text{ s}^{-1}$, we find an activation energy for the CO dissociation of 0.9 ± 0.2 eV. The uncertainty is found by assuming a 25 K uncertainty in the temperature and a 2 orders of magnitude uncertainty in the pre-exponential factor. The value deviates from the CO dissociation barriers on Ni(111) step edges of 1.92 eV and 2.08 eV, found in two recent DFT studies by Li *et al.* and Bengaard *et al.* [16,17]. These DFT calculations, however, do not take into account the

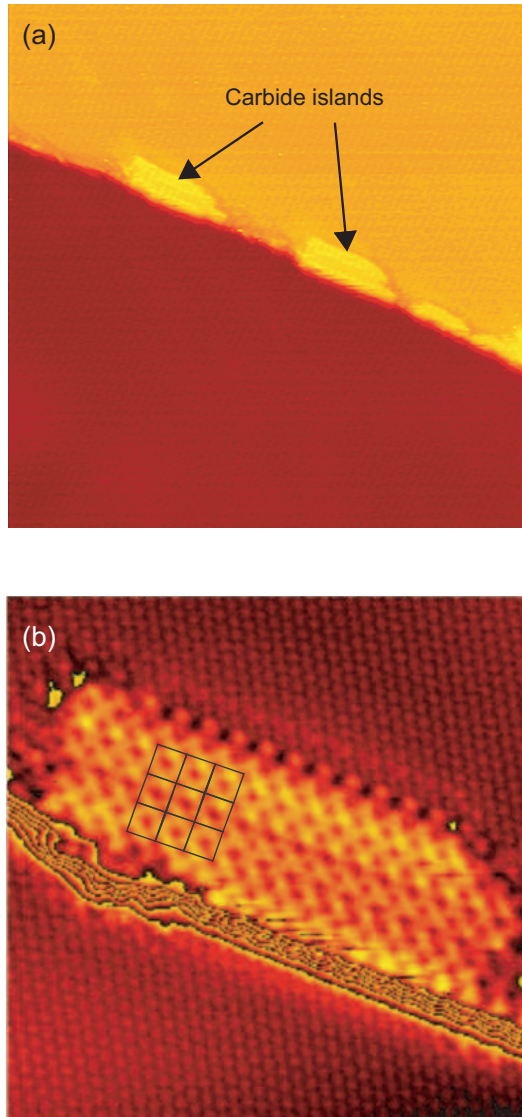


Fig. 1. **(a)** STM image ($500 \times 500 \text{ \AA}^2$) of a Ni(111) surface after exposure to 50 L CO at 400 K. Carbide islands have nucleated along the upper step edges. **(b)** Zoom-in ($87 \times 87 \text{ \AA}^2$) on a carbide island. A $5 \times 5 \text{ \AA}^2$ unit mesh is superimposed. A cyclic color scale is used to enhance the resolution on both terraces.

effect of the CO coverage and of a possible surface reconstruction. A CO-CO repulsion at the step edges may lead to a destabilization of the initial state, or adsorbed carbon atoms may induce a reconstruction of the step edge, which gives a more favorable reaction site. At present new DFT calculations are being performed in the group of Nørskov, which take the coverage effect into account [22].

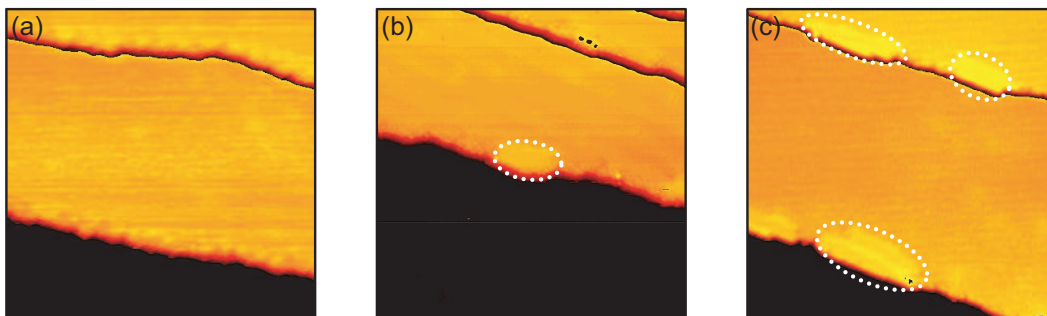


Fig. 2. A series of STM images ($300 \times 300 \text{ \AA}^2$) of a Ni(111) surface after exposure to 5 L CO at (a) 350 K, (b) 375 K, and (c) 400 K. The nucleation of carbide islands is seen at and above temperatures of 375 K.

3.2 Step blocking on Ni(111)

As discussed in the previous section, the preferential nucleation of the carbide islands along the upper step edges does not necessarily mean that the step edges are also the active sites for the dissociation of CO molecules on the Ni(111) surface. To actually prove that this is the case, we selectively blocked the step edge atoms before exposing the sample to CO. In an earlier study we have shown that the step edge atoms can be completely blocked by Ag atoms [18] and we therefore started out by studying this Ag/Ni(111) system. Subsequently we investigated the effect of depositing Au and S on the Ni(111) surface. These additives are very interesting with respect to the steam reforming process, since both Au and S can increase the efficiency of the commonly used nickel catalysts as discussed in the opening section [4–6].

3.2.1 Ag/Ni(111)

The growth and nucleation of Ag on Ni(111) is described in detail elsewhere [23,24]. For the present study it suffices to note that when Ag is evaporated onto Ni(111) at room temperature and the sample is subsequently annealed at 800 K, a brim of Ag atoms decorates all of the step edges. These atoms appear as bright protrusions along the step edges in the STM images (see fig. 3(a)), and they can also be seen very clearly when a line scan perpendicular to the step edge on the Ag/Ni(111) surface is compared to a similar line scan on the clean Ni(111) surface (see fig. 3(b)).

The STM image in fig. 3(a) is obtained after the Ag/Ni(111) sample has been exposed to 5000 L CO at 400 K, but there were no indications of any nucleation of carbide islands along the step edges (or elsewhere). Since a relatively small amount of Ag ($\sim 0.1 \text{ ML}$) was used to block the step edges, and since we know from another study that the carbide phase will form on the Ag/Ni(111) surface at 400 K [24], this gives very strong evidence that only the atoms along

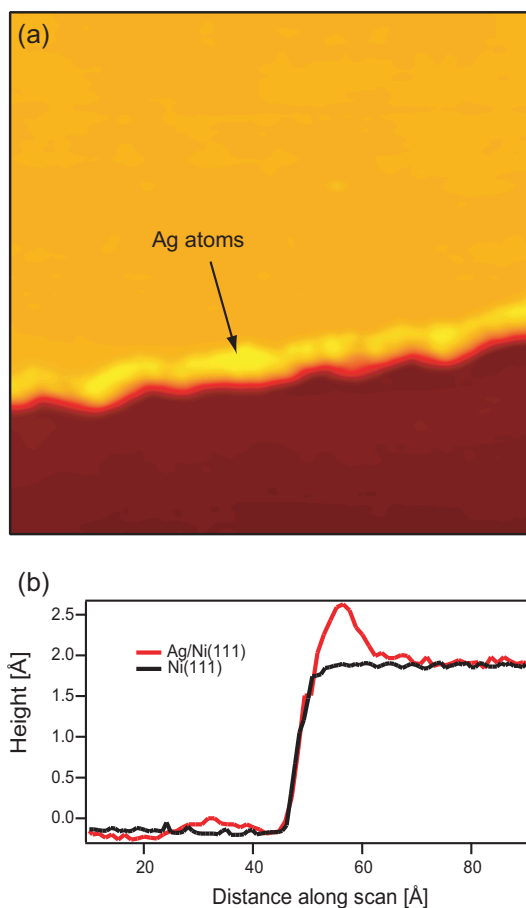


Fig. 3. **(a)** STM image ($500 \times 500 \text{ \AA}^2$) of a row of Ag atoms nucleated along the step edge of a Ni(111) surface. The surface has been exposed to 5000 L CO at 400 K; no carbide islands are formed. **(b)** Comparison of line scans perpendicular to a step edge on Ni(111) (black line) and Ag/Ni(111) (red line).

the step edges of Ni(111) are active for CO dissociation at this temperature. This observation is in full agreement with both experimental and theoretical studies in the literature that find the rate of dissociation to be significantly higher at the step edges than on the regular (111) facets [15–17].

3.2.2 *Au/Ni(111)*

Although Au and Ni are immiscible in the bulk, they form a stable surface alloy in which single Au atoms are substituted into the topmost layer of Ni(111) [25]. This surface alloy was characterized by STM, and fig. 4(a) shows an image of an alloy obtained by depositing Au onto Ni(111) at room temperature, followed by post annealing at 800 K. The Au atoms are imaged as depressions by the STM although the diameter of a Au atom is larger than that of a Ni atom. This is a classical example, which shows that the STM images depict a convolution of the geometric and electronic structure of a surface, and one

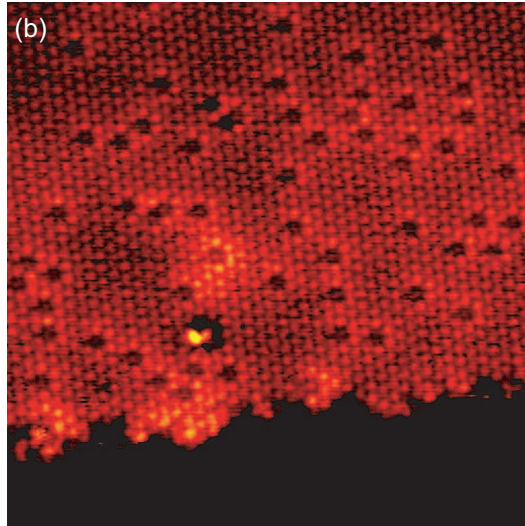
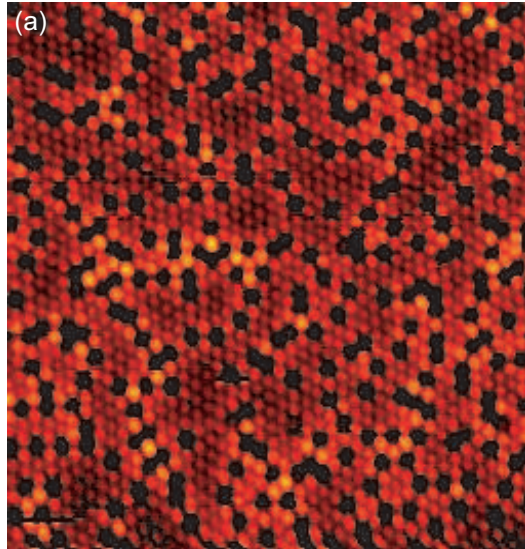


Fig. 4. STM images ($100 \times 100 \text{ \AA}^2$) of a Au/Ni(111) surface alloy **(a)** before, and **(b)** after exposure to CO at 400 K. There are no signs of carbon at the step edge.

must therefore always be careful when interpreting STM data. In contrast to when Ag was evaporated onto Ni(111) and followed by annealing, we do not observe bright protrusions along the step edges on the Au/Ni(111) surface. It may at first seem surprising, since DFT calculations show that the binding of a Au atom at a step edge site on Ni(111) is favored by 0.37 eV over binding at a regular terrace site. However, it seems reasonable to assume that Au atoms at the step edge have a lower apparent height than Ni atoms in the STM images, just as is the case for the atoms on the (111) facets. If this holds, then a single row of Au atoms at the step edge will not show up in the STM images.

When we exposed the Au/Ni(111) surface alloy to CO at 400 K we did not

observe any nucleation of carbon on the surface. This was the case even for surface alloys with a very low concentration of Au. Fig. 4(b) shows a Au/Ni(111) surface alloy with a Au coverage of ~ 0.05 ML after exposure to CO. If the Au atoms were randomly distributed in the topmost layer, many free nickel step edge atoms would be present, which could facilitate the dissociation of CO. Since this was never observed, we conclude from these experiments that Au atoms along the step edges are indeed over represented and that they block the Ni step edge atoms in a way similar to that of the Ag atoms. It might be argued that CO does in fact dissociate at the step edges of the Au/Ni(111) surface alloy and that the effect of the Au atoms is to inhibit the formation of carbide islands, thus disabling us from seeing the adsorbed carbon with the STM. This can, however, be counter-argued by the fact that the carbide structure can easily be formed on Au/Ni(111) at the same temperature by exposing the surface to ethylene, which in contrast to CO dissociates at the terrace sites of Ni(111) (and Au/Ni(111)) [24].

3.2.3 S/Ni(111)

The final additive for which we examined the influence on CO dissociation was sulfur. This was deposited onto the Ni(111) surface by exposing the sample to H₂S, which readily dissociates to form adsorbed S [26]. When we exposed the Ni(111) surface to moderate doses (5 L) of H₂S at 400 K we found single sulfur atoms at the nickel step edges (Fig. 5(a)) imaged as protrusions in the STM. Some of the sulfur atoms nucleate into islands found at the upper step edges (fig. 5(b)). These islands have an almost quadratic unit cell and are identified with the $(\sqrt{39} \times \sqrt{39})$ structure known to form above room temperature at low S coverage [27]. In agreement with this work we also observed that these islands nucleated exclusively at the upper step edges of Ni(111). The driving force for this growth mode is similar to that of the nucleation of the carbidic phase: Binding to the under-coordinated step atoms is favored, and subsequently the mass transport involved in the reconstruction takes place at the step edge, too. Increasing the dose of H₂S led to the formation of a $(5\sqrt{3} \times 2)$ structure covering all of the surface. Again this is in agreement with previous studies of sulfur on Ni(111) [26–28].

Our experiments clearly showed a preferential binding of sulfur atoms to the step edges of Ni(111), consistent with theoretical calculations showing a 0.38 eV higher binding energy of a sulfur atom at a step edge site as compared to a terrace site [16]. The protrusions at the step edges are interpreted as the nucleation of the sulfur-induced reconstruction, and we therefore expect that the coverage of sulfur has to reach a certain level before it can be observed by STM. For lower doses of H₂S we are able to prove that the step edges of Ni(111) are covered with sulfur by showing that the CO dissociation is blocked: a pre-dosing of 0.5 L H₂S at 400 K onto Ni(111) followed by exposure

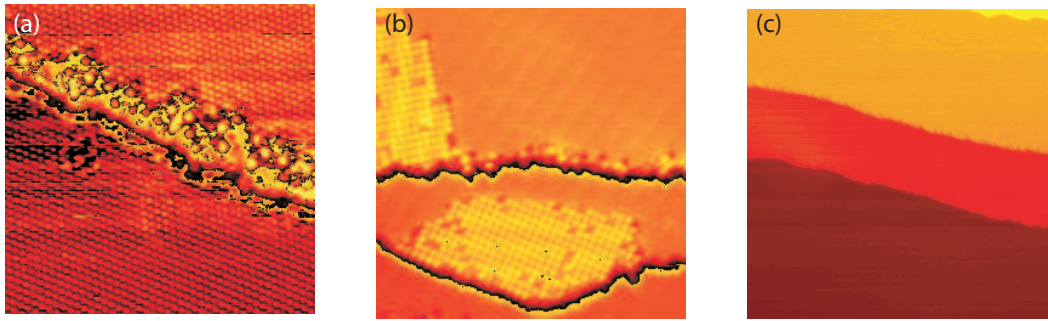


Fig. 5. **(a)** STM image ($100 \times 100 \text{ \AA}^2$) showing sulfur atoms at Ni(111) step after exposure to 5 L H_2S at 400 K. **(b)** STM image ($200 \times 200 \text{ \AA}^2$) of sulfur islands nucleated at upper step edges. **(c)** STM image ($500 \times 500 \text{ \AA}^2$) of a Ni(111) surface exposed to 500 L CO at 400 K after pre-exposure to 0.5 L H_2S .

to 500 L CO at 400 K did not lead to carbon formation. When demonstrating this blocking effect of sulfur with the STM, one has to be careful since the sulfur-induced reconstruction is very similar to the carbidic phase induced by carbon. Therefore, the crystal was first exposed to 0.5 L H_2S at 400 K, and STM images were recorded in several different areas of the surface. These images were subsequently compared to images obtained after exposing the S/Ni(111) system to 500 L CO also at 400 K. The images showed no difference in the coverage of islands, and we thus conclude that no CO dissociation takes place on the Ni(111) crystal with S-covered steps. The finding that sulphur poisons the dissociation of CO on Ni(111) by blocking the step edges, is in

good agreement with recent quantitative mass spectrometer measurements carried out in the group of Chorkendorff [29].

4 Summary

We have demonstrated how the dissociation of CO on Ni(111) at 400 K can be completely inhibited by depositing small amounts of Ag, Au, or S, which all nucleate preferentially at the step edges. Besides providing very strong evidence that the atoms at the step edges are the only active sites for the dissociation of CO at 400 K, the experiments also show that the effect of step edges is an important factor when nickel surfaces are modified by additives. In particular our results give new input to the understanding of why S and Au reduce the problem of carbon formation on nickel-based steam reforming catalysts. These new findings may help bring catalyst design into a new era, in which new and improved catalysts are developed based on surface science studies, as opposed to the present method dominated by trial and error.

Acknowledgements

We acknowledge Jens K. Nørskov and Ib Chorkendorff for sharing with us their unpublished results.

References

- [1] J. R. Rostrup-Nielsen, in *Catalysis, Science and Technology*, Vol. 5 of *Catalysis, Science and Technology*, edited by J. R. Anderson and M. Boudart (Springer-Verlag, Berlin, 1983).
- [2] J. R. Rostrup-Nielsen and T. Rostrup-Nielsen, “Large-scale hydrogen production”, *CATTECH* **6**, 150 (2002).
- [3] D. W. Goodman, R. D. Kelley, T. E. Madey, and J. T. Yates, “Kinetics of the Hydrogenation of CO over a Single Crystal Nickel Catalyst”, *J. Catal.* **63**, 226 (1980).
- [4] D. W. Goodman, “Chemisorption and Reactivity Studies of H₂ and CO on Sulfided Ni(100)”, *Surf. Sci. Lett.* **105**, L265 (1981).
- [5] J. R. Rostrup-Nielsen, “Sulfur-Passivated Nickel Catalysts for Carbon-Free Steam Reforming of Methane”, *J. Catal.* **85**, 31 (1984).

- [6] F. Besenbacher, I. Chorkendorff, B. S. Clausen, B. Hammer, A. M. Molenbroek, J. K. Nørskov, and I. Stensgaard, “Design of a Surface Alloy Catalyst for Steam Reforming”, *Science* **279**, 1913 (1998).
- [7] Y. Morikawa, J. J. Mortensen, B. Hammer, and J. K. Nørskov, “CO adsorption and dissociation on Pt(111) and Ni(111) surfaces”, *Surf. Sci.* **386**, 67 (1997).
- [8] H. Conrad, G. Ertl, J. Küppers, and E. E. Latta, “Adsorption of CO on clean and oxygen covered Ni(111) surfaces”, *Surf. Sci.* **57**, 475 (1976).
- [9] P. T. Sprunger, F. Besenbacher, and I. Stensgaard, “STM investigation of the Ni(111) -c(4×2) -2CO structure”, *Chem. Phys. Lett.* **243**, 439 (1995).
- [10] A. Eichler, “CO adsorption on Ni(111)—a density functional theory study”, *Surf. Sci.* **526**, 332 (2003).
- [11] V. Shah, T. Li, K. L. Baumert, H. Cheng, and D. S. Sholl, “A comparative study of CO chemisorption on flat and stepped Ni surfaces using density functional theory”, *Surf. Sci.* **537**, 217 (2003).
- [12] J. T. Stuckless, N. Al-Sarraf, C. Wartnaby, and D. A. King, “Calorimetric heats of adsorption for CO on nickel single crystal surfaces”, *J. Chem. Phys.* **99**, 2202 (1993).
- [13] C. Klink, I. Stensgaard, F. Besenbacher, and E. Lægsgaard, “An STM study of carbon-induced structures on Ni(111): evidence for a carbidic-phase clock reconstruction”, *Surf. Sci.* **342**, 250 (1995).
- [14] H. Nakano, S. Kawakami, T. Fujitana, and J. Nakamura, “Carbon deposition by disproportionation of CO on a Ni(977) surface”, *Surf. Sci.* **454–456**, 295 (2000).
- [15] H. Nakano and J. Nakamura, “Carbide-induced reconstruction initiated at step edges on Ni(111)”, *Surf. Sci.* **482–485**, 341 (2001).
- [16] H. S. Bengaard, J. K. Nørskov, J. Sehested, B. Clausen, L. P. Nielsen, A. M. Molenbroek, and J. R. Rostrup-Nielsen, “Steam Reforming and Graphite Formation on Ni Catalysts”, *J. Catal.* **209**, 365 (2002).
- [17] T. Li, B. Bhatia, and D. S. Sholl, “First-principles study of C adsorption, O adsorption, and CO dissociation on flat and stepped Ni surfaces”, *J. Chem. Phys.* **121**, 10241 (2004).
- [18] R. T. Vang, K. Honkala, S. Dahl, E. K. Vestergaard, J. Schnadt, E. Lægsgaard, B. S. Clausen, J. K. Nørskov, and F. Besenbacher, “Controlling the catalytic bond-breaking selectivity of Ni surfaces by step blocking”, *Nat. Mat.* **4**, 160 (2005).
- [19] E. Lægsgaard, F. Besenbacher, K. Mortensen, and I. Stensgaard, “A fully automated, ‘thimble-size’ scanning tunnelling microscope”, *J. Microscop.* **152**, 663 (1988).

- [20] F. Besenbacher, “Scanning tunnelling microscopy studies of metal surfaces”, *Rep. Prog. Phys.* **59**, 1737 (1996).
- [21] G. A. Somorjai, *Surface Chemistry and Catalysis* (Wiley, New York, 1994).
- [22] I. N. Remediakis, F. Abild-Pedersen, and J. K. Nørskov, unpublished results.
- [23] F. Besenbacher, L. P. Nielsen, and P. T. Sprunger, in *The Chemical Physics of Solid Surfaces and Heterogeneous Catalysis*, edited by D. A. King and D. P. Woodruff (Elsevier Science Publishers, ADDRESS, 1997).
- [24] R. T. Vang, K. Honkala, S. Dahl, E. K. Vestergaard, J. Schnadt, E. Lægsgaard, B. S. Clausen, J. K. Nørskov, and F. Besenbacher, “Ethylene dissociation on flat and stepped Ni(111): A combined STM and DFT study”, In preparation.
- [25] J. Jacobsen, L. P. Nielsen, F. Besenbacher, I. Stensgaard, E. Lægsgaard, T. Rasmussen, K. W. Jacobsen, and J. K. Nørskov, “Atomic-Scale Determination of Misfit Dislocation Loops at Metal-Metal Interfaces”, *Phys. Rev. Lett.* **75**, 489 (1995).
- [26] L. Ruan, I. Stensgaard, F. Besenbacher, and E. Lægsgaard, “Observation of a Missing-Row Structure on an fcc (111) Surface: The $(5\sqrt{3}\times 2)S$ Phase on Ni(111) Studied by Scanning Tunneling Microscopy”, *Phys. Rev. Lett.* **71**, 2963 (1993).
- [27] V. Maurice, N. Kitakatsu, M. Siegers, and P. Marcus, “Low-coverage sulfur induced reconstruction of Ni(111)”, *Surf. Sci.* **373**, 307 (1997).
- [28] M. Foss, R. Feidenhans'l, M. Nielsen, E. Findeisen, R. L. Johnson, T. Buslaps, I. Stensgaard, and F. Besenbacher, “Sulfur chemisorption on Ni(111): The clock structure of the $(5\sqrt{3}\times 2)S$ phase”, *Phys. Rev. B* **50**, R8950 (1994).
- [29] O. Lytken and I. Chorkendorff, unpublished results.

Ethylene dissociation on flat and stepped Ni(111): A combined STM and DFT study

Ronnie T. Vang,^a Karoliina Honkala,^{b,1} Søren Dahl^c
Ebbe K. Vestergaard,^{a,2} Joachim Schnadt,^a Erik Lægsgaard,^a
Bjerne S. Clausen,^c Jens K. Nørskov,^b
Flemming Besenbacher^{a,*}

^a*Interdisciplinary Nanoscience Center (iNANO), and Department of Physics and Astronomy, University of Aarhus, DK-8000 Aarhus, Denmark*

^b*Center for Atomic-scale Materials Physics (CAMP), Department of Physics, Technical University of Denmark, DK-2800 Lyngby, Denmark*

^c*Haldor Topsøe A/S, Nymøllevej 55, DK-2800 Lyngby, Denmark*

Abstract

The dissociative adsorption of ethylene (C₂H₄) on Ni(111) was studied by scanning tunneling microscopy (STM) and density functional theory (DFT) calculations. The STM studies reveal that ethylene decomposes exclusively at the step edges at room temperature. However, the step edge sites are poisoned by the reaction products and thus only a small brim of decomposed ethylene is formed. At 500 K decomposition on the (111) facets leads to a continuous growth of carbidic islands, which nucleate along the step edges.

DFT calculations were performed for several intermediate steps in the decomposition of ethylene on both Ni(111) and the stepped Ni(211) surface. In general the Ni(211) surface is found to have a higher reactivity than the Ni(111) surface. Furthermore, the calculations show that the influence of step edge atoms is very different for the different reaction pathways. In particular the barrier for dissociation is lowered significantly more than the barrier for dehydrogenation, and this is of great importance for the bond-breaking selectivity of Ni surfaces.

The influence of step edges was also probed by evaporating Ag onto the Ni(111) surface. STM shows that the room temperature evaporation leads to a step flow growth of Ag islands, and a subsequent annealing at 800 K causes the Ag atoms to completely wet the step edges of Ni(111). The blocking of the step edges is shown to prevent all decomposition of ethylene at room temperature, whereas the terrace site decomposition at 500 K is confirmed to be unaffected by the Ag atoms.

Finally a high surface area NiAg alloy catalyst supported on MgAl₂O₄ was synthesized and tested in flow reactor measurements. The NiAg catalyst has a much lower activity for ethane hydrogenolysis than a similar Ni catalyst, which can be rationalized by the STM and DFT results.

1 Introduction

Ever since the work by Taylor in 1925, the concept of active sites for reactions at metal surfaces has been an important notion within the field of heterogeneous catalysis [1]. Gwathmey *et al.* made extensive studies on the influence of the crystal face on catalytic reactions [2], and Yates *et al.* used stepped single crystal surfaces to study the role of step edges in surface chemical reactions [3]. Following the advent of scanning probe microscopy Zambelli *et al.* were able to provide direct evidence that the step edges are the active sites for the NO dissociation on Ru(0001) [4]. Dahl *et al.* [5] quantified the effect for N₂ dissociation on Ru(0001) by using density functional theory calculations (DFT) and detailed experiments to show that dissociation at the step edges has an activation energy which is more than 1 eV lower than that on the terraces at 500 K. Since then DFT calculations and experiments have shown that step edges in general are more reactive towards the dissociation of a number of simple diatomic molecules such as CO, NO, O₂, and N₂ [6–10]. For more complicated molecules the reactivity is not the only important factor, and in particular the selectivity of a surface for a given reaction must also be taken into account.

Recently we demonstrated that the bond-breaking selectivity for the ethylene (C₂H₄) decomposition on Ni(111) is to a high degree influenced by the presence of free step edges [11]. In the present paper we provide further insight into this reaction based on STM experiments, DFT calculations and flow reactor measurements. We show that the step edges of a Ni(111) surface are indeed more reactive than the (111) facets. The step edge sites are active for ethylene decomposition at room temperature, whereas the regular terrace atoms become active only at higher temperatures. In addition we take two further steps. First, we show that the higher reactivity of the step edges is much more pronounced for C-C bond breaking than for C-H bond breaking. This means that the number of step sites plays an important role in the selectivity of hy-

* Corresponding author. Tel.: +45 8942 3604; fax: +45 8612 0740

Email address: fbe@inano.dk (Flemming Besenbacher).

URL: www.inano.dk/besenbacher (Flemming Besenbacher).

¹ Present address: Nanoscience Center, Department of Physics, PBox 35, 40014 University of Jyväskylä, Finland

² Present address: Department of Chemistry, Box 351700, University of Washington, Seattle WA 98195-1700, USA

drogenation, dehydrogenation, and hydrogenolysis reactions. Second, we show that the steps can be blocked selectively by the deposition of small amounts of Ag on the Ni(111) surface. The conclusion is that the number of reactive step sites can be controlled, which may be used in the design of catalysts with a specific selectivity. This approach is exploited in the synthesis of a high surface area AgNi alloy catalyst, which is compared to both a pure Ni and a CuNi catalyst in hydrogenolysis experiments.

2 Methods

2.1 Experiment

The STM experiments were conducted in an ultrahigh vacuum (UHV) chamber equipped with standard sample preparation and surface science analysis tools, and a home-built Aarhus STM [12,13]. The sample was exposed to ethylene (Praxair 99.95%) by backfilling the chamber with the sample kept at a constant temperature. Subsequently the sample was allowed to cool to room temperature before being transferred to the STM.

The crystal was cleaned on a daily basis by sputtering (2 keV Ar⁺) and annealing (800 K) cycles, and whenever needed oxidation/reduction cycles (10⁻⁷ torr O₂/H₂ at 573 K) were performed. The cleanliness of the sample was checked by STM in several different areas. Although the STM possesses no chemical specificity, high-resolution, atom-resolved STM images offer a much higher sensitivity to surface impurities than conventional electron-based techniques. In this way the concentration of impurities could be estimated to be very low, and especially the cleanliness of the atomic steps could be verified, which is important for the conclusions concerning dissociation and nucleation at step sites.

The high surface area Ni catalyst for the integral flow reactor measurements was prepared by incipient wetness impregnation of an MgAl₂O₄ support with NiNO₃(aq), and the Ag/Ni (Cu/Ni) catalyst was similarly prepared by incipient wetness impregnation of AgNO₃(aq) (CuNO₃(aq)) on the reduced Ni catalyst. Following the impregnation steps the catalysts were dried and subsequently calcined at 450 °C. The metal content in the samples was aimed at 1 wt% Ni and 0.1 wt% Ag (Cu), and was verified by an inductive coupled plasma (ICP) analysis. The ethane (C₂H₆) hydrogenolysis experiments were performed in an integral plug flow reactor, a U-tube made of quartz, with an inner diameter of 4 mm. The reactor, with a pressure of about 1.0–1.2 bar, was loaded with 200 mg of catalyst, 150–300 μm sieved fraction, which was fixed between two quartz wool wads. Each run started with a reduction of the

catalyst in hydrogen (100 ml/min NTP) at 500 °C for 1 hour. Five different feed gas compositions were used, 2–3.5 % ethane, and 15–30 % hydrogen in a He flow, at temperatures from 200–400 °C. The conversion was determined by measuring the concentration of methane in the exit gas employing a calibrated mass spectrometer. Methane was the only product detected.

2.2 Theory

The spin-polarized DFT calculations were carried out with the DACAPO code [14], where the Kohn-Sham equations are solved in a plane wave basis restricted by a kinetic energy cutoff of 25 Ry. We employed the RPBE [15] generalized gradient correction self-consistently, and the core electrons of all the atoms were treated with Vanderbilt ultrasoft pseudopotentials [16]. The Ni(111) terrace was made out of a three-atomic-layer thick slab with a (3x2) unit cell. The stepped Ni(111) surface was modeled by a (2x1) unit cell of the Ni(211) surface by use of a slab with three (111) atomic layers. Both unit cells give a six-atom Ni surface unit cell. The sampling of 12 (Ni(111)) and 16 (Ni(211)) Monkhorst-Pack k-points was used. The topmost metal layer and chemisorbed species were relaxed in all calculations whereas the other substrate layers were kept fixed to the fcc ideal slab positions. Adsorbates were positioned only on one side of the slab. Two different methods were applied to determine the transition states. In some cases the transition state was localized constraining the C-C distances (or C-H distances) and relaxing all other degrees of freedom. In cases where we did not know the location of the transition state we used the nudged elastic band method [17] to determine the transition state.

3 Results and discussion

3.1 Room temperature exposure of ethylene

By exposing the Ni(111) surface to ethylene at the lowest temperature for which decomposition is observed, one can assure to probe only the most reactive sites. We found that an exposure to ethylene at room temperature led to the formation of a narrow brim of reaction products along the upper step edges on Ni(111), as can be seen by comparing the two STM images of Figure 1, which show a Ni(111) surface before and after exposure to 1 L ($= 10^{-8}$ torr·100 s) ethylene at room temperature. The brim, which in the STM images appears as areas of different corrugation as compared to the (111) facets, was found all along the step edges and with a width of typically no more than 40

Å, independent of the size of the terraces. Since the cleanliness of the sample, and in particular that of the step edges, was checked prior to ethylene exposure, the formation of this brim could unambiguously be associated with the ethylene adsorption. No indication of nucleation of islands on the terraces of the surface was observed upon exposure to ethylene. When the exposure time was increased by a factor of 20 while the ethylene pressure was kept at 10^{-8} torr, we again observed a brim formation along the upper step edges, and furthermore we found that the width of this brim did not increase in time. From this we may conclude that the process of forming the brim is self-poisoning. Since the only adsorbates observed on the surface are the ones at the step edges, we furthermore conclude that the mechanism behind the formation of the brim is the decomposition of ethylene at the step edge atoms, and the decomposition products adsorb at the step edges and prevent further reaction. We cannot say whether or not the decomposition is complete into adsorbed C and H, but we can rule out that the brim merely consist of molecularly adsorbed ethylene. We base this assumption on the fact that the brim extends up to 40 Å into the terrace, and so most of the brim is adsorbed on regular terrace sites. If these adsorbates were molecular ethylene one would expect the width of the brim to increase with increasing exposure time, which is not the case. A further proof that the observed brim is not formed by molecular ethylene adsorption was found when we exposed the Ni(111) surface to 1 L ethylene at 200 K. At these conditions no brim was formed, thus indicating that a kinetic barrier is associated with its formation. From the STM measurements at room temperature we can therefore conclude that the step edges of the Ni(111) surface have a higher reactivity for ethylene decomposition than the regular atoms of the (111) facets. Since the STM cannot distinguish between different chemical species we cannot, however, determine through which reaction pathway this decomposition proceeds and what are the final products. These important issues were addressed by performing state of the art *ab initio* DFT calculations.

3.2 DFT calculations

According to our DFT calculations, the most stable binding geometry of ethylene on both the terrace and the step edge sites is the top site given in Fig. 2. The adsorption energy of C_2H_4 on Ni(211) (step sites) is -0.76 eV, whereas on Ni(111) it is only -0.16 eV. In the same figure we present the optimized geometries of all the intermediates given in the potential energy diagram in Fig. 3. CH_2 (methylene) and $CHCH_2$ (vinyl) are the possible primary intermediates in an ethylene decomposition reaction which will eventually lead to adsorbed carbon and hydrogen atoms. The binding geometry of methylene is rather different on the Ni(111) and Ni(211) surfaces: on the terrace methylene prefers a three-fold hollow site whereas on the step it binds to a two-fold site.

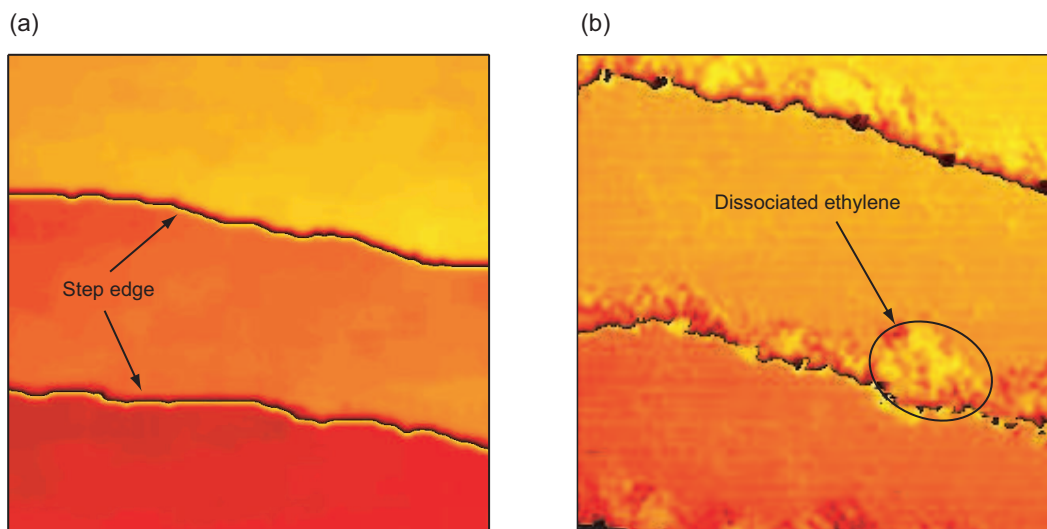


Fig. 1. STM images ($200 \times 200 \text{ \AA}^2$) of a Ni(111) surface before (a) and after (b) exposure to 1 L ethylene at room temperature. A brim of reaction products is adsorbed along the step edges upon exposure. A cyclic color scaling has been used to enhance the features of each terrace.

The binding geometry of vinyl follows that of methylene on both surfaces, which is probably due to the fact that the vinyl attaches to the surface from the methylene end. The adsorption of methylene and vinyl, respectively, with respect to gas phase ethylene is endothermic on Ni(111) while on Ni(211) it is exothermic, with vinyl binding being the strongest with the adsorption energy -0.60 eV . The adsorption geometry and energy of C_2H_2 (acetylene) are identical on both surfaces. On Ni(211) the most stable geometry for acetylene has an adsorption energy -0.70 eV and is located behind the step: the adsorption on a bridge site at the step is endothermic. The product of acetylene decomposition, CH (methylidyne), adsorbs on a three-fold site on Ni(111) and on a four-fold site on the Ni(211) step edge, the latter being more strongly bound with an adsorption energy -0.4 eV per methylidyne and one hydrogen. We note that all the intermediates are more stable on step surface sites than on terrace sites; an observation which is in agreement with the experimental findings.

Fig. 3 shows the calculated potential energy diagram both for the ethylene dissociation into two adsorbed CH_2 molecules and for the primary dehydrogenation to adsorbed CHCH_2 and H on the close-packed Ni(111) terrace and on the stepped Ni(211) surface (the full lines). In the same figure we also present the dehydrogenation step from CHCH_2 to C_2H_2 , from CH_2 to CH and a C-C bond breaking step from C_2H_2 to CH (the dotted lines). As a zero energy level we have chosen a clean Ni surface and ethylene in vacuum far away from the surface. This approach corresponds to the low-coverage limit of molecular ethylene.

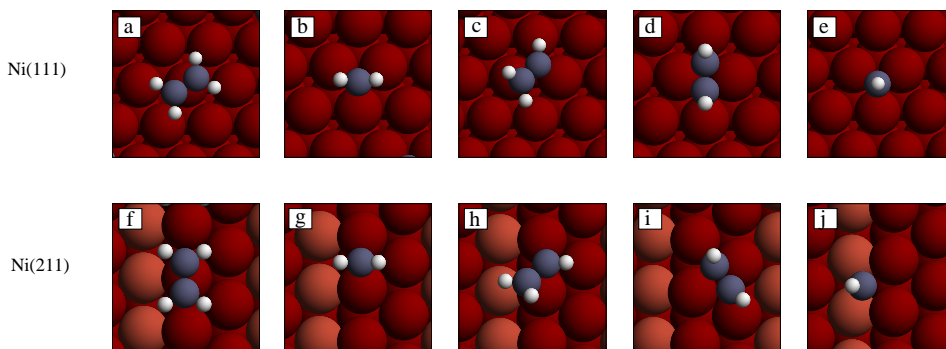


Fig. 2. Calculated adsorption geometries on the Ni(111) (Ni(211)) surface: a) ethylene (f)), b) methylene (g)), c) vinyl (h)), d) acetylene (i)), e) methylidyne (j)). The Ni atoms are colored red, C atoms blue and hydrogen atoms white.

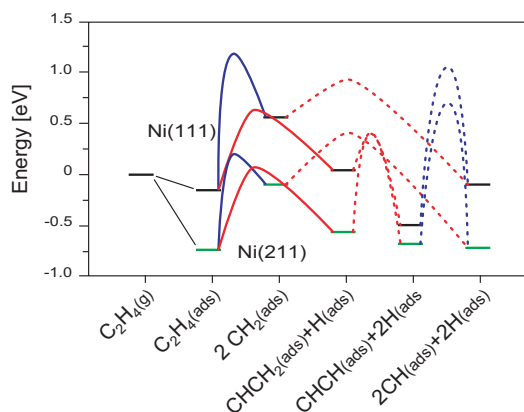


Fig. 3. Potential energy diagram for C–C bond breaking (blue line) and C–H bond breaking (red line) on Ni(111) and Ni(211). The transition state energy for C–H bond breaking of CH_2 is for one CH_2 .

Our results show that the transition state energy for ethylene C-C bond breaking is 0.2 eV on Ni steps, which is 1.0 eV lower than the transition state energy on the Ni(111) terrace. At the step edge the transition state is oriented parallel to the step edge. The optimized transition state perpendicular to the step edge has an energy as high as 0.9 eV. For the ethylene dehydrogenation the DFT calculations give a transition state energy of 0.08 eV on Ni(211) which is 0.6 eV lower than the dehydrogenation transition state energy on the terrace. Almost identical transition state geometries of vinyl on Ni(111) and Ni(211) explain why we get the same transition state energy for dehydrogenation on both surfaces. Note that the vinyl dehydrogenation takes place behind the Ni step, not at the step like the ethylene dehydrogenation. Although the transition state energy for vinyl dehydrogenation to acetylene is low, the reaction leads to the formation of strongly bound acetylene which has a high transition state energy for the C-C bond cleavage. At first sight the acetylene transition states on Ni(111) and Ni(211) look similar, but a closer look reveals a difference in transition state geometries: on Ni(111) CH species are on the two-fold sites whereas on Ni(211) they are on the three-fold sites. The fact that the

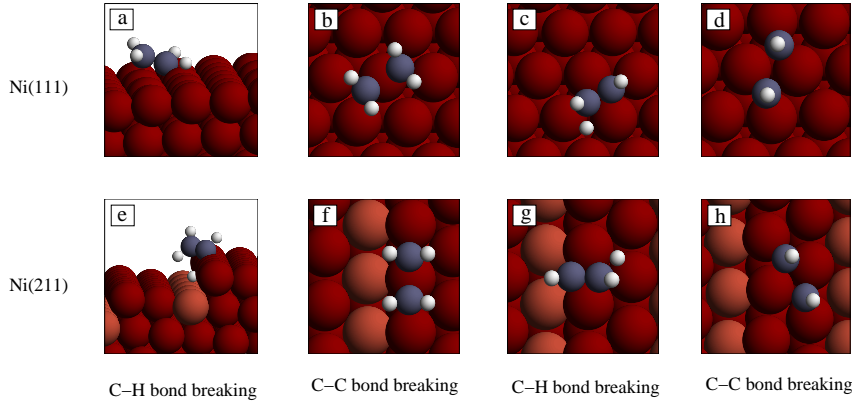


Fig. 4. Optimized transition state geometries for (a) and (e) ethylene dehydrogenation, (b) and (f) ethylene dissociation, (c) and (g) vinyl dehydrogenation, and (d) and (h) acetylene dissociation on the Ni(111) (Ni(211)) surfaces. The color coding is the same as in Fig. 2.

difference in C-C bond breaking energies is smaller for acetylene than for ethylene arises from the position of the transition state geometry on the surface. On Ni(211) C_2H_2 decomposes behind the step whereas the C_2H_4 decomposition takes place at the step, meaning that for ethylene the role of the higher reactivity of step atoms is larger.

The reduction in the height of the transition state energies when comparing step sites with terrace sites, is considerably more pronounced for dissociation than for dehydrogenation at the level of C_2H_4 . The origin of this difference lies in the structure of the transition states. For dehydrogenation the transition states are rather similar on both surfaces, whereas for dissociation they differ somewhat. After the C-C bond cleavage the CH_2 groups end up in three-fold sites on the terrace. This is in contrast to the geometry at the step edge, where the optimized final structure for a methylene is a two-fold site. Since the distance between CH_2 groups in the final state is shorter at the step edge than at the terrace, it means that at the step edge CH_2 is stabilized at an earlier point, and thus the transition state energy for dissociation is lower. On both types of sites the transition state energy for dehydrogenation of ethylene is lower than for dissociation. The transition state energy for dehydrogenation at the terrace is, however, higher than the transition state energy for dissociation at the step site. This indicates that dissociation/dehydrogenation always takes place at the step if free step sites are available. The fact that the reactivity is significantly higher at step sites compared to terrace sites, as predicted by DFT, agrees with the present STM measurements as well as with EELS data. [18].

3.3 Ethylene exposure at 500 K

As shown in section 3.1, the (partial) decomposition of ethylene at the step edge is self-poisoning. This is also rationalized by the DFT calculations in the sense that the carbon binding energy is 1 eV larger on a step site than on a terrace site, and thus all of the step edges will eventually be covered with adsorbed carbon. This implies that after a short initial period in which ethylene decomposes primarily at the step edges, the terraces will provide the only active sites for the decomposition process. The formation of complete carbon overlayers has previously been reported in the literature, where it has been shown that at 500 K carbon adsorbs in the carbidic phase, in which the carbon atoms induce the so-called “clock reconstruction” of the Ni(111) surface [19,20]. A ball model of the “clock reconstruction” is presented in fig. 5(c), from which it is seen that the topmost layer of the Ni(111) surface is reconstructed into an almost (100)-like quadratic structure but with the squares of Ni atoms rotated in a clockwise/anticlockwise fashion. The carbon atoms, which show up as depressions in the STM images, are adsorbed in a $c(2 \times 2)$ structure with respect to the reconstructed surface (see ref. [19] for a detailed discussion on this structure). For ethylene exposure at 500 K we observe ordered islands growing from the upper step edges of the Ni(111) surface as illustrated by Fig. 5(a). A zoom-in on these islands (Fig. 5(b)) reveals the quadratic unit cell of the carbidic structure, and these images thus confirm that ethylene decomposes fully at 500 K and leaves adsorbed C on the surface. Just as was the case for the brim of decomposed ethylene formed after room temperature exposure, the carbidic islands, formed by dissociated ethylene at 500 K, always nucleate at the upper step edges and no isolated islands are observed on the terraces. The knowledge of the nucleation site of the carbidic islands does, however, not allow us to make any conclusions about the active site for the dissociation of ethylene. To obtain insight into this we have investigated the dependency of the island coverage on the ethylene dose. This has been done by measuring the carbon coverage for different dosing times at a constant ethylene pressure of 1×10^{-9} torr. The analysis of this series of experiments is presented in Fig. 5(d), where the coverage (measured as the width of the carbidic islands averaged over the length of the step edges) is plotted as a function of the dosing time. From the graph it is seen that an increased dose of ethylene leads to an increased coverage of carbon on the Ni(111) surface, which indicates that the decomposition of ethylene is no longer restricted to the step sites, as was the case for room temperature exposure. This is seen even more clearly when the data is fitted with a Langmuir adsorption curve, in which the rate of dissociation is assumed to be proportional to the coverage of free Ni(111) terrace atoms. We plot the average width of carbon islands, $\phi = l \cdot \theta$, where l is the average terrace width, and θ is the coverage. Then the Langmuir adsorption curve changes from its usual expression, $\theta(t) = 1 - e^{-kt}$,

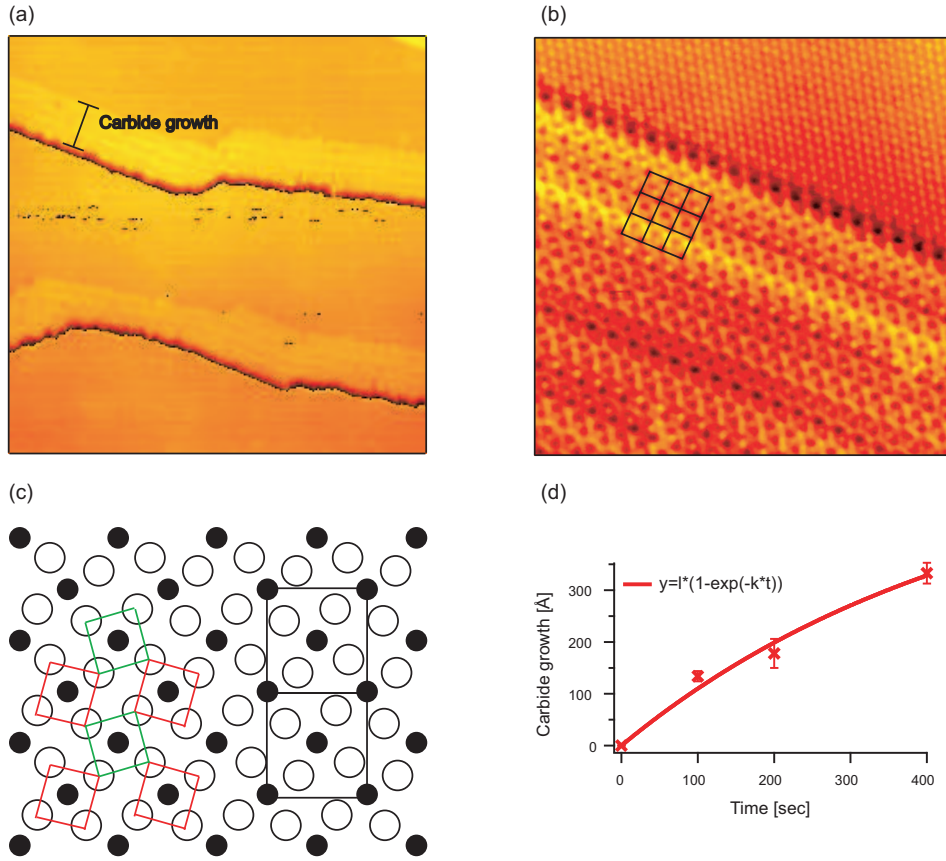


Fig. 5. **(a)** STM image ($500 \times 500 \text{ \AA}^2$) of carbidic islands at the step edges of Ni(111) formed upon exposure to 0.1 L ethylene at 500 K. **(b)** Zoom-in ($100 \times 100 \text{ \AA}^2$) on a carbidic island. The square unit cell of the carbidic structure is indicated. **(c)** Ball model of the carbon atoms (filled circles) and the topmost layer of Ni atoms (open circles) in the “clock” reconstruction. The Ni atoms are arranged in (100)-like squares rotated clockwise (red) and anticlockwise (green). The $c(\times 2)$ grid of the C atoms is indicated. **(d)** Plot of the coverage of carbidic islands vs. the exposure time.

to

$$\phi(t) = l \cdot (1 - e^{-kt}).$$

This expression fits nicely with the data, and furthermore the deduced average terrace width of approx. 600 \AA agrees well with that of the used crystal.³ On this basis we can conclude that at 500 K the process of ethylene decomposition on Ni(111) is completely dominated by the terrace atoms.

³ The actual average terrace width is lower than 600 \AA , but the smallest terraces were omitted in the analysis.

3.4 Selectivity

To gain information about the influence of the step edges on the selectivity between the initial dissociation (C–C bond breaking) and the dehydrogenation (C–H bond breaking), we compare these initial steps on the Ni(111) and the Ni(211) surfaces. Fig. 4 shows the transition state structures for the C–C bond and the C–H bond cleavage of ethylene. Recall that ethylene dissociation to CH₂ and the primary dehydrogenation to vinyl both have higher transition state energies on the Ni(111) terrace than on the step. The absolute difference between the transition state energies on steps and terraces is, however, larger for the C–C bond breaking (1.0 eV) than for the C–H bond breaking (0.6 eV). This shows that the step effect is more pronounced for the dissociation than for the dehydrogenation.

On the terrace the transition state energy for dehydrogenation is about 0.5 eV lower than for dissociation which indicates that ethylene first, at least partially, dehydrogenates before the C–C bond breaks. Thus, by blocking the step sites one can prevent the instant C–C bond breaking and control the formation of CHCH₂. Vinyl is unstable ($E_{\text{ads}} = +0.04\text{eV}$) on Ni(111) and so its coverage is low over the terrace. It can desorb, dissociate, or go through one or more secondary dehydrogenation steps and form, for example, ethylidyne (CCH₃), acetylene (C₂H₂), or acetylide (C₂H). Of these species ethylidyne is the most stable on Ni(111) with a binding energy -0.7 eV, but the dissociation transition state energy is as high as about 1.5 eV. Acetylene is not quite as stable (adsorption energy -0.5 eV) but its transition state energy is 0.5 eV lower. As far as the transition state energy is concerned, acetylide lies in between the acetylene and ethylidyne transition state energy for dissociation. However, acetylide is highly unstable; the binding energy is +0.5 eV. The tendency of ethylene towards dehydrogenation prior to the C–C bond breaking on Ni(111) agrees with the EELS measurements of Lehwald *et.al* [18]. These authors have studied the adsorption of ethylene and acetylene on the flat and stepped Ni surface at 150 K and the decomposition of these molecules after annealing to higher temperatures. They found that on Ni(111) ethylene dehydrogenates to acetylene and hydrogen above 230 K. The situation on the stepped surface is more complicated and the identification of surface species was only partially possible. We believe that the identification is more difficult because the number of different species on the surface is larger, which is due to the fact that the dissociation and primary dehydrogenation transition state energies are close to each other and hence both reaction pathways are possible.

3.5 *Ag/Ni(111)*

The growth of Ag on Ni(111) and its influence on the reactivity towards ethylene decomposition were studied. From earlier work within our group we know that Ag nucleates preferentially at the step edges of Ni(111) [22], and also Ag is generally a less reactive atom than Ni [23]. For these reasons we considered Ag to be a good candidate for blocking the step edge sites on the Ni(111) surface.

When Ag is evaporated onto Ni(111) at room temperature it nucleates via step flow into large islands, as shown in Fig. 6(a). The growth of these islands is not pseudomorph, which can be seen by the appearance of a moiré pattern caused by the mismatch between the Ag and Ni lattices (see small insert in Fig. 6). Because of the nucleation into very large islands the majority of the step edge atoms are unaffected by this room temperature evaporation of Ag. Post-annealing of the Ni(111) surface after Ag evaporation, however, causes the Ag atoms to completely wet all the step edges. An STM image of a Ni(111) surface annealed to 800 K after evaporation of Ag at room temperature is seen in Fig. 6(b). When comparing this to the clean Ni(111) (see fig. 1(a)), we find a row of protrusions along the step edges. These protrusions appear bright in the STM image and they are also observed when comparing a line scan across a step edge on the Ag/Ni(111) surface with a similar scan on the clean Ni(111) surface, as illustrated in Fig. 6(c). These protrusions are ascribed to Ag atoms wetting the step edges, and for this Ag/Ni(111) surface no free Ni step edge atoms are found.

When the post-annealed Ag/Ni(111) surface was exposed to 1 L ethylene at room temperature we observed no formation of a brim along the step edges (or anywhere else), as can be seen from the STM image in fig. 7(a). We interpret this in the way that the Ag atoms are effectively blocking the step edge atoms of the Ni(111) surface, so that these can no longer act as the active sites for ethylene decomposition at room temperature. In this way we both provide further evidence that the step edge atoms are indeed the active sites for ethylene decomposition at room temperature, and we also demonstrate how the reactivity of the Ni(111) surface can be altered by blocking these very reactive sites.

When the post annealed Ag/Ni(111) was exposed to ethylene at 500 K we observed the growth of carbidic islands at the step edges (fig. 7(b)), exactly as we did for the clean Ni(111) surface. This again shows that the atoms of the (111) facets are the active sites for ethylene decomposition at 500 K, and it also demonstrates that the addition of Ag to the Ni(111) surface blocks only the step edges and not the terraces.

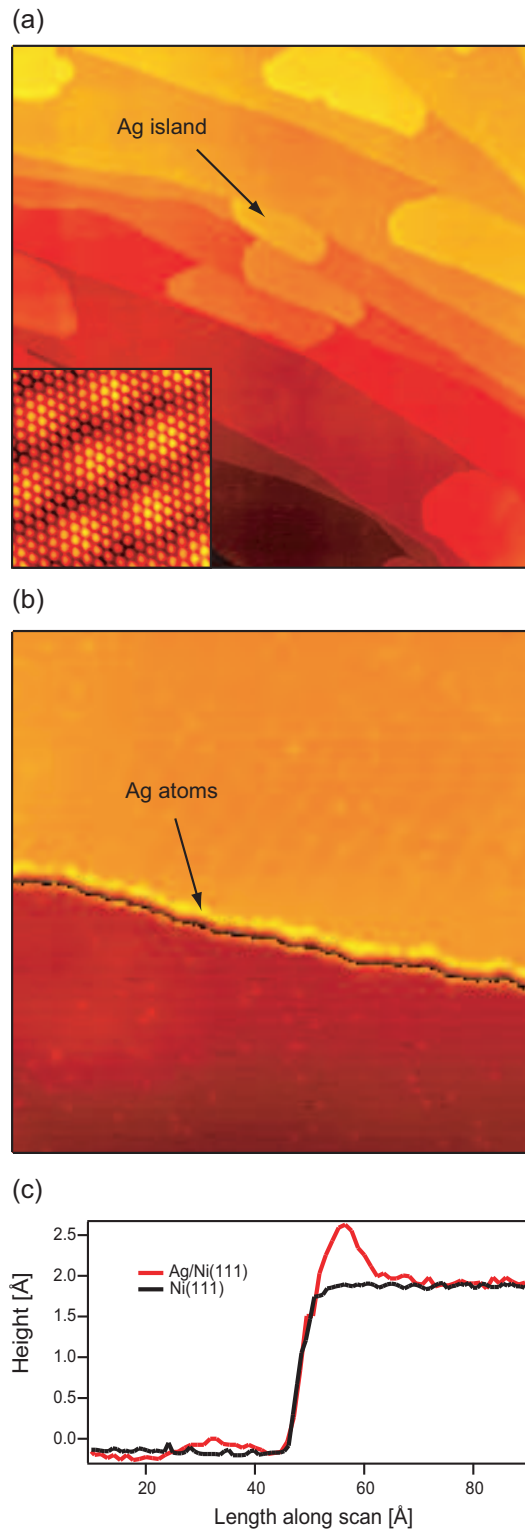


Fig. 6. **(a)** STM image ($7000 \times 7000 \text{ \AA}^2$) of Ag islands nucleated along the step edges of Ni(111) after evaporation of Ag at room temperature. The small insert is a zoom-in ($50 \times 50 \text{ \AA}^2$) showing the moiré pattern formed on the Ag islands. **(b)** STM image ($400 \times 400 \text{ \AA}^2$) of a Ag/Ni(111) surface after post-annealing at 800 K. A bright row of Ag atoms is seen along the step edges. **(c)** Line scans across the step edges of clean Ni(111) and the post-annealed Ag/Ni(111) surface.

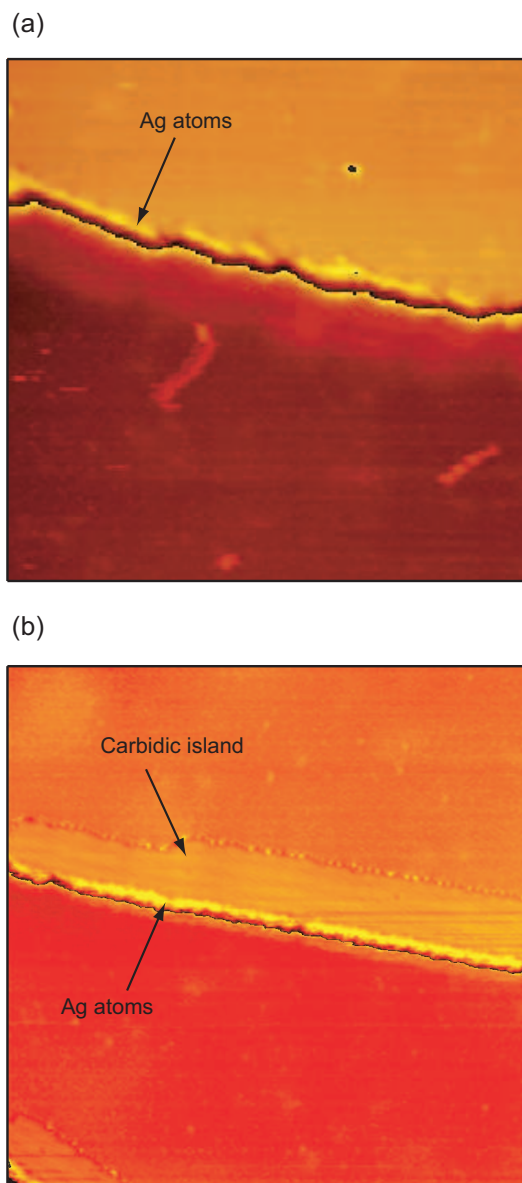


Fig. 7. STM images ($300 \times 300 \text{ \AA}^2$ and $500 \times 500 \text{ \AA}^2$) of a Ni(111) surface with the step edges decorated by Ag atoms after exposure to ethylene at room temperature **(a)** and 500 K **(b)**. No adsorption is observed upon room temperature exposure, whereas the exposure at 500 K leads to a nucleation of carbidic islands along the Ag-decorated step edges. The elongated features in (a) are single impurities that are dragged along the direction of the scanning tip.

3.6 Reactivity measurements

The results discussed above indicate that we should be able to control the selectivity of catalytic reactions where the C-H and C-C bond breaking compete by controlling the availability of step edge sites on the catalyst surface. We have also shown that one efficient way of blocking the step edge sites is

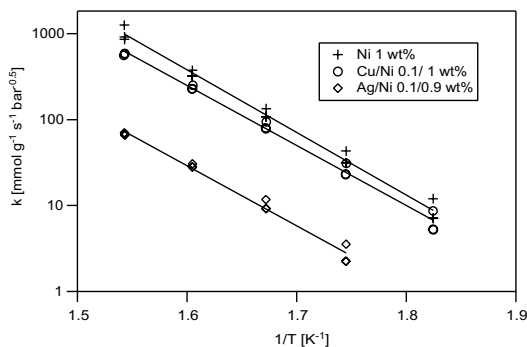


Fig. 8. Arrhenius plots of the rate constant for ethane hydrogenolysis over Ni/MgAl₂O₄ and Ag/Ni/MgAl₂O₄. The slope of the straight line fits gives the activation energies for the hydrogenolysis process.

by introducing Ag at the surface. Since Ag readily segregates out of Ni [24], such step edge blocking only requires small amounts of Ag in a Ni catalyst. Hydrogenolysis of ethane is the simplest reaction which can be used to probe the activity for the C–C bond breaking. Sinfelt *et al.* exploited this in their work on bimetallic catalysis [25]. They studied, for instance, the ethane hydrogenolysis reaction over unsupported Ni and Cu/Ni and found a dramatic effect of even small amounts of Cu [26]. In the present study we performed reactor experiments on ethane hydrogenolysis on various oxide-supported Ni catalysts (the metal contents are given in Fig. 8).

In order to obtain a rate constant which is independent of the gas composition, the ethane hydrogenolysis experiments were analyzed assuming the reaction to be first order with respect to ethane pressure and furthermore that the surface is mainly covered by atomic hydrogen resulting in a negative reaction order in hydrogen. We used the following rate expression in the analysis

$$r = k p_{C_2H_6} / p_{H_2}^{0.5}.$$

In Fig. 8 it is seen that this rate gives an adequate description of the data since the different feed compositions give rise to similar rate constants. In the data analysis it was assumed that the reactor is an ideal integral reactor. From the figure it is evident that the addition of Ag to the Ni catalyst has a severe negative influence on the rate constant for ethane hydrogenolysis, which is decreased by an order of magnitude. In Fig. 8 it is seen that the apparent activation energy is the same for the two catalysts, which strongly indicates that the active sites on the two catalysts are the same; i.e. Ag does not cover all of the Ni step edges. This finding does not contradict the results obtained for the Ni(111) single crystal surface, but it can be rationalized by the complexity of the high surface area supported Ni catalyst. The small Ni particles will expose a relatively higher number of step edges and defect sites than the flat Ni(111) surface, and also the Ag/Ni ratio will vary in the bimetallic catalyst due to statistic variation and non-perfect catalyst preparation. Thus, a high

average Ag/Ni ratio is required if all Ni step edge sites are to be blocked by Ag. It is seen that Ag is a much more efficient blocker of step edges than Cu when the catalysts are prepared by the present method. Sinfelt *et al.* [26] only investigated the effect of Cu and not Ag on the hydrogenolysis rate. They found a much stronger effect of adding ca. 5 % of Cu to Ni than we have seen; this was, however, on unsupported systems with a surface area of 1m²/g where 5 % of Cu is enough to cover the whole metal surface if it segregates to the surface, as one would expect [24].

3.7 Summary

In summary, we have shown that the step edge sites of Ni(111) are far more reactive towards ethylene decomposition than the regular sites on the (111) facets and that the step edges furthermore play a very important role in the bond-breaking selectivity between the initial C–H and C–C bond breaking. When the step edges are blocked, ethylene will always go through an initial dehydrogenation, and as shown explicitly for the case of acetylene, dehydrogenation generally leads to species with stronger C–C bonds than ethylene and thus even higher barriers for dissociation. The fact that free step edge sites are essential for the splitting of the C–C bond is exactly what is demonstrated in the reactor measurements performed on the high surface-area, oxide-supported catalysts. In these experiments we demonstrate that the idea of blocking the step edges with Ag atoms can be transferred from the fundamental UHV studies to a practical applicable catalyst. The present study is thus an example of how new insight gained from basic science can lead to the development of new and improved catalysts with potential for industrial use; an approach that provides a very strong alternative to the trial-and-error method which has been the backbone of catalyst development for more than a century.

References

- [1] Taylor, H. S. *P. Roy. Soc. Lond. A Mat.* **1925**, *108*, 105.
- [2] Gwathmey, A. T; Cunningham, R. E *Adv. Cat.* **1958**, *10*, 57.
- [3] Yates Jr., J. T. *J. Vac. Sci. Technol. A* **1995**, *13*, 1359.
- [4] Zambelli, T.; Wintterlin, J.; Trost, J.; Ertl, G. *Science* **1996**, *273*, 1688.
- [5] Dahl, S.; Logadottir, A.; Egeberg, R. C.; Larsen, J. H.; Chorkendorff, I.; Tørnquist, I.; Nørskov, J. K. *Phys. Rev. Lett.* **1999**, *83*, 1814.
- [6] Nørskov, J. K.; Bligaard, T.; Logadottir, A.; Bahn, S.; Hansen, L. B.; Bollinger, M.; Bengaard, H.; Hammer, B.; Sljivancanin, Z.; Mavrikakis, M.; Xu, Y.; Dahl, S.; Jacobsen, C. J. H. *J. Catal.* **2002**, *209*, 275.

- [7] Liu, Z.P.; Hu, P. *J. Am. Chem. Soc.* **2003**, *125*, 1958.
- [8] Zubkov T.; Morgan Jr., G.A.; Yates Jr., J.T.; Köhlert, O.; Lisowski, M.; Schillinger, R.; Fick, D.; Jänsch, H.J. *Surf. Sci.* **2003**, *526*, 57.
- [9] Gambardella, P.; Sljivancanin, Z.; Hammer, B.; Blanc, M.; Kuhnke, K.; Kern, K. *Phys. Rev. Lett.* **2001**, *87*, 056103.
- [10] Ciobîcã, I. M.; van Santen, R. A. *J. Phys. Chem. B* **2002**, *106*, 6200.
- [11] R. T. Vang, K. Honkala, S. Dahl, E. K. Vestergaard, J. Schnadt, E. Lægsgaard, B. S. Clausen, J. K. Nørskov, F. Besenbacher, *Nat. Mat.* **4** (2005) 160.
- [12] Lægsgaard, E.; Besenbacher, F.; Mortensen, K.; Stensgaard, I. *J. Microsc.* **1988**, *152*, 663.
- [13] Besenbacher, F. *Rep. Prog. Phys.* **1996**, *59*, 1737.
- [14] <http://www.fysik.dtu.dk/CAMPOS>
- [15] Hammer, B; Hansen, L.B; Nørskov, J. K. *Phys. Rev. B* **1999**, *59*, 7413.
- [16] Vanderbilt D. *Phys. Rev. B* **1990**, *41*, 7892.
- [17] Jónsson, H; Mills, G; Jacobsen, K.W in *Classical and Quantum dynamics in Condensed Phase Simulations*, Berne, B. J.; Ciccotti, G.; Coker, D. F., Eds. (World Scientific, Signapore) **1998**.
- [18] Lehwald, S.; Ibach, H. *Surf. Sci.* **1979**, *89*, 425.
- [19] Klink, C.; Stensgaard, I.; Besenbacher, F.; Lægsgaard, E. *Surf. Sci.* **1995**, *342*, 250.
- [20] Nakano, H.; Ogawa, J.; Nakamura, J. *Surf. Sci.* **2002**, *514*, 256.
- [21] Rostrup-Nielsen, J. R. in *Catalysis, Science and Technology*, Anderson, J. R.; Boudart, M., Eds. (Springer, Berlin) **1984**, *vol. 5*, 1.
- [22] Besenbacher, F.; Nielsen, L. P.; Sprunger, P. T. Chapter 10 in *The Chemical Physics of Solid Surfaces and Heterogeneous catalysis*, King, D. A.; Woodruff, D. P., Eds. (Elsevier Science Publishers) **1997**, *vol. 8*.
- [23] Hammer, B; Nørskov, J.K. *Nature* **1995**, *376*, 238.
- [24] Ruban, A.V.; Skriver, H.L; Nørskov, J.K. *Phys. Rev. B* **1999**, *59*, 15990.
- [25] Sinfelt, J.H. *Bimetallic Catalysts, Discoveries, Concepts, and Applications* John Wiley & Sons, Inc, **1983**.
- [26] Sinfelt, J.H.; Carter, J.L.; Yates, D.J.C. *J. Catal.* **1972**, *24*, 283.

X

From Atom-resolved Scanning Tunneling Microscopy (STM) Studies To the Design of New Catalysts

Jeppe V. Lauritsen, Ronnie T. Vang and Flemming Besenbacher*

*Interdisciplinary Nanoscience Center (iNANO)
Department of Physics and Astronomy,
University of Aarhus
DK-8000 Aarhus C, Denmark*

Email: fbe@inano.dk

The Scanning Tunneling Microscope (STM) is today established as the technique of choice for resolving the atomic-scale structure of surfaces. STM studies of model systems relevant to heterogeneous catalysis have made it possible to address and resolve many important, fundamental questions related to catalytic processes by imaging in direct space the atomic-scale structure of catalytically relevant model systems, i.e. adsorbate covered single crystal surfaces or small supported nanoclusters kept under well-controlled vacuum or pressure conditions. Here we discuss three recent STM studies of model catalysts, which all illustrate how the insight gained from fundamental studies of idealized model systems has successfully been linked to studies on real catalyst systems operating under realistic conditions and how this interplay may facilitate the development of new and superior high surface area catalysts.

Introduction

The need for a better understanding of catalysis has led to the development of a number of specialized experimental techniques which give detailed structural and chemical insight into complex heterogeneous catalysts. The multitude of techniques used today in catalysis research [1-4] are nearly all developed as general, solid state or surface science techniques with limited

direct application for the study of complex catalysts. Major developments and refinements of techniques like e.g. X-ray absorption spectroscopy, X-ray diffraction, infrared spectroscopy, and high-resolution electron spectroscopy have made it possible today to achieve a fairly good understanding of some catalyst systems. Most traditional diffraction and spectroscopic methods are, however, in general averaging techniques where the information about individual atoms and particles is lost and although these techniques have given unprecedented new insight into both model catalysts of e.g. supported nanoclusters and technical catalysts, they are thus not able to resolve individual defect sites, edge sites or other active sites often determining the catalytic activity.

The Scanning Tunneling Microscope (STM) technique is on the contrary a real-space, local probe technique that is capable of resolving the atomic-scale structure of surfaces in atomic detail. What has fascinated many scientists, and what sets the STM apart from most other surface science techniques is its ability to investigate atom-by-atom the geometric structure of surface structures. STM therefore stands out as an outstanding, unique and versatile tool for exploring the direct-space structure of conducting surfaces, supported nanoclusters and adsorbates on these. Since the development of the STM more than two decades ago [5], the STM has matured enormously and from being a complicated highly specialized physics instrument, sensitive to vibrations and drift, STM has developed into a compact and stable analytical tool which now finds widespread application in a number of disciplines. The confidence gained in the operation and interpretation of STM results has led to a situation where we can now use STM to solve different problems related to the geometrical and electronic structure of surfaces and nanostructures [6-8]. Since it also resolves signatures of adsorbed particles (sometimes even with high temporal resolution), it has become an outstanding tool for monitoring atom and molecule dynamics and chemical reactions on surfaces with direct relevance to catalysis [9, 10]. The ability of the STM to achieve atom-resolved real-space images of localized regions of the surface has thus often revealed

unprecedented new insight on catalytically active sites and, in particular, emphasized the catalytic importance of edges, kinks, atom vacancies or other defects, which are often difficult or impossible to detect with other techniques [10-12].

The STM technique is as such conceptually very simple and relies on the measurement of a small tunneling current floating between an atomically sharp metal tip which is raster-scanned at a sub-nm distance to the surface to be imaged (see Refs. [6, 8] for a detailed description). It is, however, evident that STM cannot be used to image real catalyst nanoparticles supported on a porous and often insulating carrier. Rather the STM requires flat and conductive samples, and like in most surface science techniques, the complexity of a catalyst is therefore in STM model studies stepwise broken down into simplified problems which can be dealt with in detail. Typically one investigates the unsupported material in the form of single crystal surfaces, or, more elaborate model systems consisting of particles deposited on a substrate when there is a distinct relation between the catalytic properties and the size of the clusters. The STM thus offers a unique view of such structures on the atomic scale, and it can undoubtedly give unprecedented new fundamental insight which subsequently can trigger new ideas for the development of better catalysts. Here we discuss three such examples; an STM study of supported MoS₂ nanoclusters as a model catalyst for hydrodesulfurization/hydrotreating and two studies on the role of Ag and Au modifiers on Ni(111) as a model system for steam reforming catalysis.

Hydrodesulphurization model catalyst studied with STM

The MoS₂-based hydrodesulphurization (HDS) catalyst has been the subject of extensive studies using a large variety of different tools and several extensive reviews on the subject exist [13-17]. A considerable effort has been aimed at relating fundamental characteristics such as catalyst activity and selectivity to microscopic properties such as catalyst composition, electronic structure and geometric structure. In particular, *in situ* EXAFS studies and Mössbauer spectroscopy studies have given information on the structure, and today the “CoMoS” model of

Topsøe, Clausen and coworkers is widely accepted to describe the active structures in the catalysts. In the model, it is concluded that the active phase is present as supported single-layer MoS₂-like particles with a size of 10-20 Å under operating conditions, and that the promoting effect of Co in the CoMoS structures is due to promoter atoms replacing Mo at positions near the edges of the MoS₂ clusters. [18-21].

Despite the impressive number of studies of HDS catalysts, a series of fundamental questions remain, however, unanswered. Much of the controversy is directly related to the fact that the traditional spectroscopy-based techniques are not able to unequivocally map the real-space atomic structure of the few nanometer wide CoMoS nanoclusters. It was early recognized that only the edges of the S-Mo-S layers in MoS₂ are catalytically active [13, 22], but in order to pinpoint and understand more precisely the active sites it is necessary to get a more detailed picture of the atomic-scale structure. For instance, what is the preferential shape of the MoS₂-like crystallites, what are the active edge structures, and what is the role of the promoters in CoMoS? To investigate these and a number of other issues related to the structure of the HDS catalyst we have recently successfully used the STM to study directly the atomic-scale structure of individual MoS₂ and CoMoS nanoclusters. The ability of the STM to achieve atom-resolved real-space images of the nanoclusters has made it possible to address experimentally for the first time directly the MoS₂ morphology and the structure of the catalytically important edges. We do this by synthesizing ensembles of single-layer MoS₂ or CoMoS nanoclusters on a flat Au(111) single crystal substrate as a realistic model system of the catalyst. The Au support is chosen since the close-packed Au(111) is rather inert and we can therefore study the intrinsic properties of MoS₂. Furthermore the Au(111) reconstructs in the characteristic herringbone pattern which is used as a template for the synthesis of a highly dispersed ensemble of nanoclusters [23]. The detailed preparation method for the synthesis of MoS₂ and CoMoS nanoclusters supported on Au(111) is reported in [24] and [25]. As illustrated in Fig. 1 in the case of MoS₂, the clusters synthesized by

this method are characterized by a high degree of dispersion and a narrow size-distribution. The average size of the clusters is approximately 500 \AA^2 . This corresponds to a side length of $\sim 30 \text{ \AA}$, which matches well the spatial extension of the active particles in typical HDS catalysts. A detailed analysis of STM images reveals that the morphology of the nanoclusters is also remarkably uniform with respect to the shape, and as shown in the figure we find that the triangular shape of MoS_2 clusters is strongly favored under the conditions of the experiment. As a model system for the HDS catalyst, the MoS_2 clusters synthesized in this study therefore form a well-characterized reference for experiments elucidating details on the atomic structure of the catalytically active MoS_2 edge structures and their reactivity with adsorbed molecules.

An atomically resolved STM image of a triangular MoS_2 nanocluster consisting of a single S-Mo-S layer is illustrated in Fig. 2. The cluster is observed to be oriented with the (0001) basal plane in parallel to the Au substrate and with the protrusions reflecting the hexagonally arranged S atoms in the topmost layer. At the edges, however, the protrusions are seen to be imaged *out* of registry with the basal plane S atoms. In fact, the protrusions are shifted exactly half a lattice constant along the edge, but retain their interatomic distance of 3.15 \AA . The atomically resolved image thus provides the first direct information on the atomic-scale structure of the MoS_2 edges. The shifted registry along the edge could indicate that the catalytically active edges are severely reconstructed compared to a model based on bulk properties of MoS_2 , but this is in fact not the case. It is important to point out that STM images obtained in the constant current mode reflect contours of constant local density of states (LDOS) at the Fermi level measured at the position of the STM tip [26]. This means that the contrast in STM images may be dominated by electronic structure, and if this is the case, a rather complicated convolution of geometric and electronic features results. This is in particular so for materials which exhibit a band gap, e.g. metal oxides or sulfides. MoS_2 is a semiconductor with a band gap $\sim 1.2 \text{ eV}$ in the bulk form [27], and for the MoS_2 nanoclusters in the present study we indeed find that a pure geometrical model is not

adequate to account for the STM images. Especially a pronounced bright *brim* of high electron state density is seen to extend all the way around the cluster edge adjacent to the edge protrusions in Fig. 2a. Rather than a geometrical effect, this is attributed to an electronic effect probed by the STM, reflecting the existence of localized electron-states at the cluster perimeter, so-called *edge states*. A full density functional theory (DFT) calculation by Bollinger *et al.* [28] solved the problem and it was found that the signatures observed with STM matches the $(10\bar{1}0)$ Mo edges fully saturated with S_2 dimers (Fig. 2b). The calculations also directly show that the electronic structure near the Mo edges of the triangular MoS_2 nanoclusters is indeed significantly perturbed relative to the bulk, and reveals that the edges are in fact metallic due to the existence of two distinct electronic edge states [28, 29]. An STM simulation based on the Tersoff-Hamann model [26] (i.e. a contour map of constant surface LDOS) shows that both the bright brim and the apparent shifted registry of the edge protrusions (Fig. 2c) can be traced back to the existence of the two edge states on the fully sulfided Mo edges, and the theory thus fully reproduces the experimentally observed features. Under the sulfiding conditions in the experiment, it is therefore concluded that triangular single-layer MoS_2 nanoclusters are terminated with the Mo edge fully covered with S dimers, and that the electronic structure of these edges is dominated by one-dimensional electronic “brim” states which give the edge a metallic character.

From a coordination chemistry point-of-view, fully sulfur saturated edges like the one in Fig. 2b are normally not considered to be particularly reactive, but due to the metallic character of the edges we find evidence of a rather different chemistry than what has ordinarily been assumed. We investigate this by selectively adsorbing thiophene (C_4H_4S) molecules under ultra-high vacuum conditions on the MoS_2 clusters at different temperatures, and in this way we can mark the adsorption sites and map out the interaction strength. Specifically, we find that thiophene adsorbs non-dissociatively onto sites near the bright brims associated with a metallic one-dimensional

edge state of MoS₂ at temperatures below 200 K, whereas we do not see thiophene adsorption on the inert (0001) basal plane of the MoS₂ clusters [30]. The thiophene molecules thus seem to bind considerably stronger near the metallic edge state of the fully sulfided Mo edges than to internal regions of the MoS₂ basal plane although the edges are still fully sulfur saturated. When the MoS₂ nanoclusters are treated with pre-dissociated hydrogen we observe an even stronger chemisorbed state of thiophene[31]. Figure 3 shows an atom-resolved STM image of a triangular MoS₂ nanoclusters first exposed to atomic hydrogen and subsequently to thiophene. Adjacent to the edges, bean-like features are now visible that mark the position of adsorbates. We identify these molecules as reaction intermediates from a hydrogenation reaction occurring on the metallic brim states. The hydrogen that drives this reaction is provided by H atoms adsorbed on the terminal S atoms on the edge to form S-H groups [30], which are also observed under reaction conditions in the real catalyst. Presumably, the combination of having hydrogen atoms adsorbed at the edges in the form of S-H groups and the unusual sites for thiophene adsorption on the metallic brim presents a favorable situation for a hydrogenation reaction. Based on STM image simulations from extensive density functional theory (DFT) calculations we find that the observed reaction intermediates are in fact *cis*-but-2-ene-thiolates (C₄H₇S) coordinated through the terminal sulfur atom to sites near the metallic brim. These species are formed by a sequential hydrogenation of one of the double bonds in thiophene by hydrogen adsorbed on the edges (from the S-H groups) followed by C-S bond cleavage. DFT calculations show that the reaction barrier associated with the most difficult step, the C-S bond breaking, is actually quite modest ~100 KJ/mol. The configuration observed in the STM image associated with a ring-opened structure is simply an ordinary thiol in which the S is much more reactive. The final extrusion of this S may therefore proceed on sulfur vacancies. We have thus identified a route for an initial activation of a relatively inert S-bearing molecule like thiophene, and the reaction intermediates observed in the STM image may therefore be the result of an important first step of hydrodesulfurization. Interestingly, these processes take place on the metallic brim states of the fully saturated Mo

edges, which have the ability to accept or donate electrons and thus act as catalytic sites just like ordinary metal surfaces.

Also the edges of promoted CoMoS nanoclusters seem to possess metallic edge states, and we therefore propose that metallic edge states may play a role also for the catalytic properties of the promoted phase. Figure 4 shows an atomically resolved STM image of a single-layer CoMoS cluster formed by co-deposition of Mo and Co onto the Au substrate during exposure to an H₂S atmosphere and subsequent annealing. The main new finding is that the CoMoS nanoclusters adopt a *hexagonal* shape as opposed to the triangular morphology of unpromoted MoS₂. This change in the equilibrium shape is therefore attributed to the incorporation of cobalt into the MoS₂ structure, i.e. the formation of the CoMoS phase. The predominant hexagonal morphology implies that both fundamental types of low-indexed edge terminations of MoS₂ must be present, i.e. the Mo edge and the S edge. One edge-type in the CoMoS is found to be similar to that observed for the MoS₂ triangles, with the edge protrusions clearly imaged *out* of registry with the lattice of S atoms on the basal plane and a bright brim along the edge. These edges are therefore identified as Mo edges, fully sulfided with two S dimers per Mo edge atom like in the triangles in Fig 2a. From the symmetry of MoS₂, the other, shorter edges are consequently attributed to S-type edges. On the basis of the detailed atomic-scale information provided by the STM images, a structural model of the CoMoS nanoclusters is proposed in which Co atoms have substituted Mo atoms along the S edges of hexagonally truncated nanoclusters. As depicted in the ball model in Fig 4, a *tetrahedral* environment of the Co atoms is produced if the outermost protrusions are assumed to be S monomers, which agrees well with previously published spectroscopic results on supported CoMoS catalysts [19, 32-34] and previous DFT studies [35, 36]. Interestingly, the promoted edges are in the STM images seen to exhibit an even brighter brim. This suggests that metallic edge states also exist in the promoted CoMoS structures, and in view of the result on the

unpromoted clusters it is tentatively proposed that the promoted brim states may be connected to the higher catalytic activity of the Co promoted phase.

Based on the fundamental insight on the role of metallic edge states in the MoS₂-based hydrotreating catalyst, and together with new knowledge on support interactions [37] it was recently possible to manufacture a new generation of hydrotreating catalysts which optimize the number of brim sites and enhance the hydrogenation properties [38]. Again, this shows that information gained in fundamental STM studies of idealized systems can generate the knowledge required to develop more capable catalysts in the industry. It is doubtful whether any experimental technique other than STM could unequivocally point to the presence of electronic states on the edge of highly dispersed MoS₂ nanoclusters of this size and furthermore directly identify their role in the adsorption of relevant molecules.

Au/Ni surface alloy catalyst for steam reforming

Nickel is widely used as the active material in the industrially important steam reforming reaction. In the steam reforming process, natural gas (mainly CH₄) is reacted with steam (H₂O) to form synthesis gas, which is a mixture of H₂ and CO and many of the challenges within the area of steam reforming have been discussed in an excellent review by Rostrup-Nielsen and coworkers [39-41]. A major technological challenge in the use of nickel catalysts in the steam reforming process, is that Ni is very active and also catalyzes the formation of graphite, which may lead to the growth of carbon filaments (so-called coking) and subsequently an accelerated deactivation and eventually complete breakdown of the catalyst [42, 43]. Rostrup-Nielsen found that one possible way of circumventing the problem of graphite formation is by the addition of minute amounts of H₂S to the feed gas [44]. The adsorbed S acts as a poison of the Ni catalyst which on one hand inhibits the reforming process, but poisons the graphite formation even more, so the

overall gain is a better selectivity and thus a longer life-cycle of the catalyst. This was developed by Rostrup-Nielsen *et al.* into the so-called SPARG (Sulfur PAssivated ReforminG) process [44]. This is, however, not an ideal solution to the problem since sulfur is also a strong poison for most other transition-metal based catalysts which are used downstream to catalyze the formation of products, and the presence of sulfur in the catalytic stream is therefore generally unwanted.

Another way of addressing the problem of graphite formation on nickel during steam reforming reaction would be to alter the chemical properties of the nickel surface by e.g. forming an alloy with another metal. It is well-known that alloys in certain cases have superior catalytic properties compared to elementary metals [45, 46], but typically the focus has been on the class of binary metal systems which form ordered or random bulk alloys. However, another class of 2-dimensional surface alloys have been revealed to exist for two-component metal systems that do not mix in the bulk, but which do form stable alloys in the outermost surface [47-50].

From STM studies we showed that the Au/Ni system belongs to this family of bulk-immiscible metals that form stable surface alloys. When Au is deposited on a Ni (111) surface, a surface alloy is formed: the Au atoms squeeze out Ni atoms and are subsequently substituted into Ni atom lattice positions as depicted in the atom-resolved STM images in Fig. 5, which were obtained after depositing Au atoms at 700 K. [51]. By correlating the number of atoms imaged as depressions to the amount of evaporated Au one sees that the Au atoms are in fact imaged as depressions in the STM, although one would expect the Au atoms to protrude from the surface based on pure geometric arguments. This imaging effect is due to the nature of STM images, which are in general a convolution of geometric and electronic structure, i.e. the LDOS at the positions of the Au atoms is lower than on the Ni sites.

The fact that a Au/Ni surface alloy is formed whereas no bulk 3D Au/Ni alloy exists (reflecting the fact the heat of solution of Au and Ni is large and positive, 27 kJ/mol) can easily be explained as follows. The Ni atoms in the surface layer are under coordinated compared to the Ni atoms in the bulk. The Au atoms have an electron density which is more extended than that of the Ni atoms and when the Au atoms are alloyed into the surface layer, the neighboring Ni atoms will feel a higher electron density or, equivalently, a higher effective coordination number. The Au atoms that are alloyed into the surface layer thus help lowering the Ni surface energy. This simple reasoning is confirmed by extensive theoretical calculations [51].

Three fundamental findings originated the idea that the Au-Ni surface could have interesting catalytic properties for the steam reforming process. First, it was seen in the high resolution STM images that the Au atoms alloyed into the Ni surface layer perturbs the electronic structure of the nearby Ni atoms. Ni atoms with a neighboring Au atom are imaged brighter in the STM, and this effect is even more pronounced for those Ni atoms having two Au neighbors. DFT calculations confirm [52] that this effect cannot be explained by an outwards relaxation of the Ni atoms but is rather owing to an alteration of the electronic structure. So the Ni surface layer consist basically of three different types of Ni atoms, those which only have Ni neighbors, those which have one Au neighbor, and those which have two Au neighbors. Second, DFT calculations showed that these three different types of Ni atoms have different reactivity with respect to activation of hydrocarbon molecules such as CH₄. Finally, the DFT calculations (Figure 7) reveal that the tendency of the surface to bind carbon and form graphite is strongly impeded by the presence of the substituted Au in the topmost layer of the Ni (111) surface [51].

These findings inspired the synthesis of a high surface area MgAl₂O₄ supported Ni catalyst (with 16.5 wt. % Ni) which was modified with 0.3 wt. % Au [51]. By means of extended X-ray absorption fine structure spectroscopy (EXAFS) we verified that the Au is indeed alloyed into the

first layer of the Ni catalyst. This high surface-area Ni catalyst was then tested by measuring the activity for steam reforming of n-butane and comparing this to a similar measurement on a pure Ni catalyst, and the results are shown in Fig. 6b. The only difference between the two samples is the Au modification of the Ni nanoclusters. n-butane was used to test the activity since it is known to give rise to the most severe graphite formation problems. Whereas the pure Ni catalyst is deactivated rapidly due to the formation of graphite as confirmed by e.g. electron microscopy, it was found that the conversion for the Au/Ni sample is almost constant. This proves that the novel Au/Ni catalyst does not produce graphite under the catalytic conditions, and the results illustrate nicely that we in this case have reached a situation where fundamental insight into surface structure and reactivity have been applied directly to the design of a new steam reforming catalyst operating under technically relevant conditions.

Selective site blocking by Ag atoms on Ni(111)

It is generally accepted that often the reactivity of a catalyst surface is dominated by a very small fraction of the surface, and this has led to the concept of the active site [53]. From STM and DFT it has been shown in recent years that the step edges dominate the dissociation of most simple diatomic molecules [54-60]. Whereas the *activity* of a catalyst is often a primary property to characterize a good catalyst, the *selectivity* is another and equally important factor for reactions with several possible reaction pathways. Very little information, however, exist on the ways in which the selectivity is controlled by special active sites, such as step edges or kinks. To gain further insight and generate ideas how to design new catalysts with improved selectivity, we recently investigated the initial steps of the decomposition of ethylene on Ni(111) surfaces. In the combined STM and DFT study we have revealed interesting information on the role of the step edges for the rate of C-H and C-C bond breaking. The results give important insight on the bond breaking selectivity of the Ni catalyst between dissociation and primary dehydrogenation. This

bond breaking selectivity will eventually show up in the selectivity between the final products in e.g. hydrogenolysis or dehydrogenation of hydrocarbons.

The most reactive sites on Ni(111) can be probed by dosing ethylene at the lowest temperature for which a reaction occurs. For room temperature exposure of ethylene we observed the formation of a brim of reaction products along the upper step edges of the Ni(111) surface as can be seen in the STM image of Fig. 7a. The formation of this brim was found to be self-poisoning, i.e. the width of the brim did not increase with increasing dosing time. This shows that the active sites for decomposing ethylene are blocked by the reaction products found in the brim, and we thus concluded that only the sites at the step edges of Ni(111) are active for ethylene decomposition at room temperature. [61].

The STM data were complemented by DFT calculations where the activation barriers were calculated for the two possible initial steps of the decomposition of ethylene: dissociation (C-C bond breaking) and dehydrogenation (C-H bond breaking). Step edges were introduced by performing the calculations both for the flat Ni(111) surface and for the stepped Ni(211) surface. The calculations showed that both energy barriers (dehydrogenation and dissociation) on the stepped surface were significantly lower than the lowest barrier (dehydrogenation) on the flat surface, consistent with the high reactivity of the step sites observed in the STM study. By comparing the step sites to terrace sites, the DFT calculations furthermore showed that reduction in the height of the activation barrier, was much more pronounced for dissociation than for dehydrogenation, indicating that the selectivity of the Ni(111) surface towards ethylene dissociation/dehydrogenation to a large extent is determined by the ratio of step sites to terrace sites.

The selectivity of the Ni(111) may thus be controlled by modifying the number of free step sites, and we demonstrated by STM experiments that the step edges could be blocked by the addition of small amounts of Ag [61]. In other STM studies we have found that when Ag is deposited on Ni(111) at room temperature, Ag preferentially nucleates and grows as islands at the step edges [49]. When this system is post-annealed to 800 K the Ag atoms become highly mobile and decorate all of the step edges of Ni(111), as seen in the STM image of Figure 7b and illustrated by the inserted ball model. To test that the Ag atoms block the step edges, we subsequently exposed this Ag/Ni(111) surface to ethylene at room temperature and found by STM in this case no ethylene induced brim structure neither at the step edges nor on the terraces. This clearly indicates that the step edge sites are indeed the active sites for the decomposition of ethylene at room temperature and the experiments showed that addition of silver effectively blocks these sites and changes the overall selectivity of the stepped Ni(111) surface.

To bridge the gap from the fundamental studies on model systems and exploit the new knowledge in a real catalyst, we have synthesized a new oxide-supported Ag/Ni catalyst [61]. The Ag-doped catalyst was tested for hydrogenolysis of ethane, which is the simplest possible reaction to probe the activity for C-C bond breaking. The results are depicted in Fig. 7c and it is seen that the design of the new Ag modified catalyst has led to a decrease in the rate constant for ethane hydrogenolysis by approximately an order of magnitude. It is also seen that the activation energy (slope of the Arrhenius plots) are similar for the two catalysts, indicating that they have the same active sites. This was interpreted in the way that not all the step edges were blocked on the Ag/Ni catalysts, which is due to the complex structure of the highly dispersed and supported catalyst. The blocking of the dissociation pathway was attributed to the addition of silver to the Ni catalyst, and here the STM has played a vital role in determining the role of step edges and providing clues on how to change the nature of these sites.

The very reactive step sites on Ni surfaces are also strongly involved in the formation of graphite during the steam reforming process as shown in recent STEM studies by Helveg *et al.* [42]. The poisoning effect of S utilized in the SPARG process may therefore also be speculated to relate to the step edges. We performed experiments with S on Ni(111) and especially studied its effect on the dissociation of CO. CO was used as the test molecule since it dissociates exclusively at the step edges and forms carbon structures, which are readily observed by STM (see figure 8 (a)). When the Ni(111) surface was exposed to H₂S at 400 K we found that the sulfur atoms adsorb preferentially along the step edges (Figure 8 (b)), and furthermore we found that CO did not dissociate on the Ni(111) surface when the step edges were decorated with S atoms. Although these data are for CO dissociation, we expect that S will block the step edges for activation of any hydrocarbon molecule, and the step edges may thus play an important role in explaining the effect of S in the SPARG process.

Outlook and perspectives

In this article a few examples are presented on how studies of catalyst model systems has given new insight that could be transferred to a real system and facilitate the synthesis of a new and better catalysts. This so-called *surface science approach*, where detailed investigations are made by applying sophisticated analysis methods to well-defined single crystal surfaces often under well-controlled high vacuum conditions as catalyst model systems, is able to provide us with fundamental microscopic insight into the principles underlying the elementary steps of heterogeneous catalysis. As a relatively new technique used in catalysis, the STM enables a direct atomic-scale view of active sites with a low density such as edges, kinks or atomic defects, which in many cases turn out to dominate the catalytic properties. The results of these studies thus demonstrate that one cannot in general neglect the cluster nature of the active materials in catalysts and model it from the usually well-known bulk properties. Atomic-scale insight is essential, and the STM is an excellent tool to resolve such issues on nanoclusters deposited on

conducting substrates. However, one should be aware of the fact that catalyst model systems may differ significantly from the real high surface area catalysts, both with regards to the nature of the surface morphology and the applied pressure range. Today different routes are being developed to overcome the materials and pressure gaps, and it is very likely that the STM will play a central role in this progress. A great number of new developments of the STM and related techniques are under way [62-64], and they have already shown promising results with clear significance for the fundamental studies of catalysis.

Acknowledgements

This paper is dedicated to Jens Rostrup Nielsen and Henrik Topsøe in connection with the Symposium “Frontiers in Catalysis”. We and in particular FB thank them both for a very fruitful, stimulating collaboration and for their support for many years of the STM activities at the University of Aarhus. We also gratefully acknowledge the large number of colleagues who have been involved at different stages in the presented work; M. Bollinger, I. Chorkendorff, B.S. Clausen, S. Dahl, B. Hammer, K. Honkala, S. Helveg, E. Lægsgaard, M. Nyberg, J.K. Nørskov, J. Schnadt, I. Stensgaard, H. Topsøe, and E.K. Vestergaard. Finally J.V.L acknowledges financial support from the Carlsberg Foundation.

Figure Captions

Figure 1: STM image of MoS₂ nanoclusters synthesized on Au(111) surface at 673 K in a sulfiding atmosphere. The size is 744Å × 721Å. Reproduced from [24].

Figure 2: Atomically resolved STM image ($V_t = 5.2\text{mV}$, $I_t = 1.28\text{nA}$) of a triangular single-layer MoS₂ nanoclusters on Au(111). The size of the image is 41Å × 42Å. Adapted from [24]. (b) Side

view and front view of the Mo edge fully saturated with S dimers. (c) Simulated STM image of a two atom wide section of the Mo edge with S dimers. The simulation is based on DFT calculations including the effect of the Au substrate (from [28]). The positions of the individual atoms in the simulated image are represented with shadowed atom balls (small: S, big: Mo). For clarity the Au atoms of the support are omitted.

Figure 3: (a) Atom-resolved STM image ($V_t = -331\text{mV}$, $I_t = 0.50\text{nA}$) of an atomic hydrogen pretreated MoS_2 cluster subsequently exposed to thiophene. Image dimensions are $50\text{\AA} \times 54\text{\AA}$. The dashed circle indicates the features which are associated with individual adsorbed molecules. (b) A close-up which illustrates in detail the features associated with the adsorption of individual thiolate species at the edge of a MoS_2 nanocluster. (c) STM line scans along the edge protrusions of a cluster (black) corresponding to the line in (b). A line scan of an equal section of an unreacted, fully sulfided edge (gray dashed) is also shown. From Ref. [31]

Figure 4: (a) Atom-resolved STM image of a CoMoS nanocluster. Size is $51\text{\AA} \times 52\text{\AA}$ and $V_t = -95.2\text{ mV}$, $I_t = 0.81\text{ nA}$ (From Ref. [25]). Notice the very intense brim associated with the Co-substituted S edge (shorter edges). (b) Ball model of the proposed CoMoS structure. The CoMoS cluster is shown in top view exposing the unpromoted Mo edge and a Co-promoted S edge (Mo: dark, S: bright Co: dark with spot). Also shown on the basal plane is a single Co inclusion. The Mo edge appears unaffected by Co and is shown in side view ball model. The Co substituted S edge with a tetrahedral coordination of each edge Co is also shown.

Figure 5: Two STM images of the Ni(111) surface with 2% and 7% Au coverage respectively. Au is imaged as dark depressions in the surface. The Ni atoms surrounding the Au appear brighter due to a local modification of the electronic structure, indicating a changed chemical activity of these. Adapted with permission from [51]

Figure 6 : (a) The probability of nucleation of graphite is determined by the stability of the adsorbed C atoms, The less stable the adsorbed C, the larger the tendency to react with adsorbed O to form CO and the lower the coverage. On the pure Ni (111) surface, the most stable adsorption site is the three-fold (hcp) site. The figure shows that three-fold sites next to a Au atom are seen to be completely unstable, and even the three-fold sites that are next nearest neighbors to the Au atoms are substantially destabilized. (b) Conversion of n-butane as a function during steam reforming. The bright curve shows the conversion of the pure Ni catalyst whereas the dark curve is for the Au/Ni catalyst. Adapted with permission from [51]

Figure 7: (a) STM image ($200 \text{ \AA} \times 200 \text{ \AA}$) of a Ni (111) surface after exposure ethylene (10^{-8} torr; 100s) at room temperature. (b) STM image ($400 \text{ \AA} \times 400 \text{ \AA}$) of a Ni (111) surface with the step edges blocked by Ag atoms. The small insert shows a ball model of a row of Ag atoms decorating a step edge on Ni(111). (c) Arrhenius plot of the rate constant for hydrogenolysis over Ni/MgAl₂O₄ and Ag/Ni/MgAl₂O₄. The rate (k) of ethane hydrogenolysis is one order of magnitude lower on then Ag/Ni catalyst as compared with the Ni catalyst, while the activation energy (slope of the Arrhenius curve) is similar.

Figure 8: (a) STM image ($500 \text{ \AA} \times 500 \text{ \AA}$) of a Ni (111) surface showing the nucleation of carbon islands along the step edges after exposure to CO at 400 K. (b) STM image ($100 \text{ \AA} \times 100 \text{ \AA}$) of single S atoms adsorbed at the step edge of a Ni(111) surface.

- [1] J.W. Niemantsverdriet, *Spectroscopy in Catalysis*. 2nd. ed, Weinheim: Wiley-VCH Verlag GmbH, 2000.
- [2] G.A. Somorjai, *Surface Chemistry and Catalysis*, New York: Wiley, 1994.
- [3] G. Ertl, H. Knözinger, and J. Weitkamp, eds. *Handbook of Heterogeneous Catalysis*. Vol. 1-5. 1997, VCH: Weinheim.
- [4] H. Topsøe, *Stud. Surf. Sci. Cat.* 130 (2000) 1.

- [5] G. Binnig and H. Rohrer, *Rev. Mod. Phys.* 59(3) (1987) 615.
- [6] F. Besenbacher, *Rep. Prog. Phys.* 59 (1996) 1737.
- [7] J.C. Chen, *Introduction to Scanning Tunneling Microscopy*, Oxford: Oxford University Press, Inc., 1993.
- [8] R. Wiesendanger, *Scanning Probe Microscopy and Spectroscopy*, Cambridge: Cambridge University Press, 1994.
- [9] J. Winterlin, *Adv. Catal.* 45 (2000) 131.
- [10] R. Schaub, E. Wahlström, A. Rønnau, E. Lægsgaard, I. Stensgaard, and F. Besenbacher, *Science* 299 (2003) 377.
- [11] H. Over, Y.D. Kim, A.P. Seitsonen, S. Wendt, E. Lundgren, M. Schmid, P. Varga, A. Morgante, and G. Ertl, *Science* 287 (2000) 1474.
- [12] T. Zambelli, J.V. Barth, J. Winterlin, and G. Ertl, *Nature* 390 (1997) 495.
- [13] H. Topsøe, B.S. Clausen, and F.E. Massoth, *Hydrotreating Catalysis, Science and Technology*, (J.R. Anderson and M. Boudart, eds.). Vol. 11, Berlin: Springer Verlag, 1996.
- [14] R. Prins, in *Handbook of Heterogeneous Catalysis*, (G. Ertl, H. Knözinger, and J. Weitkamp, eds.) 1997, VHC: Weinheim. p. 1908.
- [15] D.D. Whitehurst, T. Isoda, and I. Mochida, *Adv. Catal.* 42 (1998) 345.
- [16] T. Kabe, A. Ishihara, and W. Qian, *Hydrodesulfurization and Hydrogenation - Chemistry and Engineering*, Kodansha: Wiley-VCH, 1999.
- [17] J.W. Gosselink, *Cattech* 4 (1998) 127.
- [18] T.G. Parham and R.P. Merrill, *J. Catal.* 85 (1984) 295.
- [19] B.S. Clausen, B. Lengeler, R. Candia, J. Als-Nielsen, and H. Topsøe, *Bull. Soc. Chim. Belg.* 90 (1981) 1249.
- [20] M. Boudart, R.A. Dalla-Batta, K. Foger, D.G. Lffler, and M.G. Samant, *Science* 228 (1985) 717.
- [21] H. Topsøe and B.S. Clausen, *Catal. Rev.-Sci. Eng.* 26 (1984) 395.
- [22] M. Salmeron, G.A. Somorjai, A. Wold, R. Chianelli, and K.S. Liang, *Chem. Phys. Lett.* 90 (1982) 105.
- [23] J.V. Barth, H. Brune, G. Ertl, and R. Behm, *Phys. Rev. B* 42(15) (1990) 9307.
- [24] S. Helveg, J.V. Lauritsen, E. Lægsgaard, I. Stensgaard, J.K. Nørskov, B.S. Clausen, H. Topsøe, and F. Besenbacher, *Phys. Rev. Lett.* 84 (2000) 951.
- [25] J.V. Lauritsen, S. Helveg, E. Lægsgaard, I. Stensgaard, B.S. Clausen, H. Topsøe, and F. Besenbacher, *J. Catal.* 197 (2001) 1.
- [26] J. Tersoff and D.R. Hamann, *Phys. Rev. B* 31 (1985) 805.
- [27] K.K. Kam and B.A. Parkinson, *J. Phys. Chem.* 86 (1982) 463.
- [28] M.V. Bollinger, J.V. Lauritsen, K.W. Jacobsen, J.K. Nørskov, S. Helveg, and F. Besenbacher, *Phys. Rev. Lett.* 87(19) (2001) 196803.
- [29] M.V. Bollinger, K.W. Jacobsen, and J.K. Nørskov, *Phys. Rev. B* 67 (2003) 085410.

- [30] J.V. Lauritsen, M. Nyberg, J.K. Nørskov, B.S. Clausen, H. Topsøe, E. Lægsgaard, and F. Besenbacher *J. Catal.* 224 (2004) 94.
- [31] J.V. Lauritsen, M. Nyberg, R.T. Vang, M.V. Bollinger, B.S. Clausen, H. Topsøe, K.W. Jacobsen, F. Besenbacher, E. Lægsgaard, J.K. Nørskov, and F. Besenbacher, *Nanotech.* 14(3) (2003) 385.
- [32] W. Niemann, B.S. Clausen, and H. Topsøe, *Catal. Lett.* 4 (1990) 355.
- [33] S.P.A. Louwers and R. Prins, *J. Catal.* 133 (1992) 94.
- [34] S.M.A.M. Bouwens, J.A.R. van Veen, D.C. Koningsberger, V.H.J.d. Beer, and R. Prins, *J. Phys. Chem.* 95 (1991) 123.
- [35] L.S. Byskov, J.K. Nørskov, B.S. Clausen, and H. Topsøe, *J. Catal.* 187 (1999) 109.
- [36] P. Raybaud, J. Hafner, G. Kresse, S. Kasztelan, and H. Toulhoat, *J. Catal.* 190 (2000) 128.
- [37] B. Hinnemann, J.K. Nørskov, and H. Topsøe, *J. Phys. Chem. B* (2005) in print.
- [38] P. Zeuthen and L. Skyum, *Hydrocarbon Engineering* 11 (2004) 65.
- [39] J.R. Rostrup-Nielsen, J. Sehested, and J.K. Nørskov, *in Advances in Catalysis, Vol 47*, eds.). 2002. p. 65.
- [40] J.R. Rostrup-Nielsen, *in CATALYSIS - Science and Technology*, (J.R. Anderson and M. Boudart, eds.). 1984, Springer-Verlag: Berlin. p. 1.
- [41] J.R. Rostrup-Nielsen and T. Rostrup-Nielsen, *CATTECH* 6(4) (2002) 150.
- [42] S. Helveg, C. Lopez-Cartes, J. Sehested, P.L. Hansen, B.S. Clausen, J.R. Rostrup-Nielsen, F. Abild-Pedersen, and J.K. Nørskov, *Nature* 427(6973) (2004) 426.
- [43] H.S. Bengaard, J.K. Nørskov, J. Sehested, B.S. Clausen, L.P. Nielsen, A.M. Molenbroek, and J.R. Rostrup-Nielsen, *J. Catal.* 209(2) (2002) 365.
- [44] J.R. Rostrup-Nielsen, *Journal of Catalysis* 85 (1984) 31.
- [45] V. Ponc, *Appl. Catal. A* 222(1-2) (2001) 31.
- [46] J.H. Sinfelt, *Bimetallic catalysts, Discoveries, Concepts, and Applications*, New York: Wiley, 1983.
- [47] L.P. Nielsen, F. Besenbacher, I. Stensgaard, E. Lægsgaard, C. Engdahl, P. Stoltze, K.W. Jacobsen, and J.K. Nørskov, *Phys. Rev. Lett.* 71 (1993) 754.
- [48] F. Besenbacher, L.P. Nielsen, and P.T. Sprunger, *in The Chemical Physics of Solid Surfaces and Heterogeneous Catalysis*, (D.A. King and D.P. Woodruff, eds.). 1996, Elsevier: Amsterdam.
- [49] F. Besenbacher, L.P. Nielsen, and P.T. Sprunger, *in Chemical Physics of Solid Surfaces and Heterogeneous Catalysis*, eds.). 1997, Elsevier Science Publishers. p. Chapter 10.
- [50] J. Jacobsen, L.P. Nielsen, F. Besenbacher, I. Stensgaard, E. Lægsgaard, T. Rasmussen, K.W. Jacobsen, and J.K. Nørskov, *Phys. Rev. Lett.* 75 (1995) 489.
- [51] F. Besenbacher, I. Chorkendorff, B.S. Clausen, B. Hammer, A.M. Molenbroek, J.K. Nørskov, and I. Stensgaard, *Science* 279 (1998) 1913.
- [52] B. Hammer, private communication.
- [53] H.S. Taylor, *Proc. R. Soc. London, Ser. A* 108 (1925) 105.
- [54] T. Zambelli, J. Wintterlin, J. Trost, and G. Ertl, *Science* 273 (1996) 1688.

- [55] S. Dahl, A. Logadottir, R.C. Egeberg, J.H. Larsen, I. Chorkendorff, E. Törnquist, and J.K. Nørskov, *Phys. Rev. Lett.* 83(9) (1999) 1814.
- [56] J. K. Nørskov, T. Bligaard, A. Logadottir, S. Bahn, L. B. Hansen, M. Bollinger, H. Benggaard, B. Hammer, Z. Sljivancanin, M. Mavrikakis, Y. Xu, S. Dahl, and C.J.H. Jacobsen, *J. Catal.* 209(2) (2002) 275.
- [57] Z.P. Liu and P. Hu, *J. Am. Chem. Soc.* 125 (2003) 1958.
- [58] T. Zubkov, G.A. Morgan Jr., J.T. Yates Jr., O. Köhlert, M. Lisowski, R. Schillinger, D. Fick, and H.J. Jänsch, *Surf. Sci.* 526 (2003) 57.
- [59] P. Gambardella, Z. Sljivancanin, B. Hammer, M. Blanc, K. Kuhnke, and K. Kern, *Physical Review Letters* 87 (2001) 056103.
- [60] I.M. Ciobică and R.A.v. Santen, *J. Phys. Chem. B* 107(16) (2003) 3808.
- [61] R.T. Vang, K. Honkala, S. Dahl, E.K. Vestergaard, J. Schnadt, E. Lægsgaard, B.S. Clausen, J.K. Nørskov, and F. Besenbacher *Nature Materials* 4 (2005) 160.
- [62] B.L.M. Hendriksen and J.W.M. Frenken, *Phys. Rev. Lett.* 89 (2002) 046101.
- [63] P. Thostrup, E.K. Vestergaard, T. An, E. Laegsgaard, and F. Besenbacher, *J. Chem. Phys.* 118(8) (2003) 3724.
- [64] L. Österlund, P.B. Rasmussen, P. Thostrup, E. Lægsgaard, I. Stensgaard, and F. Besenbacher, *Phys. Rev. Lett.* 86(3) (2001) 460.

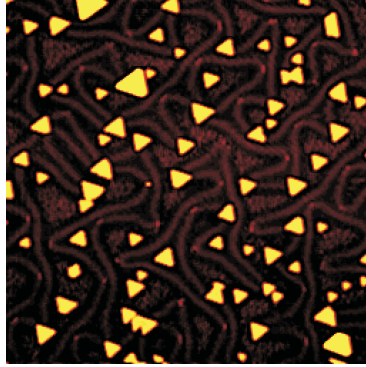


Figure 1:

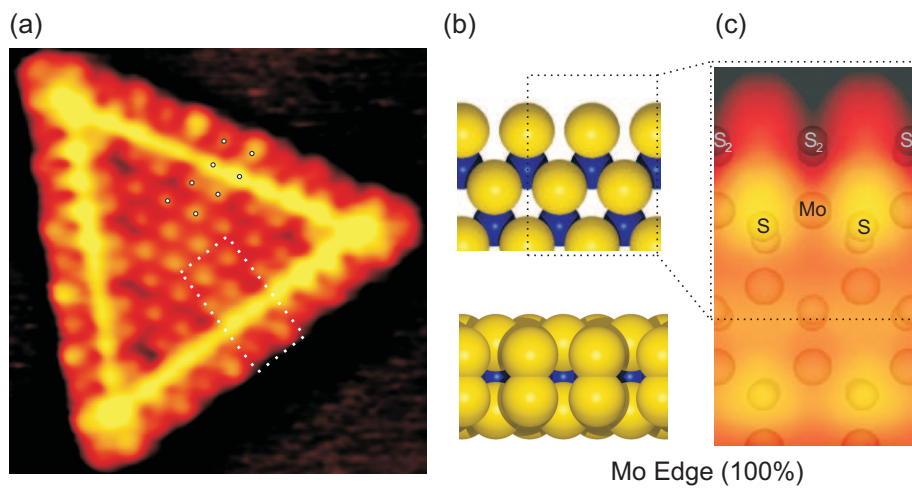


Figure 2:

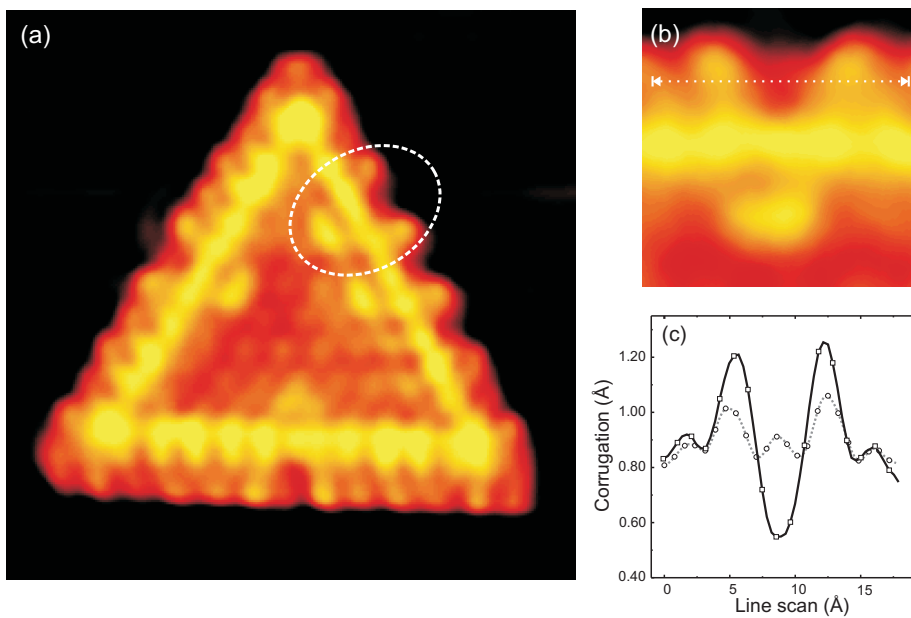


Figure 3:

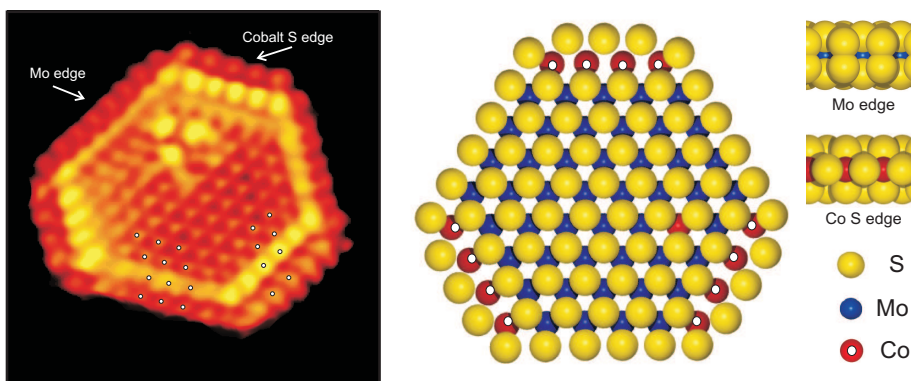


Figure 4:

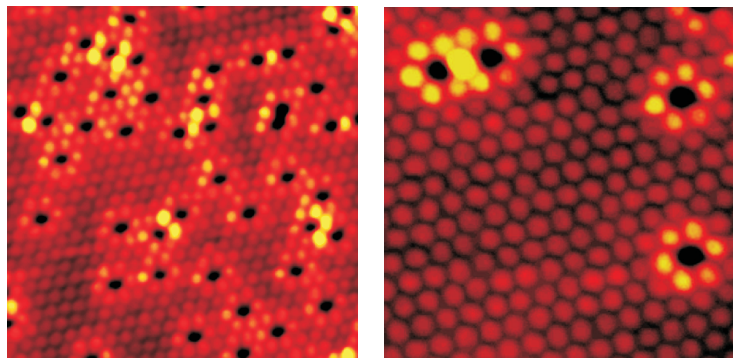


Figure 5:

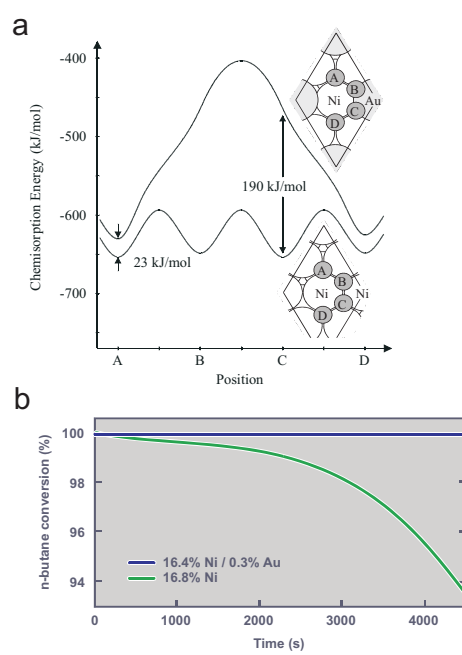


Figure 6:

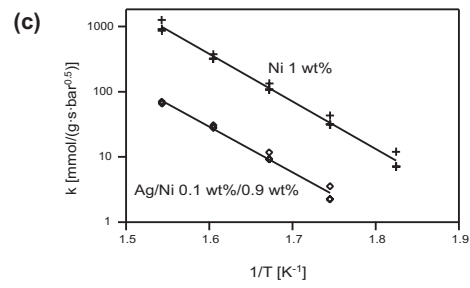
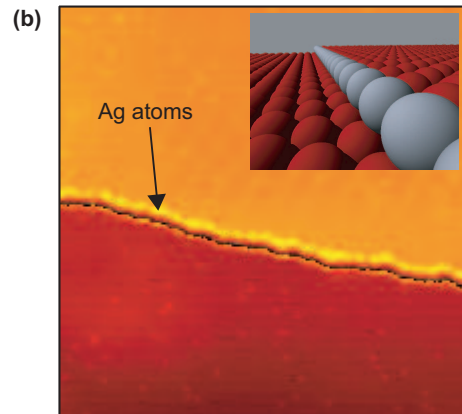
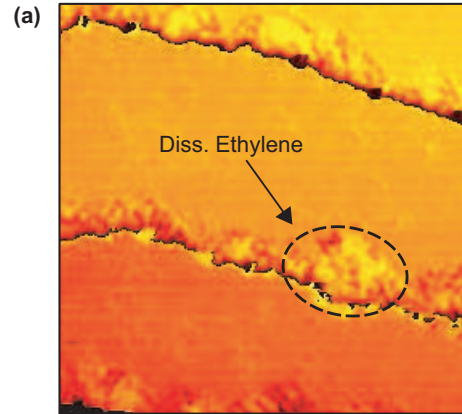


Figure 7:

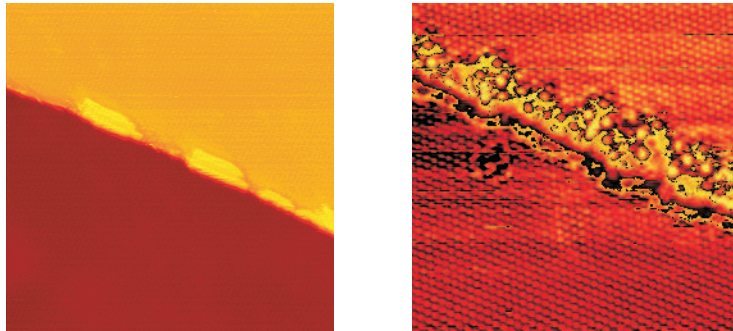


Figure 8: